Saharan dust deposition in the equatorial North Atlantic Ocean and its impact on particle export fluxes

Korte, L.F.

2018

document version
Publisher's PDF, also known as Version of record

VRIJE UNIVERSITEIT

Saharan dust deposition in the equatorial North Atlantic Ocean and its impact on particle export fluxes

ACADEMISCH PROEFSCHRIFT

ter verkijging van de graad Doctor of Philosophy
aan de Vrije Universiteit Amsterdam,
op gezag van de rector magnificus
prof.dr. V. Subramaniam,
in het openbaar te verdedigen
ten overstaan van de promotiecommissie
van de Faculteit der Bètawetenschappen
op dinsdag 16 oktober 2018 om 11.45 uur
in de aula van de universiteit,
De Boelelaan 1105

door

Laura Franziska Korte

geboren te Coesfeld, Duitsland

promotor: prof.dr. G.J.A. Brummer

copromotor: dr. J.B.W. Stuut

Members of the dissertation committee (in alphabetical order):

dr. C.J. Beets

prof.dr. K. Desboeufs

dr. C. Guieu

prof.dr. T. Jickells

prof.dr.dr.h.c. G. Wefer

prof.dr. G.R. van der Werf

This research was funded by the European Research Council (no. 311152):

DUSTTRAFFIC - Transatlantic fluxes of Saharan dust: changing climate through fertilising the ocean?

ISBN: 978-94-028-1131-5

Printed by Ipskamp Printing

Continents on the cover were taken from freepik.com

Contents

Summary

This thesis investigates the effects of Saharan dust deposition in the equatorial North Atlantic Ocean underneath the most prominent dust plume at 12°N. For the first time, Saharan dust transport and deposition was monitored from source to sink along a transect of five stations across the equatorial North Atlantic from 23°W in the east to 57°W in the west. Sediment traps at 1200 m and 3500 m water depth collected marine particle fluxes simultaneously and synchronously between October 2012 and October 2014. The traps were deployed and recovered during three research cruises (Stuut et al., 2012; 2013; 2015). In addition, bottle incubation experiments were carried out and drifting traps were deployed during two cruises (Stuut et al., 2015; 2016), while Saharan dust from the atmosphere was sampled shipboard on all cruises. All these observations and measurements are essential parts of this thesis, addressing:

1) the spatial and temporal variability in marine particle fluxes along the transect,
2) the potential of Saharan dust to act as fertilizer for primary production,
3) the interplay between Amazon River freshwater input, Saharan dust deposition, nitrogen fixation by cyanobacterial plankton, and ocean mixed-layer deepening in the western Atlantic Ocean,
4) the ballasting effect of Saharan dust accelerating the settling of organic matter aggregates.

The results of this study provide an understanding of Saharan dust deposition in the equatorial North Atlantic Ocean and give new insights into open-ocean particle fluxes that hitherto were poorly known. Consequently, the study contributes to our knowledge of the dust's role in the global carbon cycle, and subsequently, global climate. Since dust measurements are of interest to many disciplines working on climate change in the past and future, the field data obtained during this study will help to refine global particle fluxes and predictions of future climate scenarios.

The main findings from the first-year particle-sampling campaign in 2013 show that (1) lithogenic particles collected in the sediment traps are similar to the Saharan dust collected from the atmosphere on the African coast, and (2) that with increasing distance from the source, lithogenic elements associated with clay minerals become more important relative to quartz, which settles out closer to the dust sources (Korte et al., 2017). Such preferential particle settling is considered to affect the dust's radiative properties, influencing the Earth's atmosphere's incoming solar radiation (Li et al., 1996; Sokolik and Toon, 1999), which also depends on the dust abundance and particle size (Mahowald et al., 2014; Kok et al., 2017).

This study shows that closest to the source at 12°N and 23°W, the lithogenic particle flux is higher during summer and fall and lower during winter and spring. This is attributed to precipitation pattern and the different active wind systems in summer and winter (Moulin et al., 1997; Adams et al., 2012; Yu et al., 2015a). In summer and fall dust is transported within the Saharan air layer at high altitudes and mainly deposited by rain under the influence of the Intertropical Convergence Zone. This is also the time when dust outbreaks to the arrival in the sediment traps can be traced back best using satellite images. In winter, when dust is transported at lower altitudes, dust observation on satellite images might be obscured by cloud coverage. In addition, tracing back individual dust outbreaks from satellite images until arrival in the sediment traps is hampered by the lower sampling resolution of the traps, the time lags involved for particle settling and lateral dust transport in between.

The lithogenic particle flux from sediment traps is usually calculated from the total mass flux by using conventional conversion factors (Wefer and Fischer, 1993; Fischer et al., 2007; Fischer and Karakas, 2009) for biogenic calcium carbonate ($CaCO_3$), organic matter (OM) and biogenic silica ($BSiO_2$). Biogenic bulk fluxes are subtracted from the total mass, which then yields the lithogenic (dust) fraction. However, in this study application of these conversion factors appears to overestimate this lithogenic fraction, especially in the conversion of organic carbon to organic matter, and ignoring the water content of the biogenic silica fraction (Mortlock and Froelich, 1989). Indeed, the measured dust fraction was 2 to 18 times lower than the calculated fraction using the conventional conversion factors (Chapter 3). Still, the patterns are similar showing seasonality with high fluxes in summer and fall and low fluxes in winter and spring. However, when working with the lithogenic fraction derived from marine particle fluxes, one should be aware of how the mass fractions were analyzed and interpreted.

The dust amount deposited into the surface waters is also important regarding the potential nutrient input for primary productivity. To what extent Saharan dust would stimulate marine productivity was tested empirically in bottle incubation experiments for both dry and wet Saharan dust deposition. Two types of Saharan dust with grain-size distributions similar to those observed along the transect (Van der Does et al., 2016) were used in low (0.25 mg L^{-1}) and high (1.5 mg L^{-1}) concentrations. For wet dust deposition the added dust was exposed to artificial low pH rain (H_2SO_4, pH = 2) to mimic cloud processing in the atmosphere before amending the oceanic surface waters in the incubation bottles, while the dust for dry deposition was added to the ocean surface waters untreated. Results show large differences between dry

and wet Saharan dust deposition. While dry deposition did not increase nutrient concentrations, wet deposition resulted in elevated phosphate (P), silicate (Si) and dissolved iron (DFe) concentrations in the surface waters when dust deposition was high ($\geq$ 1.5 mg L^{-1}). Although the experiment showed that Saharan dust has the potential to deliver macro- and micronutrients (P, Si, DFe) to the ocean, a major fertilization impact from these nutrients in terms of picophytoplankton and organic-carbon production was not observed. This is most likely due to a missing nitrogen source in the nitrogen limited Atlantic Ocean. However, even without a fertilization effect, Saharan dust might have an impact on marine particles in as much as the dust is incorporated into organic matter aggregates, the so-called 'marine snow'. Marine snow becomes denser and is therefore ballasted, accelerating aggregate settling through the water column after dust deposition. Both wet and dry deposition resulted in equally high organic carbon concentrations at the end of the experiment suggesting that marine snow formation is more effective with Saharan dust in the incubation bottles. However, such ballasting effects could not be determined in the bottle experiments.

In the western Atlantic Ocean, a combination of different processes was observed influencing the marine particle fluxes. It was found that the Amazon River disperses far into the open ocean and affects surface waters seasonally to at least 49°W and 12°N when the freshwater is carried by the retroflecting North Brazil Current (Muller-Karger et al., 1988). The Amazon impacted the oceanic surface waters by stimulating cyanobacterial nitrogen fixation and diatom diazotrophic productivity in fall. XRF-measurements show that virtually all silica in the west consists of biogenic silica produced by marine biota which may have been fertilized by iron input caused by wet deposition of Saharan dust. While during fall, nutrients in the surface waters were introduced from the top, mixed-layer deepening brought nutrients up into the (sub-) surface in spring triggering a peak in calcium carbonate export. During winter and spring, dry Saharan dust deposition predominates, while increased precipitation from summer onwards, favors wet deposition during late summer and fall. Saharan dust deposition and organic carbon fluxes appear highly correlated during times of wet deposition. This suggests that Saharan dust both stimulates primary productivity and ballasts aggregated organic carbon through the water column, relevant for an effective CO_2 burial.

The ballast theory was tested under natural conditions with freely drifting traps in ten experiments at five sites during two research cruises (Stuut et al., 2015; 2016). These drifting traps collected marine particles at three different depths (100, 200 and

400 m) for 24 hours. Molar C/N ratios of the particle fluxes were used as a proxy for the degradation state of the organic carbon and nitrogen. Since nitrogen compounds in organic matter degrade faster (Gordon, 1971; Schneider et al., 2003), stable molar C/N ratios at different water depths would indicate fast particle settling through the water column with little degradation because of ballasting by Saharan dust. In our experiments, we were fortunate to experience a dust outbreak at one site during each cruise. For the stronger event in January 2015, molar C/N ratios did remain stable implying accelerated particle transport through the water column by Saharan dust ballasting, while without dust in the atmosphere, molar C/N ratios varied with depth.

To conclude, this thesis shows that Saharan dust deposition impacts marine particles fluxes in the equatorial North Atlantic Ocean in several ways. Saharan dust sources emit particles of different mineralogy and grain size that are carried by different wind systems, changing in altitude depending on the season. While mainly coarse and heavy quartz particles are deposited closest to the sources, the finer and platy clay particles are transported much further west. Due to this sorting gradient, wet deposition becomes more important with increasing distance from the sources, washing out the finer particles that do not settle out by gravitation alone.
During transport through the atmosphere the dust is exposed to acid conditions that process the particles by leaching their nutrients and metals. After atmospheric processing the nutrients are more readily released in ocean surface waters particularly when introduced by wet deposition. Indeed, while wet deposition of Saharan dust enhances the release of bio-available macro- and micronutrients (phosphate, silicate and dissolved iron), a nitrogen-nutrient source is vital for phytoplankton growth in the oligotrophic equatorial North Atlantic. Such a nitrogen-nutrient might be introduced into the ocean after dust processing by HNO_3 as atmospheric acid component, by mixed-layer deepening re-introducing nutrients from the subsurface, or by breakdown of organic matter produced by diazotrophic nitrogen fixers.
Especially in the oligotrophic warm waters of the western equatorial North Atlantic Ocean, the interplay of these processes may generate large particle export fluxes relevant to the global organic carbon cycle. In addition, the Amazon River contributes nutrients (e.g. silicate and iron) when retroflected eastward into the North Atlantic Counter Current, thus promoting diatom diazotrophic associations and nitrogen fixation. When Saharan dust is introduced by wet deposition, it will (1) bring additional nutrients and (2) act as ballast material by incorporation into marine snow, enhancing particle export to the deep ocean deep. Export fluxes are also affected by dry dust deposition. Although this type of deposition does not enhance nutrient

concentrations in surface waters, the dust particles will still act as ballasters.
Along the transect, particle export fluxes decreased downwind from east to west with low and dry deposition dominating during winter and high and wet deposition dominating in summer. This gradient implies different predominating processes depending on the state of atmospheric processing, the season and the geographical location, through dry and/or wet deposition, ballasting and/or fertilization, which all impact the magnitude of particle export fluxes and thus the global carbon cycle.

CHAPTER 1

Introduction

1 General introduction

1.1 Mineral dust impacts on climate and ecosystems

Natural aerosols, e.g. mineral dust, soot and smoke, sea salts and sulfates, are ubiquitous components of the Earth's atmosphere. These aerosols affect the Earth's climate by cooling or warming and affect marine and terrestrial life with positive (boosting) or negative (harming) consequences, all to a yet poorly-known extent. Desert dust, being one of the major aerosols, plays multiple roles in mediating physical and biogeochemical exchanges between atmosphere, land and ocean (Harrison et al., 2001; Jickells et al., 2005; Mahowald et al., 2005; Shao et al., 2011). Dust is emitted by aeolian deflation into the atmosphere, transported by winds and deposited by dry or wet deposition over land and ocean (Fig. 1).

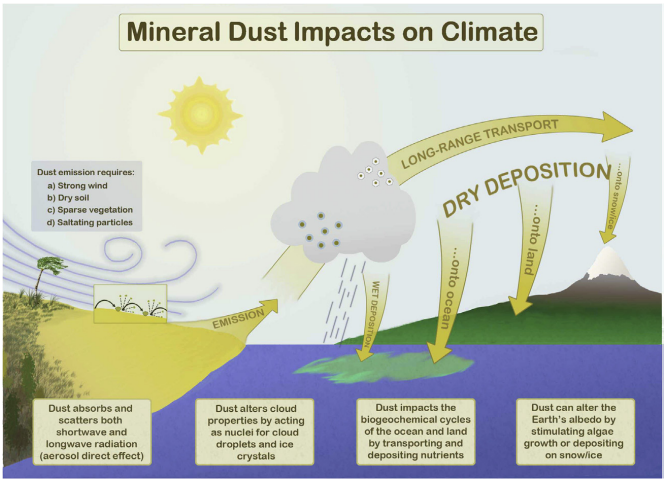

Figure 1. Schematic interactions between dust, climate and biogeochemistry (from Mahowald et al., 2014, with permission).

Mineral dust in the atmosphere has direct and indirect climatic effects. Direct effects include interactions with solar radiation (Sokolik and Toon, 1999; Kok et al., 2018) and darkening of landscapes, changing the Earth's albedo (Yasunari et al., 2015), while indirect effects refer to the dust's ability to alter cloud properties by acting as cloud and ice nuclei (Twomey et al., 1984; DeMott et al., 2003) and to influence precipitation pattern (Rosenfeld et al., 2001; Creamean et al., 2013). All effects depend on the dust's chemical composition, abundance and particle size (Mahowald et al., 2011; Mahowald et al., 2014; Kok et al., 2017). The chemical composition controls the fraction of light absorbed or scattered (Mahowald et al., 2011), and fine- and

coarse-grained particles impact shortwave- and longwave radiation, which generally cools and warms the atmosphere, respectively (Miller et al., 2006; Mahowald et al., 2014). Furthermore, the particle size also determines the distance of transport which in turn impacts the mineral and chemical composition in long-range transported dust (Glaccum and Prospero, 1980; Sarnthein et al., 1981; Van der Does et al., 2016; Korte et al., 2017). While fine-grained and light particles are uplifted more easily and transported much further, coarse and heavy particles are less mobile and settle out closer to the source. Dry and wet deposition are the two processes by which dust is removed from the atmosphere (Duce et al., 1991; Schulz et al., 2012). While dry deposition by gravitation is the dominant removal process of the coarser particles proximal to the arid sources, wet deposition of the remaining dust particles that do not settle by gravitation alone becomes more dominant with increasing distance to the source (Bergametti et al., 1989; Zhao et al., 2003).

Once deposited in the ocean or on land, mineral dust impacts the biogeochemical cycles by delivering nutrients that boost marine and terrestrial life (Martin, 1990; Swap et al., 1992; Jickells et al., 2005; Bristow et al., 2010), but also pathogens that harm it (Shinn et al., 2000; Griffin et al., 2001). Marine- and ice-core archives of dust deposition show an inverse correlation with paleo-temperature and CO_2 levels in the atmosphere (Lambert et al., 2008), suggesting that dust acts as fertilizer by delivering (micro-) nutrients that increase primary production in the ocean (Martin, 1990) and thus result in a reduction of CO_2 by photosynthesis (Falkowski et al., 1998). In addition, mineral dust is needed to ballast marine snow through the water column transporting newly formed organic matter to the deep ocean (Armstrong et al., 2001; Klaas and Archer, 2002; Fischer et al., 2007), eventually sequester CO_2 from the atmosphere (paragraph 1.4). On the other hand, recent studies also show a reduction of CO_2 drawdown due to dust-induced heterotrophic bacterial growth (Marañon et al., 2010; Guieu et al., 2014b) as well as a decline of coral reefs attributed to enhanced dust input (Shinn et al., 2000). In addition to fertilizing and poisoning, the dust particles can affect air quality, and therefore human health (Prospero, 1999).

1.2 Dust sources and meteorological setting

With the aid of modern satellite measurements (e.g. AVHRR, TOMS, CALIPSO) major dust sources, dust activities and dust transport become visible on a global scale (Prospero, 1999; Chiapello and Moulin, 2002; Prospero et al., 2002; Adams et al., 2012; Yu et al., 2015a). Satellite data reveal that the largest and most persistent dust plumes emanate in the Northern Hemisphere, mainly from arid and

semiarid regions in North Africa, the Middle East and Asia (Maher et al., 2010; Adams et al., 2012). The Sahara Desert in northern Africa is by far the strongest dust source (Fig. 2), contributing about 40-60 % to the global dust emission (Prospero, 1996; Ginoux et al., 2001). Earliest Cloud-Aerosol Lidar and Infrared Pathfinder Satellite Observations (CALIPSO) measurements suggest that an estimated 182 Tg of Saharan dust is transported yearly from northwest Africa across the Atlantic Ocean (Yu et al., 2015a). Saharan dust is transported with the wind over and into the North Atlantic Ocean towards the Americas (Prospero, 1999; Prospero et al., 2014; Yu et al., 2015a), the Mediterranean Sea (Bergametti et al., 1989; Stuut et al., 2009), and the Arabian Sea (Tindale and Pease, 1999).

The north-easterly trade winds are dominant throughout the year (Fig. 2) at low altitudes (0.5-1.5 km above sea level) depositing dust from the northwest Sahara (Atlas Mountains, coastal regions of Morocco and parts of northern Sahara) along the African coast onshore and offshore in a zone from the Canary Islands to the Cape Verde Islands (Sarnthein et al., 1981; Stuut et al., 2005). Across the Atlantic Ocean, the Intertropical Convergence Zone (ITCZ) influences the dust transporting wind systems by season (Wefer and Fischer, 1993; Rea, 1994; Stuut et al., 2005; Skonieczny et al., 2013; Prospero et al., 2014; Van der Does et al., 2016, **Chapters 2 and 3**). The ITCZ is a low-pressure zone near the equator where northeast and southeast trade winds converge, forming a region of increased convection, precipitation and cloudiness (Nicholson, 2000; Basha et al., 2015). The ITCZ shifts seasonally from around 12°N in July and around 5°S in January (Basha et al., 2015), with an accompanied dust transport occurring predominantly at 10-20°N during summer and 0-10°N during winter (Yu et al., 2015a). With the southward migration of the ITCZ, the Harmattan winds (Dobson and Fothergill, 1781) intensify from October to May (McTainsh et al., 1997). These winds occur at altitudes below approximately two km (Dubief, 1979) and transports dust from the Central Sahara towards the southwest (Fig. 2). The cold and dry winds can be undercut by warm and moist tropical air which results in an uplift of the dust-laden air and subsequently long-range transport of the dust within the Saharan Air Layer (SAL) towards South America (Prospero et al., 1981). The dust-bearing SAL is thicker during boreal summer when the ITCZ migrates north (Prospero et al., 1970; Carlson and Prospero, 1972; Prospero and Carlson, 1972; Prospero and Lamb, 2003; Tsamalis et al., 2013). The SAL is generated by convergence of moist tropical air from the south and dry hot Saharan air from the north. The dust is lifted by these strong winds and can reach altitudes up to five km near the sources in Africa (Tsamalis et al., 2013). At these altitudes above the trade wind zone, the winds are easterly and therefore the dust is transported far across

the Atlantic Ocean towards North America (Muhs, 2013). Dust transported within the SAL travels with an average speed of 1000 km d^{-1} and can reach Barbados and the Caribbean Islands in about a week after departure of the western African coast (Prospero et al., 1970; Huang et al., 2010).

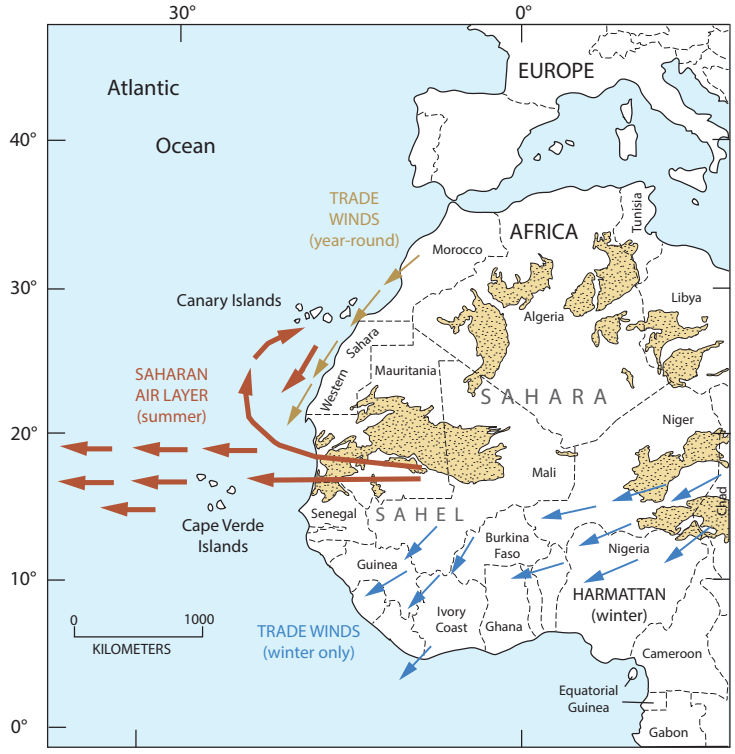

Figure 2. Map showing north-western Africa with major active sand seas (yellow areas) and the three main dust-transporting wind systems (from Muhs, 2013, with permission).

1.3 Cloud processing and fertilization

On the dust's transit across the Atlantic Ocean, it is transferred from the atmosphere into the marine boundary layer by turbulent and convective downward mixing, with gravitational settling of supermicron particles, resulting in changes of the dust's size distribution (Weinzierl et al., 2016), optical properties (Kanitz et al., 2014) and chemical composition (Meskhidze et al., 2003). Dust in the atmosphere is altered by cloud processing (Spokes et al., 1994; Desboeufs et al., 2001), which will leach its metals and nutrients (Herut et al., 2005; Shi et al., 2012). Figure 3 shows a schematic overview of aerosol processing in clouds: hygroscopic aerosol particles,

such as dust, preferentially act as cloud condensation nuclei on which cloud droplets can form (Hoose et al., 2008). These droplets can collect more aerosol particles and other cloud droplets in which atmospheric gases dissolve. As a result, aerosol waters can become highly acidic with a pH as low as 1, especially through strong acids such as H_2SO_4 and HNO_3, produced from industrial SO_2 and NO_x as precursors (Jickells et al., 1982; Zhu et al., 1992; Meskhidze et al., 2003).

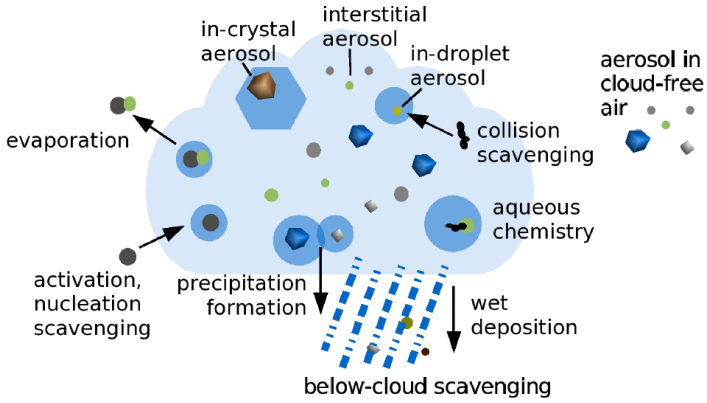

Figure 3. Aerosol processing in clouds showing physical and chemical alteration (from Hoose et al., 2008, with permission).

The low pH aerosol waters leach the extractable constituents from the atmospheric particle (dust), which are consequently transferred to rain drops when precipitation is formed and removed by wet deposition (Hoose et al., 2008, **Chapters 3 and 4**). If no precipitation occurs and the cloud droplets evaporate, the dissolved material crystallizes on insoluble material inside the droplet and forms a new internally mixed aerosol particle (Hoose et al., 2008). Atmospheric dust may be exposed for up to ten condensation-evaporation cloud cycles before removal by rain, progressively processing the dust particles (Spokes et al., 1994). Much attention has been given to iron (Fe) solubility since Fe is an important micronutrient for marine primary production, including diazotrophic nitrogen fixation and phytoplankton photosynthesis (Mills et al., 2004; Jickells et al., 2005; Moore et al., 2009), resulting in a potential drawdown of atmospheric CO_2 when new organic matter is transported towards the deep ocean, with little degradation in the surface waters (paragraph 1.4).

Several large-scale seeding experiments were designed and conducted in so-called high nutrient, low chlorophyll (HNLC) oceans (Martin et al., 1994; Watson et al., 1994; Coale et al., 1996; 1998; 2004; Boyd et al., 2000; 2004), introducing dissolved Fe into the surface waters. Results showed that Fe limits phytoplankton growth but

that the response is only for a short period of time and the fate of algal carbon remains largely unknown. Incubation experiments in the form of bottle incubations, or meso- and microcosm experiments in the Mediterranean Sea (Bonnet et al., 2005; Guieu et al., 2010; Desboeufs et al., 2014; Ridame et al., 2014), and in the North Atlantic Ocean (Blain et al., 2004; Mills et al., 2004) concentrated on fresh and aged Saharan dust seeding. Medium- and small scale incubation experiments showed that aged or leached dust, deposited with rain had a greater effect on phytoplankton growth and chlorophyll-*a* concentrations (Ridame et al., 2014) and nitrogen fixation (Mills et al., 2004), but also lead to enhanced bacterial growth (Guieu et al., 2014b) as opposed to fresh dust. Incubation experiments conducted in the present work (**Chapter 4**) show large differences in nutrient release between dry and wet Saharan dust deposition, however with minor changes in eventual particulate organic carbon production. Other mesocosm experiments revealed that up to 50 % of the particle export can be dust induced (Bressac et al., 2014) and that the export production of particulate organic carbon is higher with wet dust deposition (Desboeufs et al., 2014). Consequently, Saharan dust deposition plays a key role in the biological carbon pump by fertilizing phytoplankton and ballasting particulate organic carbon from the surface waters towards the deep ocean.

1.4 Ballasting and the biological carbon pump

The biological carbon pump (Fig. 4) transfers organic matter (OM) from the sunlit surface waters to the deep ocean (Fowler and Knauer, 1986; Boyd and Trull, 2007; Buesseler et al., 2007). In the sunlit surface waters, nutrients (e.g. nitrate, phosphate, silicate, and iron) and carbon dioxide (CO_2) are fixed during photosynthesis by phytoplankton producing particulate organic carbon (POC) and, depending on the organism, biominerals such as biogenic calcium carbonate ($CaCO_3$, e.g. coccolithophores) or opaline silica ($SiO_2 \cdot xH_2O$, e.g. diatoms, silicoflagellates). Nutrients are introduced into the sunlit surface waters via atmospheric dust deposition (paragraph 1.3), river discharge, meltwater and (submarine-) volcanism, or resuspended by bacterial OM breakdown and mixing of deep water layers. On a global annual mean, newly produced POC contains a molar carbon/nitrogen (C/N) ratio of 6.625 corresponding to the 'Redfield ratio' of 106 C : 16 N (Redfield, 1963, Eq. 1).

$$106\ CO_2 + 122\ H_2O + 16\ NO_3^- + H_2PO_4^- + 3\ H^+ \leftrightarrow [(CH_2O)_{106}(NH_3)\ 16\ H_3PO_4]_{organic} + 138\ O_2 \quad \text{(Eq. 1)}$$

Deviations from the Redfield ratio, however, may occur during settling and degradation processes. As organic carbon has a density close to that of seawater it needs additional ballast to be effectively exported to the deep ocean. Both biominerals and lithogenic particles (mainly dust and riverine clay) will be incorporated into OM aggregates, thus increasing the density of organic carbon and enhancing the settling velocity through the water column by ballasting, resulting in marine particle export fluxes (Deuser et al., 1983; Ittekkot and Haake, 1990; Klaas and Archer, 2002; Iversen and Robert, 2015). Also, OM is processed by a complex biological food web (Laws et al., 2000) and compressed into fecal pellets, having a relatively high sinking velocity (Ploug et al., 2008). Settling velocities of marine particle export fluxes are in the order of a few hundred m d^{-1} (Knappertsbusch and Brummer, 1995; Ploug et al., 2008; Armstrong et al., 2009; Lee et al., 2009).

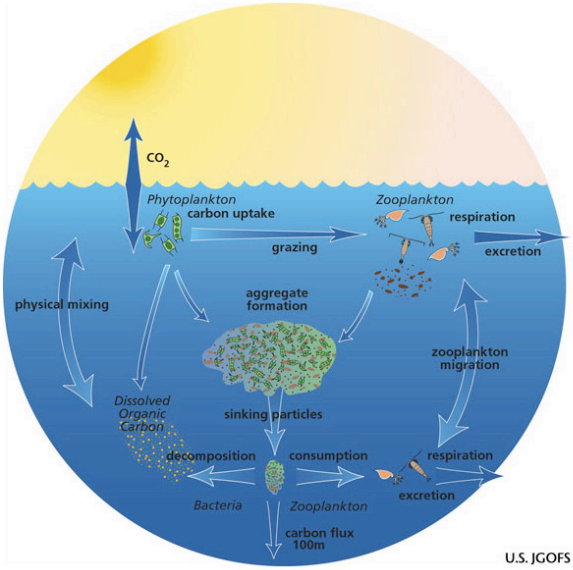

Figure 4. Sketch showing the biological carbon pump with particle export towards the deep ocean. © United States Joint Global Ocean Flux Study.

While the role of biominerals in ballasting OM is obvious in the global ocean, with calcium carbonates being more efficient than opaline silica, the effect of lithogenic particles is less clear (Francois et al., 2002). Due to the subordinate contribution of lithogenic particles compared to biominerals in open ocean mass fluxes, lithogenic particles become increasingly important towards the continental margins where riverine and dust deposition is relatively high. Off Cape Blanc, Mauritania, lithogenic particles introduced from the Saharan Desert are the second-most important component of the total flux and contribute up to 50 % to the total mass (Nowald et al.,

2015). There, incubation experiments showed that Saharan dust enhances aggregate formation in a natural plankton community in the surface waters (Van der Jagt et al., 2018). These dust-ballasted aggregates have a higher size-specific sinking velocity than non-ballasted aggregates and thus settle more quickly (Van der Jagt et al., 2018).

Another point of view is discussed by Passow and De la Rocha (2006) who argue that at times the concentration of particulate organic carbon (POC), rather than the concentration of ballast, may limit the formation of sinking aggregates. However that be, ballasting by biotic or abiotic minerals is important for organic particle acceleration and therefore in the drawdown of atmospheric CO_2 into the deep ocean through the biological pump (Longhurst and Glen Harrison, 1989; Ittekkot and Haake, 1990; Ittekkot, 1993; Rixen et al., 2005; Honjo et al., 2008).
Rapid settling through ballasting will shorten the residence time of OM in the water column, decreasing the exposure time to bacterial breakdown, thus reducing the release of CO_2 and regeneration of nutrients for upper ocean productivity. Since nitrogen-rich organic compounds degrade more rapidly than organic carbon-rich compounds, nitrogen-nutrients will preferentially be removed from the upper ocean which leads to higher molar C/N ratios in the degraded settling particles at depth (Gordon, 1971; Anadón et al., 2002; Schneider et al., 2003), a property that is used in this study to assess the impact of Saharan dust ballasting on organic matter transport to the deep ocean (**Chapter 6**). Pabortsava et al. (2017) investigated the relative involvement of lithogenic and biogenic ballast phases on POC export fluxes in the oligotrophic North Atlantic gyre and argued that lithogenic particles were more important than biogenic particles due to high Saharan dust input.

1.5 Surface ocean currents in the equatorial North Atlantic Ocean

Main surface ocean currents are driven and influenced by the prevailing wind systems (paragraph 1.2, Fig. 5) and an important pathway to carry nutrients. In the northeast Atlantic, the cold Canary Current (CC) entrains nutrient-rich upwelled water from the coast and flows along the west African coast south of 33°N and detaches from the continental margin between 25 and 20°N from where it gradually turns into the North Equatorial Current (Mittelstaedt, 1991). The North Equatorial Current (NEC) is the dominant open ocean surface currents across the oligotrophic North Atlantic. The NEC is driven by the north-easterly trade winds and found approximately between 7 and 20°N (see Fig. 1 in Schott et al., 2002). South of the NEC flows the North Equatorial Counter Current (NECC) in eastward direction counter to the wind (Stramma and Schott, 1999).

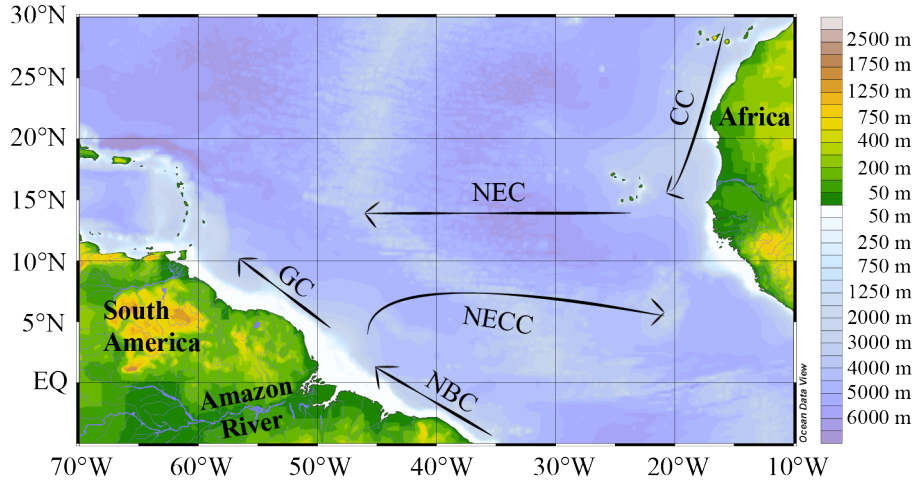

Figure 5. Map illustrating ocean surface currents in the North Atlantic Ocean. CC = Canary Current, NEC = North Equatorial Current, NECC = North Equatorial Counter Current, NBC = North Brazil Current (retroflected into the NECC from June to January), GC = Guiana Current. Color bar displays topography on land and bathymetry in the ocean.

The NECC is formed by the northward shift of the trade winds in May-June but weakens and disappears west of 18°W in winter. At the same time, the warm North Brazil Current (NBC) in the northwest Atlantic carries water from the South Atlantic to the North Atlantic while crossing the equator north-westward following the east Brazilian coast (Masson and Delecluse, 2001). At the equator, it carries the nutrient rich Amazon River outflow waters and forms the Guiana Current (GC) further northwest. From June to January, when the NECC is present, the NBC is partly retroflected after crossing the equator and is flowing eastward into the NECC, carrying the Amazon River discharge towards Africa (Muller-Karger et al., 1988, **Chapter 5**).

1.6 Particle fluxes in the North Atlantic Ocean

Marine particle flux studies which involve Saharan dust, are generally concentrated on one or the other side of the North Atlantic Ocean, i.e., either off northwest Africa or in the Caribbean. Particle fluxes in the ocean are mainly determined using time-series sediment traps at different depth in moorings anchored to the ocean floor. By far the longest time-series is the 30-year record collected in the eastern North Atlantic by colleagues of the University of Bremen, using sediment traps moored on the Mauritanian continental slope off Cape Blanc (Wefer and Fischer, 1993; Ratmeyer et al., 1999a, b; Fischer et al., 2007; Nowald et al., 2015; Fischer et al., 2016). Here it was shown that lithogenic dust particles are a major contributor to

the total mass flux enhancing the settling of organic matter through the water column (paragraph 1.4). Similar studies carried out within the framework of the Joint Global Ocean Flux Study (JGOFS) and the Biogeochemical Ocean Flux Study (BOFS), also contributed greatly to our knowledge of particle export fluxes in contrasting oceanographic environments affected by mineral dust (Newton et al., 1994; Jickells et al., 1996; Bory and Newton, 2000; Bory et al., 2001; 2002; Waniek et al., 2005).

Lithogenic material in the eastern North Atlantic Ocean off northwest Africa shows great seasonality in export fluxes and grain sizes, with finer-grained material and higher fluxes in winter and (early) spring and coarser-grained particles and lower fluxes in summer. This can be attributed to the active wind systems (paragraph 1.2, Ratmeyer et al., 1999a, b), or coastal upwelling and the winter bloom (Neuer et al., 2002; Nowald et al., 2015). Lithogenic material (dust fluxes) are often estimated by subtracting the biogenic phases (organic matter, calcium carbonate and opaline silica) from the total mass flux (Wefer and Fischer, 1993; Fischer et al., 2007; Thunell et al., 2007; Fischer and Karakas, 2009), or derived from the samples' aluminum (Al) content (Deuser et al., 1983; Jickells et al., 1990; Bory and Newton, 2000), assuming that lithogenic material is 8.4 % Al (Turekian and Wedepohl, 1961).
Lithogenic material makes up around 20-30% of the total mass in the eastern North Atlantic Ocean (Bory and Newton, 2000; Fischer et al., 2016) but can reach 50 % during dust events (Nowald et al., 2015). Results show that bulk export fluxes are higher in the upwelling area and mesotrophic North Atlantic Ocean when compared to oligotrophic sites, and that the proportion of lithogenic material decreases accordingly towards the open ocean (Fischer et al., 1996; Bory and Newton, 2000).

In the western tropical North Atlantic Ocean, lithogenic material still represents 8-30 % of the total material and increases with depth (Honjo et al., 1982). The increase is attributed to the catchment area of the sediment traps, which expands and becomes wider with increasing sediment trap depth (Siegel and Deuser, 1997; Waniek et al., 2000). Deuser et al. (1988) already speculated about Saharan dust particles affecting the variability of particle export in the western tropical North Atlantic and recent findings from Pabortsava et al. (2017) support an effective and fast Saharan-dust induced particle export to the deep ocean in their comparison of mass fluxes collected in the center of the northern and southern central gyre of the North Atlantic.

On land, Saharan dust is collected on the West African margin (Skonieczny et al., 2011; 2013; Friese et al., 2017), as well as on the opposite side of the North Atlantic mainly on Barbados, Florida and the northeast coast of South America (Prospero and Nees, 1986; Prospero and Lamb, 2003; Prospero et al., 2010; 2014). Dust concentrations

reveal a strong seasonality, with higher dust concentrations in winter and spring on the West African margin and the South American continent, and higher concentrations in summer on Barbados and Florida. On the West African margin at M'bour median dust concentrations are 76.6 µg m^{-3} but can reach a maximum of 2250 µg m^{-3} (Marticorena et al., 2010), while in Cayenne, at the other side of the ocean, dust concentrations decrease to a mean of 28 µg m^{-3} and show maximum concentrations of around 200 µg m^{-3} during spring (Prospero et al., 2014). On Barbados dust concentrations range between 20-30 µg m^{-3}, peaking up to > 100 µg m^{-3} during summer (Prospero and Nees, 1986; Prospero et al., 2002). The seasonality is related to the wind systems (paragraph 1.2) shifting the dust plume northwards during summer and southwards during winter.

2 Thesis motivation

Although much is known about Saharan dust proximal to the sources and continents, with its different impact on primary productivity and marine particle export fluxes, the fate of Saharan dust, especially between Africa and the Caribbean remains still largely unknown. Due to the vastness of the Atlantic Ocean, data are often restricted to Saharan dust concentrations in the atmosphere and optical aerosol properties as observed by remote sensing (Liu et al., 2008; Huang et al., 2010; Yu et al., 2015a), shipboard lidar measurement (Kanitz et al., 2014) and *in-situ* aircraft measurements (Weinzierl et al., 2016). In addition, estimates of future dust abundances are still associated with large uncertainties due to several necessary assumptions in the models, and thus ranging from a 60 % decrease to a factor of three increase (Mahowald and Luo, 2003; Tegen et al., 2004; Woodward et al., 2005), making climate predictions challenging. Therefore, it needs to be investigated:

1) how much dust is actually being deposited across the North Atlantic Ocean using time-series of *in-situ* measurements and
2) if Saharan dust acts both as a potential fertilizer for primary productivity and transport agent of organic matter to the deep ocean.

Such observations would reveal valuable insights into the spatial and temporal deposition of Saharan dust and its impact on the particle export fluxes that are important for the global carbon cycle and thus climate. Hence, this thesis, in the framework of the DUSTTRAFFIC project, aims to contribute to reducing the gap of knowledge of Saharan dust deposition in the Atlantic Ocean and its impact on particle export fluxes.

2.1 Experimental Set-up

In order to investigate the spatial and temporal marine particle export fluxes, including Saharan dust, underneath the Earth's most prominent dust plume, an array of five moorings (M1-M5) were deployed during RV *Meteor* cruise M89 (Stuut et al., 2012) in the Atlantic Ocean at 12°N (Fig. 6a). The array was in between the sediment record off Cape Blanc in the east North Atlantic Ocean, and the dust record on Barbados in the west North Atlantic Ocean. Initially, two sediment traps at 1200 m (upper, U) and 3500 m (lower, L) water depth at each mooring were deployed (Fig. 6b) and recovered and redeployed during RV *Pelagia* cruises 64PE378 and 64PE395 (Stuut et al., 2013; 2015).

The sediment traps sampled sinking particle fluxes continuously between 8-16 days from October 2012 to October 2014. After recovery, all sediment trap samples were split into subsamples targeting on different analyses (**Chapter 8, appendix A1**, splitting procedure). Next to the moored sediment traps, drifting sediment traps were deployed at several locations during two cruises, RV *Pelagia* 64PE395 and RRS *James Cook* JC134 (Stuut et al., 2015; 2016), sampling sinking particle fluxes for 24 hours at 100, 200 and 400 m water depth (Fig. 6b). Incubation experiments comprising Saharan dust additions were conducted at three stations along the transect (Fig. 6b) during the RRS *James Cook* JC134 cruise (Stuut et al., 2016), while during all cruises Saharan dust from the atmosphere was sampled shipboard by high volume dust collectors.

In addition to samples taken on board, on-land sediment traps (modified Wilson and Cook samplers, MWAC, Goossens and Offer (2000)) were placed at the Mauritanian coast in Iouîk (Fig. 6b) sampling on a monthly resolution, starting in January 2012.

Also, within the project, two dust-collecting floating buoys (Michelle and Laura) were deployed for the first time during the RV *Pelagia* cruise 64PE378 along the transect at 12°N, and one dust collecting floating buoy (Carmen) off Cape Blanc (Fig. 6b), where deep ocean mass fluxes are collected since 30 years (Fischer et al., 2016). The buoys were built at NIOZ, in close collaboration with the MARUM, after a prototype of Sholkovitz et al. (1998), and are still developing and improving. They are continuously recording meteorological data, and they are actively sampling dust from the atmosphere by filtering dust-loaded air through cellulose acetate filters at the same resolution as the submarine sediment traps (Van der Does, 2018, PhD thesis Chapter 6).

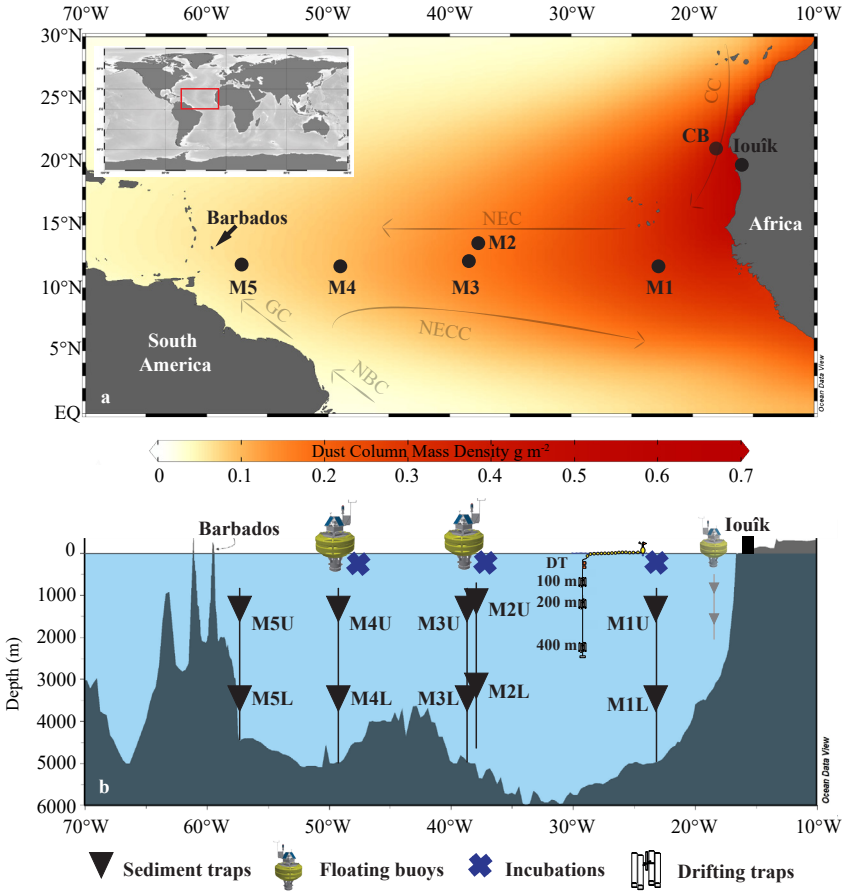

Figure 6. Schematic overview of the experimental set-up. a) Map showing the transect with five mooring locations M1-M5 in the equatorial North Atlantic Ocean between northwest Africa (sediment trap location off Cape Blanc = CB) and Barbados. While M1, M3, M4, and M5 are located at 12°N, M2 is positioned at 13.5°N to access for lateral movement of the Saharan dust plume. Location of on-land dust collector in Iouîk is indicated on the African continent. Orange color shading displays dust column mass density in the atmosphere, data obtained from the Giovanni online data system (MERRA-2, monthly temporal resolution, 0.5 x 0.625° spatial resolution over 10 years 2006-2016), developed and maintained by the NASA Goddard Earth Sciences Data and Information Services Center (GES DISC) (disc.sci.gsfc.nasa.gov). Transparent arrows indicate main ocean surface currents (cf. Fig. 5).
b) Profile sketch (not to scale) showing the initial mooring set-up with sediment traps at 1200 m and 3500 m water depth, the on-land MWAC sampler in Iouîk, the location of the incubation experiments, a schematic sketch of the drifting traps (DT), and the positions of the floating buoys at M3 (Michelle) and M4 (Laura) along the transect and CB (Carmen), where also sediment traps are collecting deep ocean fluxes since 30 years (Fischer et al., 2016).

2.2 Chapter overview

Chapter 2 has been published in Atmospheric Chemistry and Physics (Korte et al., 2017) and focuses on the temporal (year 2013) and spatial (M1-M5) downward particle fluxes from the marine sediment traps and compares the residual mass fraction (lithogenic material) to the chemical composition of the terrestrial dry dust samples from Iouîk (raw data of marine particle fluxes in Appendix A3, analyzed particle flux data). The first-year results showed that particle fluxes were highest, and seasonality strongest, at both ends of the trans-Atlantic transect (M1 and M5) closest to the African and South American continent, respectively. While the seasonality was dominated by biogenic silica at the westernmost station M5, the seasonality was strongest for the residual mass fraction at the eastern most station M1. The latter station received most Saharan dust particles in summer and fall, attributed to the prevailing wind system (paragraph 1.2) and its proximity to the source(s). The chemical composition of the marine and terrestrial Iouîk samples, both analyzed by XRF measurements, showed that they are similar and that with increasing distance to the source, elements associated with clay minerals become more important due to preferential deposition of quartz particles closest to the source(s). Tracing back individual Saharan dust outbreaks from satellite images to the arrival in the deep ocean sediment traps is, however, still challenging due to the sediment trap's sampling resolution and the particle settling time lags involved.

Chapter 3 is in preparation for Geophysical Research Letters and demonstrates that most of the Saharan dust deposited in the Atlantic Ocean is washed out by tropical summer rains, amplifying the bio-availability of nutrients needed for the surface-ocean productivity in the remote and oligotrophic parts of the ocean. In this chapter a combination of our sediment trap data and incubation experiment (Chapter 4) combined with dust deposition simulations of an comprehensive earth system model (CESM) and satellite derived precipitation (TRMM) and dust optical depth (DOD, MODIS) reveal the understanding of how (much) Saharan dust is deposited and that wet deposition of Saharan dust increases the release of nutrients as opposed to dry deposition. In addition, in this chapter the dust fraction of the sediment traps is determined by chemical removal of all marine biogenic constituents collected in the traps and weighing the mineral dust fraction on a 0.4 µm polycarbonate filter. It turned out that the weighed dust fraction is 2 to 18 times lower than the residual (lithogenic) mass fraction calculated by using conventional conversion factors for organic matter and biogenic silica (Chapter 2).

The dust's potential to act as fertilizer for primary productivity is evaluated in **Chapter 4**. Bottle incubation experiments comprising dry and wet Saharan dust deposition showed that Saharan dust has an effect on the marine environment in as much as it delivers macro- and micronutrients (PO_4, $Si(OH)_4$ and DFe), especially when high amounts of dust (> 1.5 mg L^{-1}) are processed and deposited with low pH rain (H_2SO_4, pH = 2, paragraph 1.3). Although no nutrient input was observed when dust was deposited with dry deposition, the organic matter at the end of the experiment still increased to a similar amount as detected with wet dust deposition. Therefore, Saharan dust particles may have been incorporated into marine snow aggregates. In general, no fertilization effect of Saharan dust on the phytoplankton was found, although Saharan dust will deliver vital nutrients needed for phytoplankton growth in the oligotrophic North Atlantic Ocean when deposited with wet deposition. **This chapter is ready to be submitted to Biogeosciences**.

In **Chapter 5** the interplay between Saharan dust, Amazon River discharge, mixed layer deepening, and nitrogen fixation is discussed. To this end, downward export particle fluxes, organic carbon and nitrogen isotope ratios as well as pigment measurements from the material of the sediment traps in the western Atlantic (M4 and M5) were combined with oceanographic and atmospheric satellite images. In spring, mixed layer deepening introduced nutrients into the (sub-)surface layer of the oligotrophic ocean triggering a carbonate-rich peak export, while in fall 2013, wet Saharan dust deposition possibly plays a fertilizing and ballasting role when the dust is introduced into the retroflected Amazon River waters (paragraph 1.5). The coincidence of the latter processes enhances diazotrophic nitrogen fixation and results in a massive biogenic silica export flux, indicative for an efficient CO_2 removal. **This chapter is also ready to be submitted to Biogeosciences.**

The hypothesis, if Saharan dust ballasts organic matter through the water column was tested with drifting sediment traps collecting marine export fluxes at 100, 200 and 400 m water depth during two consecutive research cruises. In **Chapter 6** we used the molar C/N ratios of the collected material at the three depths as a proxy for degradation of organic matter with stable C/N ratios supposing to represent an effective transport. Results were evaluated and compared with satellite images and atmospheric dust sampled shipboard by the dust collectors. It was observed that in January 2015 the C/N ratios did remain stable with depth when dust was present in the atmosphere and thus dust deposition in the ocean was high. This observation led us to believe that Saharan dust deposition may play a key role in ballasting organic matter

through the water column and impact its export efficiency and carbon sequestration (paragraph 1.4) by reducing its time for microbial degradation. **This chapter is in preparation for Deep Sea Research**.

Finally, **Chapter 7** gives conclusions made during this study as well as ideas of future projects resulting from conducted experiments and analyses carried out in the framework of this thesis. It suggests a new method to evaluate dust abundance in sediment traps, will give an idea of future mesocosms experiments combining fertilization and ballasting of Saharan dust and suggests future work regarding buoy deployments. In **Chapter 8, appendix A2** preliminary results of a sequential method approach, determining the fraction in which trace metals (e.g. iron) are incorporated in dust minerals, are shown. This method is still to be improved for marine sediment trap samples and suggestions are made for further proceeding.

CHAPTER 2

Downward particle fluxes of biogenic matter and Saharan dust across the equatorial North Atlantic

Laura F. Korte, Geert-Jan A. Brummer, Michèlle van der Does, Catarina V. Guerreiro, Rick Hennekam, Johannes A. van Hateren, Dirk Jong, Chris I. Munday, Stefan Schouten, Jan-Berend W. Stuut

Atmos. Chem. Phys., 17, 6023-6040, 10.5194/acp-17-6023-2017, 2017.

Abstract

Massive amounts of Saharan dust are blown from the coast of northern Africa across the Atlantic Ocean towards the Americas each year. This dust has, depending on its chemistry, direct and indirect effects on global climate including reflection and absorption of solar radiation as well as transport and deposition of nutrients and metals fertilizing both ocean and land. To determine the temporal and spatial variability of Saharan dust transport and deposition and their marine environmental effects across the equatorial North Atlantic Ocean, we have set up a monitoring experiment using deep-ocean sediment traps as well as land-based dust collectors. The sediment traps were deployed at five ocean sites along a transatlantic transect between northwest Africa and the Caribbean along 12°N, in a down-wind extension of the land-based dust collectors placed at 19°N on the Mauritanian coast in Iouîk. In this paper, we lay out the setup of the monitoring experiment and present the particle fluxes from sediment trap sampling over 24 continuous and synchronized intervals from October 2012 through to November 2013. We establish the temporal distribution of the particle fluxes deposited in the Atlantic and compare chemical compositions with the land-based dust collectors propagating to the down-wind sediment trap sites, and with satellite observations of Saharan dust outbreaks.

First-year results show that the total mass fluxes in the ocean are highest at the sampling sites in the east and west, closest to the African continent and the Caribbean, respectively. Element ratios reveal that the lithogenic particles deposited nearest to Africa are most similar in composition to the Saharan dust collected in Iouîk. Down-wind increasing Al, Fe and K contents suggest a downwind change in the mineralogical composition of Saharan dust and indicate an increasing contribution of clay minerals towards the west. In the westernmost Atlantic Ocean, admixture of re-suspended clay-sized sediments advected towards the deep sediment trap cannot be excluded. Seasonality is most prominent near both continents but generally weak, with mass fluxes dominated by calcium carbonate and clear seasonal maxima of biogenic silica towards the west. The monitoring experiment is now extended with autonomous dust sampling buoys for better quantification of Saharan dust transport and deposition from source to sink and its impact on fertilization and carbon export to the deep ocean.

Keywords: Saharan dust; North Atlantic Ocean; sediment traps; particle fluxes; XRF element ratios; trans-Atlantic

1 Introduction

The latest estimates of transatlantic Saharan-dust transport and deposition based on 3-D satellite imagery indicate that on a yearly basis (2007-2013, between 10°S and 30°N) an average amount of 182 Tg dust is blown from the northwest African coast, at 15°W, westward towards the Americas (Yu et al., 2015a). Of this dust, about 132 Tg reaches 35°W and 43 Tg reaches 75°W (Yu et al., 2015a). Due to the dust's impact on global climate (e.g. Goudie and Middleton, 2001; Griffin et al., 2001; Jickells et al., 2005; Maher et al., 2010; Mahowald et al., 2014), Saharan dust has been examined extensively on either side of the equatorial North Atlantic Ocean, using ample different approaches. At the eastern side, northwest African *in-situ* measurements of dust events were performed on land (e.g. Kandler et al., 2009; Marticorena et al., 2010; Kandler et al., 2011; Skonieczny et al., 2011; 2013; Kaly et al., 2015), in addition to ship board atmospheric dust sampling (e.g. Baker et al., 2003; Stuut et al., 2005) and deep ocean sediment fluxes (e.g. Ratmeyer et al., 1999a, b; Bory et al., 2002; Fischer and Karakas, 2009). On the other side of the ocean, Prospero and colleagues have been sampling Saharan dust mainly on Barbados since the late 1960's, resulting in the longest continuous time series of Saharan-dust sampling (Prospero et al., 1970; Prospero and Lamb, 2003; Prospero et al., 2014). All observations of Saharan dust showed a strong seasonality with higher dust concentrations during the winter season close to the dust sources in the east, and higher dust concentrations during the summer season in the Caribbean. This seasonal pattern is related to the prevailing wind systems, which are influenced by the movement of the Intertropical Convergence Zone (ITCZ). Saharan dust is transported year-round by the north-easterly trade winds at relatively low altitudes, carrying the dust to the proximal parts of the Atlantic Ocean (Pye, 1987; Stuut et al., 2005). In winter, easterly winds transport the dust in surface winds at altitudes below three km (Chiapello et al., 1995), when the ITCZ reaches its most southern position, and the dust crosses the Atlantic Ocean in the direction of South America (Prospero et al., 1981; 2014). As the ITCZ migrates northward during summer, the dust is transported by the Saharan Air Layer (SAL) at higher altitudes up to five km (Tsamalis et al., 2013), and crosses the Atlantic Ocean above the trade-wind zone in the direction of North America and the island of Barbados (Prospero et al., 1970; 2014).

The knowledge of the fate of Saharan dust in between the sources and sinks is, however, limited due to the vastness of the North Atlantic Ocean, though observed by remote sensing (e.g. Liu et al., 2008; Huang et al., 2010; Yu et al., 2015a) and shipboard lidar measurements (Kanitz et al. 2014). From the latest approximation

(Yu et al., 2015a) it can be derived that around 50 Tg a^{-1} of dust is deposited into the eastern equatorial North Atlantic Ocean, and 140 Tg a^{-1} of dust is deposited into the equatorial North Atlantic Ocean and the Caribbean Sea as well as onto parts of the Amazon rainforest. The deposited dust onto the ocean has a great influence on the particle fluxes as well (Ittekkot et al., 1992; Jickells et al., 2005; Armstrong et al., 2009). Sediment trap studies within for example the Joint Global Ocean Flux Study (JGOFS) and Biogeochemical Ocean Flux Study (BOFS), dealing with deep ocean particle fluxes, show elevated total mass fluxes with a high contribution of lithogenic particle fluxes in the North Atlantic Ocean off Mauritania (Jickells et al., 1996; Bory and Newton, 2000; Bory et al., 2001). In addition, Saharan dust particles are thought to contribute to the total flux in the Sargasso Sea (Deuser et al., 1988).

A 25-year time series of northwest African dust fluxes was established at the University of Bremen, Germany, using sediment traps moored on the Mauritanian continental slope. First results were presented by Wefer and Fischer (1993), Ratmeyer et al. (1999a, b) and Nowald et al. (2015), followed by the 25-year record by Fischer et al. (2016). On average, lithogenic particles make up about a third of the total mass flux and up to 50 % during dust events (Nowald et al., 2015). Biogenic mass fluxes in this area are generally high as well, as the sediment traps are located in one of the four major Eastern Boundary Upwelling Ecosystems (EBUEs) (Fréon et al., 2009), bringing cold, nutrient-rich waters to the surface waters stimulating primary productivity. Fischer et al. (2016) demonstrate that the Cape-Blanc sediment-trap series showed a weak relationship between dust input and productivity as reflected by the biogenic silica, mainly derived from diatoms as important primary producers. In addition, dust particles were found to strongly enhance the settling of organic matter through the water column by means of mineral ballasting, although no evidence was found for a relation between bulk fluxes and dust particle size.

In order to determine the simultaneous downward particle flux of the deposited Saharan dust across the entire Atlantic Ocean between the source in Africa and the sinks in the Atlantic Ocean and Caribbean Sea, we deployed an array of five moorings below the core of the dust plume, starting in 2012. Based on eight years of satellite observations, the Saharan dust plume is very consistently located between 7 and 17°N (Mulitza et al., 2008). Therefore, the array of moorings was positioned along the 12th northern parallel between 23°W and 57°W, each equipped with two time-series sediment traps. In addition, we positioned land-based dust collectors in Iouîk on the Mauritanian coast nearest to the source (Fig. 1). Here, we present the initial set-up of the monitoring experiment and the first-year results of the mass fluxes and their composition as intercepted by the sediment traps in the Atlantic and the land-based

samplers in Iouîk. The results are compared both with each other, and satellite images of atmospheric Saharan dust transport, recorded by the Moderate Resolution Imaging Spectroradiometer (MODIS) carried by the Terra satellite. Complementary results of the size distributions of Saharan dust from the sediment traps were discussed by Van der Does et al. (2016), showing a strong seasonality with coarser grained dust in summer and finer grained dust in winter and spring, as well as a fining in particle size with increasing distance to the source.

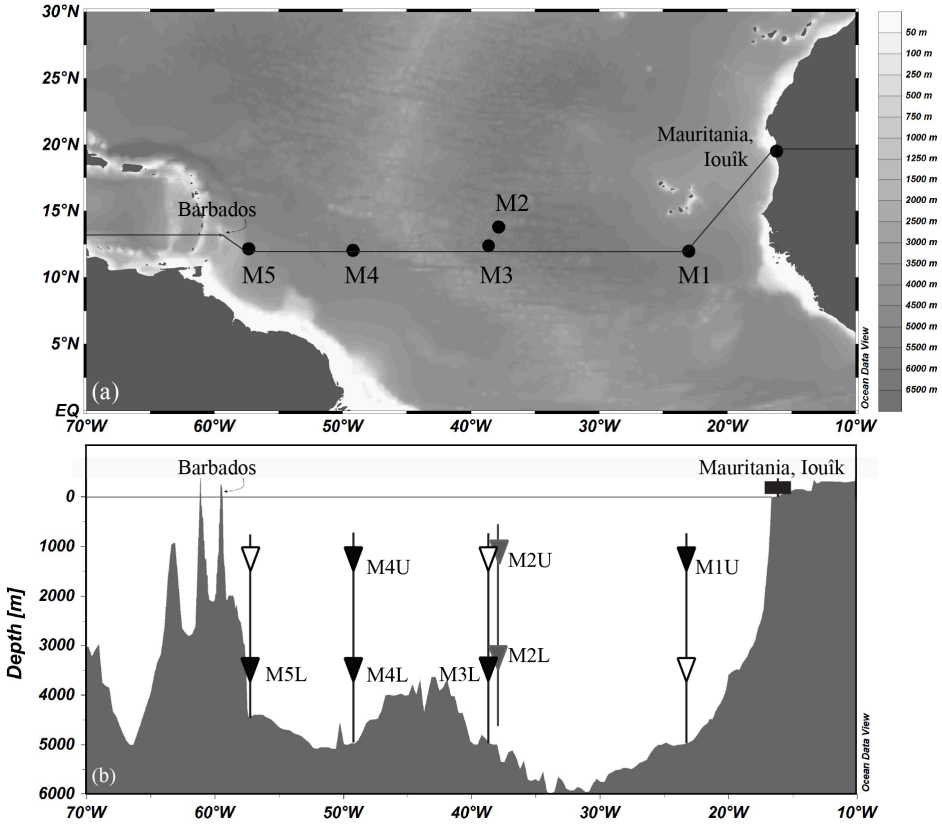

Figure 1. (a) Location of land-based dust collectors on the Mauritanian coast in the village of Iouîk and sediment trap moorings M1-M5 between northwest Africa and Barbados. (b) Bathymetric profile, on the line in (a), through the equatorial North Atlantic between Mauritania (15°W) and Barbados (60°W) showing the five moorings with sediment traps (triangles) and the land-based MWAC dust collectors (rectangle). MxU and MxL indicate the upper and the lower traps on the five moorings at 1200 m and 3500 m nominal water depth, respectively. Open symbols refer to sediment traps that failed or were lost during recovery.

2 Instrumentation and Performance

2.1 Land-based dust collectors

Saharan dust transport and deposition is traced from source to sink, starting on the Mauritanian coast with two masts with passive modified Wilson and Cooke samplers (MWAC dust collectors; Goossens and Offer (2000), located in Iouîk (19°53.11'N, 16°17.64'W), which have been sampling dust over monthly intervals since January 2013. Each mast contains a total of ten MWAC samplers, deployed in pairs at five heights, equally spaced at 90 to 290 cm from the ground. The masts contain a wind vane that directs the opening of the MWAC collectors into the wind.

2.2 Ocean moorings

Sediment traps are a common tool for direct and accurate time-series measurements of settling particles in the ocean when conditions are favorable, e.g. low currents (< 12 m s^{-1}), no deep eddy penetration and a vertical mooring line (Knauer and Asper, 1989). Moorings were deployed at five sites (M1-M5) along a transect in the equatorial North Atlantic during RV *Meteor* cruise M89 (Stuut et al., 2012) in October 2012 (Fig. 1). Four of the five moorings (M1, M3, M4, and M5) were deployed at 12°N and 23, 38, 49, and 57°W, respectively, and one mooring (M2) was positioned to the north of station M3 and deployed at 13.5°N, 37.5°W to assess potential north-south movements of the Saharan dust plume. Each mooring was equipped with a number of oceanographic instruments (Table 1). These include two Technicap PPS 5/2 sediment traps provided with a tilt meter at a nominal water depth of 1200 m (upper) and 3500 m (lower), two SBE MicroCat CTDs for conductivity, temperature and depth measurements, two Aanderaa RCM-11 current meters, and four floatation bodies to keep the mooring upright. The uppermost float included a downward-looking Acoustic Doppler Current Profiler (ADCP, 75 Hz) for measuring current profiles (velocity and direction) and particle backscatter intensities, and a XEOS iridium beacon and flasher on top.

Generally, current velocities did not exceed 12 cm s^{-1}, which is considered a threshold for unbiased collection of settling particles (Knauer and Asper, 1989). Current-meter measurements showed that the average velocities around each mooring were < 6 cm s^{-1} in the deep and bottom ocean at around 3500 and 4600 m water depth, respectively and < 10 cm s^{-1} at around 1200 m water depth as measured by the ADCPs. For only a few days during the entire sampling period current velocities exceeded the 12 cm s^{-1} for the upper sediment traps at 1200 m at the sites M2

and M3, while at M4 maximum velocities at 3350 m reached 19 cm s^{-1} in early August 2013. All other sensors showed that the sediment traps at sites M1 to M4 remained well within 5° from the vertical and at constant depths during the entire sampling period. Only during two periods at site M5 current velocities exceeded 12 cm s^{-1} to the extent of biasing collection efficiency: in February 2013 and late March 2013. This caused a downward movement of the traps as recorded by increased pressure (depth) by both CTDs, as well as deviations of up to 14° and 12° from the vertical, respectively, as measured by the tilt meters, affecting three sample intervals at station M5 (intervals #8, 10 and 11). For these three intervals we adjusted the total mass flux using $F = F_t - (1+1.4\sin 2\theta)$ with F being the vertical flux, F_t the flux in the tilted trap, and θ the degree of tilt from the vertical (Gardner, 1985).

Table 1. Layout of mooring instruments as an example of sampling site M1.

Instrument name	Description	Approx. water depth (m)
Benthos floats	Floats	**720**
Smartie float 500	Float with beacon + flasher + downward looking ADCP	**750**
SBE MicroCat CTD	CTD – Conductivity Temperature & Depth sensor	**1190**
Technicap PPS 5/2	Sediment trap with 24 bottles + tilt meter	**1200**
Smartie float	Float with 500 kg buoyancy	**1250**
Aanderaa RCM	Current meter	**3480**
SBE MicroCat CTD	CTD – Conductivity Temperature & Depth sensor	**3490**
Technicap PPS 5/2	Sediment trap with 24 bottles + tilt meter	**3500**
Benthos floats	Floats to retrieve mooring	**40 m above bottom**
Aanderaa RCM	Current meter	**20 m above bottom**
Releasers	To detach mooring from anchor	**10 m above bottom**
Anchor	Steel weight 2000 kg	**bottom**

Each sediment trap has a collecting area of 1 m^2 and is equipped with an automated rotary collector carrying 24 sampling cups. All traps collected the settling particles simultaneously and synchronously in 16-day intervals, starting on 19 October 2012 and ending on 7 November 2013. Prior to deployment in 2012, sampling cups had been filled with filtered seawater from the respective sampling depths at 1200 and 3500 m, using $HgCl_2$ as a biocide (to an end concentration of 1.3 g L^{-1}) and Borax

($Na_2[B_4O_5(OH)_4]\cdot 10H_2O$; end concentration 1.3 g L^{-1}) as a buffer at pH 8.5. Both additives increased the density to limit exchange with ambient seawater. Seven sediment traps were recovered successfully during RV *Pelagia* cruise 64PE378 in November 2013 (Stuut et al., 2013). These include three upper (1200 m) sediment traps at sites M1, M2, and M4 and four lower (3500 m) sediment traps at sites M2, M3, M4, and M5 (Fig. 1, Table 2). On board, the pH of the supernatant solution was measured, and an aliquot of supernatant liquid was analyzed for nutrient concentration (SiO_4^{4-}, NH_4^+, PO_4^{3-}) for shipboard quality control. When necessary, samples were post-poisoned and brought to an appropriate pH when lower than 8 to prevent $CaCO_3$ dissolution. Samples were kept dark and cool at 4°C until further processing.

Table 2. Sediment trap details. Sampling was performed simultaneously and synchronously from October 19, 2012 until November 7, 2013 (384 days).

Trap	Position	Bottom depth (m)	Trap depth (m.b.s.l)	Distance to African coast (km)	Closest horizontal distance to seafloor at trap depth (km)
M1U	12.00°N, 23.00°W	5000	1150	700	610
M2U	13.81°N, 37.82°W	4790	1235	2300	2260
M2L			3490		520 (MAR)
M3L	12.39°N, 38.63°W	4640	3540	2400	500 (MAR)
M4U	12.06°N, 49.19°W	4670	1130	3500	640
M4L			3370		580 (MAR)
M5L	12.02°N, 57.04°W	4400	3520	4400	63

m.b.s.l. = meter below sea level. MAR = mid-Atlantic Ridge.

3 Methods

The following paragraphs describe the different methods used to analyze particle fluxes and the element and biological composition of the specific samples. Due to the different nature and amount of material, i.e. the dry dust from the on-land dust collector in Iouîk and the wet sediment trap samples from the deep ocean, not all methods were applicable to all samples. While for the marine sediments the total, biological and residual mass fluxes were determined, as well as their element composition, the Iouîk samples were analyzed exclusively for their total mass and horizontal dust flux at 290 cm as well as their element composition.

3.1 Particle Mass Fluxes

From the land-based dust collectors, all dust was removed from each sample bottle by loosening and shaking the dust out of the bottles. The removed dust was weighed on a micro-balance. Dust fluxes represent the horizontal transport fluxes of Saharan dust in the source. It is estimated by Eq. (1):

$$F_{MWAC} = MAR/A \cdot 1/n, \quad (1)$$

where F is the dust flux (g m^{-2} d^{-1}), MAR is the mass accumulation rate (g d^{-1}), A is the cross-sectional area of the inlet tube of the MWAC sampler (m^2) and n is the estimated sampling efficiency of the MWAC bottles. The sampling efficiency of the MWAC samplers is between 75 and 90 % for 30 µm dust (Goossens and Offer, 2000), which is within a similar size fraction of the Iouîk dust (Friese et al., 2017).

For the vertical (downward) marine particle fluxes from the sediment traps, the samples were wet-sieved over a 1 mm mesh, wet-split in five aliquot subsamples using a rotary splitter (WSD-10, McLane Laboratories), washed to remove the $HgCl_2$ and salts, and centrifuged. Afterwards samples were freeze-dried and ground. Total mass fluxes refer to the < 1 mm size fraction and were determined by weighing two freeze dried 1/5 aliquots for every sample. Average weight differences between replicate aliquots were within 2.4% (SD = 2.2) and less than 12%, with 87% of all samples differing < 5% between splits.

Total mass fluxes were determined by Eq. (2):

$$F = MAR \cdot A^{-1} \cdot d^{-1}, \quad (2)$$

where F is the total mass flux (mg m^{-2} d^{-1}), MAR is the mass accumulation rate (mg), A is the sediment trap funnel opening (m^2), and d the sampling time interval.

Total nitrogen (TN), total carbon (TC) and organic carbon (TOC) content were determined with a Thermo Scientific Flash 2000 Elemental Analyser. Samples for TOC measurements were decalcified by acid fuming with a subsequent addition of 2 N HCl and dried in an oven at 60°C. Samples for TN and TC measurements remained untreated. Carbonates were calculated as $CaCO_3$ = (TC - TOC) · 8.33 and organic matter as OM = 2 · TOC. The conversion factor for $CaCO_3$ is based on its stoichiometry, given 100 mol g^{-1} of $CaCO_3$ for 12 mol g L^{-1} of carbon, resulting in a factor of 100/12 = 8.33.

The calculation factor for organic matter varies from 2.0 in the eastern Atlantic Ocean to 2.5 in upwelling areas (Jickells et al., 1998; Klaas and Archer, 2002; Thunell et al., 2007; Fischer and Karakas, 2009); due to poorly constrained composition of the actual organic matter.

We chose to use the factor of 2 for better comparison to particle fluxes influenced by Saharan dust deposition off Cape Blanc (Wefer and Fischer, 1993; Fischer et al., 2007; Fischer and Karakas, 2009).

Biogenic silica (BSi) was analyzed by sequential alkaline leaching on a HITACHI U-1100 spectrophotometer after Koning et al. (2002). A standard amount of 25-30 mg of ground sample was placed in a 0.5 M NaOH solution at 85°C, to dissolve the biogenic silica, which subsequently reacted with a sulfuric acid-molybdate solution to form a blue molybdate complex. The complex was prevented from molybdate reduction and stabilized by adding oxalic and ascorbic acid, respectively. The solution was flushed through a photocell where the absorption of the blue complex was measured at the defined 660 nm (Grasshoff et al., 1983) and recorded every second. Each sample was run for 60 to 90 minutes. Results were evaluated with a weekly measured standard calibration curve ($R^2 > 0.99$) and calculated with the MS Excel data solver tool, extrapolating the dissolution curve to time zero to correct for contribution of non-biogenic silica (DeMaster, 1981) The diatom reference material (pure *Thalassiosira punctigera* from the North Sea) is measured with a reproducibility of ± 0.46 % and sample reproducibility is ± 0.36 %. For estimating mass fluxes, BSi is expressed as $BSiO_2$ (BSi · 2.139), although this conversion systematically underestimates the actual mass by 10-20 % given the crystal water associated with the opaline silica of which the siliceous plankton consists (Mortlock and Froelich, 1989).

The remaining, residual mass fraction is often referred to as the lithogenic fraction (Wefer and Fischer, 1993; Fischer and Wefer, 1996; Neuer et al., 2002; Fischer and Karakas, 2009; Fischer et al., 2016) since it contains all the refractory lithogenic particles (quartz, clay minerals, feldspars). The residual mass is defined by subtracting the biogenic $CaCO_3$, $BSiO_2$ and OM from the total mass (Eq. 3) and includes all Saharan dust.

$$\text{Residual mass} = \text{Total mass} - CaCO_3 - BSiO_2 - \text{OM} \quad (3)$$

However, this residual fraction potentially also includes biogenic phosphates and sulfates, as well as particles of volcanogenic, cosmogenic and anthropogenic origin. In addition, crystal water associated with the opaline silica and the OH content of organic matter and clay minerals also contribute to the residual mass. Therefore, the residual mass fraction is most likely overestimated while the marine biogenic fraction is underestimated.

3.2 XRF element analysis

The elemental composition of each sediment trap sample was determined by X-ray fluorescence (XRF) using the Avaatech XRF core scanner (Richter et al., 2006). This analytical technique has the important advantage that it is non-destructive, allowing that very small-size samples – such as sediment trap samples – can be used for other analyses after measurement. XRF scanning results in semi-quantitative compositional data (Richter et al., 2006), being expressed as intensities (i.e. counts or counts per second), which we normalize to the total counts to take into account the closed sum of geochemical data. We analyze our data as normalized element intensities, using the advantage that XRF-scan measurements on homogenized dry sediment trap samples largely avoid physical properties biasing, e.g. wet down-core XRF measurements (Tjallingii et al., 2007; Weltje and Tjallingii, 2008). For dry-powder samples, Tjallingii et al. (2007) showed that element intensities are proportional to their chemical concentration, which we confirm by measuring 13 standards with various matrices, including marine sediments that have a similar matrix to sediment trap samples (Table S1).

Ground sediment trap samples (~25 mg) were pressed in polyethylene cylinders with a circular recess of 6 mm and 1.5 mm depth and covered with SPEXCerti Ultralene® foil. All samples were measured with a 4 x 4 mm slit size at a voltage of 10, 30 and 50 kV (elements: Al, Si, K, Ca, Ti, Cr, Mn, Fe, Cu, Zn, Sr, Zr and Ba), with an electric current of 1.5, 1.3 and 0.8 mA and a measurement time of 20, 40 and 80 s, respectively. All measurements were performed 5 times, and average values for these measurements are shown. The elements Ti, Al, Fe and K were chosen and shown, since they are only present as main or minor elements in lithogenic minerals like clays, quartz, and feldspars, rather than in any biogenic mineral formed in the ocean, while Si represents both lithogenic Si minerals (clays, quartz, and feldspars) but also biogenic produced silica ($BSiO_2$), as found in phytoplankton diatoms or zooplankton radiolarians. Pearson correlation was applied to the whole dataset of which we show the five elements Ti, Al, Fe, Si and K in Table S2 in the Supplement. Five of the sediment trap samples (M1U #9, 12 and 24; M4U #12 and 24) could not be analyzed due to insufficient material.

Two certified external standards (powdered marine sediment MESS-3 and PACS2) were used for quality control of the XRF measurements (Table S1) and were both analyzed within each run of ~25 samples in exactly the same way as the sediment trap samples. These standards showed a precision, expressed as relative standard deviation (RSD = standard deviation divided by the average of replicates x 100 %),

< 7 % for all normalized element intensities. Moreover, the normalized intensities of these two standards closely follow the calibration line of all 13 standards (Table S1).

4 Results

Horizontal transport fluxes from the land-based MWAC sampler are given in in grams per square meter per day (g m^{-2} d^{-1}). The vertical (downward) deposition fluxes from seven sediment traps deployed across the Atlantic Ocean are treated in downwind succession from east to west, starting at ocean site M1 closest to Africa, to ocean site M5, closest to the Caribbean. For each trap, the relative contribution of the biogenic components $CaCO_3$, $BSiO_2$, OM, and the residual mass fraction are given, in addition to the total mass flux, the flux of each biogenic component and that of the residual mass fraction, expressed in both milligram per square meter per day (mg m^{-2} d^{-1}) and grams per square meter per year (g m^{-2} $year^{-1}$).
The biogenic components are produced by autotrophic phytoplankton and heterotrophic zooplankton. In particular, phytoplankton $CaCO_3$ producers are mainly coccolithophores while zooplankton $CaCO_3$ is mainly from foraminifera and gastropod shells. The $BSiO_2$ is primarily produced by the phytoplankton diatoms and zooplankton radiolarians. Seasonal variations are shown for specific fluxes as deviation from their annual mean, together with the grain-size distribution of Saharan dust (Van der Does et al., 2016) for the residual mass fraction in the same material. To evaluate the residual mass fraction in the sediment traps, we compare XRF data from MWAC samplers with those from the sediment traps. The horizontal mass fluxes of the land-based dust collectors in Iouîk are almost 100 % pure dust with negligible contribution of organic matter and fresh water diatoms from paleo-lakes, and can therefore be used for chemical element comparison to the residual mass fraction from the sediment traps. Deviations between the chemical composition of the MWAC samplers and the sediment traps reveal compositional changes.

4.1 Horizontal land-based transport fluxes at Iouîk

The total mass fluxes of the MWAC samples at 290 cm height show significant month-to-month differences (Fig. 2). Highest dust fluxes of around 360 and 230 g m^{-2} d^{-1} were found during spring in April 2013 and during summer in August 2013, respectively. Local wind speeds at 10 m above the displacement height (MERRA model, NASA GES DISC) show monthly average velocities between 3 and 7 m s^{-1} with higher wind speeds in early summer and lower wind speeds in fall.

Throughout the entire sampling period, the wind speeds are above desert pavement threshold velocities of 1.5 to 3 m s^{-1} (Pye, 1987), also suggesting dust contribution from adjoining areas.

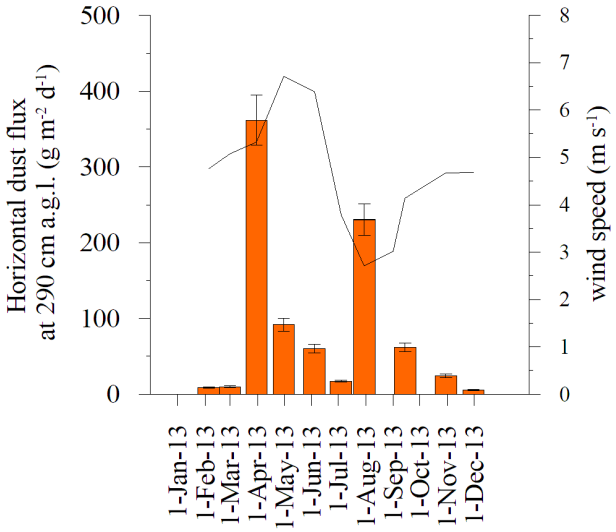

Figure 2. Horizontal transport fluxes of Saharan dust from the land-based MWAC sampler in Iouîk, Mauritania (19°N, 16°W) between January and December 2013 in orange bars. Error bars show the MWAC sampler efficiency of 75 to 90 %. Monthly averaged wind speed at 10 m above displacement height (MERRA model) around the Iouîk location is indicated as a black line (data obtained from the Giovanni on-line data system, NASA GES DISC). a.g.l. = above ground level.

4.2 Mass fluxes at ocean site M1

The shallow sediment trap at 1150 m water depth at site M1 collected a fairly steady total mass flux year-round (Fig. 3) with a daily average of approximately 100 mg m^{-2} d^{-1} which equals an annual export of 40.7 g m^{-2} $year^{-1}$ (Table 3). The mass fluxes of the marine biogenic constituents ($CaCO_3$, $BSiO_2$ and OM) follow those of the total mass and are in close relation to each other. The composition of the trapped material is dominated by $CaCO_3$ (21-45 %) and the residual mass fraction (30-58 %), with minor OM (14 %) and $BSiO_2$ (10 %). A clear seasonal pattern in the total mass flux is absent, although a peak flux is recorded in March (interval #9). Relative to the annual mean, biogenic matter fluxes are high during winter and spring and low during fall and especially summer (Fig. 4). Consequently, the residual mass fraction shows the opposite, with a low relative abundance in winter and spring and a high in summer and fall. The variation of the residual mass flux is consistent with the long-term seasonal transport of Saharan dust above the eastern tropical

North Atlantic (Chiapello and Moulin, 2002). The residual mass flux ranges from 32-71 mg m^{-2} d^{-1} with an average of 47.7 mg m^{-2} d^{-1} (17.4 g m^{-2} $year^{-1}$) and slightly elevated values during summer and fall (#16, 18, 19 and 22) but with a peak in March (#9). A pronounced seasonality is also seen in the grain-size distributions of the same material with coarser grained Saharan dust in summer and finer grained dust in winter (Van der Does et al., 2016).

Table 3. Yearly mass fluxes of measured flux parameters.

Trap	Total Mass Flux	$CaCO_3$	$BSiO_2$	OM	Residual mass
	mg m^{-2} d^{-1} (g m^{-2} $year^{-1}$)	% mg m^{-2} d^{-1} (g m^{-2} $year^{-1}$)			
M1U	116.6 (40.7)	**33.9** 37.8 (13.8)	**9.7** 10.9 (4.0)	**13.6** 15.2 (5.6)	**42.7** 47.7 (17.4)
M2U	39.5 (14.4)	**56.0** 22.2 (8.1)	**5.9** 2.3 (0.8)	**11.3** 4.5 (1.6)	**26.8** 10.6 (3.9)
M2L	54.6 (19.9)	**59.2** 32.3 (11.8)	**5.7** 3.1 (1.1)	**7.2** 3.9 (1.4)	**27.9** 15.3 (5.6)
M3L	70.4 (25.7)	**52.0** 36.6 (13.4)	**6.9** 4.9 (1.8)	**8.4** 5.9 (2.2)	**32.7** 23.0 (8.4)
M4U	84.8 (30.9)	**48.3** 41.0 (14.7)	**10.8** 9.2 (3.4)	**12.6** 10.7 (3.9)	**28.3** 24.0 (8.7)
M4L	63.6 (23.2)	**53.0** 33.7 (12.3)	**10.7** 6.8 (2.5)	**8.9** 5.7 (2.1)	**27.4** 17.4 (6.4)
M5L	115.6 (42.2)	**32.5** 37.6 (13.7)	**16.5** 19.1 (6.7)	**5.7** 6.6 (2.4)	**45.3** 52.3 (19.1)

4.3 Mass fluxes at ocean site M2

Total mass fluxes at site M2 average 40 mg m^{-2} d^{-1} (14.4 g m^{-2} $year^{-1}$) in the upper trap at 1235 m and 55 mg m^{-2} d^{-1} (19.9 g m^{-2} $year^{-1}$) in the lower trap at 3490 m (Fig. 3, Table 3). Peak fluxes are recorded in March and late April (intervals #9 and 12). The composition of the material is rather similar in the upper and lower trap. In general, the trapped material is dominated by $CaCO_3$ (56 % and 59 %, respectively), followed by the residual fraction (27 % and 28 %, respectively), OM (11 % and 7 %, respectively) and $BSiO_2$ (both about 6 %). No clear seasonal pattern is seen in either traps in the total mass fluxes despite some peaks occur in the upper or the lower trap during the same sampling intervals (Fig. 4). No clear seasonal pattern appears in the biogenic fractions, although $CaCO_3$ and $BSiO_2$ tend to be relatively

enhanced during spring and summer, and OM in fall. Therefore, the resulting residual fraction is relatively enriched during summer and fall and suppressed during winter and spring. The small contribution of the residual fraction in spring is also expressed in its mass flux, yet is more variable in the upper trap than in the lower trap. It ranges between 4 and 32 mg m^{-2} d^{-1} with an average of 10.6 mg m^{-2} d^{-1} (3.9 g m^{-2} $year^{-1}$) in the upper trap and varies between 10 and 22 mg m^{-2} d^{-1} with an average of 15.3 mg m^{-2} d^{-1} (5.6 g m^{-2} $year^{-1}$) in the lower trap. This also holds for the grain-size distributions, while the dust particles in the upper trap show a distinct seasonality with coarser grains in summer and fall, the grain sizes of the dust particles in the lower trap fluctuate with no clear seasonality (Van der Does et al., 2016).

4.4 Mass fluxes at ocean site M3

At site M3, about 220 km south of site M2, the total mass flux at 3540 m water depth amounts to 70 mg m^{-2} d^{-1} (14.4 g m^{-2} $year^{-1}$) (Table 3). A double peak flux occurs during summer (intervals #15 &16). The peak fluxes are mainly $CaCO_3$, which forms more than half of the total mass (52 %) followed by OM (8 %) and $BSiO_2$ (7 %). Around one third (33 %) of the total mass resides in the residual fraction, with maxima during fall and minima during spring. Although the seasonality is weak small peaks appear, especially in June (Fig. 3). The residual mass fraction varies between 13 and 38 mg m^{-2} d^{-1} with an average of 23.0 mg m^{-2} d^{-1} (8.4 g m^{-2} $year^{-1}$). The differences from the mean contribution of the biogenic components show enhanced $CaCO_3$ in winter and spring and $BSiO_2$ in summer and fall 2013 (Fig. 4). The OM shows little seasonal variation, albeit slightly suppressed during spring.

4.5 Mass fluxes at ocean site M4

Average total mass flux amounts to 85 mg m^{-2} d^{-1} (30.9 g m^{-2} $year^{-1}$) in the upper trap and 64 mg m^{-2} d^{-1} (23.2 g m^{-2} $year^{-1}$) in the lower trap (Table 3). Both traps intercepted two striking peak flux events, the first during spring (late April) and the second during fall 2013 (late October/early November), when total mass fluxes exceeded 200 mg m^{-2} d^{-1} in the upper and 100 mg m^{-2} d^{-1} in the lower trap (Fig. 3). The peak fluxes differ in composition: while the peak in spring is $CaCO_3$ dominated (60 % in the upper trap and 73 % in the lower trap), the peak in fall is marked by $BSiO_2$ (25 % and 28 % in the upper and the lower trap, respectively). In addition, both peaks show elevated OM fluxes in both traps. Residual fluxes are elevated in the upper trap for the peak fluxes as well, but in the lower trap only in fall. Overall,

the residual mass fraction ranges between 14 and 87 mg m^{-2} d^{-1} with an average of 24.0 mg m^{-2} d^{-1} (8.7 g m^{-2} $year^{-1}$) in the upper trap and varies between 8 and 42 mg m^{-2} d^{-1} with an average of 17.4 mg m^{-2} d^{-1} (6.4 g m^{-2} $year^{-1}$) in the lower trap. The seasonal variability of the grain-size distributions become smaller but are still visible in the upper trap with coarser grained dust during summer and fall (Van der Does et al., 2016). Seasonal variability of $BSiO_2$ is dominated by the exceptionally high peak in fall (Fig. 4).

4.6 Mass fluxes at ocean site M5

The sediment trap at 3520 m water depth at the western most ocean site, M5, intercepted an average total mass flux of 116 mg m^{-2} d^{-1}, which equals an annual mass flux of 42.2 g m^{-2} $year^{-1}$ (Fig. 3, Table 3). Most of the trapped material resides in the residual mass fraction (45 %), followed by $CaCO_3$ (33 %), $BSiO_2$ (17 %) and OM (6 %) Seasonal variability is clear in the total mass flux with maxima during spring and halfway through summer, followed by a changeover in August to lower values during the second half of summer and fall 2013 (Fig. 4). Clearest seasonality is shown by $BSiO_2$ with a pronounced maximum in summer to late fall and minima in winter and spring. Seasonality is less clear in $CaCO_3$ and absent in OM, while the residual mass shows maxima in spring and minima in summer to late fall. It ranges between 17 and 125 mg m^{-2} d^{-1} with an average of 52.3 mg m^{-2} d^{-1} (19.1 g m^{-2} $year^{-1}$). The grain sizes of the residual fraction become smallest at this western most station and varies around the clay size fraction (Van der Does et al., 2016).

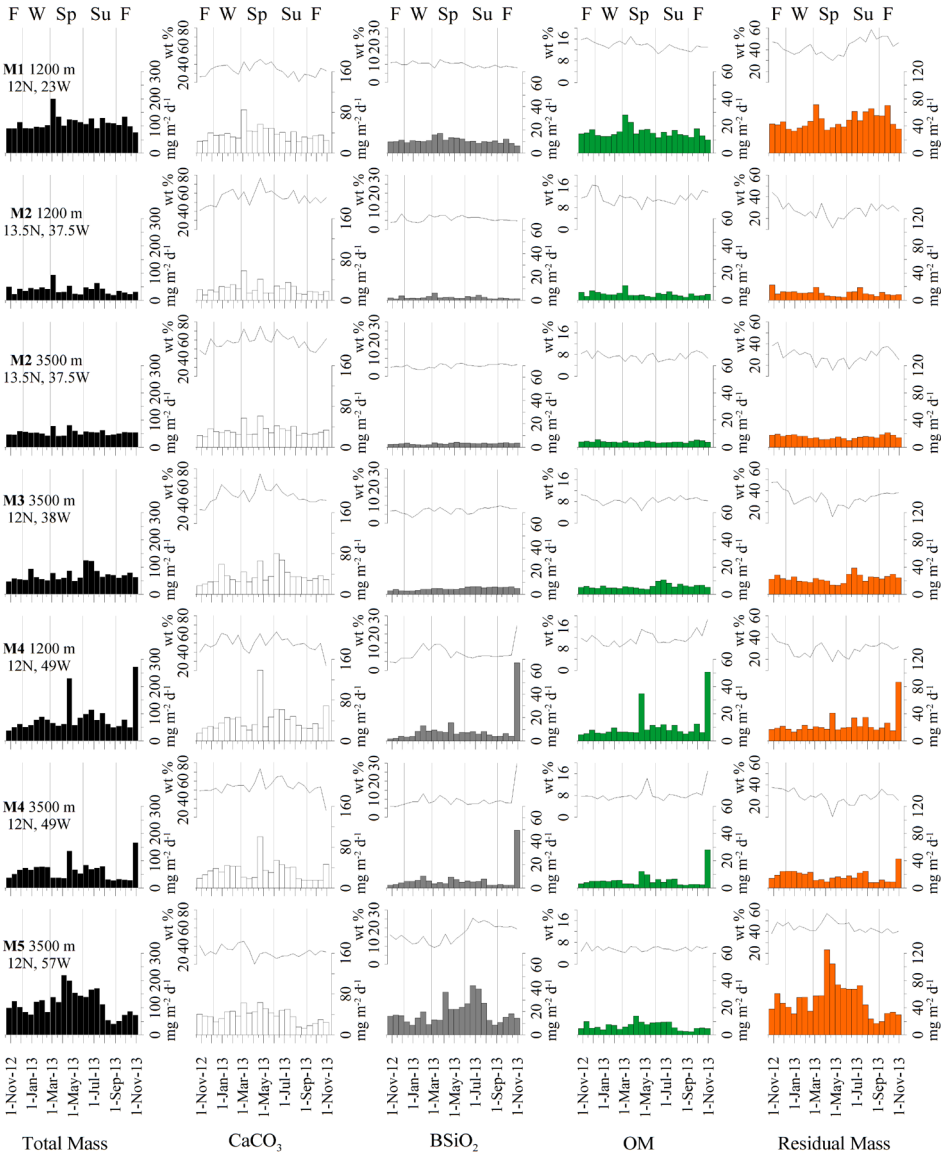

Figure 3. Mass fluxes at ocean site M1U to M5L in mg m^{-2} d^{-1} (bars) for total mass (black), $CaCO_3$ (white), $BSiO_2$ (grey), organic matter (green) and the residual mass fraction (orange); black lines represent their relative contributions (wt %). F = Fall, W = Winter, Sp = Spring, and Su = Summer.

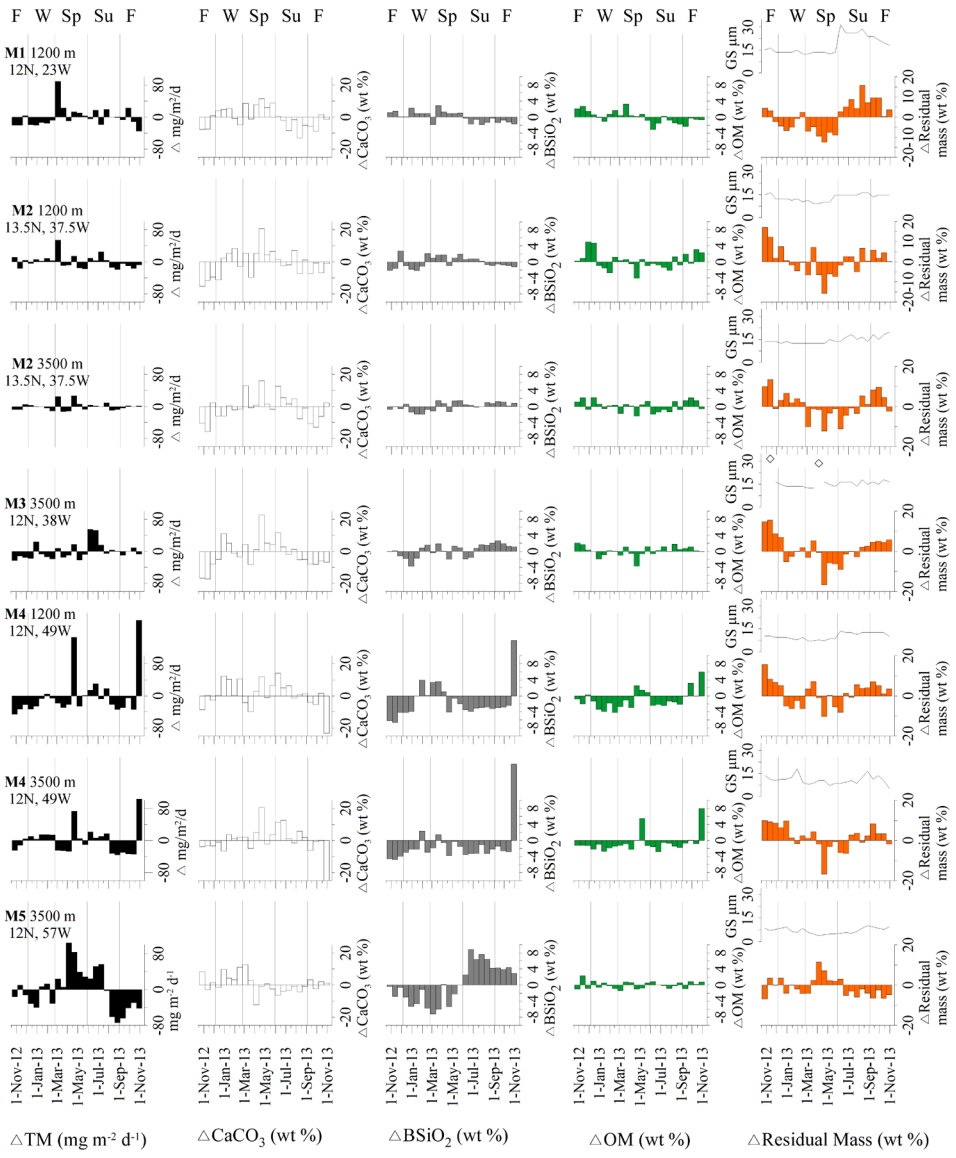

Figure 4. Deviation from the flux-weighted annual mean for total mass (black), $CaCO_3$ (white), $BSiO_2$ (grey), organic matter (green) and the residual mass fraction (orange) at ocean sites M1U to M5L. Black line represents modal grain sizes of Saharan dust of the same sample, diamonds in M3 are outliers (data Van der Does et al., 2016). F = Fall, W = Winter, Sp = Spring, and Su = Summer.

4.7 Molar C : N ratios

Total organic carbon (TOC) and nitrogen (TN) are highly correlated at both trap depths (Fig. 5). The upper traps of the moorings M1, M2 and M4 show higher TOC and TN contents than the lower traps of the moorings M2, M3, M4 and M5. However, two fluxes (interval #13 and 24) at site M4L contain as much TOC and TN as found in the upper traps. The molar C : N ratio of all traps is on average 9.17 with a standard deviation of 0.95. Overall, the ratios in the lower traps are slightly higher than in the upper traps, but without significant changes. The highest value (10.26) is reached at site M3L and the most uniform ratios between 8.46 and 9.65 are observed at ocean site M1U. The molar C : N ratios are in the typical range of sinking detritus collected in deep sediment traps and are comparable to the material collected off Mauritania but without seasonal differences (Fischer et al., 2016).

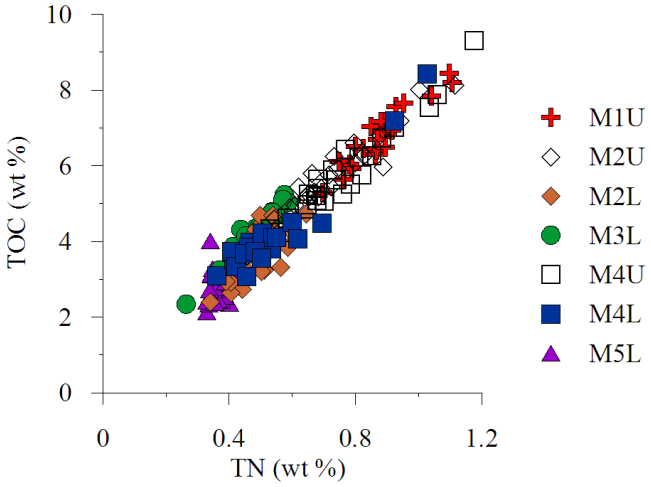

Figure 5. Total organic carbon (TOC) versus total nitrogen (TN) content for all ocean sites M1-M5.

4.8 XRF element ratios

We identify the residual mass fraction as lithogenic fraction by elements such as titanium (Ti), aluminum (Al), iron (Fe) and potassium (K). These elements are incorporated in mineral dust, in especially in aluminosilicates and feldspar, oxides and hydroxides and are incorporated in crystal lattice (Scheuvens et al., 2013). Although K is also detected in biomass burning aerosols (Cachier et al., 1995), the high correlations between K and the other lithogenic elements show that the contribution of biomass burning K is minor in our samples. Normalized intensities

of the lithogenic elements are highly correlated with the residual mass fraction and are therefore thought to represent the deposition flux of Saharan dust (Fig. 6). However, spatial differences from east to west indicate the continuous enrichment of especially Al and Fe from M1 to M5, and to an offset of higher K at M5, while Ti stays constant. The modal particle sizes of the dust (Van der Does et al., 2016) do not show a relation to the lithogenic elements. Best relations found were in the west, at site M5, where sizes and lithogenic elements are negatively correlated (Al, $R^2 = 0.54$ and K, $R^2 = 0.44$).

Normalized intensities of Al and Ti are highly correlated as well, both within the time series in Iouîk and throughout all seven sediment traps deployed in the deep ocean (Fig. 7; Table S2, S3). The dust sample from Iouîk and the samples at the proximal ocean site M1 are most similar in element composition, having the same slope and intercept for Ti and Al normalized intensities (Table S3). Further downwind, Ti-Al intensity ratios are lower but very similar at M2, M3 and M4U, while those at M4L and M5L have very similar but lower slopes (Fig. 7).

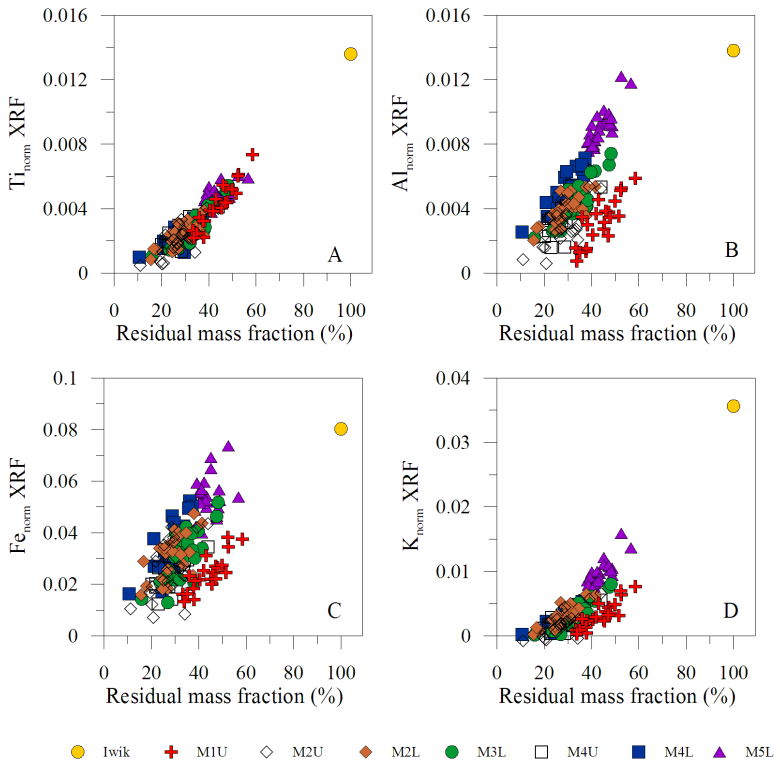

Figure 6. Comparison of the lithogenic elements Ti (a), Al (b), Fe (c) and K (d) normalized to total XRF counts versus the residual mass fraction in all sediment traps and the average of the land-based dust collectors in Iouîk.

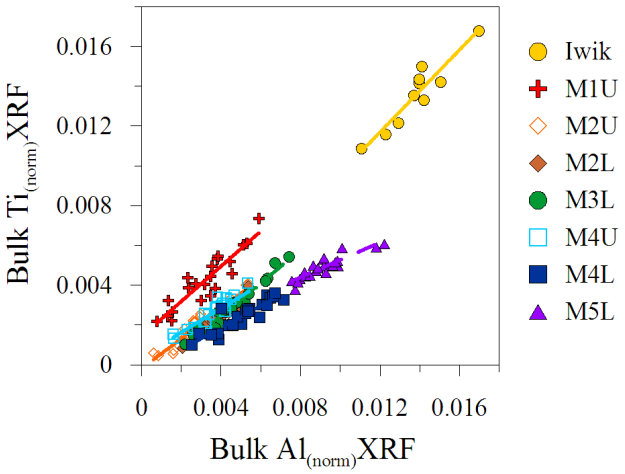

Figure 7. Comparison of bulk Ti and Al, normalized to total XRF counts for all seven sediment traps and the on-land dust collectors in Iouîk, Mauritania.

Saharan dust mostly consists of lithogenic silicates such as quartz, clay minerals and feldspars (Caquineau et al., 2002) that contribute to the total silica content in addition to the biogenic silica found in the sediment traps derived from skeletal plankton such as diatoms and radiolarian. Regression of biogenic silica, determined by sequential leaching to the total silica determined by powder XRF, shows a clear downwind increase from M1 to M5 (Fig. 8). Starting at ocean site M1, closest to the Saharan dust source, correlation is weakly negative, then vanishes at M2 and becomes positive and progressively stronger from M3 to M5.

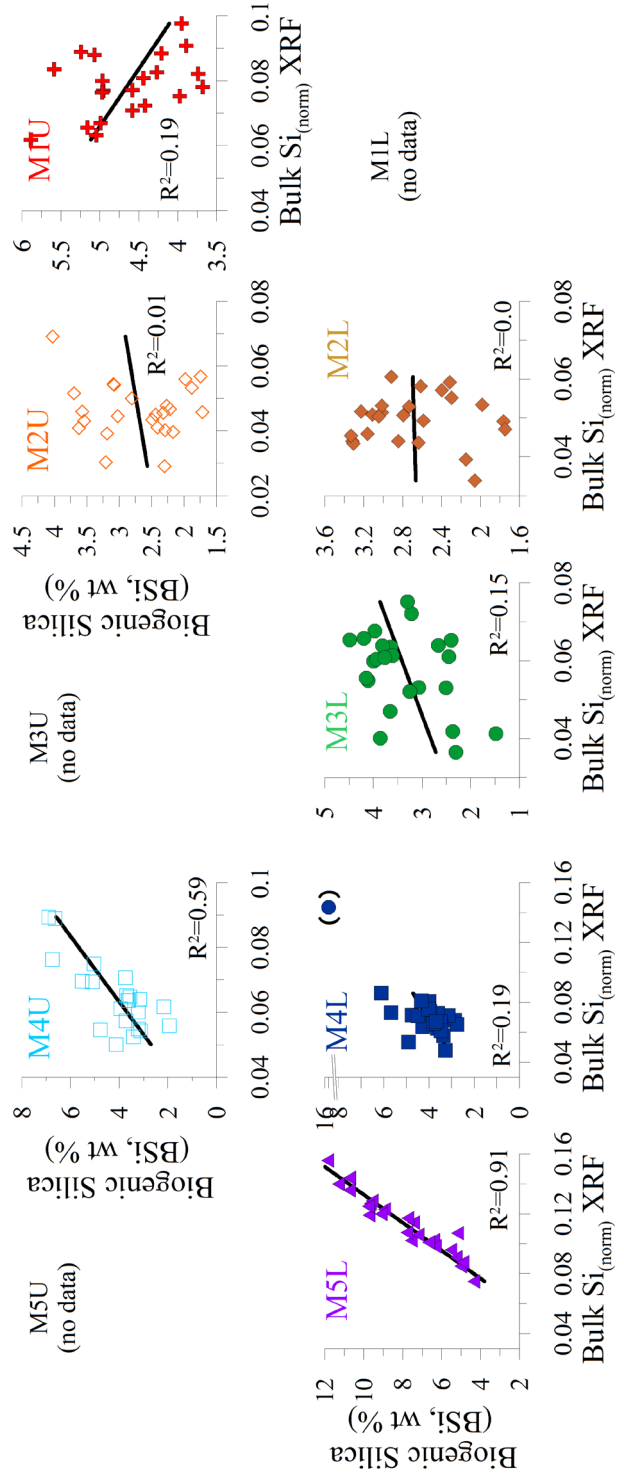

Figure 8. Biogenic silica versus total silica in particulate fluxes at five sites across the North Atlantic with sampling site M1 in the east (right) and M5 in the west (left).

5 Discussion

We provide the first comprehensive time series of biogenic particle fluxes and Saharan dust deposition from source to sink across the equatorial North Atlantic Ocean. The land-based dust collectors in Iouîk are located in the coastal region of western Mauritania, in potential source area 2 (PSA 2), which is one of the major source areas of dust that is transported across the Atlantic Ocean to the Americas (Scheuvens et al., 2013). The transport fluxes are highest in spring and summer (Fig. 2). The spring high can be related to the trade-wind intensities at lower altitudes, whereas the summer high point to sporadic dust storms, invisible on land by satellites. Backward trajectories reveal that the location in Iouîk is a transit area for long-range transported Saharan dust (Friese et al., 2017).

Overall, the horizontal Saharan dust flux from the land-based MWAC samplers in Iouîk cannot be compared directly to the downward flux in residual mass to in the sediment traps. However, they are compositionally the same, especially at the ocean site M1 as indicated by their similar Ti-Al slopes (Fig. 7). From site M1 we observe an overall decrease in both the residual mass and the marine biogenic matter fluxes westward to M2, M3 and M4. The much higher counts of lithogenic elements Ti, Al, Fe and K found in the dust at Iouîk, result from the absence of dilution by biogenic matter produced in the marine realm. While the Ti-Al slopes are the same at Iouîk and ocean sites M1 through M4U, and Al, Fe and K counts are most similar at Iouîk and M1 as well, but become significantly higher towards the west (Fig. 6), it suggests a downwind change in mineralogical composition of Saharan dust. At ocean sites M4L and M5L, both the Ti-Al slope is lower and the Al counts are higher especially at M5, indicating that a second source in addition to Saharan dust is involved, which may be derived from admixture of re-suspended clay-sized sediments advected towards the deep sediment traps. This is especially indicated by the offset of K at M5L. Overall, we observe a downwind increase in the Al and Fe content of the residual mass fraction, which suggests an increase in clay minerals relative to quartz. A similar change in mineralogy was observed by Glaccum and Prospero (1980) who compared the mineralogy at the eastern and western Atlantic Islands. Our observation is also supported by the clear downwind trend in the correlation between biogenic silica, as determined by sequential alkaline leaching, and total silica measured by XRF (Fig. 8). Such a downwind decrease in the relative amount of quartz may result from the increase of finer particles due to their slower settling speed, and a relative increase in platy clay minerals such as micas suspended in the atmosphere that can be transported over greater distances. This is consistent with the downwind decrease in

grain size as observed by Van der Does et al. (2016) on the same material.

5.1 Gravitational settling and downward transport

Saharan dust deposited on the surface ocean is generally too fine to settle out as individual particles, except perhaps for larger and massive quartz particles. Rather, they remain effectively suspended until incorporated by organic matter aggregates such as "marine snow" and fecal pellets that accelerate settling to velocities in the order of 200 m d^{-1} (Knappertsbusch and Brummer, 1995; Berelson, 2002; Fischer and Karakas, 2009). Indeed, at site M4, both the traps at 1200 and 3500 m intercepted two peak fluxes during the same 16-day interval, one in April and one in October (Fig. 3). Since these traps are 2300 m apart, this results in a settling velocity of at least 140 m d^{-1}. Higher settling velocities are conceivable for the fall peak fluxes at station M4, since the TOC and TN content (Fig. 5) of this peak flux in the lower trap is equally high as in all the upper traps (M1, M2 and M4), indicating rapid settling and little degradation. The same is observed at ocean site M2 for the flux peaks in March and in May (Fig. 3). However, the settling pathway might be different, as indicated by the higher total mass fluxes in the lower trap than the upper trap at site M2. Over the 2300 m distance of the upper and lower trap, the sinking particles are potentially subject to a variety of processes including remineralization, disaggregation, or repacking, as well as horizontal movement of the particles, resulting in a greater catchment area (Waniek et al., 2000). Therefore, the enrichment in the lower trap at site M2 might result from the greater catchment area of the deeper trap (Siegel and Deuser, 1997; Waniek et al., 2000). The same holds for the residual mass, which is more enriched in the lower trap compared to the upper trap. Consequently, time lags between Saharan dust outbreaks and transport in the higher atmosphere as observed in satellite images and their arrival in the upper sediment traps are at least one week and might take another path until arrival in the lower trap two weeks later. In this respect, buoys deployed now for time-series sampling of atmospheric dust just above the ocean surface at the same sites will serve as an intermediate between satellite observations of dust outbreaks and the actual deposition of dust on the surface ocean, which can be then followed down by the fluxes in the ocean.

5.2 Comparison with satellite observations

Saharan dust needs about a week (5-6 days) to cross the Atlantic Ocean from east to west as observed in satellite images (Prospero et al., 1970; 2014). Since the sampling interval of all sediment traps is 16 days, it is difficult to identify individual

dust outbreaks as individual peaks in mass fluxes that decrease in amplitude from east to west. However, this seems to be the case for the peak fluxes occurring in summer, when there is an enhanced contribution by the residual fraction, especially closest to the African coast at the ocean site M1. Such enhanced fluxes in residual mass are found in intervals #16, #18 and #19 at site M1U, and M4U and #16 of M3L, corresponding to the period from 16 June to 2 July, from 18 July to 3 August, and 3 August to 19 August 2013, respectively. During these summer intervals, dust outbreaks leave the African coast at high altitudes and propagates westwards across the Atlantic (Fig. 9). Despite this apparently good correspondence between the satellite data and the sediment trap record, there are also other cases where the sediment traps did not seem to record specific dust outbreaks observed in satellite images. This may relate to the altitude at which the dust is traveling; in summer, dust travels through the high atmosphere, as opposed to winter-dust that travels in the low-level trade-wind zone. The diffuse cloud that is observed across a relatively wide band throughout the atmosphere in summer is interpreted from nadir-looking satellites as higher aerosol optical thickness than the relatively narrow and dense dust cloud that crosses the atmosphere in winter. Conversely, some sediment trap intervals recorded a residual mass peak in spring, e.g. interval #9 which could be followed in M1U, M2U, and M3L (Fig. 3), when no evidence is found for the occurrence of dust events during that period (24 February-12 March 2013) in satellite imagery. This could be reflecting the timing of satellite overpasses, which could potentially lead to missing short-term events. However, most dust events that are recorded by satellite images are visible as multiple-day events. The presence of clouds in virtually all satellite images is likely to at least partially obscure low-level winter dust outbreaks. Although satellite products are a great help to follow huge dust outbreaks crossing the Atlantic, our results illustrate that there is still a high degree of difficulty in matching specific dust outbreaks observed by satellites and the fluxes we measure in the deep sediment traps. This may also be enhanced by time lag between the deposition of Saharan dust on the ocean surface and their arrival at depth.

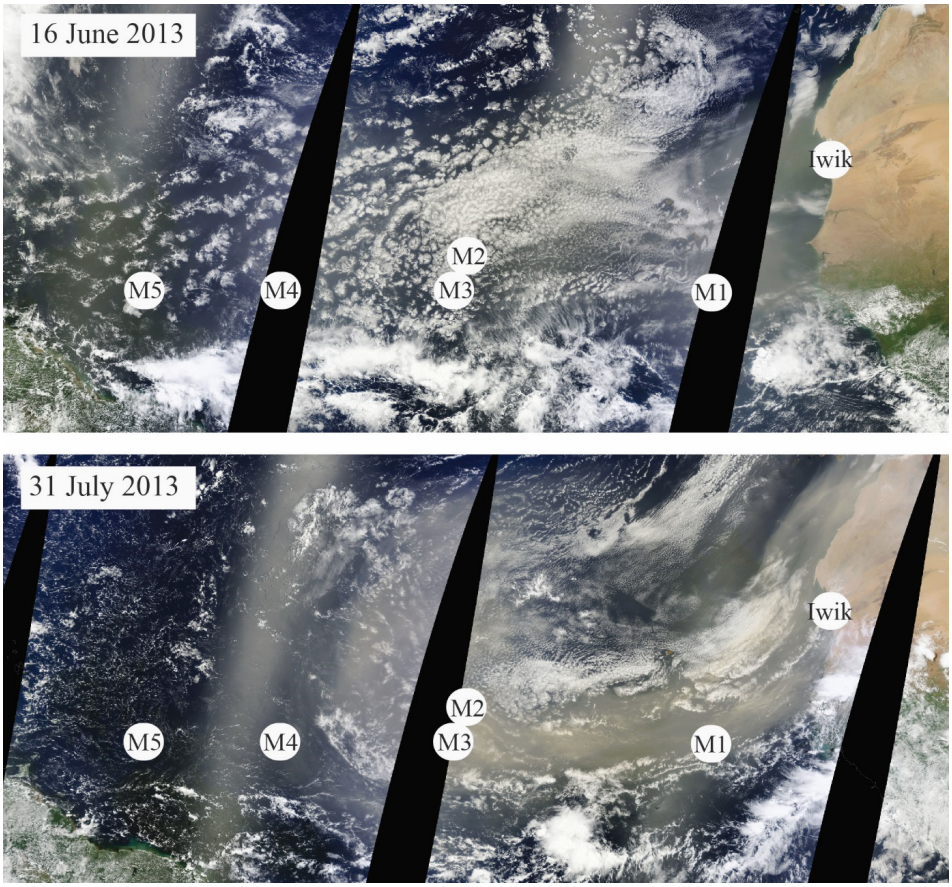

Figure 9. Satellite images (Images from NASA Worldview, MODIS Terra satellite) showing dust outbreaks propagating westwards from the African coast across the Atlantic Ocean, the location of the land-based dust samplers at Iouîk and the five ocean moorings M1 through M5.

5.3 Comparison with deep ocean mass fluxes off northwest Africa

The mass fluxes that we observe in the traps along the transect are in line with observations from sediment traps further north, off Cape Blanc on the Mauritanian continental slope at ~21°N, 20°W. For that site, Fischer et al. (2016) report total mass fluxes of 40.2 g m^{-2} $year^{-1}$ averaged over a period of 25 years with much interannual but little seasonal variability. This compares well with our sampling site M1, where we measured a total mass flux of 40.7 g m^{-2} $year^{-1}$. Cape Blanc residual mass fluxes vary about 5 to 26 g m^{-2} $year^{-1}$ (Fischer et al., 2016) and Bory and Newton (2000) found a lithogenic mass flux of around 20 g m^{-2} $year^{-1}$, both agree very well with the average residual flux at site M1 of 17.4 g m^{-2} $year^{-1}$. At all sites the residual mass

fluxes make up about a third of the total mass flux and up to 50 % during dust events (Nowald et al., 2015). Biogenic mass fluxes in the Cape Blanc area are generally also high, also owing to the upwelling of cold, nutrient-rich waters that cause high primary productivity in the surface waters. However, biogenic mass fluxes are about the same as found at M1, where no upwelling-stimulated productivity occurs. At site M1 all biogenic particle fluxes are highest in comparison to the other sampling sites. The only exception is the $BSiO_2$ at site M5, which is by far the highest contribution of $BSiO_2$. The low flux of biogenic particles in the mid-Atlantic Ocean (M2 to M4) reflect the limited availability of nutrients and low productivity in the oligotrophic ocean. The higher biogenic mass fluxes closest to either continent (M1 and M5) may have been enhanced by the higher lithogenic input, especially from higher Saharan dust input at site M1, as mineral dust enhances the settling of organic matter through the water column (Ittekkot et al., 1992; Hamm, 2002).

Moreover, mass fluxes collected by sediment traps off Cape Blanc, for example, are affected by lateral input from re-suspended sediments that are advected from the Mauritanian continental slope in nepheloid or bottom layers (Fischer et al., 2009). Similar lateral transport of resuspended sediments (Van Raaphorst et al., 2001; Bonnin et al., 2006) may also have come from the nearby Barbados continental slope and contributed to the high fluxes of the residual mass fraction at ocean site M5 (Fig. 3), which is relatively close to the Barbados margin, around 63 km to the trap depth at 3500 m (Fig. 1b, Table 2). This admixture of resuspended sediments is also suggested by the lower Ti-Al ratios and high K contents at M5, and to a far lesser extent also in the deep trap at M4 although residual mass fluxes at this site are significantly lower (Fig. 3). The enrichment in Al, Fe, and K indicates the addition of Al-Fe-K-rich clay minerals from a second source next to the Saharan dust deposited at these sites. This second source of sediments in the deep traps potentially also causes the negative correlation between the residual masses at M5 and M1, while those between M1 to M4 are all positively correlated (Table S4). Nevertheless, the particle-size distributions at M4 and M5 (Van der Does et al., 2016) alone do fit the general pattern of decreasing particle size with increasing distance from the Saharan dust source, not expecting fluvial input from the west.

The particle fluxes at ocean site M5 deviate from the general pattern in terms of enhanced total and residual mass fluxes and seasonal biogenic-silica contribution. Due to its westernmost position, the deep sediment trap may have received considerable amounts of lithogenic or biogenic material originating from either the Amazon or Orinoco River, or both. The freshwater Amazon outflow disperses kilometers from the river mouth and affects the oceans' biogeochemistry (Yeung et al., 2012). Due

to nutrient input, the occurrence of diatom-diazotroph associations is stimulated (Subramaniam et al., 2008). The fact that the biogenic silica correlates perfectly with the bulk silica (Fig. 8) possibly relates to the appearance of diatom phytoplankton and less contribution of quartz minerals.

6 Conclusions

The first-year results of our monitoring experiment yield valuable insights into the transport and deposition fluxes of Saharan dust between the African continent and the Americas. We demonstrate that the lithogenic particles collected in the sediment traps are similar to the dust collected on the African coast. With increasing distance from the source, lithogenic elements associated with clay minerals become more important relative to quartz settling out closer to the source. The total silica analyses show that the contribution by biogenic silica, produced by marine biota, increases significantly from east to west to the extent that virtually all silica consists of biogenic silica and lithogenic quartz is minor in the west furthest away from the African source(s). At the westernmost ocean site, enhanced residual mass fluxes collected by the deep sediment trap suggest admixing with a second source from resuspended ocean floor sediments. Tracing back individual dust outbreaks from satellite images to the arrival in the deep ocean sediment traps is still demanding given sampling resolution and the time lags involved. The best accordance of satellite images and the residual mass fraction was found for summer. The relative contribution of the residual mass fraction is found to be highly co-variant with typically lithogenic elements such as Al and Ti from Saharan mineral dust. While the temporal and spatial variability in residual mass fluxes corresponds to the changing chemical composition of Saharan mineral dust, they seem to overestimate the net fluxes due to underestimation of marine biogenic matter. To better approximate the deposition of Saharan dust, buoys that were deployed in 2013 should give information on precise fluxes, which can then be followed in the underlying sediment traps.

Data availability. Additional data are available at https://doi.pangaea.de/10.1594/PANGAEA.872093.

The Supplement related to this article is available online at doi:10.5194/acp-17-6023-2017-supplement.

Acknowledgements

This project is funded by ERC (project no. 311152) and NWO (project no. 822.01.008). We thank the crew of *Meteor* Cruise M89, *Pelagia* Cruise 64PE378 and NIOZ technicians for their contributions. Camara from the Parc National de Banc d'Arguin (PNBA) is thanked for assistance with the dust sampling in Iouîk, Mauritania. Jort Ossebaar is thanked for helping with the EA analysis, and Sharyn Ossebaar for assisting with the biogenic silica measurements. XRF-analysis was supported through the SCAN2 program (NWO project no. 834.11.003) and assistance by Rineke Gieles. Furu Mienis is thanked for helping with interpreting the current-meter data and assistance in the sediment-trap lab. The authors also acknowledge the MODIS mission scientists and associated NASA personnel for the production of the data used in this research effort. We thank three anonymous reviewers for their helpful contribution.

Table S1. Chemical composition and concentration of various standards, including MESS-3 and PACS-2 (grey) used as quality control.

Standard	Description	Al (cnts/TC)	Al (StDev)	Al (ppm)	Si (cnts/TC)	Si (StDev)	Si (ppm)	K (cnts/TC)	K (StDev)	K (ppm)
GSR-4	Sandstone	0.00716	0.00022	18635	0.33305	0.00063	422276	0.01280	0.00012	5394
GSR-6	Carbonate rock	0.00236	0.00010	26471	0.02338	0.00014	72732	0.00278	0.00016	6555
GSS-7	Soil	0.02229	0.00009	154641	0.04826	0.00019	152429	0.00157	0.00003	1660
JGb-1	Gabbro	0.01366	0.00015	92594	0.06871	0.00020	204080	-0.00045	0.00008	1991
JLk-1	Lake sediment	0.01681	0.00012	88571	0.12502	0.00043	267183	0.04116	0.00024	23276
JLs-1	Limestone	0.00018	0.00004	110	-0.00052	0.00004	561	-0.00064	0.00005	25
JSd-3	Stream sediment	0.01433	0.00020	52454	0.17607	0.00078	355247	0.03010	0.00014	16355
MESS-3	Marine sediment	0.01854	0.00030	85900	0.12643	0.00029	270000	0.04626	0.00017	26000
PACS-2	Marine sediment	0.01153	0.00025	66200	0.12830	0.00011	280000	0.01617	0.00030	12400
SARM-1	Granite	0.01947	0.00020	63953	0.23204	0.00094	353845	0.09650	0.00048	41406
SARM-2	Syenite	0.02333	0.00030	91800	0.17068	0.00048	297426	0.26810	0.00037	127372
SARM-3	Lujavrite	0.01396	0.00030	72212	0.10678	0.00041	244933	0.07206	0.00013	45721
SARM-4	Norite	0.01482	0.00033	87353	0.08476	0.00018	246055	-0.00056	0.00014	2074

Standard	Description	Ca (cnts/TC)	Ca (StDev)	Ca (ppm)	Ti (cnts/TC)	Ti (StDev)	Ti (ppm)	Fe (cnts/TC)	Fe (StDev)	Fe (ppm)
GSR-4	Sandstone	0.00502	0.00012	2143	0.00798	0.00041	1590	0.11867	0.00032	22242
GSR-6	Carbonate rock	0.54608	0.00028	254929	0.00161	0.00015	1950	0.03038	0.00017	17416
GSS-7	Soil	0.00151	0.00011	1143	0.07487	0.00028	20100	0.41156	0.00027	131774
JGb-1	Gabbro	0.18885	0.00028	85000	0.01978	0.00026	9589	0.22578	0.00037	105335
JLk-1	Lake sediment	0.00965	0.00022	4900	0.01516	0.00019	4004	0.20102	0.00025	48464
JLs-1	Limestone	0.60965	0.00054	393500	0.00008	0.00006	10	0.00164	0.00016	124
JSd-3	Stream sediment	0.00574	0.00020	4000	0.00778	0.00010	2415	0.10576	0.00046	30551
MESS-3	Marine sediment	0.03356	0.00017	14700	0.01479	0.00033	4400	0.17640	0.00038	43400
PACS-2	Marine sediment	0.04499	0.00018	19600	0.01508	0.00023	4400	0.17280	0.00041	40900
SARM-1	Granite	0.01432	0.00014	5571	0.00183	0.00021	540	0.06600	0.00041	14269
SARM-2	Syenite	0.00759	0.00023	4857	0.00025	0.00026	265	0.03782	0.00018	10072
SARM-3	Lujavrite	0.04442	0.00023	23000	0.00645	0.00027	2877	0.18540	0.00057	70223
SARM-4	Norite	0.16505	0.00027	82190	0.00126	0.00023	1199	0.13679	0.00023	63649

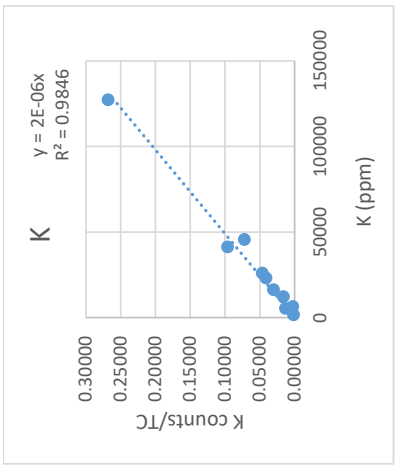
K
y = 2E-06x
R² = 0.9846
K counts/TC
K (ppm)
0.00000
0.05000
0.10000
0.15000
0.20000
0.25000
0.30000
0
50000
100000
150000

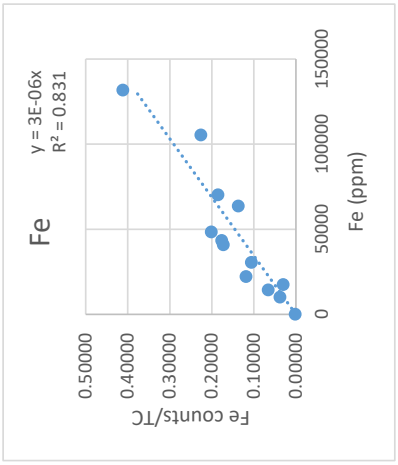
Fe
y = 3E-06x
R² = 0.831
Fe counts/TC
Fe (ppm)
0.00000
0.10000
0.20000
0.30000
0.40000
0.50000
0
50000
100000
150000

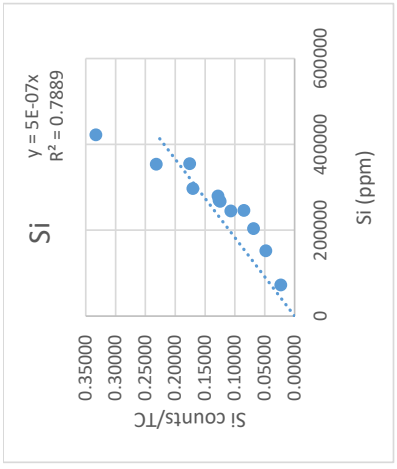
Si
y = 5E-07x
R² = 0.7889
Si counts/TC
Si (ppm)
0.00000
0.05000
0.10000
0.15000
0.20000
0.25000
0.30000
0.35000
0
200000
400000
600000

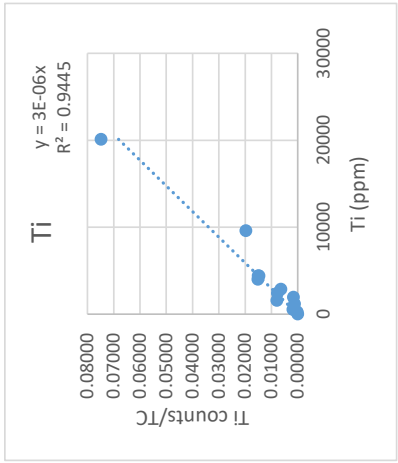
Ti
y = 3E-06x
R² = 0.9445
Ti counts/TC
Ti (ppm)
0.00000
0.01000
0.02000
0.03000
0.04000
0.05000
0.06000
0.07000
0.08000
0
10000
20000
30000

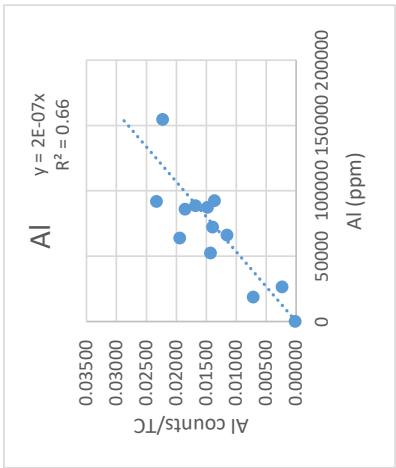
Al
y = 2E-07x
R² = 0.66
Al counts/TC
Al (ppm)
0.00000
0.00500
0.01000
0.01500
0.02000
0.02500
0.03000
0.03500
0
50000
100000
150000
200000

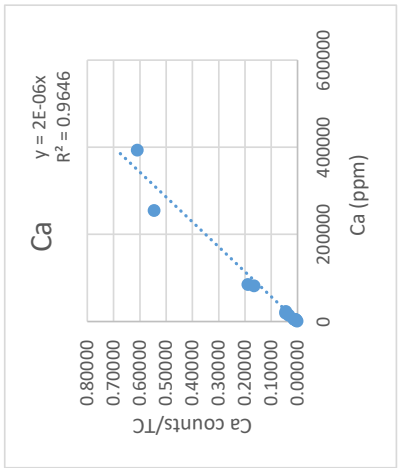
Ca
y = 2E-06x
R² = 0.9646
Ca counts/TC
Ca (ppm)
0.00000
0.10000
0.20000
0.30000
0.40000
0.50000
0.60000
0.70000
0.80000
0
200000
400000
600000

Table S2. **Pearson correlation coefficients, r, of measured parameters of all sediment traps and MWAC sampler.**
Left (lower) side of the tables represent *r* values, and right (upper) side of the tables represent *p* values.
Green marked values show *p* values < 0.01 and yellow marked values represent *p* values < 0.05 for *p* and r values, respectively.

M1U	TM	CaCO3	BSiO2	OM	Rest	Al	Si	K	Ti	Fe
TM		0.860	0.282	0.660	0.648	0.505	0.355	0.924	0.761	0.961
CaCO3	-0.04		0.091	0.855	0.000	0.000	0.000	0.000	0.000	0.000
BSiO2	-0.25	0.38		0.001	0.001	0.014	0.048	0.002	0.004	0.003
OM	-0.10	-0.04	0.66		0.153	0.161	0.398	0.143	0.226	0.154
Rest	0.11	-0.92	-0.67	-0.32		0.000	0.000	0.000	0.000	0.000
Al	-0.15	-0.75	-0.53	-0.32	0.83		0.000	0.000	0.000	0.000
Si	-0.21	-0.79	-0.44	-0.19	0.81	0.84		0.000	0.000	0.000
K	0.02	-0.78	-0.63	-0.33	0.87	0.95	0.86		0.000	0.000
Ti	-0.07	-0.88	-0.60	-0.28	0.94	0.91	0.93	0.95		0.000
Fe	-0.01	-0.74	-0.62	-0.32	0.83	0.95	0.86	0.98	0.92	

<0,01
<0,05

M2U	TM	CaCO3	BSiO2	OM	Rest	Al	Si	K	Ti	Fe
TM		0.220	0.693	0.233	0.255	0.903	0.644	0.676	0.651	0.859
CaCO3	0.26		0.812	0.000	0.000	0.005	0.003	0.001	0.000	0.034
BSiO2	0.09	0.05		0.420	0.133	0.134	0.613	0.020	0.064	0.109
OM	-0.25	-0.74	0.17		0.009	0.484	0.095	0.167	0.136	0.617
Rest	-0.24	-0.94	-0.32	0.52		0.000	0.006	0.000	0.000	0.007
Al	0.03	-0.56	-0.31	0.15	0.66		0.000	0.000	0.000	0.000
Si	0.10	-0.58	0.11	0.35	0.55	0.88		0.000	0.000	0.000
K	-0.09	-0.62	-0.47	0.29	0.72	0.93	0.77		0.000	0.000
Ti	-0.10	-0.68	-0.38	0.31	0.77	0.95	0.82	0.96		0.000
Fe	0.04	-0.43	-0.34	0.11	0.54	0.93	0.84	0.90	0.87	

<0,01
<0,05

M2L	TM	CaCO3	BSiO2	OM	Rest	Al	Si	K	Ti	Fe
TM		0.000	0.102	0.003	0.001	0.008	0.002	0.017	0.009	0.011
CaCO3	0.66		0.272	0.000	0.000	0.000	0.000	0.001	0.000	0.008
BSiO2	-0.34	-0.23		0.097	0.818	0.240	0.942	0.238	0.587	0.152
OM	-0.58	-0.92	0.35		0.000	0.008	0.004	0.013	0.003	0.084
Rest	-0.62	-0.98	0.05	0.85		0.000	0.000	0.000	0.000	0.002
Al	-0.53	-0.67	-0.25	0.53	0.73		0.000	0.000	0.000	0.000
Si	-0.61	-0.67	0.02	0.57	0.69	0.93		0.000	0.000	0.000
K	-0.48	-0.64	-0.25	0.50	0.70	0.96	0.93		0.000	0.000
Ti	-0.52	-0.74	-0.12	0.57	0.79	0.96	0.93	0.96		0.000
Fe	-0.51	-0.53	-0.30	0.36	0.61	0.88	0.89	0.92	0.88	

M3L	TM	CaCO3	BSiO2	OM	Rest	Al	Si	K	Ti	Fe
TM		0.01	0.02	0.13	0.01	0.01	0.02	0.01	0.01	0.24
CaCO3	0.54		0.01	0.00	0.00	0.00	0.00	0.00	0.00	0.00
BSiO2	-0.46	-0.52		0.00	0.13	0.70	0.06	0.62	0.43	0.79
OM	-0.32	-0.85	0.57		0.00	0.01	0.00	0.01	0.00	0.01
Rest	-0.50	-0.97	0.32	0.75		0.00	0.00	0.00	0.00	0.00
Al	-0.50	-0.80	0.08	0.53	0.88		0.00	0.00	0.00	0.00
Si	-0.48	-0.86	0.39	0.66	0.86	0.92		0.00	0.00	0.00
K	-0.49	-0.79	0.11	0.54	0.86	0.98	0.92		0.00	0.00
Ti	-0.49	-0.85	0.17	0.63	0.91	0.98	0.92	0.98		0.00
Fe	-0.25	-0.66	0.06	0.51	0.72	0.88	0.89	0.91	0.87	

<0,01
<0,05

M4U	TM	CaCO3	BSiO2	OM	Rest	Al	Si	K	Ti	Fe
TM		0.04	0.51	0.59	0.01	0.22	0.87	0.04	0.06	0.27
CaCO3	0.44		0.63	0.01	0.00	0.01	0.23	0.01	0.01	0.09
BSiO2	0.15	-0.11		0.45	0.14	0.47	0.00	0.04	0.01	0.01
OM	-0.12	-0.56	-0.17		0.07	0.48	0.09	0.88	0.55	0.87
Rest	-0.51	-0.87	-0.33	0.39		0.00	0.92	0.00	0.00	0.00
Al	-0.27	-0.55	-0.16	-0.16	0.73		0.08	0.00	0.00	0.00
Si	0.04	-0.27	0.77	-0.37	0.02	0.38		0.56	0.94	0.98
K	-0.45	-0.54	-0.43	0.03	0.79	0.90	0.13		0.00	0.00
Ti	-0.41	-0.57	-0.51	0.13	0.84	0.85	0.02	0.93		0.00
Fe	-0.25	-0.37	-0.56	0.04	0.67	0.83	0.01	0.91	0.93	

<0,01
<0,05

M4L	TM	CaCO3	BSiO2	OM	Rest	Al	Si	K	Ti	Fe
TM		0.588	0.003	0.007	0.015	0.022	0.030	0.043	0.160	0.038
CaCO3	-0.12		0.000	0.003	0.002	0.054	0.000	0.065	0.001	0.174
BSiO2	0.58	-0.67		0.000	0.495	0.330	0.000	0.219	0.791	0.142
OM	0.53	-0.59	0.75		0.431	0.056	0.008	0.080	0.801	0.031
Rest	-0.49	-0.61	-0.15	-0.17		0.000	0.373	0.000	0.000	0.000
Al	-0.47	-0.40	-0.21	-0.40	0.85		0.322	0.000	0.000	0.000
Si	0.44	-0.80	0.89	0.53	0.19	0.21		0.446	0.041	0.546
K	-0.42	-0.38	-0.26	-0.36	0.86	0.97	0.16		0.000	0.000
Ti	-0.30	-0.63	0.06	-0.05	0.83	0.91	0.42	0.91		0.000
Fe	-0.42	-0.29	-0.31	-0.44	0.80	0.94	0.13	0.96	0.84	

<0,01
<0,05

M5L	TM	CaCO3	BSiO2	OM	Rest	Al	Si	K	Ti	Fe	
TM		0.067	0.440	0.916	0.001	0.000	0.929	0.000	0.001	0.222	<0,01
CaCO3	-0.38		0.007	0.006	0.004	0.002	0.002	0.031	0.002	0.367	<0,05
BSiO2	-0.17	-0.53		0.715	0.061	0.543	0.000	0.170	0.752	0.864	
OM	-0.02	-0.54	0.08		0.063	0.714	0.600	0.910	0.958	0.917	
Rest	0.63	-0.56	-0.39	0.39		0.000	0.224	0.000	0.001	0.208	
Al	0.78	-0.60	-0.13	0.08	0.84		0.765	0.000	0.000	0.007	
Si	-0.02	-0.61	0.96	0.11	-0.26	0.06		0.715	0.225	0.409	
K	0.73	-0.44	-0.29	0.02	0.82	0.97	-0.08		0.000	0.001	
Ti	0.63	-0.60	0.07	0.01	0.65	0.90	0.26	0.89		0.001	
Fe	0.26	-0.19	-0.04	0.02	0.27	0.53	0.18	0.62	0.63		

Iwik	Al	Si	K	Ti	Fe	
Al		0.000	0.000	0.000	0.000	<0,01
Si	0.89		0.000	0.002	0.002	<0,05
K	0.98	0.90		0.000	0.000	
Ti	0.94	0.81	0.96		0.000	
Fe	0.96	0.81	0.95	0.95		

Table S3. Linear regressions and correlation coefficients for Ti versus Al for Iwik and all sediment traps.

Site	Regression equation	R^2
Iwik	y = 0.8391x + 0.04	0.81
M1U	y = 0.8824x + 0.03	0.83
M2U	y = 0.757 x - 0.00	0.89
M2L	y = 0.8062x - 0.01	0.92
M3L	y = 0.8235x - 0.02	0.96
M4U	y = 0.6037x + 0.01	0.72
M4L	y = 0.5439x - 0.01	0.82
M5L	y = 0.4358x + 0.02	0.81

Table S4. **Pearson correlation coefficients, r, of the residual mass fraction in % for the seven sediment traps M1 to M5.**
Left (lower) side of the tables represent *r* values, and right (upper) side of the tables represent *p* values.
Green marked values show *p* values < 0.01 and yellow marked values represent *p* values < 0.05 for *p* and r values, respectively.

	M1U	M2U	M2L	M3L	M4U	M4L	M5L
M1U		0.005	0.031	0.026	0.034	0.208	0.003
M2U	0.56		0.000	0.000	0.000	0.000	0.078
M2L	0.44	0.72		0.000	0.011	0.000	0.158
M3L	0.45	0.86	0.73		0.000	0.000	0.159
M4U	0.43	0.73	0.51	0.83		0.000	0.093
M4L	0.27	0.71	0.74	0.75	0.64		0.056
M5L	-0.59	-0.38	-0.3	-0.35	-0.4	-0.69	

<0,01
<0,05

CHAPTER 3

Tropical rains control Saharan dust deposition and bio-availability of nutrients

Michèlle van der Does, Laura F. Korte, Geert-Jan A. Brummer, Corina P. D. Brussaard, Fleur C. J. van Crimpen, Patrick Laan, Natalie M. Mahowald, Ute Merkel, Franziska Pausch, Joseph M. Prospero, Scarlett Trimborn, Hongbin Yu, Paquita Zuidema, and Jan-Berend W. Stuut

in preparation for Geophysical Research Letters

Mineral dust plays an important role in the ocean's carbon cycle through the input of nutrients and metals which potentially fertilize phytoplankton, and by ballasting organic matter from the surface ocean to the deep sea floor (Pabortsava et al., 2017). Because open-ocean dust-flux measurements are either based on shipboard- (Baker et al., 2010) or sediment-trap data (Pabortsava et al., 2017), they are biased by interpolation and extrapolation of point observations in space and time. Alternatively, dust-flux estimations can be made using satellite observations (Yu et al., 2015a), but these are often hampered by the presence of clouds.

Here, we present a two-year time series of sediment-trap dust-deposition fluxes directly below the core of the Saharan dust plume along a transatlantic array at 12°N, which shows the spatial and temporal evolution of Saharan-dust deposition across the Atlantic Ocean. We demonstrate that most of the dust deposited in the Atlantic Ocean is washed out of the atmosphere by summer rains. These field data are corroborated by comprehensive earth system model (CESM) dust-deposition data across the same transatlantic transect. In addition, nutrient-release bottle experiments in ambient sea water carried out along the same transect demonstrate how wet deposition of Saharan dust increases the release of both macro- (P, Si) and micronutrients (Fe) up to an order of magnitude as opposed to dry deposition. Rain-amplified bioavailability of these nutrients may well be the key to increased surface-ocean productivity in the remote and oligotrophic parts of the oceans and, potentially, also continental ecosystems (Yu et al., 2015b).

Large quantities of mineral dust are blown from the Sahara Desert across the Atlantic, impacting both the atmosphere and the ocean by altering the atmospheric radiation budget (Ryder et al., 2013), serving as cloud condensation nuclei (Twohy et al., 2009) and ice nuclei (Atkinson et al., 2013), as well as influencing the ocean's carbon cycle through the delivery of nutrients which stimulate phytoplankton growth (Martin and Fitzwater, 1988; Pabortsava et al., 2017) and by ballasting organic particles to the ocean floor (Pabortsava et al., 2017; Van der Jagt et al., 2018). These effects depend on the size, shape, and mineralogy of the dust particles (Shao et al., 2011), which in turn vary seasonally and along the downwind trajectory as a result of preferential settling of coarse particles (Van der Does et al., 2016; Korte et al., 2017) and atmospheric processing by cloud systems and chemical reactions (Shi et al., 2011). Transport of Saharan dust across the Atlantic Ocean was studied at sea during research expeditions (Stuut et al., 2005), estimated by remote sensing (Yu et al., 2015a), and monitored at stations on the eastern- (Bory and Newton, 2000) and western sides of the Atlantic (Carlson and Prospero, 1972). However, the general dust paradox "how are dust-derived nutrients available for phytoplankton?" remains unanswered (Blain et al., 2004).

Quantifications of actual nutrient inputs into the ocean are biased by estimates that rely on extrapolations of single depositional events encountered at sea during research expeditions. While deposition of dust into the ocean was recognized to be potentially affected by interaction with storm systems or wet deposition (Duce et al., 1991), it remains elusive how the processing by storm systems would influence the bio-availability of nutrients carried by dust particles.

We monitored two years of Saharan dust deposition fluxes *in-situ* at four sites across the Atlantic Ocean using time-series of submarine sediment traps (M1-M4). The traps were moored at 1200 meters water depth, three positioned along a transect at 12°N and a fourth at 13°N (Fig. 1a), sampling from October 2012 to October 2014 (Supplement Table S1). This transect is complemented by two years (2013-2014) of Saharan dust concentrations measured on Barbados (Fig. 1b). We combine these observational data (Fig. 1c) with dry- and wet-dust deposition fluxes simulated with a coupled earth system model (Fig. 1d), and dust optical depth from the Moderate Resolution Imaging Spectroradiometer (MODIS, Fig. S1) as well as precipitation from the Tropical Rainfall Measuring Mission (TRMM, Fig. S1) along the transect (see Methods). In addition, we experimentally determined the release of nutrients from a Saharan dust source into Atlantic surface waters, contrasting dry- and wet deposition (Fig. 2). The wet-deposited dust was pre-treated with sulfuric acid of pH = 2, mimicking chemical conditions that have been observed to occur in clouds

(Zhu et al., 1992; Shi et al., 2011) (see Methods), although in actual rainwater, the pH is obviously higher (Spokes and Jickells, 1996).

Observed dust mass fluxes were highest at station M1 and decreased sharply downwind to M4 (Figs. 1c and S1a). Dust deposition showed distinct seasonality across the Atlantic, peaking in summer and autumn, and with lowest fluxes in winter and spring (Figs. 1c and S2b-e). Although station M2 is positioned only about 160 km north of station M3, it appears to have registered lower fluxes and less seasonality, which we hypothesize is caused by a position away from the center of the Saharan dust cloud. Overall, the fluxes' seasonal amplitude decreased from east to west, coinciding with seasonal particle-size trends along the transect (Van der Does et al., 2016), and with previously reported Saharan dust fluxes in the eastern Atlantic (Bory et al., 2002; Fischer et al., 2016).

The modelled dust deposition fluxes (Fig. 1d) should be interpreted in a general sense as they are the average across 15 years. As a result, they cannot be compared one-to-one to the observed fluxes, which may be subject to interannual variability. Yet, generally the modelled fluxes also generally reveal a strong decrease from east to west, albeit more gradual than the downwind decrease in fluxes observed in the sediment traps (Fig. 1c). More importantly, the modelled data show a sharp seasonal contrast between dry- and wet deposition, which is more pronounced than observed in the sediment traps. Modelled wet deposition is highest in summer and fall, following the meridional movement of precipitation along with the Intertropical Convergence Zone (ITCZ) (Nicholson, 2000). From east to west, the modelled dominant deposition mode changes from winter/dry- to summer/wet deposition, which also match observations in Florida, where wet dust deposition was found to dominate (Prospero et al., 2010). Dry deposition is highest in winter and spring in the east and decreases westward in both magnitude and seasonal amplitude. The modelled deposition maxima in winter and spring (dry deposition) and late summer and fall (wet deposition) in the Atlantic Ocean are corroborated by the sediment-trap observations and the incidence of precipitation.

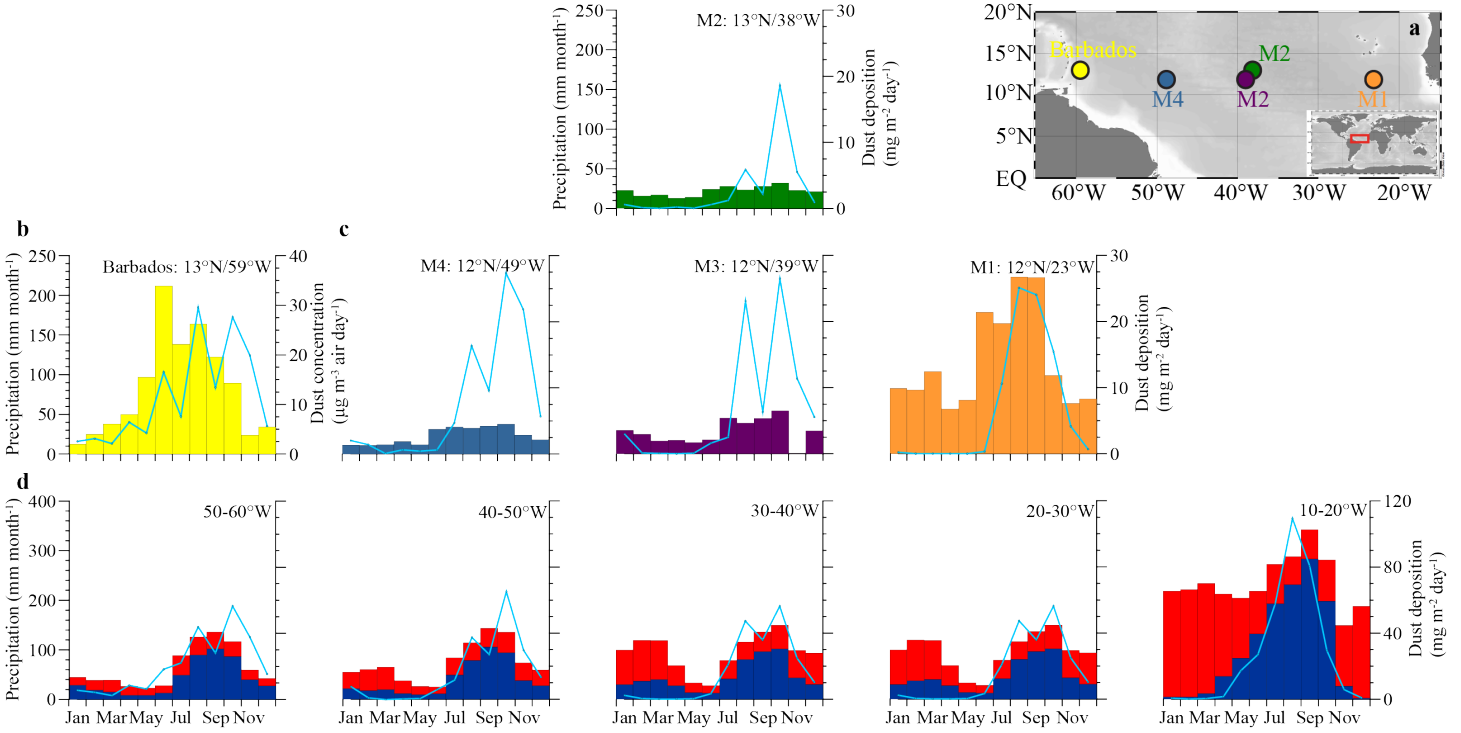

Figure 1. Setup of transatlantic dust-monitoring experiment with a) map projection of sediment-trap sampling stations M1-M4, and Barbados (Prospero et al., 1970). b) average daily dust concentrations at Barbados (bars; right Y-axis) and averaged monthly precipitation (1×1°, blue lines; left Y-axis), both averaged for 2013-2014. c) daily dust deposition in the sediment traps M1-M4 (various longitudes across Atlantic, bars; right Y-axes), with monthly precipitation (1×1°) both averaged per month for 2013-2014 (blue lines; left Y-axes). d) stacked diagram of simulated transatlantic dust deposition fluxes averaged over 5°×10° latitude-longitude areas between 10°-15°N and 10°-60°W (dry deposition [red bars], stacked upon wet deposition [blue bars]); Y-axes on the right) and over a period of 15 model years. Monthly precipitation (5×10° lat-lon) averaged per month for 2013-2014 (blue lines; left Y-axis).

In concert with increased deposition fluxes observed in the traps, atmospheric dust loads as measured by DOD, which can only be quantified in clear-sky conditions, were also highest in early summer, and decrease in mid-summer when precipitation washes the dust out of the atmosphere (Fig. S1). In late summer, increased dust deposition fluxes coincided further with intensified precipitation along the entire transect, although less clear at M2 (13°N) where precipitation is lower.

On Barbados, atmospheric dust loads increased in summer and autumn (Fig. 1b). Saharan dust arriving at Barbados is the residual of dust not being washed out by rains during its transatlantic crossing, and dust concentrations peak before precipitation peaks over the Atlantic. Reported Saharan dust concentrations in the western Atlantic peaked in spring (French Guyana) and summer (Barbados) (Prospero et al., 2014), and previous studies have hypothesized that previous-year Sahel precipitation controls dust generation and emission (Prospero and Nees, 1986). In light of our current findings, we argue that North Atlantic precipitation in turn strongly influences the amounts of Saharan dust reaching the western Atlantic Ocean.

Sulfuric- and nitric acids are thought to be the most important acids for chemical processing of dust particles in the atmosphere (Shi et al., 2009) that increase the solubility of, foremost, iron (Baker and Croot, 2010). Acid-processing of dust particles was shown to occur in clouds, where acidity may be as low as pH = 1 and the solubility of ferric iron increases by three orders of magnitude for each unit decrease in pH (Zhu et al., 1992). Mesocosm experiments in the Mediterranean already suggest that wet-deposition leads to increased concentrations of bio-available nutrients, particularly iron (Pulido-Villena et al., 2014), as opposed to dry-deposition (Ridame et al., 2014). Our nutrient-release experiments showed that deposition of pre-treated (wet) dust into sea water leads to an initial doubling of the release of phosphate and silicate and to an order-of-magnitude increase in dissolved iron, compared to dry deposition, which show no significant difference from the control runs (Fig. 2). In addition, concentrations of the leached nutrients remained significantly higher during the course of the nutrient-release bottle experiments.

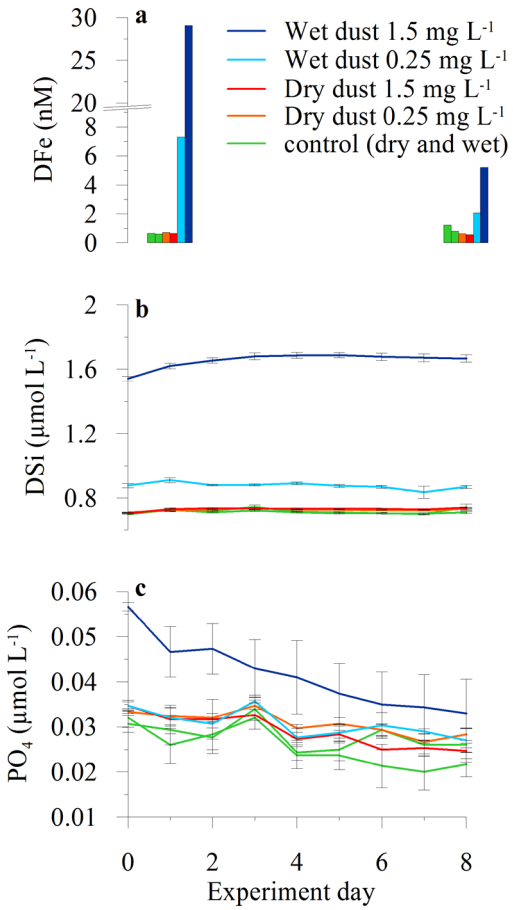

Figure 2. Development of a) total dissolved iron (DFe), b) silicate (DSi), and c) phosphate (PO_4) concentrations on each experiment day (DFe only measured on day 1 and 8) as a result of dry- and wet-dust additions of 0.25 and 1.5 mg L^{-1} Saharan dust to seawater sampled at station M1 (12°N, 23°W). Nutrient concentrations of dry-dust additions hardly differ from control runs, whereas wet-dust additions increase the amount of released nutrients significantly.

In summary, our combined results of *in-situ* dust deposition fluxes, model simulations, remote-sensing analyses, and shipboard observations show that the wet deposition is the main mechanism that deposits Saharan dust into the tropical Atlantic Ocean. Moreover, our shipboard experiments clearly showed wet-deposition events leading to a doubling in the release of macronutrients (P, Si) and up to an order-of-magnitude release of micronutrients (Fe). Consequently, and as was suggested from surface-ocean measurements (Schlosser et al., 2014), wet deposition of bio-available nutrients from mineral dust may well be key to increased surface-ocean productivity, particularly in oligotrophic parts of the world's oceans. Considering future changes

in global and regional precipitation patterns and the many uncertainties regarding the dust cycle (Stocker et al., 2013), an improved understanding of these mechanisms is key to future climate predictions and the impact of mineral dust on global carbon budgets through ocean fertilization.

Author Contributions

JBS led the project and designed the study including sea-going expeditions; MvdD, LK, JBS, GJB prepared the sediment traps and processed the samples for analyses; MvdD performed the dust-flux analyses and collected satellite data; CB, FP and ST helped LK design and perform the shipboard dust-addition experiments; PL performed the Fe-analyses; Barbados samples were collected by JP and PZ and analyzed by FvC; NM designed the dust module of the climate model, and UM ran the model and processed the data; HY processed the MODIS dust optical depth data. MvdD and LK wrote the paper together with GJB and JBS; All authors discussed the results and commented on the manuscript.

Acknowledgements

This project is funded by NWO (project no. 822.01.008, TRAFFIC), and ERC (project no. 311152, DUSTTRAFFIC) awarded to JBS. HY was supported by the NASA CALIPSO/CloudSat project managed by Dr. David Considine. FP and ST were funded by the Helmholtz Impulse Fond (HGF Young Investigators Group EcoTrace, VH-NG-901). The captains, crews, and scientists of FS *Meteor* cruise M89, RV *Pelagia* cruises 64PE378 and 64PE395, RRS *James Cook* cruise JC134, and NIOZ technicians are thanked for deployment and retrieval of the sediment-trap moorings. Chris Munday, Laura Schreuder, Monica Martens, Piet van Gaever, and Juliane Steinhardt are thanked for their assistance in onboard incubation-experiment and sediment-trap sample processing, and Claudia Alvarez for assistance with obtaining Barbados dust concentrations. Barbados measurements were supported by US NSF grant AGS-0962256 to JP.

Methods

This paper presents the particle fluxes from sediment traps moored along a transatlantic transect positioned directly below the main path of the Saharan dust cloud off northwest Africa. Deployment and recovery of the moorings and sediment traps, as well as specific information on the mooring equipment and sampling intervals, is described in the respective cruise reports (Stuut et al., 2012; 2013; 2015; 2016). In addition, the paper describes nutrient-release experiments carried out during an additional research cruise in the Atlantic Ocean (Stuut et al., 2016) in which we incubated ambient sea water with different kinds of dust to mimic cloud processing of dust resulting in wet deposition, contrasted with dry deposition. In this supplement, more details are provided about the applied methods.

Sediment traps

The transect consists of four mooring stations (M1-M4), which sampled for two consecutive years (Table S1; for more details, see Van der Does et al. (2016)). Three moorings were positioned at 12°N, and a fourth at 13°N. Here we present data from the upper sediment trap of each mooring at approximately 1200 meters water depth, sampling continuously at 8 or 16-days intervals (Table S1). Sediment trap 2014-M1 only sampled the first nine intervals due to a technical failure.

Table S1. Details of the sediment traps at station M1-M4, for the two sampling years 2013 (2013M*x*) and 2014 (2014M*x*).

Sediment trap	Lat (°N)	Lon (°W)	Trap depth (m.b.s.l)	Distance to African coast (km)	Sampling intervals (days)	Sampling period
2013-M1U	12.00	23.00	1150	700	16	19 Oct 2012 - 7 Nov 2013
2013-M2U	13.81	37.82	1235	2300	16	19 Oct 2012 - 7 Nov 2013
2013-M4U	12.06	49.19	1130	3500	16	19 Oct 2012 - 7 Nov 2013
2014-M1	12.00	23.01	1200	700	8 + 16	23 Nov 2013 - 31 Mar 2014
2014-M2	13.81	37.82	1190	2300	8 + 16	1 Dec 2013 - 25 Oct 2014
2014-M3	12.40	38.63	1362	2400	8 + 16	1 Dec 2013 - 17 Oct 2014
2014-M4	12.04	49.22	1100	3500	8 + 16	9 Dec 2013 - 25 Oct 2014

Prior to deployment of the sediment traps, a biocide was added to the sampling cups ($HgCl_2$, end concentration 1.3 g L^{-1}) and a pH buffer (borax, $Na_2B_4O_7$ $10H_2O$; end concentration 1.3 g L^{-1}, pH ≈ 8.5). As a result, the density inside the sampling cups was higher than the ambient seawater, to avoid water from leaking out. After recovery, the samples were sieved through a 1 mm mesh to remove zooplankton, and subsequently wet-split in five equal splits using a WSD10 rotor splitter (McLane Laboratories, USA). Samples were then washed with Milli-Q water and centrifuged (5 minutes at approximately 1800×g) three times. Bulk-sample mass was determined by weighing two freeze-dried 1/5 aliquots of each sample, resulting in an average deviation of 2.67% (σ = 2.38) by mass between paired splits. For determining the dust content of the samples, 1/25 of the original sample was used.

Mineral dust fluxes

Next to Saharan dust, the sediment-trap samples contained numerous particles derived from the marine environment, including biomineral particles (e.g. foraminifera, radiolarians, diatoms, coccolithophores) and organic matter (marine and atmospheric from e.g. biomass burning). To isolate the mineral dust fraction, all biogenic constituents were removed chemically, following the procedure described by Filipsson et al. (2011). The samples were then filtered over a pre-weighed 25 mm, 0.4 µm polycarbonate filter and rinsed with Milli-Q water. By weighing the filter, the Saharan dust mass flux > 0.4 µm could be determined. The weight of the sediment fraction smaller than 0.4 µm is considered negligible (Rosenberg et al., 2014). The filtration over 0.4 µm filters also allows for a direct comparison with particle-size distributions of the same samples as presented by Van der Does et al. (2016), who describe particle sizes from 0.4 to 2000 µm. Samples were assigned a mid-date, which is the middle of their 8 or 16-day sampling period. A short delay between ocean surface and sediment traps must be considered as the organic aggregates that incorporate the dust particles and carry them downward, have settling velocities of about 200 m per day (Nowald et al., 2015; Van der Jagt et al., 2018), which is in line with previously determined settling velocities for our sediment-trap samples of at least 140 m per day (Van der Does et al., 2016; Korte et al., 2017). Dust mass fluxes are highest at M1, with average values of 14.3 mg m^{-2} day^{-1} in 2013 and decrease sharply downwind to M4 with 3.3 and 2.3 mg m^{-2} day^{-1} in 2013 and 2014, respectively (Fig. S1a).

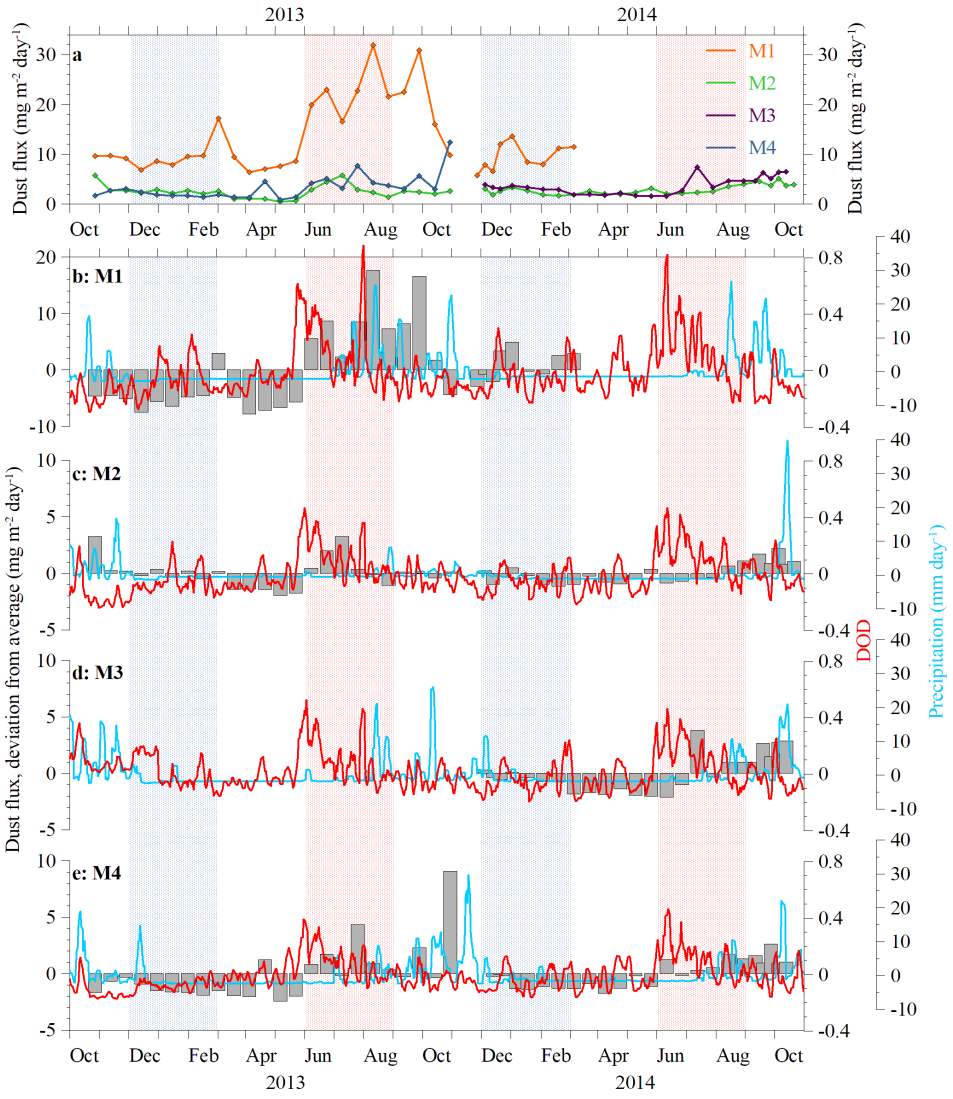

Figure S1. Time series of observed Saharan dust and precipitation across the Atlantic, a) Total mass fluxes of Saharan mineral dust (particles > 0.4 µm) collected by sediment traps M1-M4 from autumn 2012 to autumn 2014. b-e) Dust mass fluxes from the sediment traps as deviation from the annual 24-sample average (bars), Dust Optical Depth (DOD, MODIS Terra; red lines) and precipitation (TRMM; blue lines), as deviation from the yearly averages at station M1-M4. Note the different scale for dust fluxes at station M1 (b). Due to instrument failure after the ninth sample at 2014-M1, the average was calculated for those samples only (N = 9). Stippled areas represent winter (DJF, blue) and summer (JJA, red) seasons.

Dust fluxes derived from the total mass of the terrigenous fraction with the method described above appear smaller than so-called residual-mass fluxes, which are calculated by subtracting the weights of all biogenic constituents from the bulk-sample mass, and which are often assumed to represent the lithogenic or mineral dust fraction (Fischer et al., 2016). Residual mass fluxes were determined for the samples from October 2012 to November 2013 by (Korte et al., 2017). Although the residual flux is highly correlated with the dust flux presented here (R^2 = 0.69-0.80), absolute values are 2 to 18 times higher (average 5.8, σ = 3.3; Fig. S2). Korte et al. (2017) concluded that the residual fraction is most likely an overestimation, due to various uncertainties and assumptions in the mass of organic matter and biogenic opal, which is demonstrated by comparing these two representations of the dust fraction.

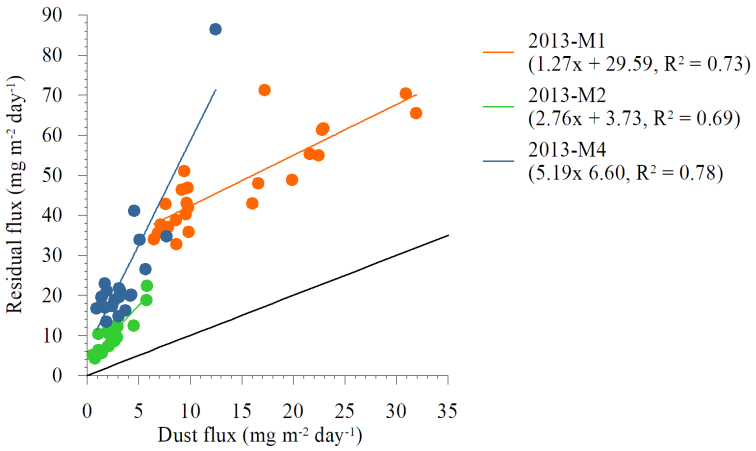

Figure S2. "Residual" flux (calculated after sequential leaching; Korte et al. (2017)) versus dust flux (presented here) for 2013-M1-M4. Black line represents 1:1 relation.

Remote sensing

Dust Optical Depth (DOD) was derived from the Moderate Resolution Imaging Spectroradiometer (MODIS) Aerosol Optical Depth (AOD) and fine-mode fraction (FMF) Collection 6 data, from both Terra and Aqua satellites, following the method developed by Yu et al. (2009). This is based on the distinct particle sizes of mineral dust, marine aerosols and combustion aerosols. The characteristic FMF for individual aerosol types based on MODIS measurements (over ocean only) were determined, and AOD and FMF were used to derive the DOD (Yu et al., 2009). Daily DOD data were obtained for 2012-2014 (Fig. S1) and averaged for both Terra and Aqua, only when both AOD and FMF were retrieved.

Precipitation data from TRMM (Tropical Rainfall Measuring Mission) was obtained at daily resolution for 1°×1° boxes around the sampling sites from the Giovanni online data system, developed and maintained by the NASA Goddard Earth Sciences Data and Information Services Center (GES DISC). For smoothing purposes, 5-day running averages were computed for both DOD and precipitation data (Fig. S1).

Dust modelling

The model results presented here (Fig. 1 in 5°×10° lat-lon resolution and Fig. S3 in 5°×5° lat-lon resolution) were obtained with the Community Earth System Model (CESM) (Hurrell et al., 2013). Present-day boundary conditions were prescribed in a fully coupled control simulation including atmosphere, land surface, ocean, and sea ice components. The simulation uses a resolution of 0.9°×1.25° (latitude×longitude) for the atmosphere and a nominal resolution of 1° for the ocean and was conducted for 20 model years. Results are presented as multi-year averages based on the last 15 years of the simulation, to obtain a robust climatological average. In our setup, the Community Atmosphere Model (CAM4) (Neale et al., 2013) has been chosen as the atmospheric component including the bulk aerosol module (BAM) to simulate mineral dust prognostically in four size bins (particle diameters of 0.1 to 1.0 μm, 1.0 to 2.5, 2.5 to 5.0, and 5.0 to 10.0 μm). The model includes representations of dust emission, transport and deposition which comprises both dry deposition (including both turbulent and gravitational settling) and wet deposition (through in-cloud and below-cloud scavenging). More details on the representation of the dust cycle in the model can be found in (Albani et al., 2014) and references therein. The main message that we take from the modelling data is the significant difference between summer (wet) and winter (dry) deposition. The aim of our manuscript is pertinently not to calibrate a model with robust *in-situ* measured time-series data, but rather the

other way around: using the model's general outcome to provide a complementary framework to understand the processes that we infer from the *in-situ* observations.

Nutrient-release experiments

Saharan dust nutrient-release experiments were conducted at station M1 (12°N, 23°W) in spring 2016 during research cruise JC134 (Stuut et al., 2016). Seawater was sampled from the mixed layer at 20 m with a Seabird CTD equipped with a rosette holding 24 x 10L Niskin bottles. From the rosette, the seawater was tapped gently into the acid-cleaned (10% HCl) incubation bottles. Wet- and dry-deposition from a paleo lake Saharan dust source (21.08°N, 12.19°W) was mimicked in varying amounts (0.25 and 1.5 mg L^{-1}) by adding pre-leached and untreated dust to the incubation bottles, respectively. The paleo-lake is located in the foothills of the Atlas Mountains, in one potential source and transit area, from where Saharan dust is transported across the Atlantic Ocean (Scheuvens et al., 2013). Before addition, the particle size of the dust was adjusted to be comparable to the dust that was observed in the traps at site M1 (Van der Does et al., 2016) by sieving over a 32 µm sieve. For wet deposition, the dust was leached in 40 mL of artificial rain (consisting of MilliQ + H_2SO_4) at pH = 2, at an end concentration of 0.0051 M H_2SO_4. It was kept in suspension for 24 hours, resembling the timespan used for cloud processing experiments (Spokes et al., 1994; Shi et al., 2009). Untreated dust was added in the same amounts directly to the seawater in the incubation bottles as a representative for dry-dust deposition. The experiments were run in triplicates for a total of eight days. After each day of the experiment, subsamples from the water from the incubation bottles were filtered and analyzed for the macronutrients phosphorous (PO_4), silicate ($Si(OH)_4$) and nitrate (NO_3) using colorimetric methods (Murphy and Riley, 1962; Strickland and Parsons, 1972; Grasshoff et al., 1983). Nitrate measurements did not show a different behavior between dry- and wet-dust additions (Fig. S4), showing that nitrogen compounds leached from Saharan sources in sulfuric acid are negligible. The micronutrient iron (DFe) was analyzed on the first and last day (Fig. 2) of the experiment using automated Flow Injection Analysis (Klunder et al., 2011).

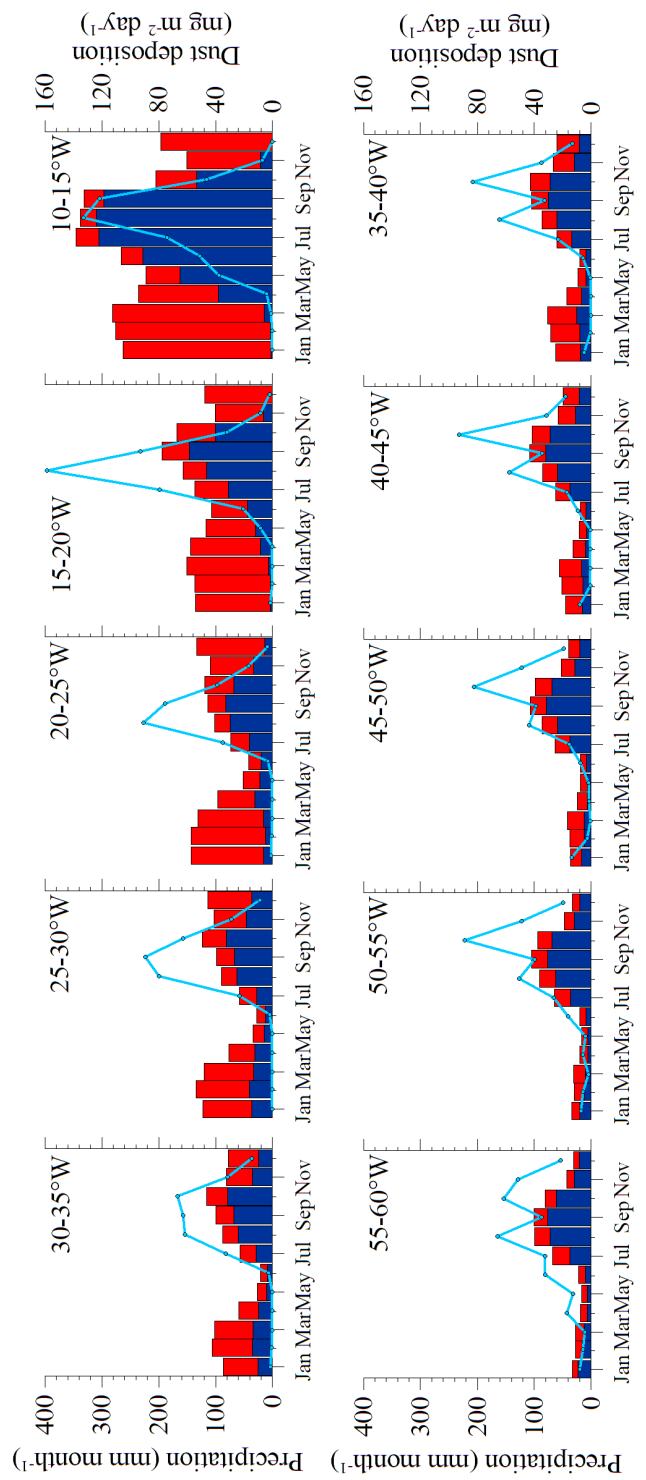

Figure S3. Dust-deposition modelling results presented in 5×5° grid cells. Stacked diagram of simulated transatlantic dust deposition fluxes averaged over 5°×5° latitude-longitude areas between 10°-15°N and 10°-60°W (dry deposition [red bars], stacked upon wet deposition [blue bars]); Y-axes on the right). Monthly precipitation (5×5°) averaged per month for 2013-2014 (blue lines; left Y-axis).

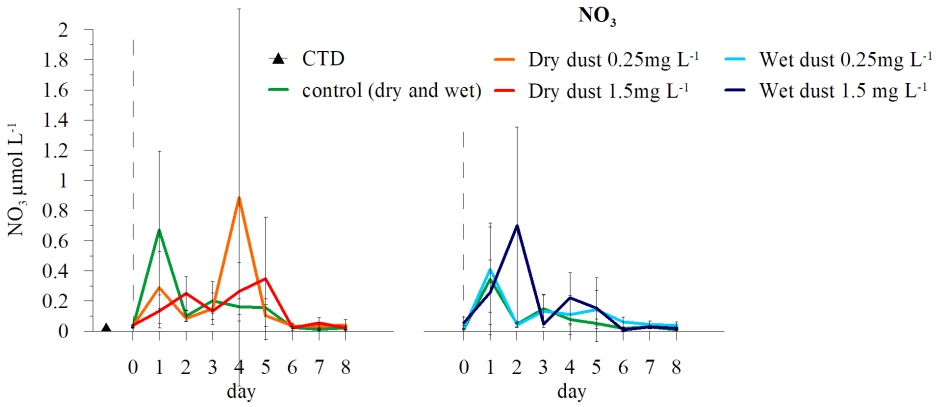

Figure S4. Development of nitrate concentrations (NO_3) of each experiment day as a result of dry- and wet-dust additions of 0.25 and 1.5 mg L^{-1} Saharan dust to seawater sampled at station M1 (12°N, 23°W). Results show no differences between controls and dry- and wet-dust additions. Dashed line represents start of the experiment.

CHAPTER 4

Effects of dry and wet Saharan dust deposition in the equatorial North Atlantic Ocean

Laura F. Korte, Franziska Pausch, Scarlett Trimborn, Corina P. D. Brussaard, Geert-Jan A. Brummer, Michèlle van der Does, Laura T. Schreuder, Chris I. Munday, Jan-Berend W. Stuut

ready to be submitted to Biogeosciences

Abstract

Incubation experiments comprising Saharan dust additions were conducted in the equatorial North Atlantic Ocean along an east-west transect at 12°N to study nutrient release and phytoplankton response in the oligotrophic seawater. Experiments were performed at three stations (M1, M3, M4), mimicking wet- and dry deposition of low and high amounts of Saharan dust from two different dust sources (paleo-lake and sand dune). Dust particle sizes were adjusted to resemble deposited dust found naturally in the deep sea at the experiment sites. For wet-dust deposition, the dust was pre-leached in acidified 'artificial rainwater' (H_2SO_4) for 16 to 24 hours, mimicking acid cloud processing at different pH values. Experiments were run up to eight days. Daily measurements of phosphate (P), silicate (Si), nitrate (N) and cell abundances were performed in addition to measurements of concentrations of total dissolved iron (DFe), dissolved inorganic carbon (DIC) and particulate organic carbon (POC) at the start and end of the experiments.

A significant initial increase and subsequent gradual decrease in P, Si and DFe concentrations after wet-dust deposition was observed, when dust amounts were high and leached in low pH rain (H_2SO_4, pH = 2). Remarkably, the experiments showed no nutrient release (P, Si, DFe) from dry-dust addition and the N concentrations remained low in all (dry and wet) experiments. The prokaryotic cyanobacterium *Synechococcus* spp. was the most prominent picophytoplankton in all mixed layer experiments. After an initial increase in cell abundance, a subsequent decrease (M1) or steady state (M3) with similar temporal dynamics in dry- or wet-dust deposition experiments was observed. The POC concentrations increased in all experiments and showed similar high values after both dry- and wet-dust deposition treatments. Therefore, no significant differences in POC concentrations between both depositions were observed, although wet Saharan-dust deposition has great potential to introduce bioavailable nutrients (i.e. P, Si and DFe) into the otherwise nutrient-starved oligotrophic ocean. These nutrients are likely predominantly promoting the phytoplankton community, when an additional N-source is also available. Saharan dust particles from both experiments might be incorporated into marine snow aggregates leading to the similar high POC concentrations.

Keywords: Saharan dust, incubation, nutrients, POC, deposition, phytoplankton, ocean fertilization

1 Introduction

Atmospheric-dust deposition into the vast ocean is one of the major processes to deliver nutrients to oligotrophic ocean waters where river runoff and upwelling are absent. Saharan dust deposition was shown to impact the biogeochemical cycle of oceanic waters downwind the most prominent dust plumes towards the Mediterranean Sea (Bonnet et al., 2005; Romero et al., 2011; Desboeufs et al., 2014; Guieu et al., 2014a; Ridame et al., 2014) and the equatorial North Atlantic Ocean (Jickells, 1999; Baker et al., 2003; Mills et al., 2004; Bristow et al., 2010). Dust deposition impacts biogeochemical fluxes in the water through fertilization (Jickells et al., 2005; Pabortsava et al., 2017) and ballasting of marine snow aggregates (Van der Jagt et al., 2018) both impacting the carbon dioxide content of surface waters. Mesocosm experiments in the Mediterranean Sea revealed that dust predominates the particulate phase exported to the base of the mesocosms (Desboeufs et al., 2014) and that up to 50 % of the total particle flux can be dust induced (Bressac et al., 2014). Wet-dust deposition resulted in a higher export production of particulate organic carbon (POC) compared to dry-dust deposition (Desboeufs et al., 2014), likely due to stimulated chlorophyll-*a* (Chl-*a*) production (Ridame et al., 2014). This is attributed to cloud processing, 'aging' of the dust minerals on their long-range transport through their exposure to acidic conditions in the atmosphere (Desboeufs et al., 2001).

Thereby, the pH is the major control on metal solubility in rainwater which can be as low as pH 1-2 as a result of anthropogenic H_2SO_4 and HNO_3 uptake as well as SO_2 oxidation (Spokes et al., 1994). Under low pH conditions, especially iron is leached from the dust particles to rain droplets, which subsequently release the iron more easily to the ocean waters (Spokes et al., 1994). In the ocean, iron is an important micronutrient needed for phytoplankton growth and nitrogen fixation (Falkowski et al., 1998; Capone, 2001; Karl et al., 2002), especially in the so-called High Nutrient Low Chlorophyll (HNLC) regions of the ocean. In those parts that are not iron (Fe), but phosphorus (P) or nitrogen (N) limited, like the equatorial Atlantic Ocean and the Mediterranean Sea, Saharan dust promotes nitrogen fixation which in turn enhances new production in the surface ocean (Ridame and Guieu, 2002; Baker et al., 2003), delivering nitrogen compounds.

By means of bioassay experiments Mills et al. (2004) showed that diazotrophic nitrogen fixation in the eastern tropical North Atlantic Ocean is Fe and P co-limited and that Saharan dust relieves this co-limitation. Also, Mahaffey et al. (2003) concluded that nitrogen fixation in the North Atlantic Ocean is temporally relieved by episodic dust deposition. Moreover, Baker et al. (2013) demonstrated that total Fe

input is higher when precipitation rates are also high. Still, P nutrient availability for phytoplankton growth across the tropical North Atlantic Ocean is low (Sohm et al., 2011) as vertical stratification reduces the introduction of nutrients from the deep into the mixed layer. Furthermore, the nutricline deepens westward across the tropical North Atlantic (Guerreiro et al., 2017) and therefore phytoplankton production in the North Atlantic Ocean may depend on atmospheric dust deposition delivering the necessary nutrients.

Massive amounts of mineral dust (182 Tg year $^{-1}$) are transported from the Sahara Desert towards the Americas (Yu et al., 2015a) and during transport a great part of the dust is deposited into the ocean. The dust is mainly deposited through precipitation, which can lead to an enhanced release of bio-available nutrients (Chapter 3). Pabortsava et al. (2017) demonstrated a link between POC fluxes and newly fixed nitrogen by diazotrophs whose activity was probably stimulated by Saharan dust deposition. However, to what extent Saharan dust deposition is responsible for new production of POC in the Atlantic Ocean, and whether dry- and wet-dust deposition have different impacts remains difficult to assess due to the complex interplay between dust sources, atmospheric processing, depositional processes, timing of deposition and surface-water conditions.

In this paper we examine the potential of Saharan dust fertilization on phytoplankton growth and POC production underneath the most prominent dust plume at 12°N (Mulitza et al., 2008). An accompanying paper discusses the bio-available nutrient release of Saharan dust in the eastern Atlantic Ocean (Chapter 3). For our experiment, we incubated two different types of Saharan dust mimicking dry- and wet-dust deposition to the ocean and quantified nutrient (PO_4, $Si(OH)_4$, NO_3, DFe) release and its effect on picoplankton cell abundances during the experiment. Further, we estimated the effect of dust additions on POC, dissolved inorganic carbon (DIC) as well as dissolved iron (DFe) at the start and end of the experiments. The results of this study contribute to a better understanding of the biogeochemistry in the equatorial North Atlantic Ocean and reveal the importance of Saharan dust deposition on the productivity in the surface waters.

2 Material and Methods

2.1 Background information

Saharan-dust incubations were conducted along a 12°N transect at three stations (M1, M3 and M4, Fig. 1) while crossing the North Atlantic in spring 2016 on board the research vessel RRS *James Cook,* cruise *JC* 134 (Stuut et al., 2016). On this transect Saharan dust was sampled using sediment traps to determine downward particles fluxes as well as Saharan dust particle sizes (Van der Does et al., 2016; Korte et al., 2017; Chapter 3). Results showed that Saharan dust contributed about 13 % to the total mass flux at M1 closest to the African coast and decreased to 4 % at M4 with distance from the source towards the west (Chapter 3). Particle sizes of the collected dust showed a decrease in modal diameter towards the west from about 18 µm at M1 to about 10 µm at M4 (on an annual basis; Van der Does et al., 2016).

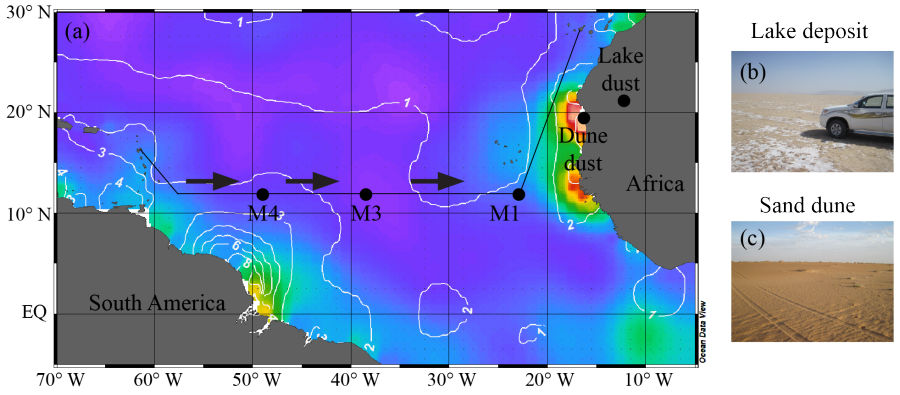

Figure 1. (a) Map showing the cruise track of JC 134 (arrows) from west to east, and the sites at which dust incubations in the tropical North Atlantic Ocean (M4-M1) were carried out. The color shading displays phosphate concentrations with values increasing from blue = 0 to red = 0.6 µmol L^{-1}, and white lines represent silicate concentrations in µmol L^{-1} in the surface waters (Ocean Data View, 1955-2010 annual averages). For the experiments, dust samples were collected at two sites in Mauritania, from (b) a lake deposit (21°N, 12°W), (c) a sand dune field (19°N, 16°W).

The major dust sources are located in the Sahara Desert, with locations in Mauritania acting as major source and transit areas from which dust is transported across the Atlantic Ocean and towards the Americas (Scheuvens et al., 2013). The two contrasting dust types which were used for the incubation experiments were collected from the foothills of the Atlas mountain (Fig. 1), located in one potential dust source and transit area in the western coastal region of Mauritania (Scheuvens et al., 2013). The first dust type was taken from an old lake deposit (lake dust), expected to contain

more bioavailable nutrients associated with fine-grained sediments, and the second dust type was taken from a sand dune (dune dust), consisting of coarser grained sediments.

2.2 Dust characteristics

The grains of the collected sand and lake soil sediments from Mauritania were too coarse to be used as an atmospheric dust sample as such. The bulk grain-size distributions of the sand and lake soil samples showed a bimodal distribution for the dune sand, with modes at 200 and 900 µm, while the lake soil had a multimodal distribution with prominent frequencies at 1, 11, 100 and 250 µm (Fig. 2a). Van der Does et al. (2016) showed that the Saharan dust deposited at site M1 is finer grained with a unimodal distribution peaking at 18 µm (Fig. 2). Therefore, the sand and lake soil sediments were sieved and sorted into different size classes (< 32, < 63, < 90, < 150, < 250 µm). For both dust types, the < 32 µm size fraction was used for the incubation experiments, which was ground for the dune dust, but not for the lake dust (Fig. 2b).

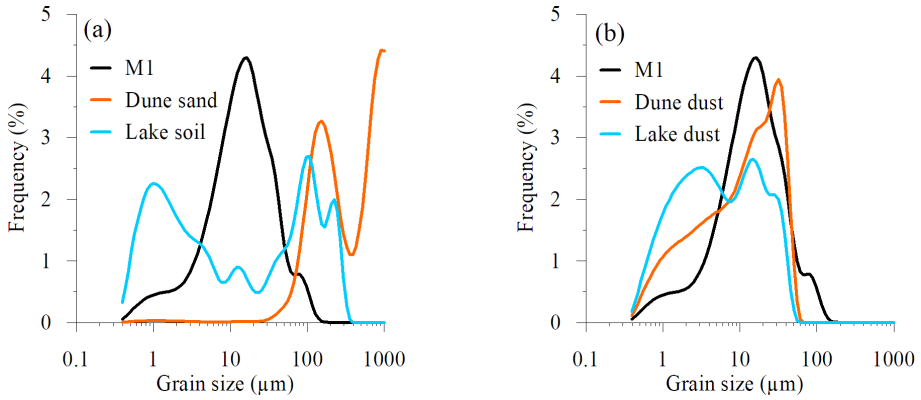

Figure 2. Grain-size distributions of dune and lake sediments (a) before and (b) after sieving. Black line represents Saharan dust from a sediment trap at 1200 m water depth at site M1 deposited in March 2013 (Van der Does et al., 2016), the month in which the incubations took place.

2.3 Incubation experiments

Before usage on board, all incubation bottles (6 L, PET) were cleaned with 10% HCl, rinsed with Milli-Q, dried, and sealed in plastic bags. Dust-addition treatments, duration and water sampling depth are given in Table 1 for each of the three incubation sites (M1, M3 and M4). Water sampling was performed with a Seabird CTD equipped with a rosette holding 24 10 L Niskin bottles. Seawater was sampled from the mixed layer (ML, ~20 m) at stations M1, M3 and M4, and additionally in the deep layer, shortly above the deep chlorophyll maximum (DL, ~72 m) at M3 where temperatures were still the same as in the surface seawater, or 100 m at M4 (temperature and fluorescence profiles are shown in supplementary Fig. S1). The water-handling procedures for incubations improved from experience gained during the first incubations in the west (M4). At M4, all sampled seawater was mixed in a darkened acid-cleaned 240 L tank. At M3 and M1, the seawater was directly and gently filled into the darkened incubation bottles, which shorted the incubation procedure. Results of the incubations at M4 are presented in the supplement (S4). In a laminar flow hood (ISO class 5), the filled incubation bottles were amended with the dune and lake dust, which was either acidified, mimicking wet-dust deposition, or kept untreated for dry-dust deposition. Control samples with no dust addition and/or addition of pure rain (rain-control) were run along the incubations. All treatments were run in replicates as summarized in Table 1.

Due to the fine-grained sediments of the lake dust and thereby expected higher nutrient content, we tested the impact of dry versus wet deposition of dust into seawater with the lake dust, while only the effects of wet deposition were tested for the dune dust. To mimic wet deposition, both dust types were leached in 40 mL 'artificial rainwater' for 16 to 24 hours before adding the treatment to the incubation bottles. This timespan was chosen according to protocols from previous cloud processing experiments (Spokes et al., 1994; Shi et al., 2009). Based on satellite-derived precipitation data, 40 mL translates to a realistic precipitation rate (0.04 mm d^{-1}, Fig. S2) for our incubation sites during the time of the experiment. A small amount of precipitation is already sufficient to wash out suspended dust from the atmosphere by wet deposition (Van der Does et al., 2016).

The artificial rain was prepared from Milli-Q water amended with sulfuric acid (H_2SO_4), which lowered the pH to either 2 or 4.5 (Table 1), mimicking atmospheric conditions or natural rain pH, respectively (Spokes et al., 1994). H_2SO_4 was used as it is known as an anthropogenic acid component in cloud water (Jickells et al., 1982;

Desboeufs et al., 2001). To prevent release of any nitrogen source other than from the Saharan dust into the experimental seawater, other atmospheric acids, such as HNO_3, were avoided. To test the impact of a low and high dust deposition event, 0.25 and 1.5 mg L^{-1} dust was added (Table 1). While for the wet-deposition treatment, the dust was added to incubation bottles together with the rain, the dust for the dry deposition treatment was given directly into the incubation bottles by rinsing the dust-containing vial with ambient seawater.

After dust addition, the incubation bottles were closed, sealed and hooked up-side down onto wooden trays at the bottom of the on-deck incubation tubs to expose them to natural light conditions. Using natural screens and meshes, ambient light was adjusted to the actual irradiance (PAR, Table S1) varying between 220 W m^{-2} (M4, 20 m), 88 and 14 W m^{-2} (M3, 20 and 72 m, respectively), and 25 W m^{-2} (M1, 20 m). The light intensity in the incubators was measured by a Li-Cor PAR meter. Circulating surface seawater surrounded the incubation bottles within a temperature range of ± 2°C from the original sampling site. From day 0 or day 1 until day 4 or day 8, subsamples from each incubation bottle were taken every day for the macronutrients (P, Si, N) and flow cytometry analyses. For subsampling, during transportation from incubators to the laboratory, the incubation bottles were placed in darkened plastic bags shielding them from direct sunlight. Subsampling was carried out inside a laminar flow hood to avoid contamination. At the start and end of the incubation, samples were taken for DFe and DIC. Samples for POC were taken at the end of the experiments. The initial CTD water composition served as baseline for all parameters of the incubations.

Table 1. Overview of incubation dust treatments at stations M1, M3 and M4. N = number of replicates. ML= mixed layer, DL = deep layer.

Site (depth)	Duration (days)	Treatment			
		Control	Wet deposition		Dry deposition
M1 (23°W)					
ML (20 m)	8	Control (N=3) Rain-control (N=3)	Lake dust 0.25 mg, pH 2 (N=3), 1.5 mg, pH 2 (N=3)	Dune dust 0.25 mg, pH 2 (N=3), 1.5 mg, pH 2 (N=3)	Lake dust 0.25 mg (N=3), 1.5 mg (N=3)
M3 (38°W)					
ML (20 m)	4	Control (N=6)	Lake dust 0.25 mg, pH 2 (N=3)		
DL (72 m)	4	Control (N=6)	Lake dust 0.25 mg, pH 2 (N=3) 0.25 mg pH 4.5 (N=3)		
M4 (40°W)					
ML (20 m)	4	Control (N=4)	Lake dust 0.25 mg, pH 2 (N=3) 0.25 mg pH 4.5 (N=3)	Dune dust 0.25 mg, pH 2 (N=3) 0.25 mg pH 4.5 (N=3)	Lake dust 0.25 mg (N=3)

2.4 Analytical measurements

Samples for dissolved inorganic macronutrient concentrations were filtered through a 0.2 µm Acrodisc filter and stored either frozen at -20°C for N and P, or cooled at +4°C for Si. All samples were analyzed on a TRAACS Gas Segmented Continuous Flow Analyser at NIOZ using the colorimetric methods (Murphy and Riley, 1962; Strickland and Parsons, 1972; Grasshoff et al., 1983). Filters (25 mm GF/F) for POC measurements were muffled at 450°C for 5 h and pre-weighed to determine the sample amount after filtration. After sample filtration on board, POC filters were stored frozen (-20°C) and analyzed using a Thermo-Interscience Flash

EA112 Series NC analyser back at NIOZ. In short, filters were freeze dried, weighed again and acid fumed to dissolve inorganic carbon. Subsequently, filters were folded into tin capsules and analyzed against the certified Acetenalide standard and were blank corrected. Flow cytometry cell counts were performed on board the ship on fresh phytoplankton samples using a BD Accuri 6 flow cytometer with a 20mW solid state blue laser (488 nm excitation). The trigger was set on red chlorophyll-*a* autofluorescence and the different phytoplankton populations were discriminated based on their red and orange phycoerythrin autofluorescence (e.g. indicative for the cyanobacteria *Synechococcus* spp.) and scatter signal. Data analysis was performed using FCSExpress5 software. Samples for DIC measurements were fixed with 10 µL of concentrated $HgCl_2$ and stored at room temperature until measured at NIOZ after Stoll et al. (2001). Statistical analysis was done with Sigmaplot one-way Anova, followed by a Bonferroni t-test when a statistical significant difference was found ($p < 0.001$).

3 Results

3.1 Characterization of the initial seawater sampled at M1, 23°W

Due to the cruise track from west to east, station M1 was the last location where incubations were conducted (Fig. 1). At this station, the incubation experiments had profited from improvements of the earlier incubation experiments at station M3 and M4 and is therefore presented first, which is also in agreement with the downwind direction of dust transport. Major adjustments relative to the earlier experiments included:

1) The duration of the incubation, with an extension from 4 to 8 days for the ML depth.
2) Higher amount of dust was added (1.5 mg L^{-1}) due to its proximity to the Saharan desert and therefore higher lithogenic dust input (Chapter 3).
3) An additional subsampling at day 0, shortly after the dust treatment was added.
4) An extra pH 2 rain-control sample, since all wet dust deposition treatments were leached in pH 2 rain before pouring the rain into the incubation bottles. Leaching dust in pH 4.5 rain was omitted at station M1.

All incubation parameters are given in Table 1. DFe, Si, P and N data of the lake dust was previously reported by Van der Does et al. (Chapter 3). The CTD profile at

station M1 showed uniform surface temperatures of 24°C with a clear and distinct DCM at 54 m water depth (Fig. S1c). As there was also an internal wave oscillating at the DCM, no seawater could be sampled from this depth. Instead, seawater was taken from 20 m depth which showed low concentrations of 0.03 µmol P L^{-1} and 0.71 µmol Si L^{-1} and 0.04 mg POC L^{-1} (Fig. 3, 4). Initial NO_3 concentrations were 0.02 µmol L^{-1} (Fig. 5). The initial total DFe concentration was 1.0 nmol L^{-1} and the DIC concentration 2125 µmol L^{-1} (Fig. 4, 6). At the start of the experiment, the water contained an abundance of $1.6 \cdot 10^4$ *Synechococcus* spp cells per mL (Fig. 6).

3.1.1 Development of the lake dust incubations at M1

For the mixed layer incubations, large differences in nutrient concentrations (P, Si, DFe) were observed between the dry and wet lake dust deposition treatments (Fig. 3, 4). The P concentrations of both low (0.25 mg L^{-1}) and high (1.5 mg L^{-1}) dry lake dust deposition treatments were similar in comparison to the control sample and remained as low as in the initial seawater (~ 0.03 µmol L^{-1}, Fig. 3a). Only after adding the high amount of wet lake dust, P concentrations doubled at day 0 (0.06 µmol L^{-1}) and showed a gradual decrease to ~ 0.03 µmol L^{-1} during the following eight incubation days (Fig. 3b).

For Si, both low and high wet lake deposition treatments resulted in higher concentrations (0.88 and 1.55 µmol L^{-1}, respectively) in comparison to the initial seawater (0.71 µmol L^{-1}) and the rain-control sample (0.70 µmol L^{-1}) at day 0 (Fig. 4). The Si concentrations increased with the high wet lake deposition treatment during the experiment, while they decreased in the low wet lake deposition treatment or remained unchanged in the rain-control sample (Fig. 4b). The Si concentrations in both dry lake dust deposition treatments resulted in similar values as found in the initial seawater and the control sample (~ 0.71 µmol L^{-1}, Fig. 4a).

While the DFe concentrations with both dry lake dust deposition treatments remained as low as the initial DFe concentration (0.8 nmol L^{-1} and 1.0 nmol L^{-1}, respectively) at day 1, they increased strongly after low and high wet lake dust deposition (7 and 30 nmol L^{-1}, respectively). Towards the end of the experiment, DFe concentrations decreased to 2 and 5 nmol L^{-1} for the low and high wet lake dust deposition treatments, respectively, while they stayed low at 0.6 nmol L^{-1} in both dry lake dust deposition treatments (Fig. 4a, b). Only the control sample had slightly higher DFe concentrations (1.2 nmol L^{-1}) at day 8, potentially caused by contamination during analysis. There were no differences in DFe concentrations between both control samples (for the dry deposition treatment and the pH 2 rain-control sample for the

wet deposition treatment). Although pH 2 seemed to affect the Si concentrations in the water, differences were small and as such not significant. This shows that the low pH rain did not alter the Si concentrations of the initial seawater. The N concentrations showed no differences between dry and wet deposition nor between the control samples (Fig. 5). Concentrations ranged between 0 and 1 µmol L^{-1} in all treatments but showed irregular peaks with large errors.

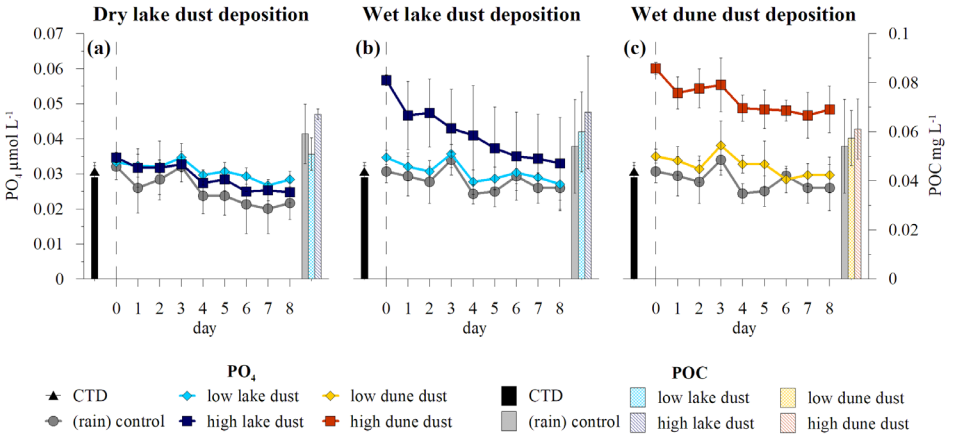

Figure 3. Phosphate (P, lines, left axis) and particulate organic carbon (POC, bars, right axis) concentrations with error bars showing triplicate standard deviation during incubations for (a) dry and (b) wet lake dust deposition (Chapter 3), and (c) wet dune dust deposition treatments at M1. Dashed line represents start of the experiment.

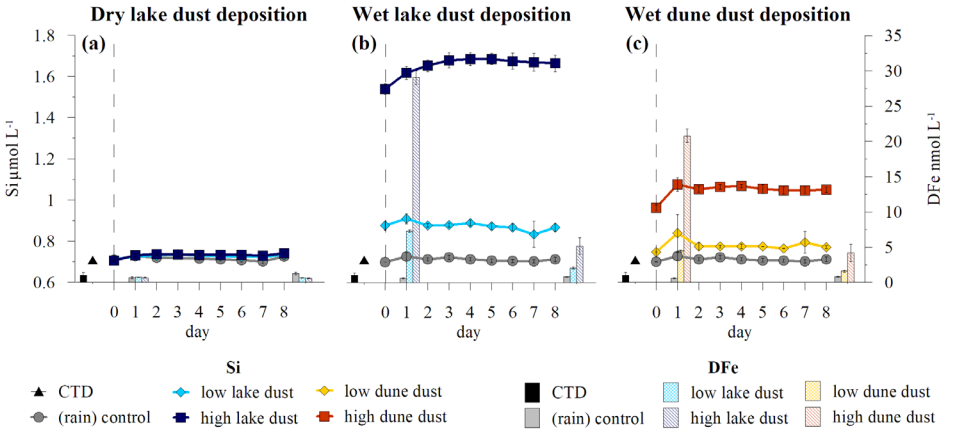

Figure 4. Temporal dynamics of dissolved silicate (Si, lines, left axis) and dissolved iron concentration (DFe, bars, right axis) with error bars showing standard deviation of triplicate measurements for incubations at M1 for (a) dry and (b) wet lake dust deposition (Chapter 3) and (c) wet dune dust deposition treatments. Dashed line represents start of the experiment.

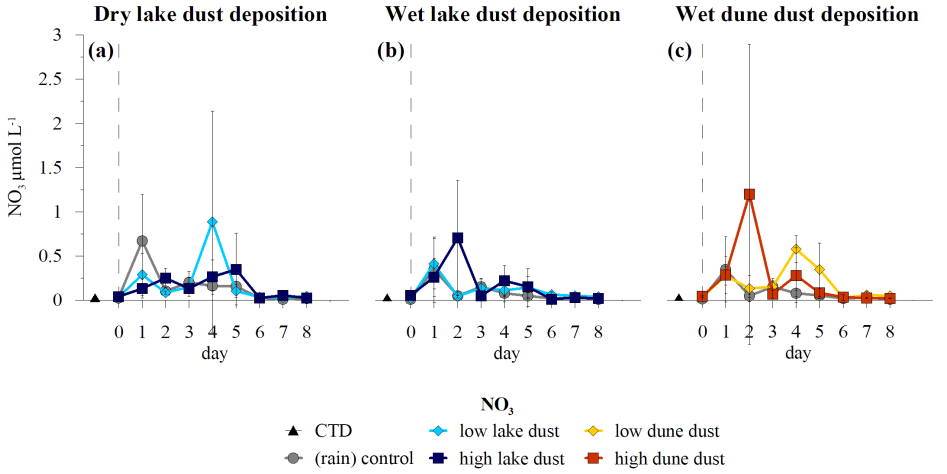

Figure 5. Temporal dynamics of nitrate (N) concentrations during (a) dry lake dust and (b) wet lake dust and (c) wet dune dust additions at site M1 (Chapter 3). Error bars show standard deviation of triplicate measurements and peaks are attributed to contamination.

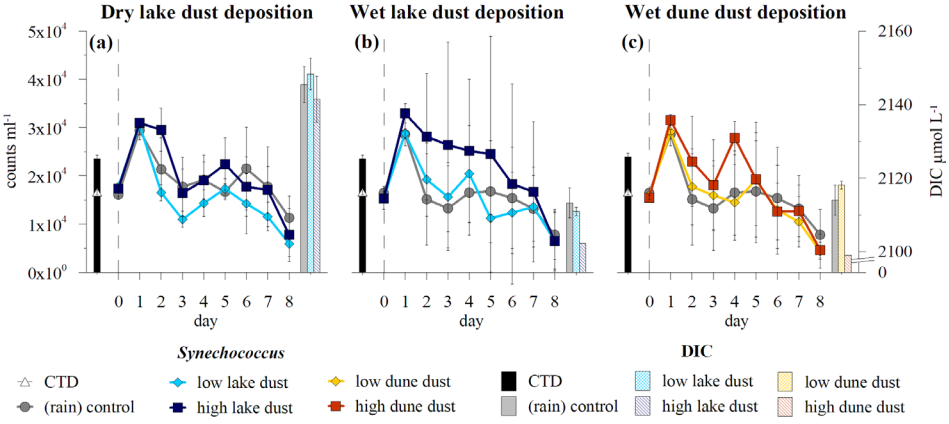

Figure 6. Temporal dynamics of *Synechococcus* spp. abundance (lines, left axis) and dissolved inorganic carbon concentration (DIC, bars, right axis) with error bars showing standard deviation of triplicate measurements for incubations at M1 for (a) dry and (b) wet lake dust deposition and (c) wet dune dust deposition. Dashed line represents start of the experiment.

While the initial POC concentration of the CTD seawater was 0.04 mg L^{-1}, concentrations ranged between 0.05 and 0.07 mg POC L^{-1} at the end of all experiments (Fig. 3). However, the increase in POC was only significantly higher from the initial values for the high dry lake dust deposition treatment (Fig. 3a). The prokaryotic cyanobacterium *Synechococcus* was by far the dominant picophytoplankton group ranging between 45 and 84 % of the total cell counts in both the dry- and wet-dust

deposition treatments (Fig. 6). *Synechococcus* abundance accounted for $1.6 \cdot 10^4$ cells mL^{-1} in the initial seawater and in all incubation bottles at day 0. Between day 0 and 1, cell abundances doubled to $3.3 \cdot 10^4$ mL^{-1} in all treatments with no significant difference between dry- and wet-dust deposition (Fig. 6a, b). Between day 1 and 8, cell counts for both dry lake dust deposition treatments decreased to around $0.7 \cdot 10^4$ mL^{-1}. In comparison, cell counts for the wet lake dust deposition treatments also decreased from $3.3 \cdot 10^4$ mL^{-1} to $0.7 \cdot 10^4$ ml^{-1}, however, more slowly after high dust addition with cell counts staying relatively high until day 5 (Fig. 6b). The initial DIC concentrations differed only slightly from the ones measured at the end concentrations and are therefore considered to remain unaltered between dry lake dust deposition treatments and wet lake dust treatment (Fig. 6).

3.1.2 Development of the dune dust incubations at M1

Dune dust was only added as wet deposition to the incubations. Similar effects for this dust type were observed as for the wet lake dust deposition. While nutrient concentrations (P, Si, DFe) were generally higher in the high wet-dust addition experiment, they remained rather low in the low dune dust treatment and the rain-control sample. The P concentration of the low wet dune dust deposition and the rain-control ranged between 0.03 and 0.04 µmol L^{-1} (Fig. 3c) and were therefore comparable to the initial seawater (0.03 µmol L^{-1}) and the low lake dust deposition treatment (~ 0.03 µmol L^{-1}, Fig. 3b). In contrast, the P concentration of the high wet dune dust deposition doubled to 0.06 µmol L^{-1} at day 0, similar to the lake dust, and decreased to 0.05 µmol L^{-1} at the end of the experiment.

The Si concentration of the dune dust deposition treatments was lower than the Si concentrations of the lake dust but displayed similar patterns. The Si concentration of the high dune dust deposition treatment was clearly offset (0.96 µmol L^{-1}) compared to the initial seawater (0.71 µmol L^{-1}) and the rain-control sample (0.70 µmol L^{-1}) at day 0. At day 1, Si concentrations increased even more to 1.08 µmol L^{-1} and subsequently stayed as high. The offset of the low dune dust treatment remained small (Fig. 4c). The DFe concentrations also showed a similar behavior as seen after wet lake dust deposition. While DFe seawater concentration of the high wet dune dust deposition was 20 nmol L^{-1} at day 1 with a significant decrease to 4 nmol L^{-1} at day 8, the low wet dune dust deposition treatment started with a DFe value of around 4 nmol L^{-1} at day 1 and decreased to 1.6 nmol L^{-1} at day 8 (Fig. 4c). The N concentrations of the dune dust stayed as low as the N concentrations of the wet lake dust treatments and showed no difference with the control sample,

concentrations ranged between 0 and 1.2 µmol L^{-1} (Fig. 5c).
The average POC concentrations for all dune dust deposition treatments ended in a small increase in comparison to the initial value of 0.04 mg L^{-1} (Fig. 3). The POC values increased from the rain-control over the low- to the high wet dune dust deposition treatment and ranged between 0.05 and 0.06 mg L^{-1}. This is in the same order of magnitude as the resulting POC concentrations of the wet lake dust deposition treatments. Overall, there was no significant difference in average POC concentrations among all samples. Cell counts of the cyanobacterium *Synechococcus* of the wet dune dust deposition treatments were slightly lower than in the lake dust deposition treatments but displayed a similar pattern with a significant increase from $1.6 \cdot 10^4$ up to $3.0 \cdot 10^4$ cells mL^{-1} between day 0 and day 1 and a subsequent decrease to $0.5 \cdot 10^4$ cells mL^{-1} at day 8 (Fig. 6c). The DIC concentrations at the end of the wet dune dust deposition treatments decreased slightly in comparison to the initial seawater, with the strongest decrease observed after the high dune dust deposition (Fig. 6c).

3.2 Characterization of the initial seawater sampled at M3, 38°W

Station M3 was the second location where incubations took place. While sailing towards this station, we passed a dust event which started on March 27th and lasted for several days. This event possibly altered the surface waters. At this location, seawater was sampled at the ML depth of 20 m and the deep layer (DL) of 72 m (Table 1). The CTD-profiles showed uniform surface temperatures of around 25°C down to 73 m water depth (Fig. S1b). At greater depth the temperatures decreased while an increase of fluorescence until 105 m water depth was recorded, indicating the DCM (Fig. S1b). For both incubation depths, only the lake dust was used, either leached in pH 2 rain for the ML incubation, or additionally also in pH 4.5 rain as for the DL incubation (Table 1). Dry deposition was not applied in these experiments due to the already present dust from the natural event. Subsampling started at day 1 and incubations lasted until day 4.
Initial nutrient concentrations in the ML were 0.02 µmol P L^{-1}, 0.82 µmol Si L^{-1} and < 0.5 nmol DFe L^{-1}. For the DCM (72 m) concentrations were higher with 0.07 µmol P L^{-1}, 1.04 µmol Si L^{-1}, and 0.5 nmol DFe L^{-1} (Fig. 7). The N concentrations in the surface water was 0.14 µmol L^{-1} and in the DCM 0.65 µmol L^{-1} (Fig. 8). Initial POC concentrations were higher in the ML (0.04 mg L^{-1}) than at greater depth (0.02 mg L^{-1}), while DIC concentrations were slightly lower in the ML in comparison to the deeper layer (2130 µmol L^{-1} and 2200 µmol L^{-1}, respectively, Fig. 9). While initially there

were around $1.8 \cdot 10^3$ *Synechococcus* spp. cells per mL in the ML, their abundance was only $0.4 \cdot 10^3$ cells per mL in the deep layer. In addition, a second picoeukaryotic phytoplankton group with starting abundances of $0.4 \cdot 10^3$ and $2.7 \cdot 10^3$ cells mL^{-1} were identified in the ML and the deeper layer, respectively (Fig. 9).

3.2.1 Development of the mixed layer incubation at M3

The initial nutrient concentrations in the mixed layer depth at station M3 sampled by the CTD were lower for P and higher for Si when compared to initial concentrations found at station M1 at 23°W. The progression of nutrient concentrations during the experiments were similar to M1: Si concentrations increased to 1.0 µmol L^{-1} at day 1 and stayed at this elevated level after wet lake dust deposition (0.25 mg L^{-1}), while no change in P concentrations was seen compared to the control sample after dust addition (Fig. 7a). The DFe remained unchanged in the control sample and only increased to > 4 nmol L^{-1} with wet lake dust deposition at day 1 and decreased to 1.5 nmol L^{-1} at the end of the experiment (Fig. 7c). The N concentrations remained low (< 1.5 µmol L^{-1}) and showed no differences between the control and the wet dust deposition treatments (Fig. 8a). The bulk POC concentrations showed similar values in all samples and stayed around 0.04 mg L^{-1} at the start and the end of the experiment (Fig. 7a). The DIC concentrations decreased to 2110 and 2075 µmol L^{-1} in the control sample and wet lake dust deposition treatment, respectively (Fig. 9a). The DIC in the wet-dust deposition treatment was significantly different to the starting value and the control value at the end of the experiment.

At the beginning of the experiment, the cyanobacterium *Synechoccocus* spp. made up about 75 % of the picophytoplankton community in the ML and decreased to 64 and 53 % in the control and the wet lake dust deposition treatment, respectively, at the end of the experiment (Fig. 9a). Absolute values of $3 \cdot 10^3$ cells mL^{-1} were about a magnitude lower than at station M1. Another unidentified picoeukaryotic phytoplankton group (*R3*) made up about 15 % at the beginning of the experiment and increased to 30 % in the wet lake dust deposition treatment at the end of the experiment, while its relative abundance in the control sample remained low (Fig. 9c). Between both picophytoplankton groups, the differences were insignificant, except between the wet lake dust deposition treatment and the starting CTD value for *R3*.

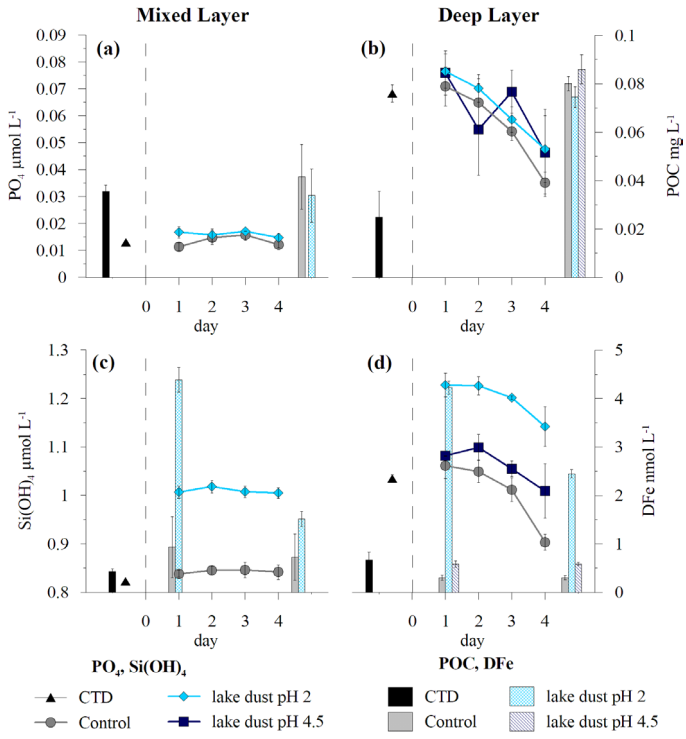

Figure 7. Nutrient concentrations (P, Si; lines and DFe; bars) and POC (bars) development with error bars showing standard deviation of triplicate measurements for incubations at M3 in the ML (a & c) and the DL experiments (b & d).

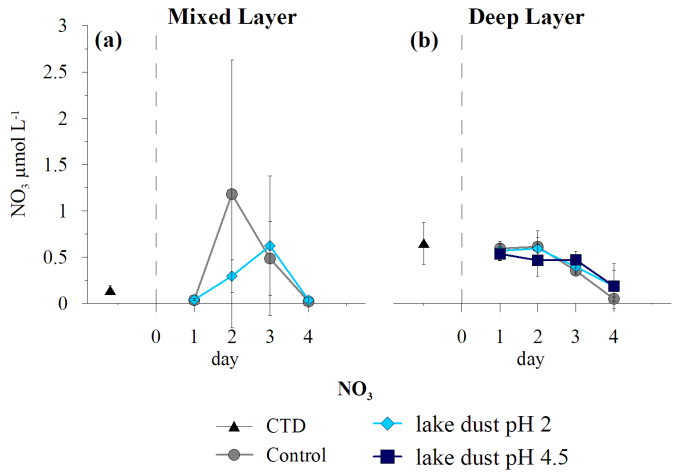

Figure 8. Nitrate (N) concentrations for the ML (a) and DL (b) at incubation site M3. Error bars show standard deviation of triplicate measurements.

3.2.2 Development of deep mixed layer incubations at M3

While the initial P concentration of 0.07 µmol L^{-1} in the DL was higher than in the ML, it did neither change after dust addition leached in pH 2 nor in pH 4.5 (Fig. 7b). The Si concentration increased to 1.23 µmol L^{-1} at day 1 and stayed at a high level when the lake dust was leached in pH 2 rain (Fig. 7d). The DFe concentrations increased significantly to 4.5 nmol L^{-1} at day 1 when lake dust was leached in pH 2 but remained low in pH 4.5. At the end of the experiments, DFe decreased to around 2.5 nmol L^{-1} for dust leached in pH 2 (Fig. 7d). The N concentrations decreased from 0.7 to 0.1 µmol L^{-1} in all experiments but showed no differences between the control and the two dust addition treatments (Fig. 8). While POC concentrations of all experiments increased to similar values at the end of the experiment (0.08 mg L^{-1}), the DIC values decreased equally to around 2140 µmol L^{-1} in all experiments. The picoplankton abundances in the DL did not show significant differences amongst each other and showed the same progression with and without dust addition, while the *R3* group showed highest counts in the control sample (Fig. 9).

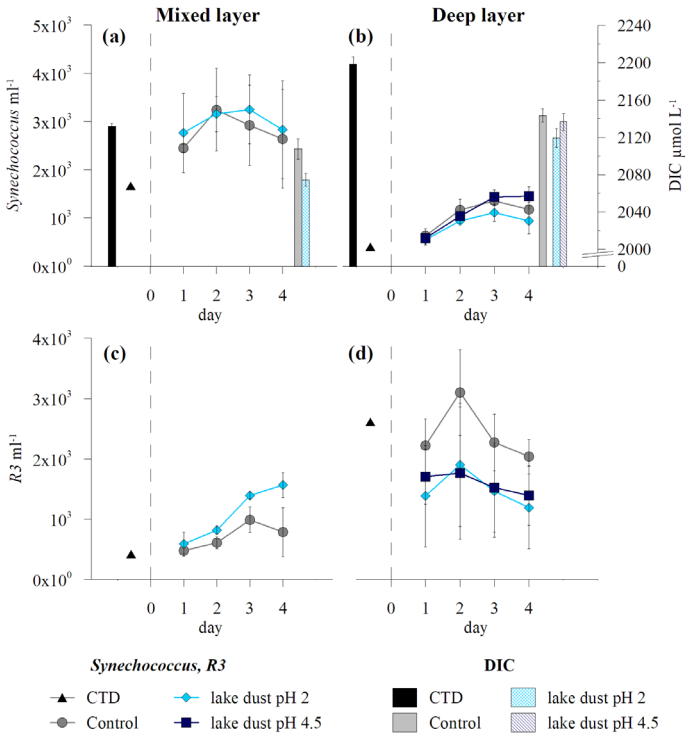

Figure 9. DIC concentrations (bars) and temporal dynamics of *Synechococcus* spp. and an unidentified picoeukaryotic phytoplankton group (*R3*) (lines) with error bars showing standard deviation of triplicate measurements for incubations at M3 for the ML (a & c) and the DL (b & d).

4 Discussion

At all stations, incubations were carried out under typical oligotrophic ocean conditions as evidenced by the initial seawater characteristics with low concentrations of macronutrients (P, Si), low POC and low picophytoplankton cell abundances. In low-latitude oceans nitrogen tends to limit productivity and the (re) supply of nutrients from the subsurface is relatively low (Moore et al., 2013). To avoid phytoplankton growth from a nitrogen source other than Saharan dust, we waived HNO_3 as atmospheric processing acid. The leached N concentrations from the wet-dust in H_2SO_4 rain ranged between 0 and 1 µmol L^{-1} and showed no differences between the N concentrations in the control sample or in the samples after dry dust deposition (Fig. 5). This implies that the Saharan dust types used in our experiments did not deliver N-nutrients to the seawater for phytoplankton growth. However, if Saharan dust is processed in condensation/evaporation cycles involving HNO_3 and H_2SO_4 (Desboeufs et al., 2001; Guieu et al., 2010; Ridame et al., 2014), Saharan dust can indeed become a significant source of N which can promote primary production by relieving the phytoplankton's potential N limitation or N/P co-limitation (Ridame et al., 2014).

Along our transect, both P and Si concentrations in the surface water were also low. The bottom depth of the ML deepened from 54 m at M1 in the east to 100 m at M4 in the west (Fig. S1). The westward deepening of the nutricline affected the local phytoplankton communities, leading for example to a contrasting coccolithophore assemblage along the transect promoting the lower photic zone flora in the west (Guerreiro et al., 2017). In the initial seawater at all incubation sites of the ML, Si concentrations increased from M1 (0.71 µmol L^{-1}, Fig. 4) to M4 (1.03 µmol L^{-1}, Fig. S3), suggesting additional nutrient input in the west, which can have a riverine origin. Concentrations of DFe and P in the initially sampled seawater (and thus controls) showed highest values at M1 (1 nmol L^{-1} and 0.03 µmol L^{-1}, Fig. 3, 4), caused potentially by enhanced mixing from the deep, advection of coastal upwelling waters or enhanced dust input in the east (Fig. 1). Nonetheless, primary productivity was low in the initial seawater which was used for the incubations. The experimental Saharan dust additions, dry- and wet-dust deposition, revealed potential fertilization by enhancing the low initial nutrient concentrations (P, Si, DFe). Depending on the location and season, dry (winter) or wet (summer) dust deposition predominates (Duce et al., 1991; Schulz et al., 2012; Chapter 3) with dry deposition generally being dominant close to source regions (Dulac et al., 1989) and wet deposition increasing with distance from the source (Bergametti et al., 1989).

4.1 Dry versus wet deposition

Substantial differences of released nutrients (P, Si, and DFe) were seen between the dry- and wet-dust deposition treatments. While the wet-dust deposition treatments resulted in an immediate increase in these nutrient concentrations, the dry-dust deposition treatments left the tested waters unchanged. At M1, the P concentrations doubled at the start of the experiment after wet-dust deposition and showed a gradual decrease during the experiment, while the Si concentrations remained high after initial release. The high increase of DFe concentration at day 1 dropped significantly to day 8 (Fig. 3, 4). Our observation show that the wet Saharan dust used in this experiment has the potential to deliver P, Si, and DFe when processed in only H_2SO_4. However, the N concentrations remained unchanged in our experiments (Fig. 5). Seeding experiments conducted in the oligotrophic Mediterranean Sea also showed that atmospherically processed dust (wet), which underwent condensation/ evaporation cycles including exposure to HNO_3 and H_2SO_4, increased the P and N nutrient concentrations in the oligotrophic waters (Pulido-Villena et al., 2010; 2014; Ridame et al., 2014), while unprocessed dust (dry) left the waters unchanged (Ridame et al., 2014). Furthermore, the wet deposited dust significantly stimulated primary productivity and Chl-*a* production (Ridame et al., 2014), in addition to an increase in bacterial activity (Guieu et al., 2014a). This stimulation was attributed to the increase of both P and N, with the latter being released from the HNO_3 processed dust (Ridame et al., 2014).

Such an effect on phytoplankton growth was not observed during our experiments. Despite the picoplankton cell abundance increased from day 0 to day 1, with a subsequent decrease until the end of the experiment at M1 (Fig. 6), they showed similar abundances and the same temporal dynamics in all experiments: dry, wet and the untreated control samples. Still, temporal progression of the decreasing P concentrations during the experiment, seemed like biological uptake, while the drop in DFe seemed to be related to both iron reprecipitation in the high pH of the seawater (~ 8) and biological uptake. At M3, where we passed a dust event starting on March 27th, the unidentified picoeukaryotic phytoplankton group (*R3*) showed a significant increase from the initial cell abundance after wet-dust addition at day 4 (Fig. 9c). This might be caused by the high DFe concentration at the start of the experiment since the P concentration stayed low and Si concentration remained high at ~ 1 µmol L^{-1}. Still, the resulting POC concentrations at M3 did not differ from the control sample, implying no major dust induced production of organic carbon (Fig. 7). Also, the POC concentrations at M1 ended in equally high values after both dry- and wet-

dust additions (Fig. 3). This implies that there are no differences in the biological production of organic carbon between both deposition types, though dust particles – wet and dry – might stimulate POC aggregation (paragraph 4.5).
The fact that there is no major fertilization effect of Saharan dust on the phytoplankton when dust is leached in only H_2SO_4, may result from two factors: (1) the missing nitrogen source which may relieve N, or due to N and P/DFe co-limitation (Mills et al., 2004; Ridame et al., 2014), and (2) the released nutrient concentrations in our experiment were still too low to impact phytoplankton growth and POC buildup. While wet-dust deposition showed an enhanced nutrient release of P, Si and DFe, concentrations were reliant on the amount of dust added.

4.2 Dust amounts

Wet-dust deposition resulted in the release of nutrients (P, Si, DFe) into the tested seawater, but was depended on the amount of dust added. The P concentrations only increased when a high amount of dust (1.5 mg L^{-1}) was added, while Si and DFe showed elevated concentrations already after addition of a low amount of dust (0.25 mg L^{-1}). This implies that Saharan dust deposition to the Atlantic Ocean needs to be high in order to deliver bioavailable P for phytoplankton growth. Earlier dust-addition experiments in the tropical Atlantic Ocean showed that 0.5 and 2 mg of Saharan dust L^{-1} stimulated nitrogen fixation by relieving its P and Fe co-limitation (Mills et al., 2004). Similarly, addition of 1.34 mg Saharan dust L^{-1} stimulated growth of the phytoplankton community in the Atlantic Ocean at 40°N (Blain et al., 2004). In the Mediterranean Sea, where Saharan dust deposition can also be high, enrichment with 0.8 mg Saharan dust L^{-1} was sufficient to stimulate phytoplankton growth (Ridame et al., 2014). Depending on the location along our transect, dust deposition varied in space and time and generally declined with increasing distance from the source (Korte et al., 2017; Chapter 3), Even though less dust is deposited westwards, the increased contribution of wet-dust deposition, however, can compensate for this, reaching up to 1000 mg Saharan dust per m^{-2} from a single rain shower (Stuut, personal communication). Therefore, Saharan dust, in particular wet deposited, has the potential to introduce sufficient amounts of nutrients (P, Si, DFe) to relieve nutrient co-limitation in the tropical Atlantic Ocean and to promote nitrogen fixation by diazotrophic cyanobacteria and ultimately provide new N-nutrients to other phytoplankton (Falkowski et al., 1998; Capone, 2001). Indeed, Mahaffey et al. (2003) showed that atmospheric dust deposition might drive the temporal variability of nitrogen fixation in the North Atlantic Ocean.

4.3 Dust types

Wet-dust incubation experiments at all stations revealed higher Si and DFe concentrations leached from the lake dust compared to the dune dust but reached similar P concentrations leached from both dust types (Fig. 3, 4). This implies that different dust types (i.e. lake deposit vs. dune sand), which are transported and processed in the atmosphere, can influence the ocean biogeochemistry in different ways and thus may impact only particular phytoplankton groups. While, for example, calcifying coccolithophores or nitrogen fixing cyanobacteria require amongst trace metals, P, biogenic silica producing organisms like diatoms require Si and DFe to thrive (Boyd et al., 2010). Regarding the high biogenic silica rich export fluxes in the western Atlantic (M4) in fall 2013 described by Korte et al. (2017), it is likely that wet deposition of Saharan dust was contributing Si and DFe for the initial bloom development. In addition, the coccolithophore export fluxes are also high in the western Atlantic, which surface blooms may have profited from the nutrients (P, DFe) provided by Saharan dust deposition (Guerreiro et al., 2017).
In seeding experiments by for example Guieu et al. (2010), Bressac et al. (2012), Ridame et al. (2014) and Desboeufs et al. (2014), it was seen that processed dust from southern Tunisia introduced (Zhu et al., 1992) N or N/P when dust was exposed to HNO_3/H_2SO_4 condensation/evaporation cycles, relieving nutrient (co-)limitation of phytoplankton activity. In turn, Blain et al. (2004) and Bonnet et al. (2005), showed that Saharan dust from the Hoggar regions in southern Algeria is a potential source of bioavailable Fe stimulating mainly diatoms and the picophytoplankton (< 2 µm) in the northeast Atlantic Ocean and the Mediterranean Sea, respectively. For the other side of the Atlantic Ocean, Bristow et al. (2010) showed that dust transported from the Bodélé Depression in Chad contains Fe and P and has the potential to fertilize the Amazon rain forest. Yu et al. (2015b) calculated that Saharan dust delivers 23 g P $year^{-1}$ onto the Amazon rain forest. All these experiments point out the importance of Saharan dust input for oceanic (and terrestrial) ecosystems, with fertilization becoming more significant when the dust is processed in low pH regimes.

4.4. Impact of pH

In our experiments, nutrient release (P, Si, DFe) was strongly dependent on the pH, to the extent that only at pH 2 nutrients were leached from the dust. In contrast, when dust was leached at pH 4.5, all nutrient concentrations remained as low as when dry dust was added, and nutrient concentrations showed a similar temporal progression as observed in the control samples. Such pH dependency is in agreement

with the results of Spokes et al. (1994), who showed that highest metal solubility was found under low pH conditions. Accordingly, atmospheric processing in a low pH regime will increase the nutrient's solubility during transport (Ridame and Guieu, 2002; Mahowald et al., 2005; Baker and Croot, 2010). Therefore, the dust needs to be processed in very low pH ranges to introduce bioavailable nutrients to the surface waters impacting the phytoplankton. The pH in aerosol solutions could be lower than pH 1 due to the acids H_2SO_4 and HNO_3 (Zhu et al., 1992). In the atmosphere, HNO_3 is also an important anthropogenic acid, not only for lowering the pH processing the dust, but also for releasing bio-limiting NO_3 to the seawater (Ridame et al., 2014). In this respect, Saharan dust is an important atmospheric vehicle for transferring N-nutrients to the seawater.

4.5 POC aggregate formation

Although the dry-dust deposition treatments did not lead to nutrient release in our experiments, the resulting POC concentrations were as high as after wet-dust deposition (Fig. 3). Interestingly, although error bars were large, the average POC concentrations increased from the rain-control sample (0.05 mg POC L^{-1}), to low wet-dust deposition (0.06 mg POC L^{-1}) to high wet-dust deposition (0.07 mg POC L^{-1}), and high dry-dust deposition (0.07 mg POC L^{-1}). This observation suggests that the suspended dust particles may become incorporated in marine snow formed by the organic matter already present in the incubated seawater. It seems that the amount of marine snow, and likely also its size, increase with higher amount of dust added. After termination by filtration, these newly formed aggregates were retained on the glass fiber filter but would have passed through without dust-stimulated aggregation. Experiments in which the POC export fluxes were measured showed that dust triggered abiotic formation of transparent exopolymeric particles, which eventually lead to the formation of sinking organic matter (Louis et al., 2017), resulting in enhanced POC fluxes that were highly correlated to the mineral dust flux (Bressac et al., 2014; Desboeufs et al., 2014; Louis et al., 2017). Also, dust addition experiments in roller tanks revealed that Saharan dust led to the formation of marine snow aggregate within the first 12 hours after its addition (Van der Jagt et al., 2018). These experiments also showed that the size-specific sinking velocities depended on the amount of added dust. The same authors argue that aggregate formation already takes place in the surface waters and no additional particles are scavenged when settling to greater depths (Van der Jagt et al., 2018). Given our experimental results that would mean that there is no abiotic increase in POC concentrations in the deep layer

caused by dust input. However, in our experiment at M3, the POC concentrations in the deep layer did increase fourfold at the end of the experiment. Therefore, the already elevated initial nutrient concentrations in the deep layer, which decreased during the experiment (Fig. 6b, d), may have biologically produced the high POC concentrations. Also, the increase of *Synechococcos* spp. in all treatments of the DL argue for phytoplankton growth, albeit not dust induced since P concentrations, required by cyanobacterium (Boyd et al., 2010), did not increase after dust addition. Nevertheless, even without a dust induced fertilizing effect, the dust suspended in the water column may have contributed to marine snow formation, eventually, resulting in enhanced POC export fluxes (Ternon et al., 2010; Bressac and Guieu, 2013). Unfortunately, export fluxes cannot be measured in bottle experiments and should therefore be studied in subsequent experiments.

4.6 Further implications

Our experiments show significant differences in nutrient release between wet and dry dust deposition with important implications for the equatorial North Atlantic Ocean, where vast quantities of Saharan dust are deposited (Moulin et al., 1997; Prospero, 1999; Yu et al., 2015a; Chapter 3). We show that wet-dust deposition of Saharan dust will deliver P, Si and DFe to the surface waters when deposition fluxes are high ($\geq$ 1.5 mg L^{-1}) after atmospheric processing at low pH (pH = 2). If in a changing climate, anthropogenic emissions, temperatures and possibly desertification are increasing, this lead to higher concentrations of anthropogenic HNO_3 and H_2SO_4 in the atmosphere in tandem with higher amounts of dust deflated from the deserts. However, high amounts of dust, which are processed in the atmosphere and deposited in the surface oceans, will not only stimulate growth of the autotrophic phytoplankton community but also that of heterotrophic bacteria (Herut et al., 2005; Guieu et al., 2014b). In addition, the dust can act as aggregate and ballast material for (newly) formed organic matter (Bressac et al., 2012; Louis et al., 2017). Combining all these effects, Saharan dust plays a key role, eventually resulting in either a source or sink of atmospheric CO_2, depending on which one of these processes predominates. This illustrates the importance to determine the relative contributions of these different processes and to assess the flux of organic matter being transported to the deep ocean without degradation. Consequently, seeding experiments in the North Atlantic Ocean are needed in which additional parameters, i.e. an atmospheric NO_3 source, carbon and nitrogen uptake by the autotrophic and heterotrophic community, Chl-*a*, and especially export fluxes will be quantified.

5 Conclusions

Wet- and dry-dust deposition incubation experiments were carried out along a transect in the equatorial North Atlantic Ocean. Results showed that both dust deposition types (dry and wet) had an effect on the ocean biogeochemistry. High amounts of dust previously leached in artificial acidified rain (H_2SO_4, pH = 2) led to higher nutrient concentrations in the seawater as opposed to dry deposited dust for which initial nutrient concentrations remained unchanged. This shows that only wet-dust deposition will release nutrients (i.e. P, Si, and DFe) which will be important for phytoplankton growth. However, phytoplankton growth was not observed in our experiments due to a missing source of new nitrogen-nutrients. Nonetheless, the deposited dust – dry and wet – resulted in equally high POC concentrations at the end of the experiment, pointing to the dust's potential to stimulate organic matter aggregation. Therefore, even without a fertilizing effect, the dust would enhance particulate organic matter export to the deep North Atlantic Ocean by formation of aggregates and ballasting.

Acknowledgements

This project is funded by ERC (project no. 311152: DUSTTRAFFIC) and NWO (project no. 822.01.008: TRAFFIC). FP and ST are funded by the Helmholtz association (HGF Young Investigators Group EcoTrace, VH-NG-901). The authors would like to thank the captain and crew of *RSS James Cook* during cruise JC 134, the shipboard NIOZ technicians Barry Boersen, and Yvo Witte, and scientists Catarina Guerreiro, Dirk Jong, Oliver Knebel, Monica Martens, and Anne Roepert as well as the technical and analytical support given on board and at NIOZ by Karel Bakker, Tessa de Bruin, Kirsten Kooijman, Patrick Laan, Anna Noordeloos, and Sharyn Ossebaar.

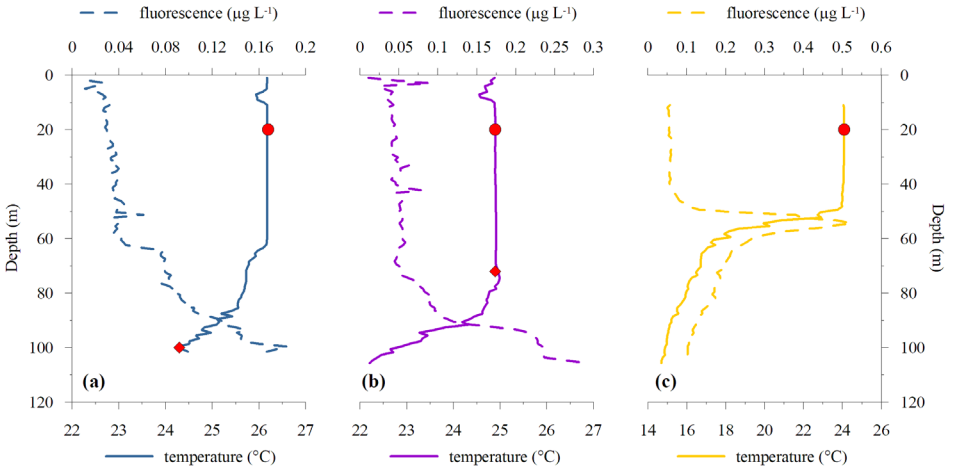

Figure S1. Temperature and fluorescence profiles from the upper 120 m at the incubation sites M4 (a), M3 (b) and M1 (c). Water sampling depths in the deep layer are indicated with red diamonds, in the mixed layer with red circles.

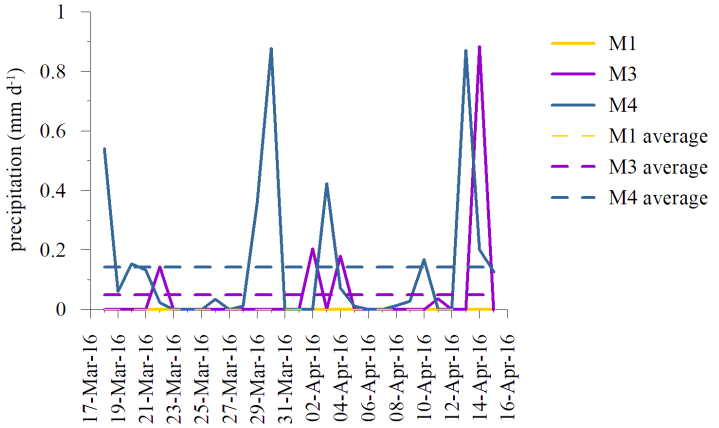

Figure S2. Daily and averaged satellite derived precipitation data (TRMM) at the incubation stations M1, M3 and M4.

Table S1. Temperature and irradiance at specific incubation sites.

	Temperature (°C)	Irradiance (PAR, W m^{-2})
M1 20 m	24	25
M3 20 m	25	88
M3 72 m	25	14
M4 20 m	26	220
M4 100 m	24	7

S4. Incubations at M4, 49°W

The first incubations were carried out at the westernmost station M4. The surface water temperature was 26°C and remained this warm from the surface down to 65 m depth (Fig. S1a). At greater depth, the temperature started to decrease, and the fluorescence started to increase and reached the DCM at 100 m at a temperature of 24°C. At this station, seawater was sampled at 20 and 100 m depth. For both depths, the seawater from all individual CTD rosette bottles was gently filled into a darkened 240 L tank to homogenize the water before filling it into the incubation bottles. Lake and dune dust were added in a concentration of 0.25 mg L^{-1}. While the lake dust was added as dry and wet deposition, the dune dust was only added as wet deposition (Table 1). Incubations lasted 4 days and were terminated by filtration.
Already after the first day, flow cytometry measurements on board showed that almost all the picoplankton groups died and only *Synechococcos* spp. survived to some extent until day 4 (starting value of about $1 \cdot 10^3$ cell mL^{-1}, ending values between 4 and $7 \cdot 10^3$ cells mL^{-1}). This was probably due to the handling of the water during the in-between step in the tank, which first of all slowed the incubation process and second of all exposed the phyto- and picoplankton to additional stress. Back at NIOZ, also the nutrient measurements revealed some anomalies i.e. the P and N concentrations were below the detection limit in most of the samples. In addition, filtration of the samples was problematic since the volume of the filtered seawater was too small to yield an appropriate sample for POC analysis, even when triplicate samples were filtered on a single filter. Therefore, we only show concentrations of Si and DFe concentrations and DIC for the ML, omitting the DL incubation, also considering the temperature difference between the deep sampling and incubation conditions on deck.

Development of the 20 m ML incubation at M4

The initial Si and DFe concentrations amounted to 1.03 µmol L^{-1} and 0.4 nmol L^{-1}, respectively. While Si concentration strongly increased to 1.2 µmol L^{-1} for the wet lake dust deposition leached in pH 2, concentrations stayed comparably low after wet lake dust leached in pH 4.5 and the dry lake dust deposition (Fig. S3). Also, the wet dune dust deposition leached in pH 2 showed elevated Si concentrations up to 1.1 µmol L^{-1} during the experiment while the wet dune dust leached in pH 4.5 remained low, too. The DFe concentrations showed the same pattern as previously observed after dry and wet deposition at M1: while DFe did not change from the initial value after dry deposition, wet deposition showed a strong increase in DFe at

day 1 for both the lake and dune dust leached in pH 2 but remained low when dust was leached in pH 4.5 (Fig. S3). At the end of the experiments, DFe decreased to around 3 and 2 nmol L^{-1} for the wet lake and dune dust, respectively. The initial DIC concentration was 2120 µmol L^{-1} and did neither change in the control sample nor in the dry lake dust deposition treatment but for all wet dust deposition treatments, DIC values decreased, most strongly after wet lake dust deposition leached in pH 2 (Fig. S4).

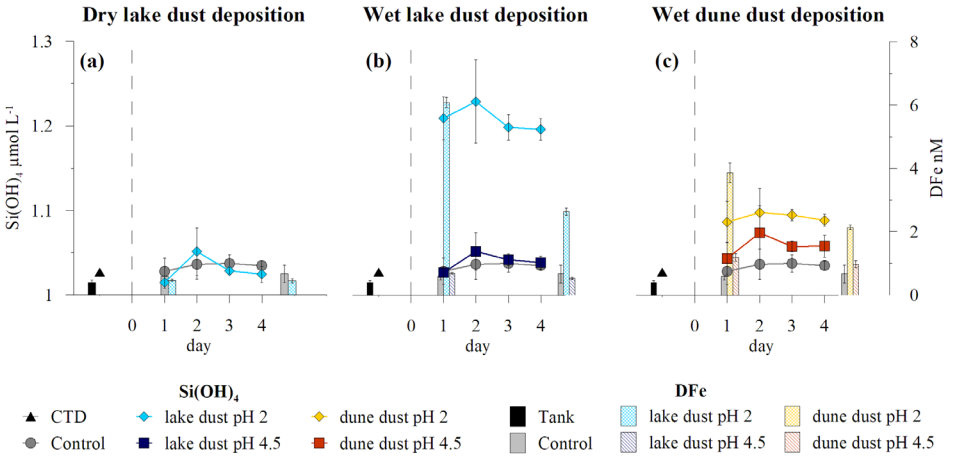

Figure S3. Silicate concentrations (lines) and DFe concentrations (bars) with error bars showing standard deviation of triplicate measurements for ML incubation at M4 for dry (a) and wet (b) lake dust and wet dune dust additions (c).

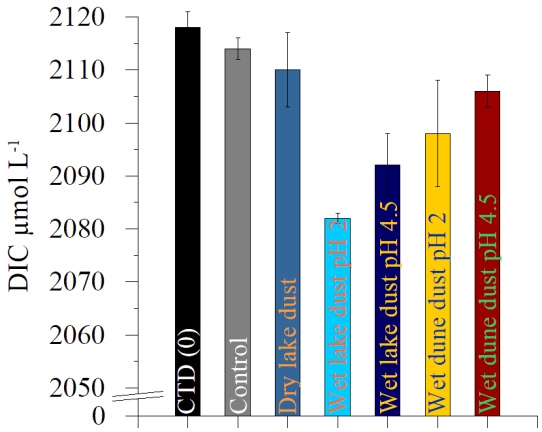

Figure S4. DIC concentrations at station M4 in the mixed layer depth for the different treatments. CTD is the start value at day 0, and other bars represent DIC at the end of the experiment at day 4.

CHAPTER 5

Productivity and particle export in the western equatorial North Atlantic driven by Amazon discharge, nitrogen fixation, mixed-layer deepening and Saharan dust

Laura F. Korte, Geert-Jan A. Brummer, Michèlle van der Does, Catarina V. Guerreiro, Furu Mienis, Chris I. Munday, Leandro Ponsoni, Stefan Schouten, Jan-Berend W. Stuut

ready to be submitted to Biogeosciences

Abstract

Export of organic matter to the deep ocean is an important process for the sequestration of atmospheric CO_2. In tropical oceans, export fluxes are considered to be rather low due to low productivity caused by low nutrient inputs. However, in the western equatorial North Atlantic productivity is enhanced by Amazon River discharge, mixed layer deepening, cyanobacterial nitrogen fixation and Saharan-dust deposition. In order to assess the impacts of these processes, time-series sediment traps were moored from October 2012 to November 2013 at two sites (49°W, 12°N and 57°W, 12°N). Samples were analyzed for the fluxes of total mass, biogenic silica, organic and inorganic carbon, as well for the stable isotope composition of total nitrogen and organic carbon and their pigment content. Here we compare the results to satellite data and *in-situ* depth profiling of the water column to evaluate which processes were at the origin of the determined particle export fluxes.

Satellite data trace peak export fluxes, rich in biogenic silica, back to Amazon River dispersal that propagated as far east as 49°W by retroflection into the North Atlantic Counter Current during fall 2013. Fucoxanthin pigment fluxes were extremely high whereas $\delta^{15}N$ was low during this period, suggesting a large contribution by marine diatoms associated with nitrogen fixating symbionts. At 57°W, the Amazon River influence is present during summer and fall 2013, leading to a high total mass fluxes rich in biogenic silica. Inorganic carbon dominated a second single event at 49°W during spring 2013, which was probably triggered by mixed layer deepening as observed by *in-situ* Argo-float data and reinforced by Saharan dust. In addition, the spring peak was accompanied by a high flux of zeaxanthin pigments in tandem with a low nitrogen isotope values, indicating a substantial contribution by nitrogen fixing cyanobacteria. Enhanced wet Saharan dust deposition during fall might have delivered bioavailable iron, while both wet and dry deposition will have accelerated the particle export. Overall, high export fluxes during times of Amazon influence and high precipitation rates in fall show higher rain ratios of biogenic silica to inorganic carbon, indicating a more efficient removal of CO_2 by the biological pump as opposed to export fluxes with low rain ratios during times when Amazon waters are absent.

Keywords: Particle fluxes, oligotrophic Atlantic, Amazon River, Saharan dust, primary production, nitrogen fixation, retroflection, North Brazil Current

1 Introduction

The western equatorial North Atlantic (WENA) is characterized by oligotrophic conditions due to persistent water-column stratification leading to nutrient depletion at the surface and little seasonal variation in primary productivity throughout the year. Nutrients are resupplied via several pathways including river runoff, eddy driven upwelling, nitrogen fixation and atmospheric-dust deposition. In the WENA, the Amazon River discharges at the equator (0°, 50°W), contributing large volumes of fresh- and nutrient-enriched water (Muller-Karger et al., 1988; Masson and Delecluse, 2001; Subramaniam et al., 2008), which is dispersed over vast areas by ocean currents as indicated by satellite observations (Fratantoni and Glickson, 2002; Del Vecchio and Subramaniam, 2004). Within the plume area, oceanic waters are fertilized by mixing with the Amazon discharge resulting in higher primary productivity and lowering of the pCO_2 (Ternon et al., 2000; Cooley et al., 2007). Several studies dealing with the Amazon River discharge area have shown its impact on primary productivity and related carbon export from the surface to depths of the mixed layer (e.g. Ternon et al., 2000; Subramaniam et al., 2008; Yeung et al., 2012) and into the deep ocean (Deuser et al., 1988). In turn, productivity in the upper ocean leads to particulate export fluxes to the deep ocean (Eppley and Peterson, 1979; Suess, 1980), of which only about 1 % arrives depths below 1500 m (Martin et al., 1987; Pace et al., 1987). The gravitational settling and export of the fixed carbon from the surface towards the deep waters is known as the 'biological pump' (Falkowski et al., 1998), which is more efficient when organic carbon is ballasted by Saharan dust and biominerals, such as biogenic silica produced by diatoms and carbonate produced by coccolithophores.

Huge amounts of atmospheric dust are emitted from the Sahara desert (Yu et al., 2015a) and are blown over and into the Atlantic Ocean, reaching the Americas and the Caribbean (e.g. Prospero et al., 1970; Prospero, 1999; Prospero et al., 2014). Recent satellite observations suggest that 182 Tg year^{-1} Saharan dust leaves the African coast, of which only 43 Tg year^{-1} reach 75°W (Yu et al., 2015a) and 28 Tg year^{-1} is eventually deposited into the Amazon Basin (Yu et al., 2015b). The dust carries important macro- and micronutrients to the Amazon basin as well as into the vast North Atlantic (Jickells, 1999; Gao et al., 2003), stimulating primary productivity in these areas (Mills et al., 2004; Yu et al., 2015b). The dust is deposited from the atmosphere into the surface of the ocean via dry or wet deposition (Duce et al., 1991; Schulz et al., 2012), with the latter dominating with increasing distance from the source regions (Zhao et al., 2003). In general, wet deposition is thought to have a greater effect on

increasing primary production and chlorophyll-*a* (Chl-*a*) concentrations (Ridame et al., 2014) due to cloud-dust interactions resulting in higher nutrient solubility and hence, higher nutrient bioavailability. This is especially the case of Fe (Spokes et al., 1994; Buck et al., 2010), which is important for Chl-*a* synthesis and nitrogen fixation in the Atlantic Ocean (Falkowski, 1997; Carpenter et al., 1999; Mahaffey et al., 2003; Mills et al., 2004). Diazotrophic nitrogen fixation by cyanobacteria (Carpenter et al., 1999) reduces atmospheric N_2 to more readily bioavailable species of nitrogen (Sohm et al., 2011), while lowering the nitrogen isotope values relative to the assimilation of e.g. nitrate (Montoya et al., 2002). The most common nitrogen fixers in the oligotrophic open ocean are the free-living diazotrophic cyanobacterium *Trichodesmium*, which abounds in the WENA (Carpenter et al., 1999; Pabortsava et al., 2017), and the endosymbiont *Richelia intracellularis* within several marine diatom species (Carpenter et al., 1999). Apart from fertilization, atmospheric lithogenic input contributes to marine snow sedimentation by acting as ballast minerals in addition to biogenic carbonates and opaline silica which also carry down marine snow aggregates (Logan and Hunt, 1987; Ittekkot, 1993; Armstrong et al., 2001; Francois et al., 2002; Klaas and Archer, 2002). As a result, organic carbon fluxes are proportional to the flux of the ballasting minerals (Brummer and van Eijden, 1992; Neuer et al., 1997; Armstrong et al., 2001; Fischer et al., 2004).

In this paper, we evaluate particle fluxes to the deep WENA using time-series sediment traps (Guerreiro et al., 2017; Korte et al., 2017) and *in-situ* vertical depth profiling in combination with satellite observations that relate to their origin, spatial and temporal variability. We address the impact of, and the interaction between Amazon River dispersal, nitrogen fixation, mixed-layer deepening and Saharan-dust deposition through a detailed analysis of both the biogenic and abiogenic particle fluxes. We highlight temporal peak events which are exceptional for the study area and which provide insights into the processes affecting the biological carbon pump. In addition, we combine isotope data of nitrogen and organic carbon together with pigment data and interpret them in terms of Saharan-dust fluxes.

2 Material and Methods

2.1 Experimental setting

Three sediment traps were retrieved from two moorings (M4 and M5; Fig. 1, Table 1) after a full year of sampling (RV *Pelagia* cruise 64PE 378; Stuut et al., 2013). Each mooring was equipped with two sediment traps at 1200 m (upper, U)

and 3500 m (lower, L) water depth. Since the upper sediment trap at station M5 was lost during recovery, our dataset is based on all material from the upper and lower sediment traps at station M4 and the lower trap of sampling site M5. Technicap PPS 5/2 sediment traps were used with a baffled collecting area of 1 m^2 and a rotating carrousel with 24 sampling bottles. Prior to deployment, sample cups were filled with a $HgCl_2$ solution in seawater collected at the deployment site and buffered with borax ($Na_2[B_4O_5(OH)_4] \cdot 10H_2O$), both to an end concentration of 1.3 g L^{-1}. All sediment traps were programmed for the same collection intervals (16 days), starting on October 19 in 2012 and ending on November 7 in 2013. After recovery, the pH and nutrient concentration of the supernatant water were determined; sample bottles were stored dark and cool at 4°C until further processing. Tilt meters showed that sediment traps at site M4 remained well within 1.4° from the vertical and a constant depth during the entire sampling period. At site M5, a downward movement and a tilt up to 14° was recorded during three sampling intervals (intervals #8, 10, and 11), affecting the total mass flux at this site, which was corrected accordingly (Gardner, 1985). For further details see Korte et al. (2017).

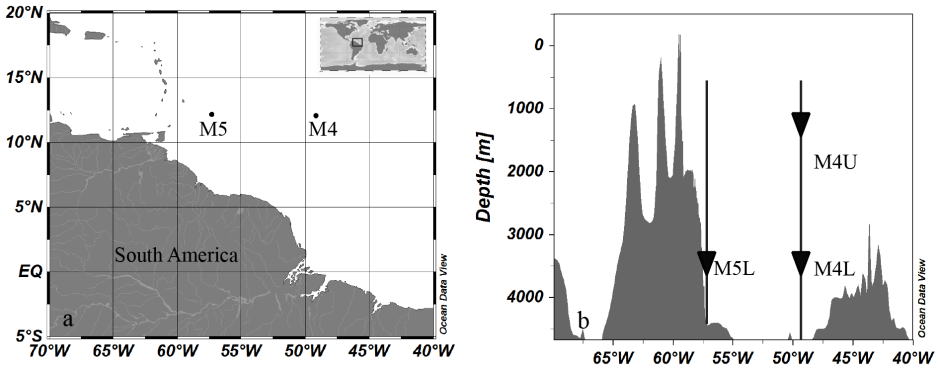

Figure 1. a) Map showing regional setting and the location of sediment-trap moorings at stations M4 (12°N, 49°W) and M5 (12°N, 57°W). b) Bathymetric profile through the WENA between 40°W and 70°W showing the two moorings with sediment traps (triangles). M*x*U and M*x*L indicate the upper and the lower traps on the moorings at 1200 m and 3500 m nominal water depth, respectively.

2.2 Satellite data

Satellite-derived atmospheric and oceanographic parameters were retrieved for the sampling period of sediment traps as complementary information to evaluate the particle export fluxes. The satellite data include aerosol optical depth (AOD), precipitation, sea surface temperature (SST) and -salinity (SSS) as well as surface

Chl-*a* and the euphotic depth. The data were retrieved for a 2° x 2° latitude-longitude box centered around each trap location. Parameters were taken from various sources and processed for the study period of 2012-2013 (see Guerreiro et al., 2017). In addition to the trap locations, SSS, sea level anomalies (SLA) and the Ekman Vertical Velocity were examined for an area covering a 26° x 20° latitude-longitude box (38°W-64°W, 16°N-4°S) in order to investigate the eddy- and wind-driven upwelling effects in the western Atlantic Ocean (Videos S2).

At each mooring site CTD profiles with *in-situ* water sampling were performed using a Sea-Bird SBE911-Plus Profiler, equipped with sensors for conductivity, temperature, pressure, oxygen, chlorophyll, fluorescence, and turbidity during the RV *Pelagia* cruise 64PE 378 late 2013 (Stuut et al., 2013). The CTD profiler was deployed in conjunction with a SBE32 (24-position) Multi Water Sampler (Rosette), which sampled water at specific depths during upward cast for nutrient analysis. Inorganic nutrient concentrations were determined colorimetrically for phosphate, silicate and nitrate (Murphy and Riley, 1962; Strickland and Parsons, 1972; Grasshoff et al., 1983) using a Seal-Analytical QuAAtro Autoanalyzer connected to an auto-sampler. In addition, Argo-float profiles (http://www.argo.net) were used for temperature and salinity around the trap locations (2° x 2° latitude-longitude box centered around each trap location) during the entire sampling period at M4 (Fig. S1), while for site M5 Argo-float profiles were only available for June 2013 and therefore not shown.

2.3 Sample analysis

Sediment-trap samples were wet-sieved through a 1 mm mesh, wet-split with a rotary splitter (WSD-10) into four 1/5 and five 1/25 subsamples. Samples were washed and centrifuged, freeze dried and ground. Total mass was determined by weighing two freeze-dried 1/5 aliquots of each sample, resulting in an average deviation of 1.96 % by mass between paired splits. Total nitrogen (N_{tot}), total carbon (C_{tot}) and organic carbon (C_{org}), together with their isotope ratios $^{15}N/^{14}N$ ($\delta^{15}N_{tot}$) and $^{13}C/^{12}C$ ($\delta^{13}C_{org}$) were obtained by combustion with a Thermo Scientific Flash 2000 Elemental Analyzer coupled to a Thermo Scientific Delta V Advantage isotope ratio mass spectrometer at NIOZ. Samples for C_{org} measurements were decalcified with 2 N HCl, while samples for N_{tot} and C_{tot} measurements remained untreated. Inorganic carbon (C_{carb}) was calculated as the difference of C_{tot} and C_{org}. Isotope ratios were expressed in standard δ-notation relative to Pee Dee Belemnite (v PDB) for $\delta^{13}C$ and atmospheric N_2 for $\delta^{15}N$ via laboratory standards calibrated to international certified reference standards. Sample reproducibility is ± 0.01 % for N_{tot}, ± 0.24 % for C_{org},

< 0.3 ‰ for $\delta^{15}N_{tot}$ and < 0.2 ‰ for $\delta^{13}C_{org}$ values. Molar C/N ratios were calculated as well as the molar rain ratios of biogenic silica and organic to inorganic carbon, respectively.

Pigment composition was analyzed on one of the 1/25 subsample from the upper trap at site M4, using Ultra-Performance Liquid Chromatograph (UPLC) according to the gradient method of Kraay et al. (1992). Lower traps of M4 and M5 were not analyzed due to their deep location in the water column. Each subsample was washed with filtered seawater from the original sampling depth, centrifuged, freeze dried and ground. Pigments in freeze-dried samples were extracted in 95 % methanol and centrifuged. Subsequently, the supernatant was filtered (0.2 µm) and 50 µl of sample was injected. The UPLC used is a Waters Acquity system, composed of a 600E controller, a 996 photodiode array in line with a 470 Fluorescence detector. Pigments and degradation products were identified by their absorption spectrum, fluorescence and elution time, and converted into concentrations using conversion factors determined with internal standards.

Biogenic silica (BSi) was analyzed on a HITACHI U-1100 spectrophotometer using a sequential-leaching technique with 0.5 M NaOH as a dissolving agent (Koning et al., 2002). Results were evaluated with a weekly measured standard calibration curve ($R^2 > 0.99$) resulting in a sample reproducibility of ± 0.36%. Lithogenic mass was determined on 1/25 split after removal of carbonates, opal and organic matter fractions using the processing protocol for lithogenic minerals (McGregor et al., 2009; Van der Does et al., 2016), followed by filtration of the residue on pre-weight polycarbonate filters (0.4 µm) and back weighing of those, rounding the weights to two decimal places (Chapter 3).

3 Regional setting

3.1 Oceanography

The surface pattern of circulation in the WENA is characterized by large westward currents and eastward counter currents that show a strong seasonality (Fig. 2; see Bourlès et al. (1999)). The North Equatorial Current (NEC) flows in westward direction between 7 and 20°N, originating from the north western coast of Africa, and approaches the shelf regions of the Americas where it feeds the north-westward flowing Guiana Current (GC). The North Equatorial Counter Current (NECC) lies between 3 and 10°N and is present west of 40°W during boreal spring. The North Brazil Current (NBC) flows in northwest direction along the coast of

Brazil carrying waters from the South Atlantic. When the NBC crosses the equator, the Amazon discharge is entrained into the NBC and dispersed with it (Masson and Delecluse, 2001). From February to May, when the NECC is not yet established in the study area, the Amazon's discharge flows northwest towards the Caribbean Sea (Fig. 2a), while between June and January it is carried eastward towards Africa by a retroflection (Fig. 2b) of the NBC into the NECC (Muller-Karger et al., 1988). Occasionally, rings are formed from the NBC, propagating in a northwest direction as shown by remote ocean color measurements (Fratantoni and Glickson, 2002).

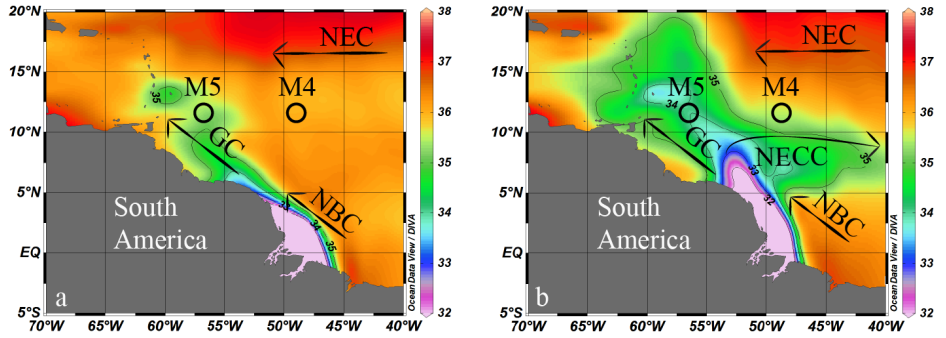

Figure 2. Amazon River dispersal represented by the sea surface salinity for a) February to May 2013 and b) June 2013 to January 2014. Months were used with respect to contrast dispersal situations given by Muller-Karger et al. (1988). Data obtained from Aquarius (monthly temporal resolution, 1° spatial resolution) downloaded from Giovanni of the Goddard Earth Sciences Data and Information Services Center (GES DISC) provided by NASA (disc.sci.gsfc.nasa.gov). Arrows indicate the North Equatorial Current (NEC), North Equatorial Counter Current (NECC), Guiana Current (GC), and North Brazil Current (NBC).

The temperature, salinity, density and fluorescence at the mooring locations, measured by CTD in November and December 2013 indicate that the surface mixed layer (SML), where salinity and density are uniform, was located at 25 m depth at site M4 and at around 50 m at site M5 (Fig. 3). While sea surface temperatures were similar at both sites (> 27°C), sea surface salinity was significantly lower at site M4 (34.1) than at site M5 (35.6) pointing to the presence of a surface fresh-water lens at M4, most likely derived from the Amazon River. The Chl-*a* concentrations in the fluorescence profiles showed two maxima at site M4, at 60 and 85 m depth, as opposed to a single maximum at site M5 at 96 m. Nitrate and phosphate concentrations were strongly depleted in the surface layers at both sites compared to the deeper layers, while silicate showed elevated concentrations in the fresh water lens forming the upper 25 m at site M4. Nitrite concentrations peak at 100 m water depth, associated with the peak in highest Chl-*a* concentrations.

The Argo-float data around the mooring M4 showed SML temperatures ranging between 26 and 29°C with deeper water column penetration in spring and summer than during fall and winter (Fig. S1). Deepest penetration of 92 m was recorded on April 23rd 2013. Surface salinity ranged between 35.5 and 36.6 during most of the year but decreased rapidly in late October to a minimum of 34.0 on November 2nd (Fig. S1), corresponding with the low salinities in the freshwater lens observed during the recovery of the sediment traps, and presumed to be Amazon derived waters. The Argo-float data around mooring M5 was very sparse with only two continuous profiles during June 2013. During this time sea surface temperature was 28°C and sea surface salinity ranges between 34.3 and 34.7 (data not shown).

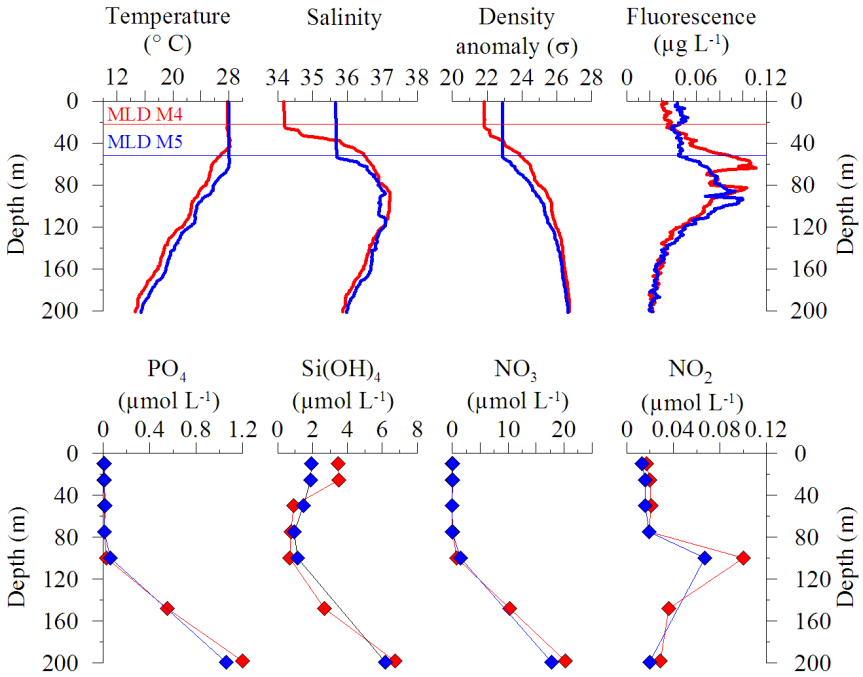

Figure 3. Temperature, salinity, density, fluorescence and nutrient profiles of the upper 200 m at sites M4 (red) and M5 (blue) during recovery cruise 64PE378 on November 28th 2013 (M4) and December 1st 2013 (M5).

3.2 Remote sensing data

The remote sensing data show similar patterns in AOD around mooring sites M4 (see also Guerreiro et al., 2017) and M5 (Fig. 4). Highest AOD values were recorded during summer, which is when typically huge dust outbreaks cross the Atlantic from the Saharan desert towards the Caribbean (Chiapello et al., 1997). Precipitation at site M4 occurred in summer and fall rather than during winter and spring, reaching a daily average up to 9 mm during November 2013 at site M4. At site M5, precipitation happened more frequently throughout the year but in similar amounts compared to site M4. Sea surface temperatures (SST) showed a similar seasonal trend at sites M4 and M5, with maxima in fall and minima in spring and summer. Maximum SSTs are reached in September 2013 at both sites, being slightly lower at site M4 than at site M5. Surface water Chl-*a* occurs in low concentrations of around 0.1 mg m^{-3} throughout the year at M4, except in fall in early October 2013 when values reached more than 1 mg m^{-3} at their maximum absorption in this area. At station M5 low Chl-*a* values of 0.1 mg m^{-3} were recorded in winter and fall that contrasted with extreme values to more than 4 mg m^{-3} during spring and summer at the same location. The SSS shows pronounced minima that coincide with maxima in surface Chl-*a* at both sites. At site M4 a SSS minimum is reached in October 2013 (~34), while at site M5 two minima in SSS are recorded (down to 32), enclosing the maxima in surface Chl-*a*. The euphotic depth is on average deeper and more stable at site M4, i.e. around 100 m for most of the year but shoaling to 40 m in October 2013, when the peaks in surface Chl-*a* occurred. At site M5 the euphotic depth is deeper in fall and winter (~100 m) than in spring and summer (~40 m). Shallower euphotic depths are accompanied by maxima in Chl-*a* coupled to minima in SSS. Overall, it should be noted that satellite derived atmospheric and oceanographic data are heavily influenced by clouds as they hamper visibility.

A combined analysis of SSS and absolute geostrophic velocity highlights the Amazon freshwater dispersal by the surface currents and shows the Amazon waters being trapped in the NBC retroflection and transported into the NECC during the second half of the year (Video S2.1). Sea Level Anomalies (SLA) overlapped by their respective anomaly of geostrophic velocity reveal potential eddy-driven upwelling in the WENA during the sampling time period (Video S2.2). During spring an anticyclonic eddy is bordering the mooring site M4 indicating a downwelling situation. Overall, during the entire sampling period, Ekman Vertical Velocities are weak and variable (Video S2.3), leading to little large-scale variation in the vertical velocities.

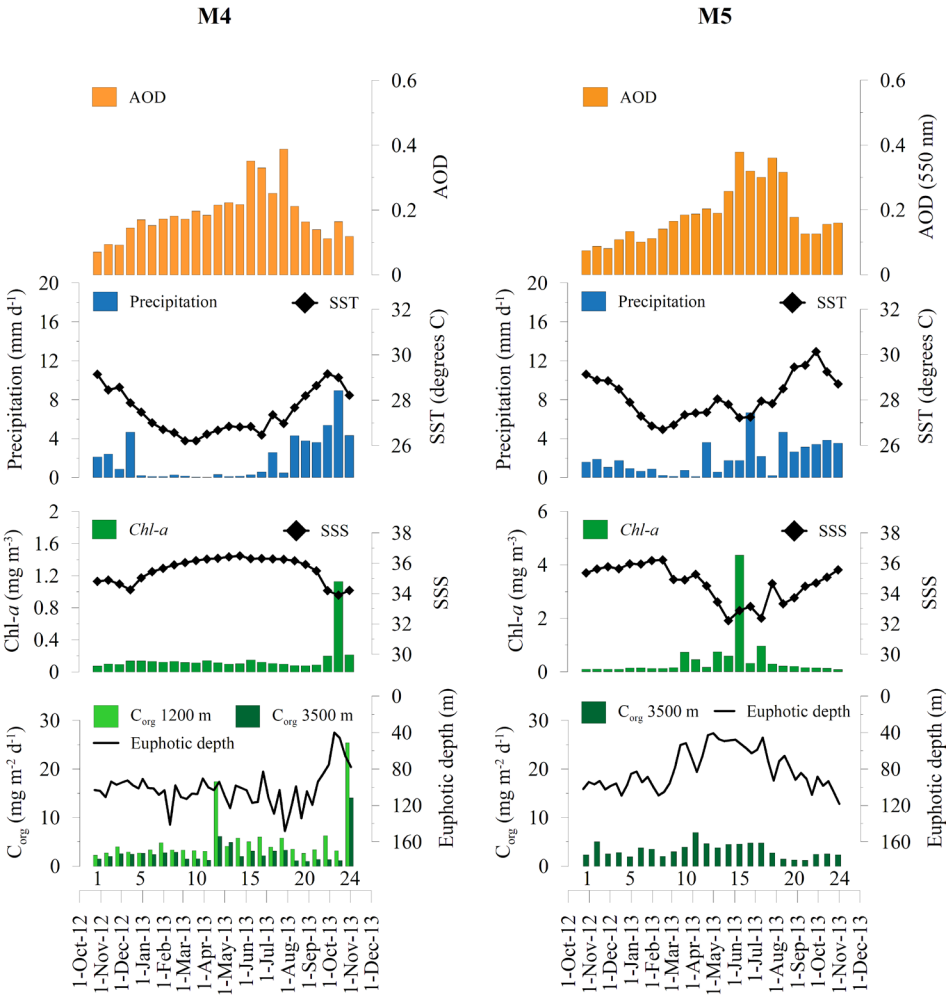

Figure 4. Remote sensing data for site M4 (left, see also Guerreiro et al., 2017) and site M5 (right). Parameters given are Aerosol Optical Depth (AOD), precipitation with Sea Surface Temperature (SST), Chl-*a* concentration (note different scale for site M5) with Sea Surface Salinity (SSS), and organic carbon fluxes (Korte et al., (2017)) with euphotic depth. Numbers 1-24 indicate sediment trap collecting intervals.

4 Results

4.1 Export fluxes in the western Atlantic Ocean

Annual total mass fluxes at site M4 (Fig. 5a) were higher in the upper trap at 1200 m (30.9 g m^{-2} $year^{-1}$) than in the lower trap at 3500 m (23.2 g m^{-2} $year^{-1}$),

without showing a pronounced seasonality (Korte et al., 2017). Trapped material consists predominantly of inorganic carbon (Fig. 5c) ranging from 2-17 mg m^{-2} d^{-1} for the upper and 2-12 mg m^{-2} d^{-1} for the lower trap with an annual average of 5 and 4 mg m^{-2} d^{-1}, respectively. Moreover, peak fluxes are observed in spring during the second half of April 2013 and in fall during late October/early November 2013, each occurring simultaneously within the same collecting interval at both depths (Fig. 5a). The two peak fluxes differ in composition; while during spring the peak flux is dominated by inorganic carbon, during fall the peak flux is dominated by biogenic silica (BSi), as observed in both the upper and lower traps (Fig. 5c, e). On average, BSi fluxes range from 0.8-7.3 mg m^{-2} d^{-1} in the upper, and between 1.1-4.8 mg m^{-2} d^{-1} in the lower trap (Fig. 5e) at an annual average of 3.1 and 2.3 mg m^{-2} d^{-1}, respectively. Exceptionally high BSi fluxes arrived in fall that exceed 30 mg m^{-2} d^{-1} (11 % of the total mass) in the upper trap and reach up to 23 mg m^{-2} d^{-1} (14 %) in the lower trap. Organic carbon fluxes (Fig. 5g) vary between 2-25 mg m^{-2} d^{-1} for the upper and between 1-14 mg m^{-2} d^{-1} for the lower trap at an annual average of 5.3 and 2.8 mg m^{-2} d^{-1}, respectively. The organic carbon fluxes peak in tandem with the two high peak total mass fluxes in spring and in fall. The lithogenic fraction at M4 is interpreted as Saharan dust and therefore presenting the dust flux (Chapter 3). These fluxes vary between 1-12 mg m^{-2} d^{-1} in the upper and between 2-9 mg m^{-2} d^{-1} in the lower trap at an annual average of 3.3 and 4.1 mg m^{-2} d^{-1}, respectively (Fig. 5i). Dust fluxes are higher during summer in the upper trap and peak in spring and fall 2013 together with biogenic fluxes. The lower trap receives a more consistent dust flux throughout the year and shows therefore higher dust fluxes in winter as compared to the winter dust fluxes in the upper trap.

At site M5 the annual total mass flux at 3500 m water depth was almost two times higher (42.2 g m^{-2} $year^{-1}$) than at site M4 at the same depth, with seasonally higher fluxes from April to June and lower fluxes from August to November 2013 (Fig. 5b). The biogenic silica and the lithogenic fluxes at M5 increase relative to the inorganic and organic carbon fluxes. The inorganic carbon fluxes vary between 2-8 mg m^{-2} d^{-1} (Fig. 5d) with an annual average of 5 mg m^{-2} d^{-1}, while organic carbon varies between 1-7 mg m^{-2} d^{-1} (Fig. 5h), with an annual average of 3 mg m^{-2} d^{-1}. High fluxes between 4-20 mg m^{-2} d^{-1} (annual average 9 mg m^{-2} d^{-1}) are found for biogenic silica (Fig. 5f) showing a clear seasonality with higher contribution during the summer and fall 2013 (Korte et al., 2017). The lithogenic fluxes (Fig. 5j) at site M5 are significantly higher than at M4 and vary between 2-45 mg m^{-2} d^{-1}. However, given the sediment trap's close proximity to the steep Barbados margin (Table 1), lithogenic material might consist, next to Saharan dust, from resuspended sediments from the seafloor which

were dispersed by nepheloid layers and contributed to the high lithogenic flux in the 3500 m deep sediment trap at M5.

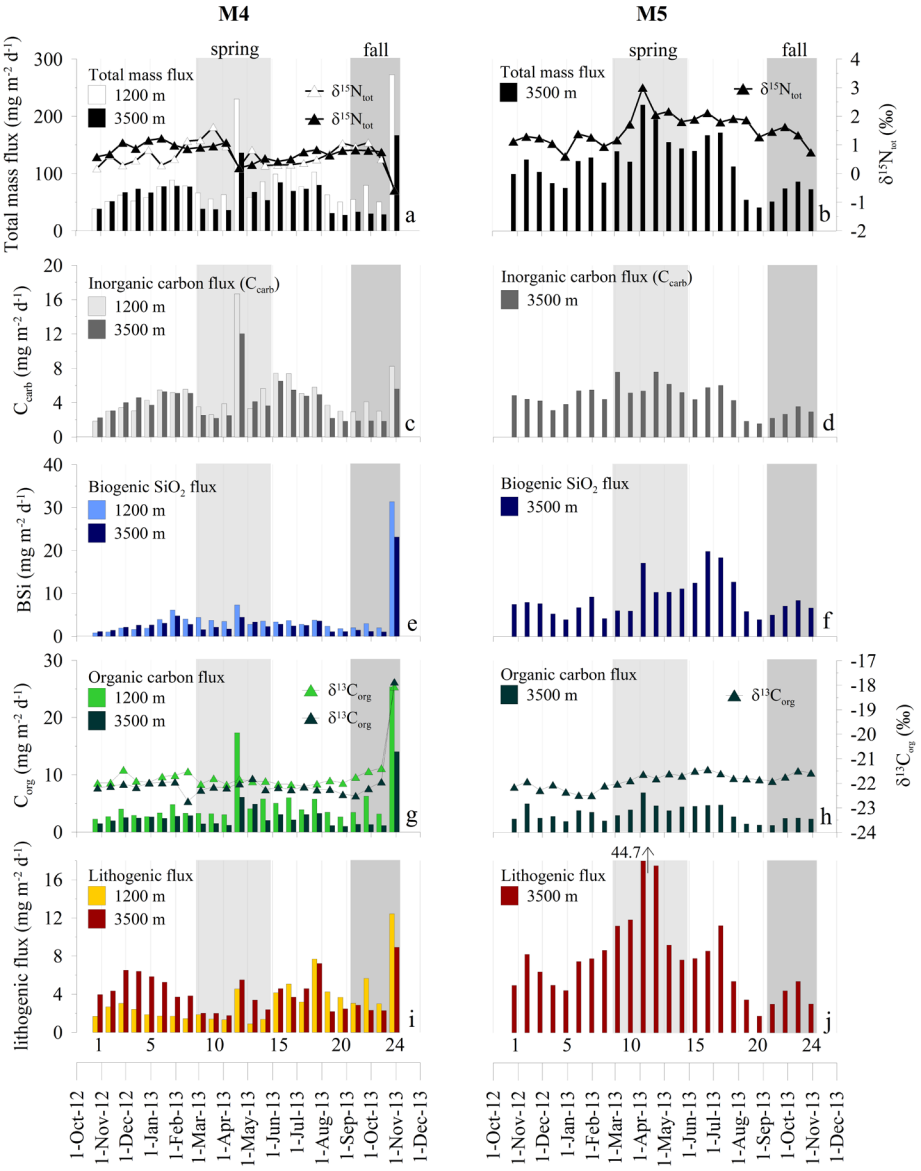

Figure 5. Particle fluxes and isotopic composition at site M4 (left) and M5 (right). Mass fluxes (mg m^{-2} d^{-1}) are shown as bars (left y-axis), and isotopic values are displayed in triangles (right y-axis in ‰). a, b) total mass together with total nitrogen isotope composition; c, d) inorganic carbon; e, f) biogenic silica; g, h) organic carbon together with their isotope composition; i, j) lithogenic mass flux (Chapter 3).

4.2 Nitrogen and organic carbon isotope composition

The isotope composition of organic carbon at site M4 ($\delta^{13}C_{org}$; Fig. 5g) remains mainly constant at around -21 ‰ for both traps, with only slightly more negative values in the lower trap than in the upper trap. Values are similar to bulk marine plankton and plankton-derived sedimentary organic matter (Hinga et al., 1994). Moreover, when the BSi flux peaks in fall (late October to early November 2013), $\delta^{13}C_{org}$ jumps by 4 ‰ to -18 ‰ at both depths. The nitrogen isotope composition ($\delta^{15}N_{tot}$, Fig. 5a) in the upper trap ranges between +0.2 ‰ and +1.6 ‰ (avg. +0.6 ‰), but drops by 1 ‰ in October/November 2013 to -0.5 ‰. Lowest values are reached in April after peaking in March 2013. For the lower trap, the $\delta^{15}N_{tot}$ values are more uniform, ranging between +0.8 ‰ and +2.8 ‰, but also drop markedly to a negative value of -0.6 ‰ in October/November 2013. At site M5, the $\delta^{13}C_{org}$ averages -22 ‰ (Fig. 5h), similar to both traps at site M4. However, $\delta^{15}N_{tot}$ show more positive values and average 1.5 ‰, reaching 3 ‰ in April 2013 (Fig. 5b).

4.3 Element rain ratios

The molar C/N ratios at site M4 amount to an annual average of 8.6 ± 0.6 for the upper trap, increasing to 9.1 ± 0.8 at the lower trap (Fig. 6a). In winter, the molar C/N ratios show higher values in the deep trap, concurrent with higher dust fluxes. The rain ratios of organic carbon to inorganic carbon (C_{org}/C_{carb}) are higher in the upper trap than in the lower trap (Fig. 6c) with averages of 1.1 and 0.7, respectively. Peak values of 3.1 and 2.5 are found during the fall peak (late October to early November 2013) in the upper and lower trap, respectively. Throughout the year, molar biogenic silica (BSi) to C_{carb} ratios are strongly co-variant in the upper and lower traps and have similar average values of 0.35 and 0.33, respectively (Fig. 6e). Also, in this case, a significant peak is found in fall (October/November 2013) when the ratios increase to around 1.7 at both trap depths at the same time. The average molar C/N ratio at sampling site M5 at 3500 m water depth is 9.1 ± 1.5 and therefore similar to the ratio in the lower trap at site M4, although values are wider spread (Fig. 6a, b). Also, the rain ratios of organic (C_{org}) to inorganic carbon (C_{carb}) are similar to site M4 with an average of 0.7 (Fig. 6d). For biogenic silica (BSi) to C_{carb}, however, values are higher at M5 than at site M4, averaging 0.9 with higher values during summer, reaching 1.5 as a maximum (Fig. 6f).

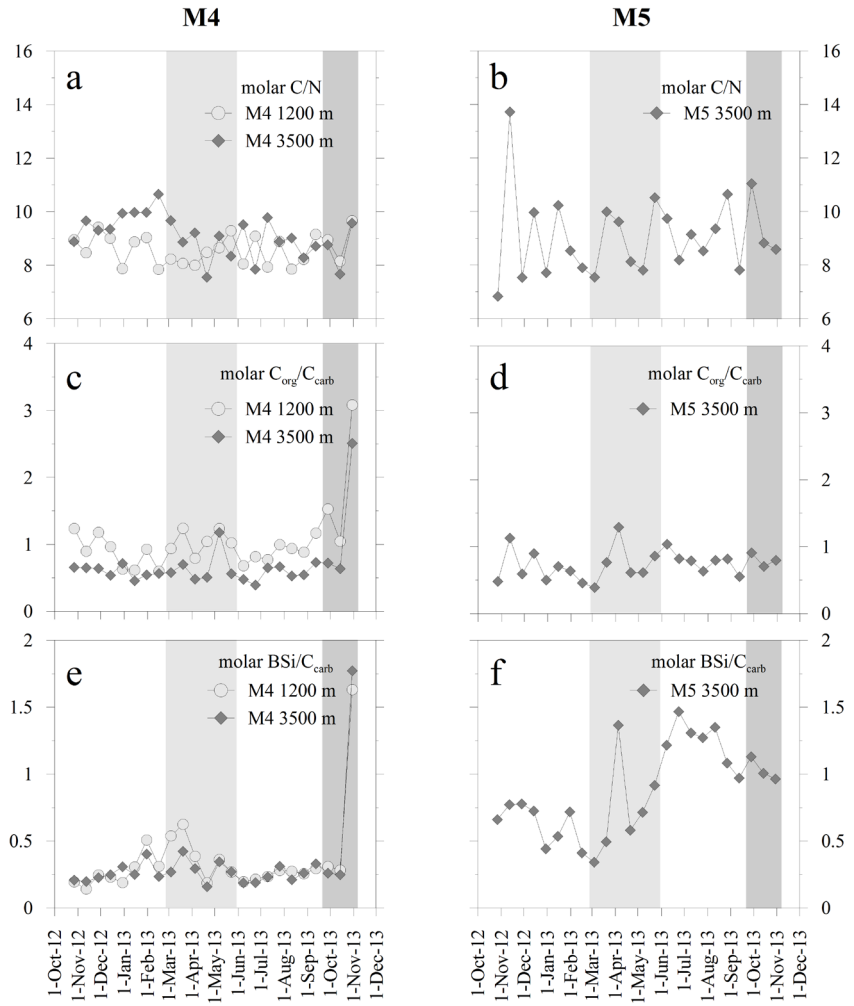

Figure 6. Rain ratios at site M4 (left) and M5 (right). Upper panel: molar C/N ratios, middle panel: C_{org}/C_{carb} rain ratio, bottom panel: molar BSi/C_{carb} rain ratio.

4.4 Pigments at sampling site M4 at 1200 m water depth

The flux of intact Chl-*a* together with its degradation products phaeophorbide and phaeophytin (Fig. 7a) show two distinct peaks in spring and fall, simultaneously with total mass peak fluxes (Fig. 5a). The Chl-*a* peak flux in spring 2013 reaches 300 µg m^{-2} d^{-1} which constitutes around 1.7 wt % of the organic carbon. The peak flux in fall 2013 reaches almost 200 µg m^{-2} d^{-1} (0.8 wt %). A third minor peak flux is observed in winter (January 2013) when Chl-*a* amounts to 33 µg m^{-2} d^{-1} (0.7 %). The ratio of Chl-*a* to its degradation products (Fig. 7b) is used to assess the extent of

degradation of the algal organic carbon (Boon and Duineveld, 1996). It shows several peaks, highest during spring and fall 2013, indicating freshest material arriving in the sediment trap at 1200 m depth. These peaks coincide with the peak fluxes in total mass and biogenic constituents (Fig. 5). In addition, higher ratios are found in summer and to a less extent during winter. Overall, elevated ratios are positively correlated with Saharan dust deposition fluxes ($r = 0.80$, $p < 0.01$) and weakly negatively correlated with $\delta^{15}N$ values ($r = -0.54$, $p < 0.05$).

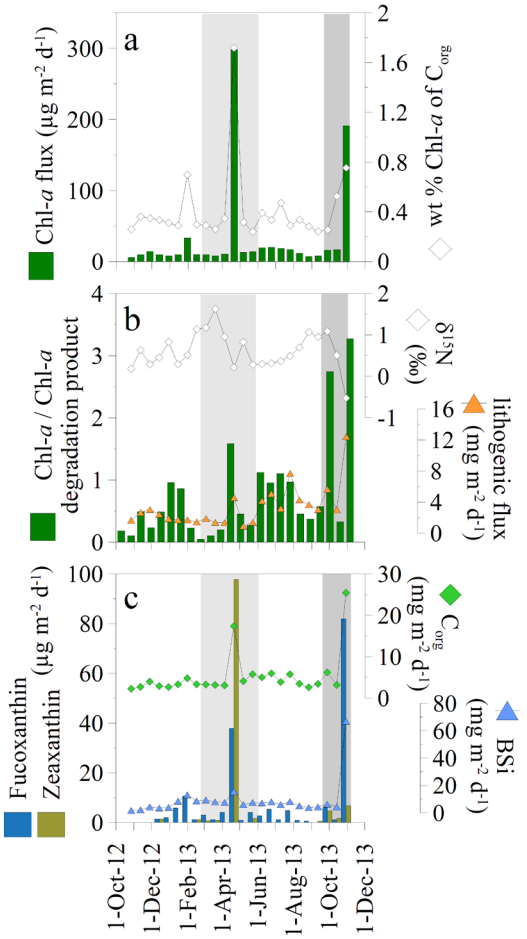

Figure 7. Pigment content at M4 – 1200 m. a) Fluxes of total Chl-*a* and relative weight % of Chl-*a* fluxes to C_{org} b) Chl-*a*/Chl-*a* degradation product ratio, $\delta^{15}N$ values and dust flux (Chapter 3), c) fluxes of fucoxanthin and zeaxanthin and organic carbon and biogenic silica flux.

The pigments fucoxanthin and zeaxanthin (Fig. 7c) indicate the contribution of specific phytoplankton communities, i.e. cyanobacteria and diatoms, respectively (Wright and Jeffrey, 1987). Fucoxanthin was recorded in almost every sample with values ranging from 8 to 82 µg m^{-2} d^{-1}. Highest values are found during spring and fall 2013 in tandem with the two peak fluxes in total mass, organic- and inorganic-carbon and biogenic silica (Fig. 5). Fucoxanthin is highly positively correlated with organic carbon and biogenic silica ($r = 0.86$ and $r = 0.99$, both $p < 0.01$) and negatively correlated with $\delta^{15}N$ ($r = -0.61$, $p < 0.01$). Although zeaxanthin is found in low fluxes and discontinuously within the time-series, it shows an exceptionally high peak during spring reaching almost 100 µg m^{-2} d^{-1}, when the inorganic carbon flux is also high.

5 Discussion

5.1 Amazon-driven productivity and export

The largest single particle export event was observed at M4, with peak fluxes arriving at both upper and lower sediment traps between October 22nd and November 7th 2013 (Fig. 5a). Shortly before (October 8-16th 2013), satellite data show a short but massive increase in surface water Chl-*a* concentrations, shoaling of the euphotic depth, a conspicuous decrease in SSS and increased precipitation around the mooring site (Fig. 4). While precipitation will lower surface salinity in a steady water column, a mass balance using a precipitation end member with a salinity of 1 and a subsurface salinity of 37 would require around 2000 mm of precipitation to bring the salinity down to the observed 34.1 in the top 25 m (Fig. 3). Given that precipitation delivers 9 mm d^{-1} at most (Fig. 4), it would need around 200 days of continuous maximum precipitation to lower the salinity down to the observed value. If so, salinities at M5 would also be expected to give the same low salinities, rather than the observed 35.6 (Fig. 3). Consequently, precipitation cannot be the main contributor of fresh water lowering the salinity during this period. *In-situ* CTD profiles obtained during expedition 64PE 378 (Fig. 3) as well as the Argo-float profiles (Fig. S1) showed a surface fresh water lens of 25 m thickness high in silica that attest to the advection of entrained Amazon-derived water, as observed earlier in the Caribbean Sea (Froelich et al., 1978). Assuming that the WENA is intrinsic oligotrophy, the sharp changes in surface Chl-*a* concentration indicate a period of high surface productivity. Monthly averages of sea surface Chl-*a* concentrations in the WENA trace this high production back to the Amazon outflow at the equator (Fig. 8). From October 2012

until April 2013, the Amazon outflow was transported north-westward within the NBC towards the Caribbean (Fig. 8, October 2012 to April 2013). From May 2013 onwards, (Fig. 8, June to October), it was increasingly entrained eastwards within the NECC. However, from August 2013 there are large patches marked by high Chl-*a* concentrations meandering towards the northwest until the patches crossed the sediment trap site M4 in October 2013 (Fig. 8, August 2013 to October 2013), when the remote sensing Chl-*a* concentration is also high (Fig. 4, left) and measured Chl-*a* in the trap is peaking as well (Fig. 7a). Export productivity and settling of particles to the depth of the sediment traps was associated with a time delay in relation to the time of production at the surface. Aggregate formation and repacking of this biomass in the surface waters until reaching a proper settling density may take a couple of days. Settling velocities are in the order of 200 m d^{-1} (Knappertsbusch and Brummer, 1995; Berelson, 2002; Fischer and Karakas, 2009), which are consistent with the settling velocity of at least 140 m d^{-1} between the shallower sediment trap at 1200 m and the deeper one at 3500 m observed for the fall peak in fluxes at site M4 (Korte et al., 2017). Extrapolating from 1200 m depth to the surface at a settling velocity of 140 m d^{-1} then yields a delay of nearly 9 days, which, added to the time needed for aggregate formation, is in line with the timing in October 2013 of high surface Chl-*a*, and low SSS generated by Amazon-discharge related peak productivity. After the bloom, Chl-*a* concentrations decreased to the low background values (Fig. 8, December 2013). Similar plumes/patches of high Chl-*a* appear to have passed over the site in fall about every five years since 2002 (Fig. S3), which are similarly expected to generate abnormally high fluxes to the deep ocean floor.

At site M5, satellite images (Fig. 8) show large patches of high Chl-*a* concentrations approaching and crossing the mooring location from March to July 2013. Remote sensing recorded periods with extremely high surface Chl-*a* concentrations around M5 from March to July 2013 which were accompanied by minima in SSS (Fig. 4, right). This indicates high productivity in the freshwater lenses from the Amazon, which in turn generate high export fluxes to the deep ocean as previously observed by Deuser et al. (1988). Indeed, total mass fluxes in this area became significantly higher from late spring to early summer in tandem with the shoaling of the euphotic depth and freshening at the surface, similarly to what occurred at site M4 later in the year, during fall (Fig. 4, left). The coupling of total mass flux and productivity by Amazon discharge has previously been reported by Deuser et al. (1988) and Beers et al. (1968). Deuser et al. (1988) ascribe high total mass fluxes at 3200 m water depth off Barbados, close to site M5 in this study, to the passage of freshwater lenses and high-nutrient water derived from the plumes of the Amazon and Orinoco rivers.

Former coastal zone color scanner (CZCS) recorded typical Chl-*a* concentrations of about 1 mg m^{-3} in plumes compared to 0.1 mg m^{-3} in their surroundings (Deuser et al., 1988), similar to the plume concentrations observed around mooring M4 during the fall peak in 2013, while around mooring M5 Chl-*a* concentrations even exceeded this maximum absorption. Our data show that Amazon-discharge stimulated productivity occasionally propagates far further east into the central Atlantic than hitherto thought, generating pulses of high export, settling at high rates in an otherwise highly oligotrophic ocean. At both M4 and M5, molar rain ratios of organic carbon and biogenic silica to inorganic carbon (Fig. 6) are higher when under the influence of Amazon-River discharge, implying a more efficient carbon dioxide sequestration by the biological pump (Berger and Keir, 1984; Ittekkot et al., 2000) compared to when Amazon waters are absent.

At both stations M4 and M5, Amazon stimulated productivity was also reflected in enhanced total-mass fluxes enriched in biogenic silica relative to organic and inorganic carbon, together with high surface Chl-*a* concentrations and high dissolved silica. The Amazon discharge is known to carry diatom-diazotrophic associations offshore (Yeung et al., 2012; Goes et al., 2014) of which the symbiont *Richelia intracellularis* fixes N_2 and support host *Hemiaulus spp.* or *Rhizosolenia spp.* (Foster et al., 2011). Indeed, the excursions of $\delta^{15}N_{tot}$ to more negative, and $\delta^{13}C_{org}$ to more positive values in both traps at site M4 (Fig. 5a, g) argue for a significant contribution by nitrogen fixation and enhancement of diatoms during the fall peak, since diatoms are fast growers and therefore more enriched in ^{13}C compared to other phytoplankton (Fry and Wainright, 1991). Nitrogen fixation produces biomass with a low $\delta^{15}N$ between -1 ‰ and -2 ‰ (e.g. Bauersachs et al., 2009) and lowers $\delta^{15}N$ of all organic pools by food-web propagation (Montoya et al., 2002). The abundance of the pigment fucoxanthin, more typically formed by diatoms (Barranguet et al., 1997) and zeaxanthin, more typically formed by cyanobacteria, also line up with the observed isotope excursions and indicate an input of both cyanobacteria and diatoms (Fig. 7c). Nitrogen fixation at M5 is, however, presumably less important than at site M4 as the low salinity waters at M5 may still carry sufficient nutrients to support 'coastal' diatom species (Subramaniam et al., 2008). Subramaniam et al. (2008) suggest that in low salinity waters there are enough nutrients (i.e. P, Si and combined N) to promote coastal diatom species without symbiotic cyanobacteria, as opposed to the mesohaline species containing symbiotic cyanobacteria. Therefore, $\delta^{15}N$ might be more positive at M5 than at site M4, especially during spring (Fig. 5b) when the first nutrient rich Amazon waters arrive at M5 (Fig. 8) inducing an increase in biogenic silica fluxes, likely consistent of coastal diatom species.

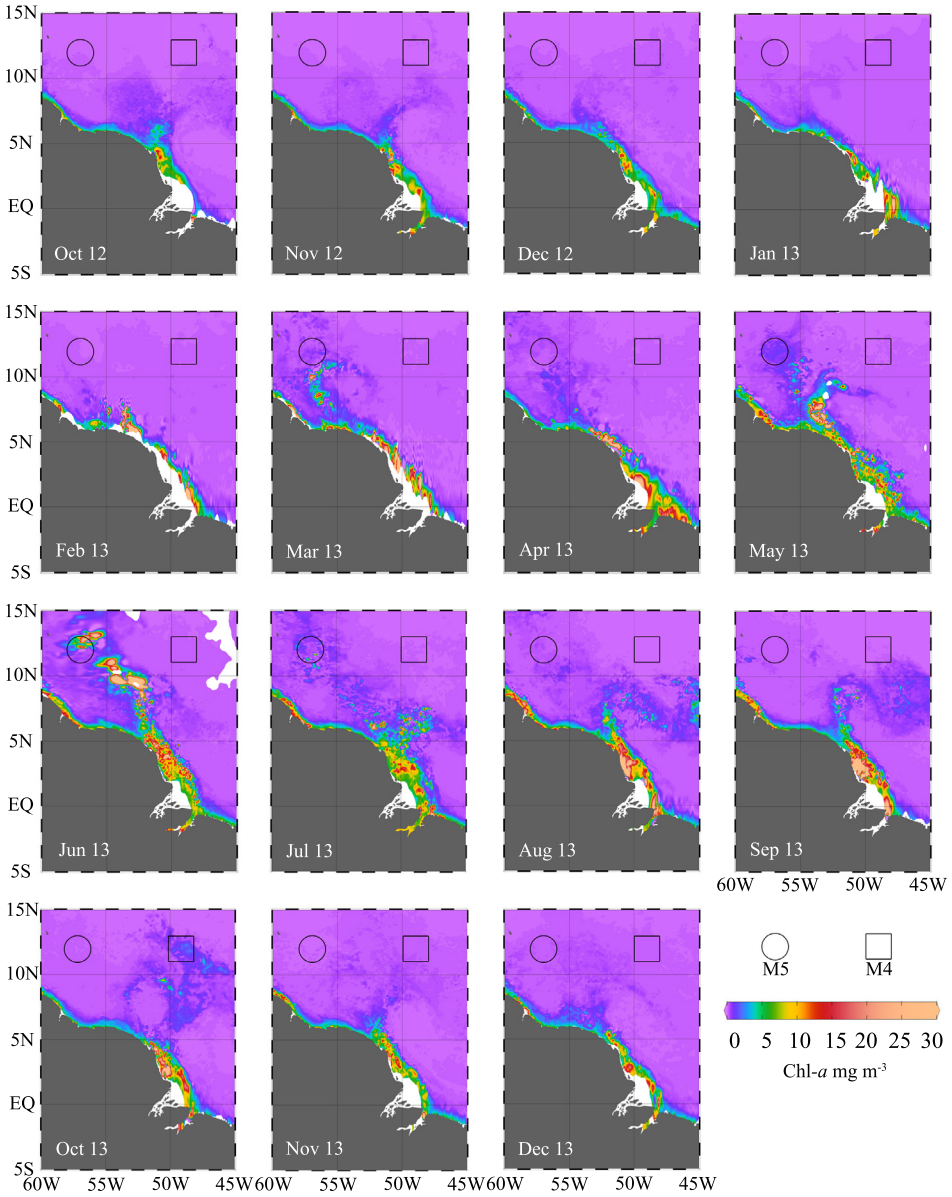

Figure 8. Monthly Chl-*a* concentrations in the surface waters of the WENA with mooring sites M5 (circle) and M4 (square). Amazon delta is located at the equator at 50°W. Data obtained from MODIS, Aqua (monthly temporal resolution, 4 km spatial resolution), downloaded from Giovanni of the Goddard Earth Sciences Data and Information Services Center (GES DISC) provided by NASA (disc.sci.gsfc.nasa.gov). Data visualized by Ocean Data View.

Besides the effect of Amazon waters on diatoms, Guerreiro et al. (2017) also report on a pulsed maximum of surface-dwelling opportunistic coccolithophore species (i.e. *Gephyrocapsa oceanica* and *Emiliania huxleyi*) during the fall event at M4, consistent with nutrient enrichment in the surface waters in this area. The same authors attribute the sharp increase of these species, together with the high surface Chl-*a* concentration observed by satellites (Fig. 4), as partially due to the Amazon plume meandering northwards towards site M4 and mixing with open ocean waters.

5.2 Deep production through mixed-layer deepening

A similar switch in species composition towards a more opportunistic coccolithophore assemblage (i.e. increased coccolith fluxes of *E. huxleyi*), indicating a nutrient-replenishment in the euphotic zone, was also observed during spring 2013 at site M4 (Guerreiro et al., 2017). Oceanographic satellite data, however, do not show any clear freshwater input or changes in surface water Chl-*a* in advance of the peak flux collected in spring 2013 at M4, between April 13th and April 29th. Euphotic depth remained at around 100 m depth, while surface water Chl-*a* concentrations remained low as well, both indicating little change in primary productivity at the surface (Fig. 4, left) and suggesting that this ecological change in the coccolithophore assemblages occurred in the upper photic zone but below the surface (Guerreiro et al., 2017). In contrast to this apparently low productivity at the surface, we find a massive increase in the export fluxes of Chl-*a* (Fig. 7a) as well as in organic- and inorganic carbon (Fig. 5c, g), all arguing for a major pulse in upper-ocean productivity. Such blooms might be driven by nutrient input from the deep through eddy upwelling in the WENA as postulated by Longhurst (1993). Indeed, Sea Level Anomalies show an anticyclonic eddy nearing site M4 around mid-April 2013 (Video S2.2). However, such anticyclonic eddies are characterized by downwelling and conventionally supposed to have a low productive warm core, although Dufois et al. (2016) argue that anticyclonic eddies in the subtropical gyres are more productive by winter mixing than previously thought. Rather, we observe that SST starts to rise at the time of the spring peak (Fig. 4b), while Argo-float profiles show a deepening of the surface mixed layer from 80 to 92 m (Fig. 9). This deepening might be induced by strong winds resulting in a breakthrough of the nutricline, entraining sufficient nutrients in the euphotic zone to generate subsurface bloom conditions. Such a scenario would imply that nutrients have been rapidly assimilated at the bottom of the mixed layer depth but have been restrictedly moved upwards towards the surface affecting the opportunistic coccolithophore species, leading in particular to a drastic coccolith-flux

increase of the opportunistic calcareous nannoplankton species *Emiliania huxleyi* and a concomitant higher ratio of the upper zone dwellers to the lower zone dwellers (UPZ/LPZ), as observed by Guerreiro et al. (2017). However, the bloom hovered in the mixed layer invisible from space. The depth over which Chl-*a* can be detected will vary with water clarity and the presence of clouds which hamper visibility and influence the Chl-*a* concentration retrieval (Smith, 1981). Cloud coverage increased by the time of the spring peak and reached its maximum in summer 2013 when under the influence of the ITCZ (Guerreiro et al., 2017).

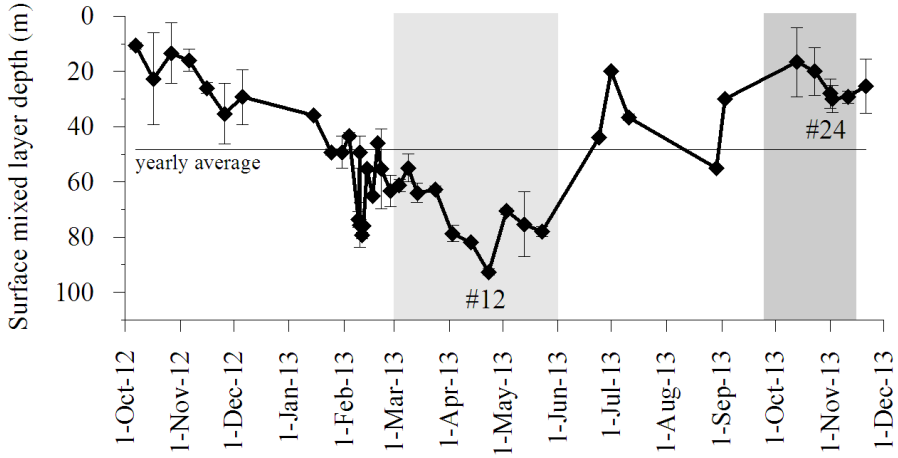

Figure 9. Depth of the surface mixed layer interpreted from the depth of consistent potential density, temperature and salinity of the Argo-float profiles (Fig. S1).

5.3 Saharan dust at M4

In addition to particle formation and nutrient input from the Amazon River and mixed-layer deepening, mineral dust from the Sahara Desert also contributes to the biological pump in the WENA. From the 182 Tg of dust leaving the coast of North Africa each year, 43 Tg of dust reach 75°W and 28 Tg are deposited into the Amazon Basin (Yu et al., 2015a, b). Actual Saharan dust deposition fluxes into the North Atlantic Ocean are still poorly constrained and differ from east and western Atlantic, giving average amounts between 2 and 18 g m^{-2} $year^{-1}$ (Honjo et al., 1982; Bory et al., 2002; Brust et al., 2011; Friese et al., 2017). However, best estimates of Saharan dust deposition fluxes in the Atlantic Ocean based on two consecutive years of sediment trap sampling along a transect from east to west, are in the order of 5 g m^{-2} $year^{-1}$ close to the coast of North Africa (12°N, 23°W) and decrease to around 1 g m^{-2} $year^{-1}$ at site M4 (Chapter 3). The deposited dust introduces both

bioavailable nutrients for phytoplankton growth (Jickells, 1999; Ridame et al., 2014) and lithogenic particles acting as ballasting material for settling organic matter aggregates (Klaas and Archer, 2002; Fischer et al., 2007; Armstrong et al., 2009). The dust-derived Fe supply plays an important role in relieving Fe-limitation of N_2-fixation in tropical surface waters and thereby increase the primary productivity in these areas (Mills et al., 2004; Jickells et al., 2014). At site M4 the Saharan dust deposition fluxes are positively correlated with the ratio of Chl-*a* to its degradation product and at the same time negatively correlated with the $\delta^{15}N$ (Fig. 7b), pointing to the interaction of Saharan dust promoting N_2-fixation and the production and export of phytoplankton. Guerreiro et al. (2017) attribute the above-mentioned switch from a typically tropical coccolithophore assemblage towards a more opportunistic and fast-blooming assemblage during the spring and fall peak in 2013 has been due to nutrient input by Saharan dust deposition. Considering the great distances to the dust sources (> 4000 km), relevant cloud processing acting on the dust's metal solubility during atmospheric transport is feasible (Spokes et al., 1994).

Transportation from the west African coast to the Caribbean takes around one week (Prospero et al., 1970; 2014) and deposits bioavailable nutrients to the ocean surface (Blain et al., 2004; Jickells et al., 2005; Guieu et al., 2010). However, deposition processes differed during this sampling time period, in as much as dry deposition was preferred during winter and spring, while increased precipitation from summer onwards, favored wet deposition during summer and fall (Fig. 4b). Ridame et al. (2014) showed that in the Mediterranean Sea dry and wet Saharan dust deposition events induced contrasting responses of the phytoplankton community due to differences in the atmospheric supply of bioavailable nutrients with nutrients deposited by wet dust deposition being more bioavailable than the nutrients deposited by dry dust deposition. Primary production and biomass increased ~2 fold after wet deposition events, while no changes were observed a dry deposition event (Ridame et al., 2014). Applying these findings to a linear regression of the Saharan dust deposition fluxes to the organic carbon fluxes at site M4, it reveals that the correlation between dust and organic carbon fluxes is higher during times of increased precipitation (summer and fall) ($r = 0.92$, $p < 0.01$) than during times of low precipitation (winter and spring) when the correlation is lower and less significant ($r = 0.62$, $p < 0.05$). The exported biomass of the two deposition events, however, was with around 5 mg m^{-2} d^{-1} very similar, although in spring and fall, the organic carbon values exceeded 15 and 25 mg m^{-2} d^{-1}, respectively. Therefore, it seems logical to argue that production of phytoplankton and the switch in coccolithophore assemblage might be co-triggered by Saharan dust deposition, especially in fall when precipitation rates

are high.

In addition to fertilization, the linear correlations of dust deposition fluxes and organic carbon, and rather all bulk biogenic components (Fig. S4, Table S1) point to the interacting ballasting effect of all these components, which is also shown by the higher ratio of Chl-*a* to its degradation product combined with enhanced dust input (Fig. 7b). The latter one indicates accelerating particle settling and also implies less degradation of the biomass with enhanced dust deposition since the high ratio of Chl-*a* to its degradation product assess the extent of degradation of the algal organic carbon (Boon and Duineveld, 1996). In terms of carbon sequestration our data shows that Saharan dust deposition impacts the biological pump in the WENA even with or without fertilization since the dust is important to transport biogenic particles to the deep. This is in good agreement with Pabortsava et al. (2017) arguing that Saharan dust enhances carbon sequestration in the central northern gyre of the Atlantic Ocean, whereas carbon sequestration is hampered by little dust contribution in the southern gyre of the Atlantic Ocean.

6 Conclusions

Particle fluxes from three sediment traps at two mooring sites in the Western Equatorial North Atlantic (WENA) were compared with satellite data and *in-situ* profiles to trace their source. Productivity appeared to be stimulated by several processes including Amazon River discharge, Saharan-dust deposition, nitrogen fixation by marine diazotrophs and mixed-layer deepening. In the more oligotrophic region at 49°W, mixed-layer deepening introduced nutrients from below the nutricline in spring, triggering a carbonate-rich peak export, which is different to a biogenic silica-rich peak in fall when particle fluxes were induced by the Amazon River. Amazon River discharge carried by the retroflecting North Brazil Current into the North Equatorial Counter Current as far east as 49°W led to a peak flux in fall 2013, stimulating nitrogen fixation and diatom diazotrophic associations, possibly enhanced by Fe input from wet deposition of Saharan dust. Saharan dust deposition led to a high correlation to organic carbon fluxes during times of wet deposition and interacted with biogenic particles accelerating particle settling. At the westernmost site at 57°W, where lithogenic particles are a mixture of Saharan dust and resuspended sediment from the sea floor, the Amazon influence generated high export fluxes throughout summer, with increased biogenic-silica fluxes relative to organic and inorganic carbon. At both sampling sites, higher rain ratios of biogenic silica to inorganic carbon indicate a more efficient removal of CO_2 by the biological

pump during times of Amazon influence, although Saharan dust deposition also influenced particle export to the deep, by effecting the biological pump.

Acknowledegments

This project is funded by the ERC (project no. 311152) and NWO (project no. 822.01.008). We acknowledge NIOZ technicians, captains and their crews for their assistance during cruises *Meteor* M89 and *Pelagia* 64PE378. We thank Jort Ossebaar for helping with the EA-IRMS analysis, Sharyn Ossebaar for assisting with biogenic silica measurements, and Evaline van Weerlee for UPLC-measurements. Carolina Sá (MARE, University of Lisbon, Portugal) is thanked for downloading and processing of the satellite data.

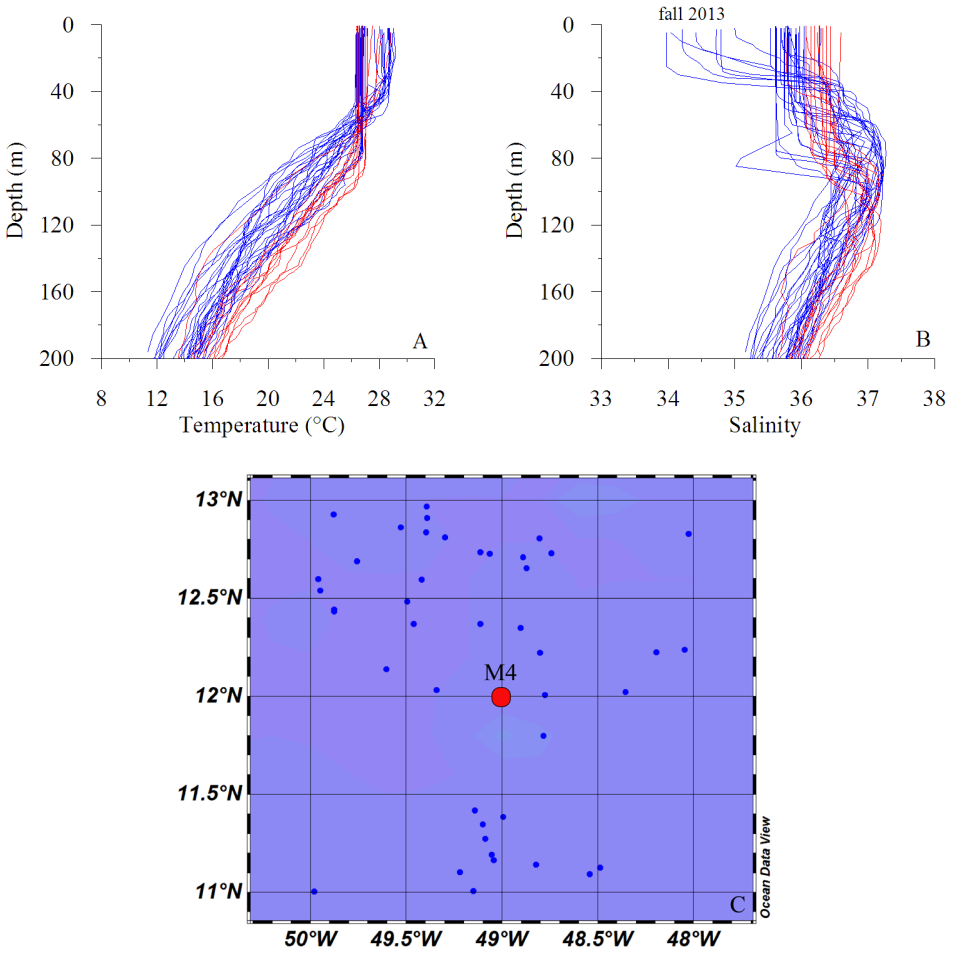

Figure S1. Argo-float profiles around mooring site M4 from October 2012 to November 2013, with summer in red and winter in blue. A) Temperature, B) Salinity, C) Locations of Argo floats at the surface.

S2. Video animations

S2.1 Sea Surface Salinity overlapped by absolute geostrophic velocity.
https://youtu.be/3wSNWlwI2rY

Daily images (September 1st 2012 to December 1st 2013) of Sea Surface Salinity (SSS) estimated from satellite (Aquarius mission) observations (contours), overlapped by the absolute geostrophic velocity (black vectors) calculated from altimeter satellite data (Aviso product) for the Western Equatorial North Atlantic (WENA) region. The blue and red lines displayed in the inset panel represent the time evolution of SSS at the locations of M5 (blue circle) and M4 (red square) moorings, respectively.

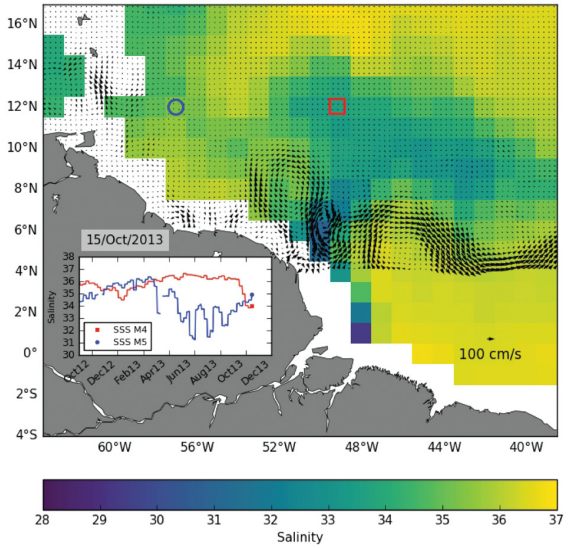

S2.2 Sea Level Anomaly overlapped by respective geostrophic velocity anomaly.
https://youtu.be/zz7X1MrpdBY

Daily images (September 1st 2012 to December 1st 2013) of Sea Level Anomaly (SLA; contours) from satellite altimeter data (Aviso product) overlapped by the respective anomaly geostrophic velocity (black vectors) for the Western Equatorial North Atlantic (WENA) region. The blue and red lines displayed in the inset panel represent the time evolution of SLA at the locations of M5 (blue circle) and M4 (red square) moorings, respectively.

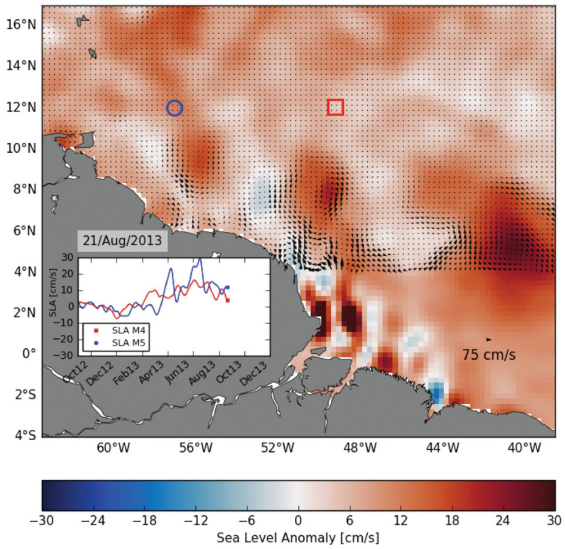

S2.3 Ekman Vertical Velocity. https://youtu.be/snEOmwXOjPA

Daily fields of Ekman Vertical Velocity (WE) computed from satellite scatterometer wind data (ASCAT product). Shades of green and red represent positive (upward) and negative (downward) velocities, respectively. The blue and red lines displayed in the inset panel represent the time evolution of WE at the locations of M5 (blue circle) and M4 (red square) moorings, respectively. The images span from September 1st 2012 to December 1st 2013, covering the deployment period of the sediment traps.

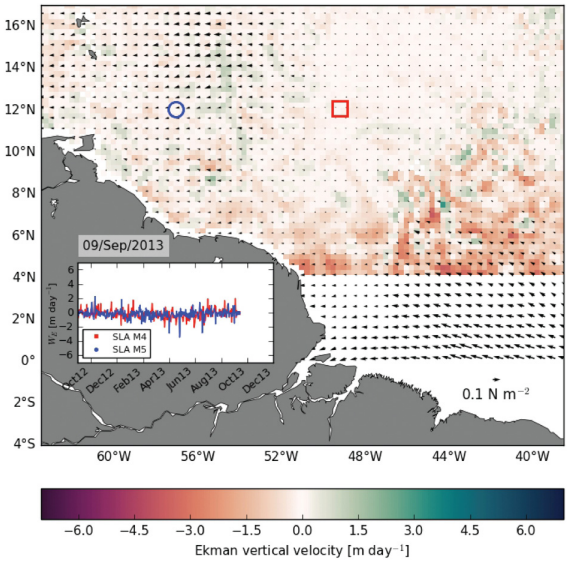

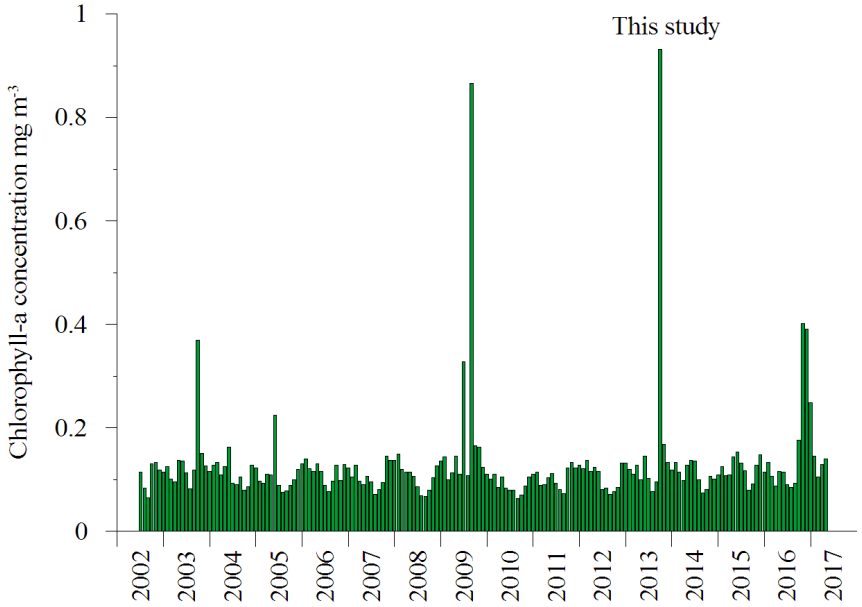

Figure S3. Satellite derived surface water chlorophyll-*a* concentrations between 2002 and 2017 at 12°N, 49°W (station M4).

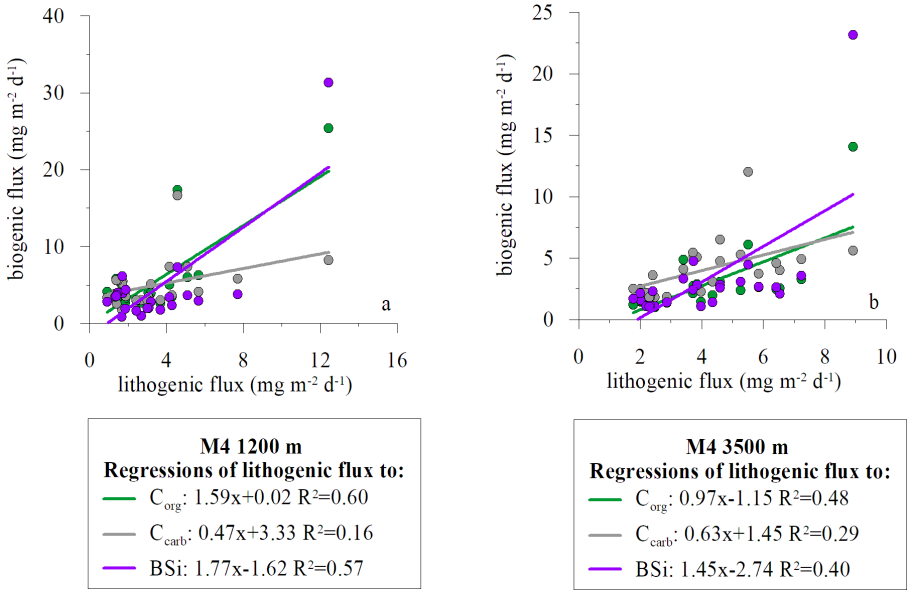

Figure S4. Linear regression of particle fluxes M4 U (left) and M4 L (right).

Table S1. Linear regression coefficients (Pearson) of particle fluxes M4 U (left) and M4 L (right). Upper right corner *p*-values, lower left corner correlation coefficient r. If $p < 0.01$, r is given in bold.

M4 1200 m	C_{carb}	BSi	C_{org}	Dust
C_{carb}		0.04	0.00	0.05
BSi	0.41		0.00	0.00
C_{org}	**0.71**	**0.89**		0.00
Dust	0.40	**0.75**	**0.77**	

M4 3500 m	C_{carb}	BSi	C_{org}	Dust
C_{carb}		0.12	0.01	0.01
BSi	0.33		0.00	0.00
C_{org}	**0.52**	**0.95**		0.00
Dust	**0.54**	**0.63**	**0.69**	

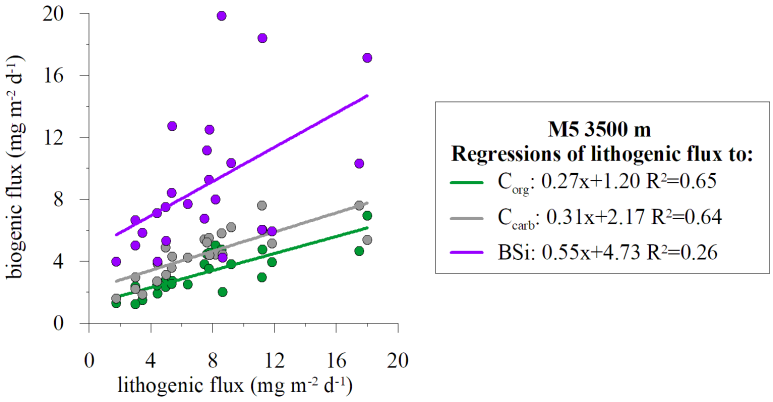

Figure S5. Linear regression of particle fluxes M5 L.

Table S2. Linear regression coefficients (Pearson) of particle fluxes M5 L. Upper right corner *p*-values, lower left corner correlation coefficient r. If $p < 0.01$, r is given in bold.

M5 3500 m	C_{carb}	BSi	C_{org}	Dust
C_{carb}		0.02	0.00	0.02
BSi	0.47		0.00	0.01
C_{org}	**0.65**	**0.75**		0.00
Dust	0.47	0.51	**0.75**	

CHAPTER 6

Mineral dust ballasting from the Saharan dust plume increases the export efficiency of organic matter in the North Atlantic Ocean

Laura F. Korte, Morten H. Iversen, Geert-Jan A. Brummer, Johannes A. van Hateren, Monica C. A. Martens, Katharina Wetterauer, Michèlle van der Does, Jan-Berend W. Stuut

in preparation for Deep Sea Research

Abstract

Export of organic matter from the surface towards the deep ocean is an important pathway for sequestration of atmospheric carbon dioxide (CO_2). Export efficiency of organic matter is increased when ballast material, such as mineral dust, is incorporated into settling aggregates. After atmospheric dust deposition into the surface ocean, dust particles are thought to play an important part in marine snow aggregation increasing their specific density and settling velocity, and thus decrease the duration of for organic matter degradation in the upper ocean. This hypothesis was tested in contrasting environmental conditions across the equatorial North Atlantic Ocean. We used free drifting sediment traps deployed at 100, 200 and 400 m water depths during two research cruises (64PE395 and JC134) in 2015 and 2016. In addition, aerosol samples were collected at the same time for direct comparison between atmospheric dust concentrations, dust deposition into the surface ocean, and export fluxes to the deep ocean.

Molar C/N ratios were used as a proxy for degradation of organic matter. In 2015, we observed constant C/N ratios of 8.1 within the upper 400 m depth during periods with high dust deposition in the eastern Atlantic close to the African coast at 12°N, 23°W. Contrastingly, molar C/N ratios were lower in the western Atlantic and increased with depth when atmospheric dust concentration and deposition was low. Lowest C/N ratios of 5.6 were observed at 12°N, 49°W at 100 m, while they increased to 6.4 at 400 m depth. In 2016, when atmospheric dust concentrations were lower than in 2015, molar C/N ratios differed with depth and were highest (9.5) in the upwelling area off Cape Blanc. It is possible that biological processes such as fecal pellet production, or lateral advection by nepheloid layers, especially off Cape Blanc closest to the African coast, influenced the molar C/N ratios. Yet, our results indicate that Saharan dust deposition may play a key role in ballasting organic matter through the water column and impact its export efficiency and carbon sequestration by reducing its time for microbial degradation.

Keywords: Ballasting, Saharan dust, Drifting traps, Organic matter (OM), C/N ratios, Redfield ratio

1 Introduction

The export of photosynthetically fixed organic carbon towards the deep ocean is an important process to lower CO_2 in oceanic surface waters (Francois et al., 2002; Rixen et al., 2005). However, for this export, organic matter (OM) needs additional ballast material like biogenic and lithogenic particles to sink to the sea floor (Ittekkot and Haake, 1990; Klaas and Archer, 2002; Armstrong et al., 2009). The formation of dense marine snow aggregates that are a combination of OM and ballast particles sink faster than non-ballasted aggregates (Fowler and Knauer, 1986; Alldredge and Silver, 1988; Iversen and Ploug, 2010). Ballasting of OM by biogenic calcium carbonate and opal is observed in the open ocean with carbonate ballasting being more efficient and mainly occurring in the low latitude oceans (Honjo et al., 1995; Francois et al., 2002). Ballasting by biogenic opal is observed to be less efficient and dominates in the high latitude oceans (Francois et al., 2002). The effect of lithogenic particles is less clear due to their relatively low contribution to the total mass flux in the open ocean (Francois et al., 2002). However, along the coasts, lithogenic input by lateral advection (Karakaş et al., 2006; Fischer et al., 2009), large river discharge and high aeolian dust input clearly accelerate OM export to the deep (Ittekkot, 1991; 1992; Ratmeyer et al., 1999a; Neuer et al., 2004; Rixen et al., 2005; Fischer and Karakas, 2009; Nowald et al., 2015; Van der Jagt et al., 2018). Aeolian dust inputs are particularly high off northern Africa, with the Sahara; the largest desert on Earth. The contribution from Saharan dust to the total mass flux measured at 1200 m depth in the North Atlantic Ocean along a transect at 12°N varies between 12 % close to the coast at 23°W, and 4 % at 49°W (Chapter 3), but may contribute to more than a third of the total mass flux closer to the northwest African coast (Wefer and Fischer, 1993; Bory and Newton, 2000; Fischer et al., 2007).

As global annual mean, marine primary producers have a molar C/N ratio of 6.625 corresponding to the '*Redfield ratio*' of 106 C : 16 N (Redfield, 1958). However, C/N ratios below Redfield are found during primary production in environments when excess nitrogen and phosphorus is available (Droop, 1973; Roelke et al., 1999), while C/N ratios higher than Redfield are observed during nutrient limitation (Gervais and Riebesell, 2001). Since microbial degradation preferentially utilize nitrogen over carbon, deviations from Redfield with higher C/N ratios occur as a result of degradation processes with time (Gordon, 1971; Anadón et al., 2002; Schneider et al., 2003). Therefore, the duration for microbial degradation in the surface ocean will determine how much the C/N ratios in settling aggregates will deviate from the ratios at the time of production. Hence, if there is high ballasting of the settling aggregates,

the initial C/N ratio should not vary dramatically with increasing depth. To test this hypothesis, we use the molar C/N ratios as a proxy for the extent of degradation and assume that less degradation, thus quasi constant C/N, occurs in aggregates ballasted especially by Saharan dust. In addition to the ballast theory, ballast minerals might also protect the OM physically from degradation (Armstrong et al., 2001) while terrigenous organic material attached to lithogenic particles might increase the C/N ratio (Schneider et al., 2003). However, this protection process was not observed in experimental tests with, for example, smectite (Iversen and Robert, 2015) which is an important clay mineral in Saharan dust (Avila et al., 1996). It seems more likely that Saharan dust enhances formation of aggregates with higher size-specific sinking velocities compared to situations with low dust deposition (Van der Jagt et al., 2018). This suggests that Saharan dust deposition increases the sinking velocities of OM and thereby decreases the duration of degradation in the water column, i.e. more efficient OM export.

For this study, we used *in-situ* free drifting sediment traps together with simultaneous aerosol sampling to study the impact of dust deposition on the *in-situ* export of OM. The drifting traps were deployed at multiple sites along a transect from northwest Africa to the Caribbean, while atmospheric aerosol sampling was performed continuously during two cruises (Stuut et al., 2015; 2016). This transect allows for studying the ballasting effects on OM export at different proximities to the Saharan sources and contrasting marine environmental conditions, with an upwelling area in the eastern Atlantic and oligotrophic conditions along the transect, and seasonal Amazon River influence in the western Atlantic. We evaluated the molar C/N ratios of the exported material in combination with atmospheric dust concentrations, which in turn were compared to satellite images and satellite-derived aerosol optical depth (AOD).

2 Material

2.1 Marine particle sampling

Settling aggregates were collected by free floating drifting traps (DTs) at five sites (M1-M5) during *RV Pelagia* cruise 64PE395 from January to February 2015, and at five sites (CB, M1, M3, M4, and M5) during *RRS James Cook* cruise JC134 from March to April 2016. The DTs consisted of four gyroscopically mounted Perspex tubes with a volume of about 6 L, at three trap depths of 100, 200 and 400 m. Only at site M3 during JC134 they were deployed at 45, 75, and 175 m depth. A

weight of 35 kg kept the entire DT array upright in the water during deployment (Fig. 1).

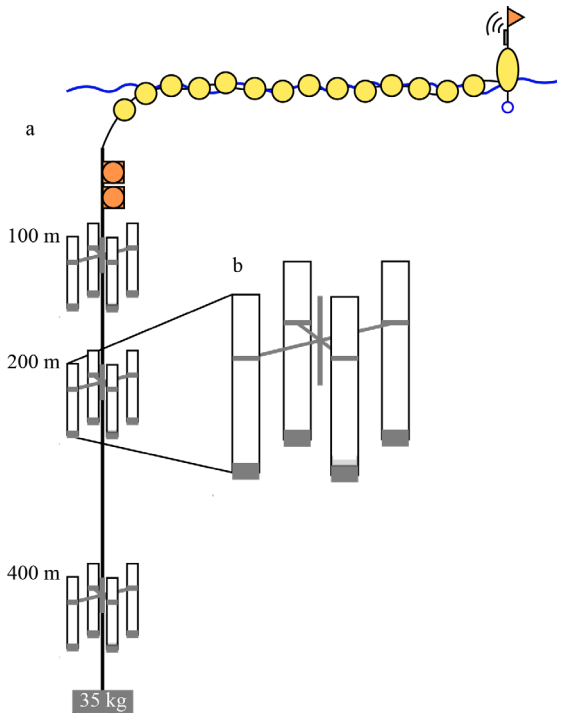

Figure 1. Schematic overview of drifting traps. a) Mooring as it floats in the water. b) Closeup of one set of traps with the four Perspex tubes gyroscopically mounted with bottom weights for vertical alignment during deployment. One of the four trap tubes of each set was equipped with a petri dish containing a viscous gel.

At the top of the DT array a series of floats was added, of which the last contained a flashing light and an Iridium beacon that sent the DT positions every 15 min via email. Prior to deployment, the Perspex tubes were filled with filtered seawater (0.4 µm cellulose acetate membrane) from the deployment area, which was densified with Borax ($Na_2B_4O_7 \cdot 10H_2O$, first deployment only) and later with table salt (NaCl) to prevent exchange with the ambient seawater during deployment. One tube held a petri dish at the bottom, filled with gel (polyvinyl alcohol and carbowax) that preserved the shape and structure of the collected particles. At all sites the upper trap depth was below the deep chlorophyll maximum (DCM), except at station M3 during JC134. Here depths of 45, 75 and 175 m were chosen because of an immediate dust event, which was now sampled at a higher vertical resolution. The DTs floated freely in the ocean for 24 hours, except at station M3 during JC134 when the DTs were only

deployed for 15 hours. After recovery, the collected particles in the tubes settled for a minimum of 5 hours after which most of the water was removed by siphoning gently, until about 1.5 L was left containing the material of interest. The water from the gel-tube was removed entirely since all particles of interest were embedded in the gel. The remaining water of the three tubes without the gel was filtered separately for later analysis of molar C/N ratios using a muffled GF/F filter (47 mm, 0.7 µm mean pore size) and for Saharan dust grain sizes using a polycarbonate filter (47 mm, 0.4 µm pore size). The gel cups were used to determine the size-distribution and abundance of marine snow. Until analysis, gels and GF/F filters were frozen at -20°C, while the polycarbonate filters for grain-size analyses were stored dark and refrigerated at 4°C.

2.2 Aerosol sampling

Aerosol sampling was performed on board using an Anderson high-volume dust collector which was mounted on the deck above the bridge of the ship. The aerosol dust collector held a rectangular cellulose acetate filter (203 x 254 mm, 0.4 µm pore size) from which cuttings were used for analyzing aerosol grain-size distributions and dust concentrations in the atmosphere. The dust collector was protected by a rain cover and equipped with a motor sucking in ambient air through the filter at a rate of about 1100 L/min. The air volume that passed through the filters was monitored and recorded, and the dust collector automatically adapted the suction to a constant air flow compensating for filter clogging. A wind vane that was connected to the dust collector which switched the dust collector on when wind was coming from a predetermined arc (-90° to +90°) from the front of the ship. If the wind vane detected wind from another direction, the dust collector turned off immediately to prevent contamination from the ship's chimney. Filters were changed daily (~24 hours), or after several hours during a dust event and stored at room temperature.

2.3 CTD profiles

Conductivity, temperature, and depth (CTD) profiles were taken during both cruises to determine the physical oceanographic parameters. A Seabird CTD was attached to a rosette of 24 Niskin bottles (10 L each) which were used to collect water for the DTs and for nutrient analysis (NO_3, PO_4, $Si(OH)_4$) at specific depths during both cruises. Dissolved inorganic carbon (DIC) samples were taken at selected locations during cruise 64PE395 in 2015.

2.4 Satellite data

For investigation of the atmospheric conditions during both cruises, aerosol optical depth (AOD) values were obtained from the Giovanni online data system, developed and maintained by the NASA Goddard Earth Sciences Data and Information Services Center (GES DISC). Daily AOD values at 550 nm extinction from MODIS Aqua were used for specific cruise sections. At the stations, a box of 2°×2° around the deployment of the DT was studied, while during transit time the east-west boxes varied between 4° to 10° and the north-south boxes remained at 2°. In addition to AOD values, true color satellite images were downloaded from EOSDIS Worldview (worldview.earthdata.nasa.gov) to detect dust in the atmosphere.

3 Methods

3.1 C/N analysis

The GF/F filters were cut in quarters, freeze dried and weighed for those filters that were pre-weighed (cruise JC134). To remove the inorganic carbon, the filter quarters were acid fumed (HCl conc.) overnight and treated with a few drops of HCl (2 M) the next day to assure full removal of carbonates. After drying, the filter quarters were folded into tin capsules and analyzed using a Thermo-Interscience Flash EA112 Series NC analyzer with a detection limit of 100 ppm and a precision of 0.3 % at the NIOZ. An international verified standard (Acetanilide) was used to evaluate carbon and nitrogen content in the samples.

3.2 Gel cups

The gel cups of cruise 64PE395 were photographed for identification of marine snow particles. The gels were placed on a luminous plate and approximately 13 overlaying pictures were taken. The photos were stitched to one image using the Hugin panorama stitching program (Fig. S2). Unfortunately, the first gel cups at M1 from 100 and 200 m depth became opaque due to a chemical reaction between the borax and the gel, although the gel from 400 m water depth stayed clear. The subsequent DT deployments had their brine solution made with table salt and the recovered gels stayed clear and could be used for further examination.

3.3 Grain size and dust concentration analysis

Particle-size analysis on the lithogenic fraction was performed using a Coulter laser diffraction particle sizer (LS13 320) with a micro liquid module for small-volume samples. To isolate the terrigenous fraction, all marine biogenic particles, including organic matter, biogenic carbonates and biogenic opal, from the polycarbonate filters of the DTs were removed chemically using a sequential procedure (McGregor et al., 2009; Van der Does et al., 2016). In short, the filter and the organics were ashed for several hours in a Low Temperature Asher (Tracer Lab Low Temperature Asher, Model LTA 600) and the remaining sample was transferred to a glass beaker in which it was treated with HCl (10 %) to remove the biogenic calcium carbonates and subsequently with NaOH pellets to dissolve the biogenic opal. Immediately prior to analysis a few drops of 1 M sodium pyrophosphate ($Na_4P_2O_7 \cdot 10H_2O$) was added to ensure disaggregation of particles. During analysis, a magnetic stirrer homogenized the samples.

For grain-size analysis of the aerosol samples from the dust collector, four circles were cut out of each filter and weighed on a micro balance (cruise 64PE395). Subsequently, the filters were ashed in a Low Temperature Asher for several hours to remove the organic matrix from the filters. After ashing, the dust from one filter was used for grain size analysis without further chemical treatment. The residual dust from the other circles was transferred into pre-weighed glass bottles (cruise 64PE395) or filtered over a pre-weighed polycarbonate filter (0.4 µm pore size), dried and weighed again for dust mass (cruise JC134). For the dust concentration, the dust mass on the filter cuts was extrapolated to the entire rectangular filter and divided by the total flow of air that passed through the filter.

3.4 Nutrient and DIC analysis

Nutrient samples were filtered through 0.2 µm acrodisc filters and stored frozen at -20°C for nitrogen and phosphorous (NO_3, PO_4) and cooled at +4°C for silicate ($Si(OH)_4$) analyses. Nutrients were analyzed colorimetrically by an QuAAtro Continuous Flow Analyser (Murphy and Riley, 1962; Strickland and Parsons, 1972; Grasshoff et al., 1983). The samples for DIC analyses were fixed with 10 µL concentrated $HgCl_2$ and kept at room temperature. DIC was analyzed spectrophotometrically by a Traacs 800 autoanalyzer after the method of Stoll et al. (2001).

4 Results

4.1 Cruise 64PE395 (2015)

4.1.1 Dust concentrations and satellite data

Already in the port of Mindelo on the island of São Vicente in Cape Verde (16.9°N, 25.0°W), from where the *Pelagia* set sail for cruise 64PE395, dust was present in the atmosphere from January 11th 2015 onwards (Fig. 2b). This dust event accompanied the ship's cruise track for two days south until January 13th prior to arrival at site M1. Thereafter, the air cleared up steadily while the ship sailed westward until January 18th. The atmospheric dust loading as derived from AOD during 64PE395 corresponds well with our *in-situ* observations of dust concentration (Fig. 2a).

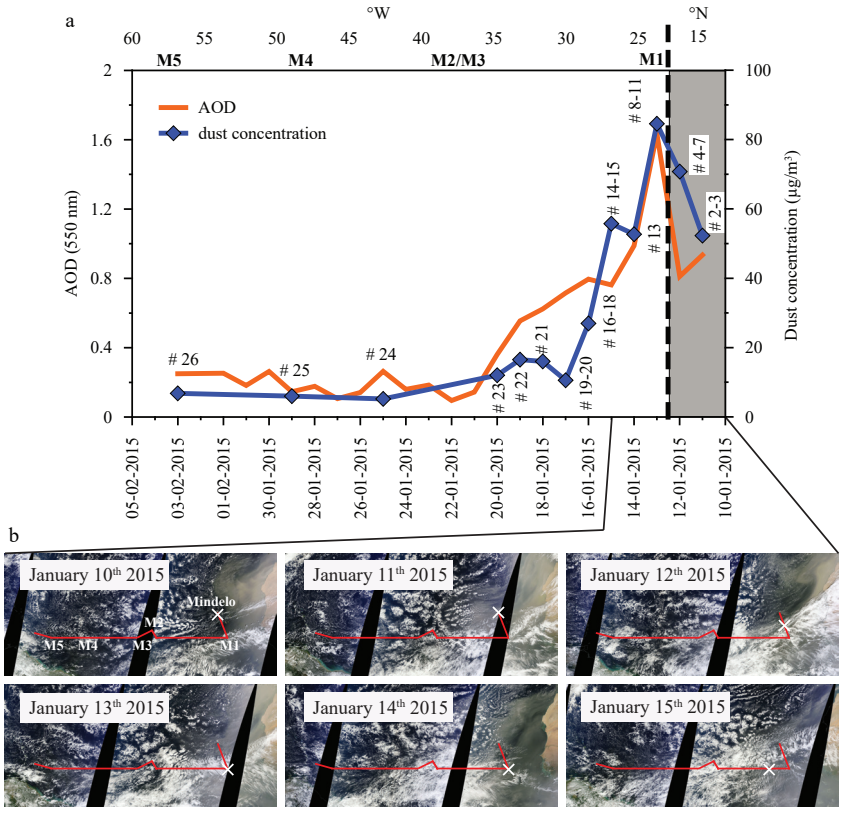

Figure 2. a) Averaged measured dust concentrations from the dust filters (# 1-26) and AOD values along the 64PE395 transect. Grey shaded area presents the NNW-SSE transect. b) Satellite images (EOSDIS Worldview NASA) showing the dust event in 2015 from January 10th to January 15th propagating over the eastern Atlantic Ocean. Red line indicates 64PE395 cruise track and sampling stations are indicated in image of January 10th, 2015. The ship's position is marked with the cross.

Aerosol sampling showed highest dust concentrations along the North African coast with maximum concentrations at station M1 (# 8-11) and decreasing concentrations downwind from east to west along the transect. Concentrations varied between 50 and 104 µg/m^3 along the NNW-SSE profile and decreased along the E-W transect from >100 µg/m^3 at M1 to around 5 µg/m^3 at M5 (Table S1). The AOD values increased from 0.9 on January 11th to a maximum of 1.6 on January 13th at station M1 (12°N, 23°W). Satellite images clearly show the dust event off northwest Africa (Fig. 2b). After the dust event, AOD values stayed relatively high around 0.7 during transit (27°W-35° W) from January 15th to January 18th and subsequently decreased to 0.2 during the rest of the cruise between site M2/M3 to M5 in the west.

4.1.2 Grain-size distributions

The aerosol samples showed fine-grained, but well-sorted particles mainly between 0.4 and 20 µm (Fig. 3a). The average modal grain size was 4 µm. Samples collected parallel to the northwest African coast were better sorted (F #1-11, #13-20) than in the west along the E-W transect (F #21-26). The latter showed a coarser shoulder in the distributions with particle sizes up to 50 µm. These coarse grain sizes are also reflected in the mean grain size of the atmospheric samples, which is coarser is the west than in the east (Fig. 3b).

The particles collected by the DTs were coarser-grained than those collected by atmospheric sampling. However, some distributions showed sharp peaks indicating a low amount of sample material, therefore the distributions from the three depths were averaged, while distributions at M4 could not be measured due to insufficient sample material (data not shown). The averaged grain-size distributions varied mainly between 0.4 and 50 µm, with a unimodal distribution at M1 and multimodal distribution at M5 (Fig. 3a). Despite the distribution at M1 is shifted to the coarser-grained sizes, its shape is comparable to the atmospheric samples, especially #1-11 and #13-20. Along the transect at 12°N, the mean grain sizes showed a fining trend along 12°N at 100 m depth with coarsest particles (9.9 µm) at M1 and finer ones (8.7 µm) at M5, while at 100 m depth to the north of the transect at 13.5°N, the finest particles (7.7 µm) were found at M2 (Fig. 3b). At 400 m depth, mean grain sizes decreased slightly at M1 (8.3 µm) and M3 (7.6 µm), and significantly at M5 (3.7 µm).

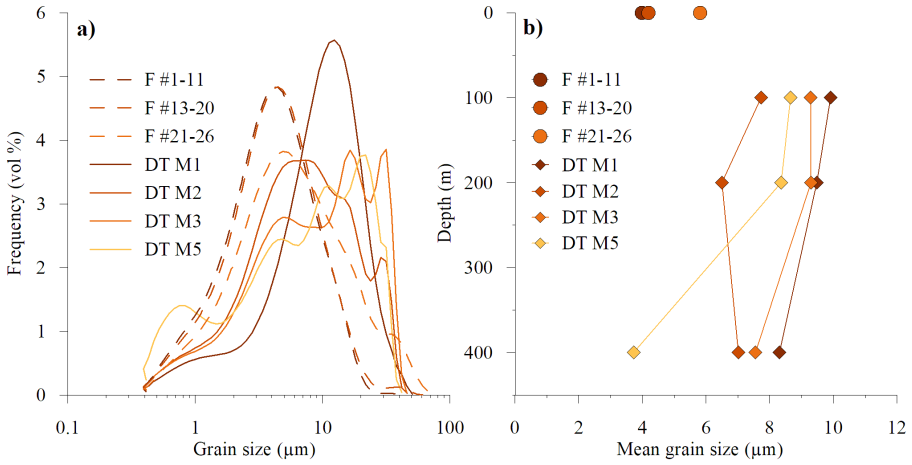

Figure 3. a) Averaged grain-size distributions of the dust filters (F) and of Saharan dust in the export flux from the DTs deployed in 2015 (cruise 64PE395) at four stations along the transect. Samples from M4 are missing due to insufficient sample material for analysis. b) Mean grain sizes as a function of depth from the drifting traps and the shipboard sampled dust filters at 0 m.

4.1.3 CTD profiles and DIC

Along the transect CTD profiles showed the depth of the deep chlorophyll maximum (DCM) as a clear band in the top 100 m, identified by the highest fluorescence concentrations in the surface waters (Fig. 4a). In January 2015, fluorescence concentrations in the DCM varied between 0.15 and 0.3 µg/L, reaching a maximum at 29°W. Surface waters and waters below the DCM showed low values of 0.05 µg/L. DIC concentrations along the transect showed a slight increasingly depletion from east to west in the surface waters, where most primary production takes place, and a rapid increase to similar concentrations with depth below the DCM (Fig. 4b). In the eastern part of the Atlantic, surface DIC concentrations were around 2090 µmol/L, while in the western part surface DIC values started were 2040 µmol/L. At 300 m water depth DIC values increased to around 2260 µmol/L at all stations but showed a divergence at 400 m water depth. Along with the DCM, nutrient analyses showed a deepening of the nutricline towards the west (Fig. S1), forced by the wind (Guerreiro et al., 2018, submitted).

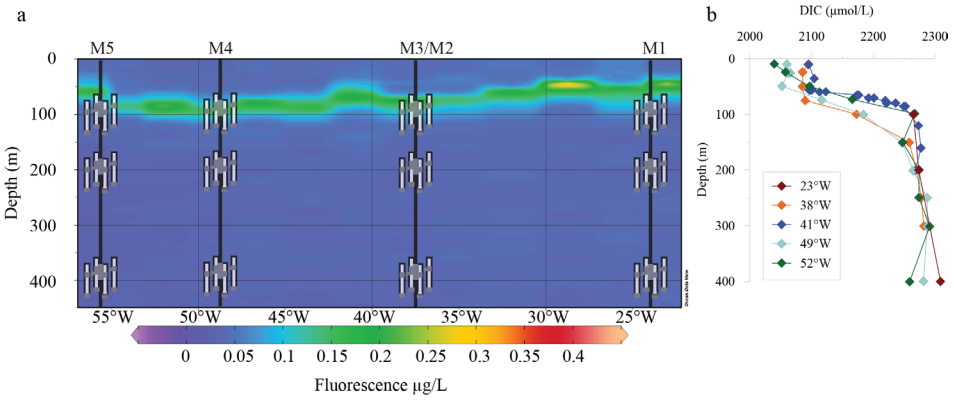

Figure 4. a) DT deployed at the five stations and fluorescence concentrations in the surface waters showing the depth of the DCM along the transect as a clear band between 50 m and 100 m water depth. b) Dissolved inorganic carbon concentrations (DIC) at various longitudes along the transect at 12°N during 64PE395 cruise.

4.1.4 Gels

Marine snow, as well as zooplankton molds and fecal pellets were collected in the gels of the DTs (Fig. S2). While smaller and lighter particles remained in the upper part of the gel, larger and heavier particles penetrated deeper into the gel or settled to the bottom of the cup. Figure 5 shows parts of the gels containing trapped material. The trapped particles showed a clear depth gradient at each site as well as spatial variation between the sampling sites. While most material at the inner stations, M2 and M4, was captured at 100 m water depth, most material at M5 was captured at 400 m water depth. Spatially, most material was trapped closest to both the African and South American continent, at station M1 (400 m) and M5, respectively.

The stations M2 and M4 in the central Atlantic yielded less material with M4 showing the least particles captured. While all stations captured marine snow, zooplankton, e.g. individual foraminifera, was most abundant at the inner stations M2 and M4, and fecal pellets were mostly captured at M2, followed by M1 and absent at M5. The marine snow particles at M5 were up to 5 mm in size and therefore the largest particles found. These particles differed in appearance from particles found at the other stations and were green to yellowish green. At M1, M2, and M4 the particles were green-brown to dark brown and smaller in size. Here, the marine snow particle sizes ranged between 1 and 2 mm in diameter.

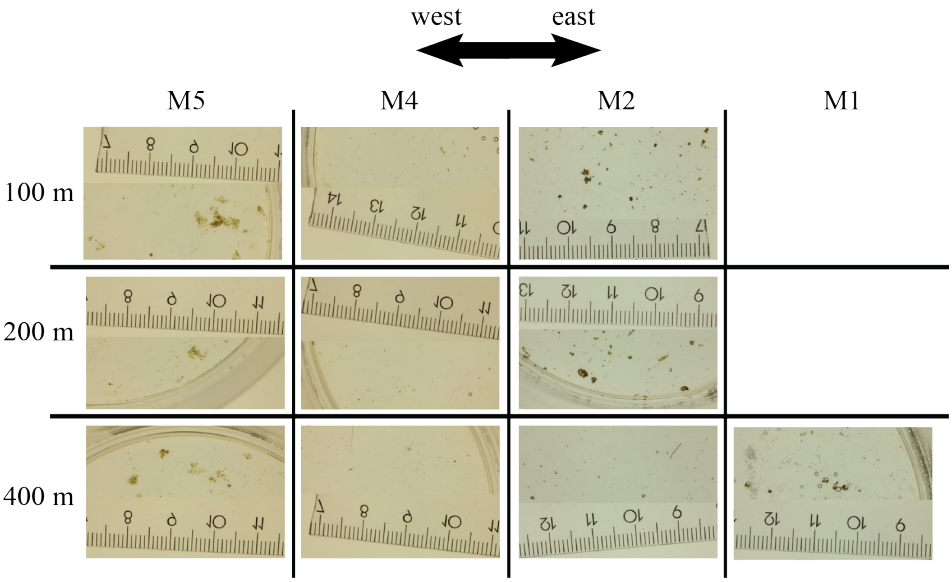

Figure 5. Images of the particles trapped in the gel cups along the 64PE395 transect. The gels at M1 100 m and 200 m turned opaque and are therefore not shown. Complete stitches are presented in Fig. S2.

4.1.5 Molar C/N ratios

The molar C/N ratio provides information about the degradation state of the OM, since nitrogen is often preferentially degraded over carbon (Schneider et al., 2003). We therefore used C/N ratios as an indicator for OM degradation of the marine snow collected by the DTs, with increased C/N ratios as a proxy for stronger degradation compared to lower C/N ratios. The average molar C/N ratios along the transect at 12°N in January and February 2015 showed an overall decrease from 8.1 in the east at station M1 to 5.7 at station M4, and subsequently an increase to 7.2 at the westernmost station M5. At all stations molar C/N ratios are higher than the Redfield ratio, except at station M4 and at 100 m at station M2 (Fig. 6). At station M2 (at 13.5°N, 38°W), although the C/N ratio at 100 m was low, the average molar C/N ratio of the three depths was highest (8.2, Table 1). In the depth profiles, molar C/N ratios stayed rather constant at station M1 and M3, with a standard deviation of 0.03 and 0.08, respectively, while they increased with depth at station M2, M4, and M5 (Fig. 6). The steepest gradient was found at station M2 where molar C/N ratios increased from 6.3 at 100 m to 9.2 at 400 m (Fig. 6).

Table 1. Molar C/N ratios of material trapped by the DTs during 64PE395 cruise in 2015.

Molar C/N ratios	M5, 57°W	M4, 49°W	M3, 38°W	M2, 37°W	M1, 23°W
100 m	6.8	5.6	6.8	6.3	8.1
200 m	7.2	6.2	6.8	8.9	8.1
400 m	7.7	5.2	7.0	9.2	8.1
Average	7.2	5.7	6.9	8.2	8.1
Standard deviation (1 σ)	0.44	0.49	0.08	1.60	0.03

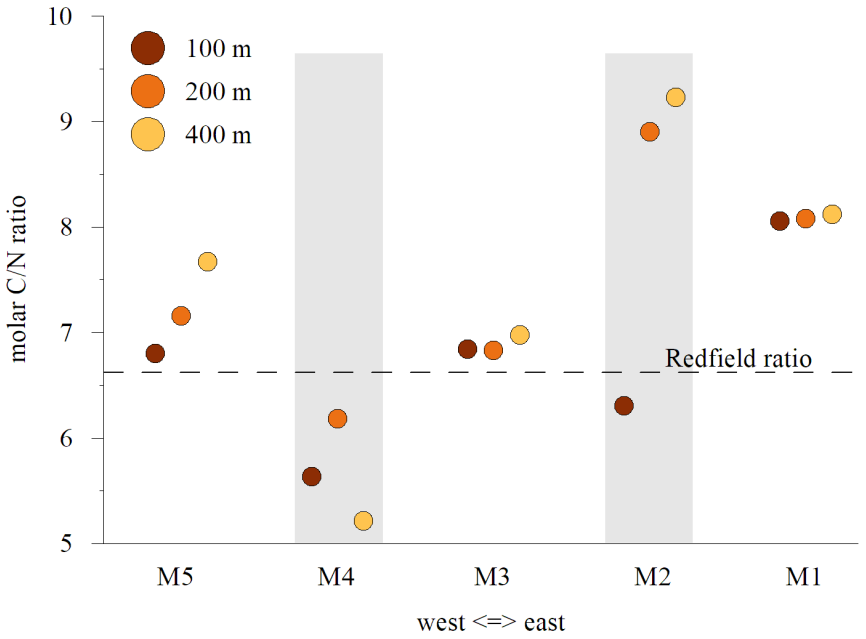

Figure 6. Molar C/N ratios of material collected by the DTs along the transect during 64PE395 cruise in 2015. Dashed line represents Redfield ratio of 6.625 (Redfield, 1958).

4.2 Cruise JC134 (2016)

4.2.1 Dust concentrations and satellite data

During cruise JC134 in March and April 2016, AOD values were lower than during cruise 64PE395, the year before, and the relation with the *in-situ* dust observations was less clear due to lack of dust observations. Average AOD values were 0.3 along the transect with a slight elevation to 0.5 around station M3 (38°W) and at M1 (23°W) from March 28th to March 31st and in early April, respectively

Fig. 7a). In late March, the air was observed to be hazy around the location of station M3 implying the presence of dust in the atmosphere, while at M1 the air was observed to be clear. Satellite images showed that dust left the African continent on March 27th and 28th and that it was transported over the Atlantic Ocean (Fig. 7b), although not obvious in color satellite images at station M3. Off Cape Blanc, although closer to the African coast, AOD values remained low in accordance with the absence of dust on satellite images.

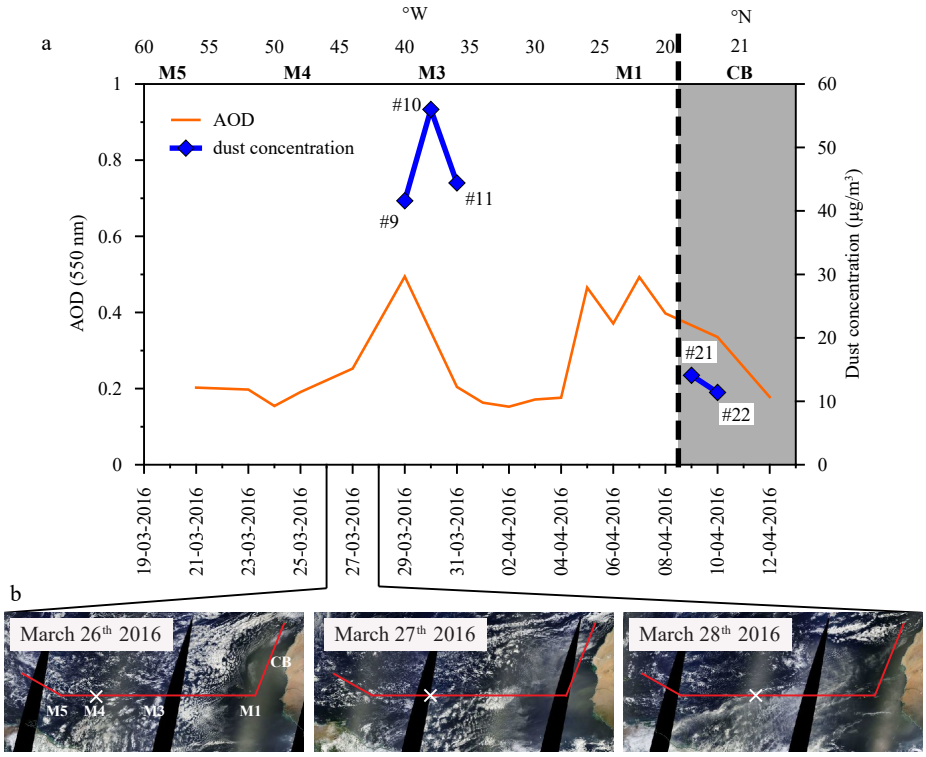

Figure 7. a) AOD values and dust concentrations in the atmosphere measured from the dust filters (# 9-11, 21-22). Grey shaded area represents the NE-SW part of the cruise track off Cape Blanc (CB), while the rest of the transect is E-W oriented. b) Satellite images (EOSDIS Worldview, NASA) showing dust leaving the African coast from March 27-28th 2016. The ship's position is marked with a cross. A dust event was encountered from March 29th to March 31st 2016 at M3 during cruise JC134. Diagonal lighter bands in the images are satellite artifacts.

Five filters (# 9, 10, 11, 21, and 22) from the aerosol sampler were used to determine dust concentrations in the atmosphere. All other filters contained too little sampling material. Three filters were chosen from the dust event (# 9, 10, and 11) around station M3 (March 29th to March 31st 2016) and two filters (# 21 and 22) off northwest

Africa (April 9th to April 11th 2016) when filters showed clear accumulation of dust. Dust concentrations showed large differences between the dust event and the non-dust period (Table S2). Dust concentrations of ~50 µg/m^3 were found during the dust event and around 12 µg/m^3 during low AOD periods off the coast of northwest Africa (Fig. 7a).

4.2.2 Grain sizes

All grain-size distributions from the aerosol sampler were well sorted and showed a unimodal distribution peaking at ~4 µm (Fig. 8a), similar to those found earlier in 2015 during cruise 64PE395. All distributions showed a coarse shoulder at ~35 µm. Grain sizes collected by the DTs during cruise JC134 in 2016 were coarser-grained than those of 64PE395 and varied between 0.4 and 270 µm (Fig. 8a). The averaged grain-size distributions were unimodal and similar at all stations and depths, except at M5 where it showed a deviation towards coarser particles. Moreover, in 2016, mean grain sizes displayed a less consistent pattern downwind, although there was still a downwind fining trend at 100 m water depth from 22.9 µm at M1 to 21.5 µm at M4 and 18.0 µm at M5 (Fig. 8b). However, at M5 the depth profile showed a coarsening of particles with water depth (Fig. 8b). At station M3, where dust was present in the atmosphere, the DTs were deployed at different depths and grain sizes were coarsest-grained with a mean of 47 µm. North of the transect at station CB (21°N), mean grain sizes were similar to those at station M5 but stayed rather uniform towards 400 m depth (Fig. 8b).

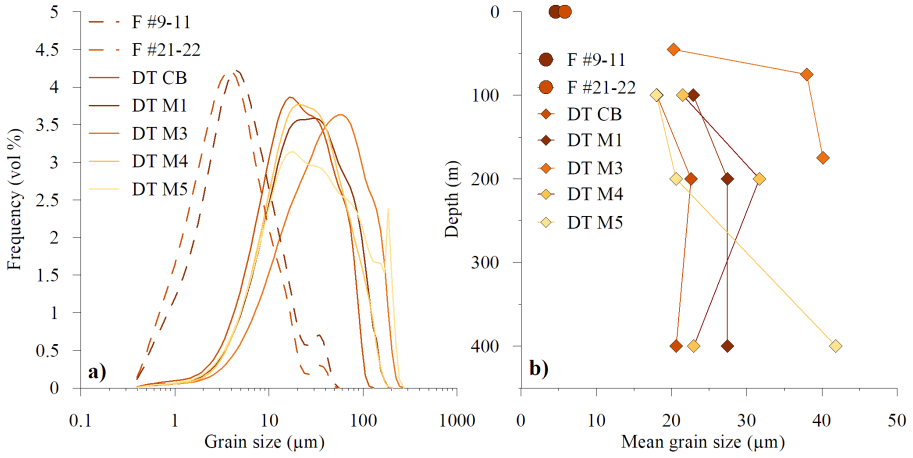

Figure 8. a) Averaged grain-size distributions of the dust filters (F) and of Saharan dust in the export flux from the DTs deployed in 2016 (cruise JC134) at five stations along the transect. b) Mean grain sizes as a function of depth from the drifting traps and the shipboard sampled dust filters.

4.2.3 CTD profiles

The CTD profiles obtained in 2016 (cruise JC134) are similar to those of 2015 (cruise 64PE395), although fluorescence concentrations in the DCM were higher (Fig. 9, note the different scale between Fig. 4 and Fig. 9), especially at CB. In March 2016, the DCM fluorescence concentrations ranged between 0.4 and 0.9 µg/L along the transect with elevated concentrations at 33°W and very low concentrations further west. Highest concentrations of 0.9 µg/L were found in a thin, low salinity surface layer at the westernmost station M5 at 56°W, showing the influence of South American river waters, and within the top 50 m off Cape Blanc in the north (21°N, 20°W) within the top 50 m, showing upwelling and continental influence.

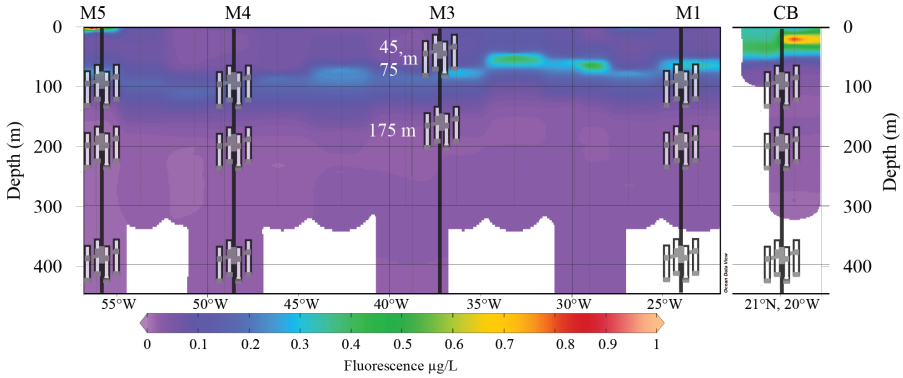

Figure 9. Deployed DTs and surface fluorescence concentrations during JC134 along the transect at 12°N and off Cape Blanc at 21°N, 20°W. The DCM shows a clear band within the top 100 m along the 12°N transect and high fluorescence concentrations within the entire surface waters down to 50 m off CB.

4.2.4 C/N ratios

During cruise JC134, the molar C/N ratios from the DTs showed a different pattern than that observed during cruise 64PE395. Along the transect at 12°N, average molar C/N ratios increased from 6.4 at M1 in the east to 8.9 at M5 in the west (Table 2). At CB (21°N, 20°W), the average molar C/N ratio was 9.5 and therefore the highest value found during the cruise. All molar C/N ratios, except at 200 m water depth at M1, were higher than the Redfield ratio (Fig. 10). While the depth profiles at stations CB, M1, and M4 showed a decrease in C/N ratios from 100 to 200 m depth and a subsequent increase to 400 m, the pattern at M5 showed an initial increase from 100 to 200 m, followed by a decrease to 400 m depth (Fig. 10). At station M3, the average ratio was 8.0 and increased from top to bottom. However, at this station, the

DTs were deployed at different depths; the shallowest above the DCM at 45 m, the middle in the DCM at 75 m and the lowest below the DCM at 175 m.

Table 2. Molar C/N ratios of material trapped by the DT during cruise JC134 in 2016.

Molar C/N ratios	M5, 57°W	M4, 49°W	M3, 38°W	M1, 23°W	CB, 20°W
100 m	7.2	7.1	6.8 (45 m)	6.9	9.2
200 m	10.4	6.7	7.9 (75 m)	5.5	9.0
400 m	9.2	7.8	9.3 (175 m)	8.4	10.4
Average	8.9	7.1	8.0	7.0	9.5
Standard deviation (1 σ)	1.62	0.37	1.25	1.44	0.72

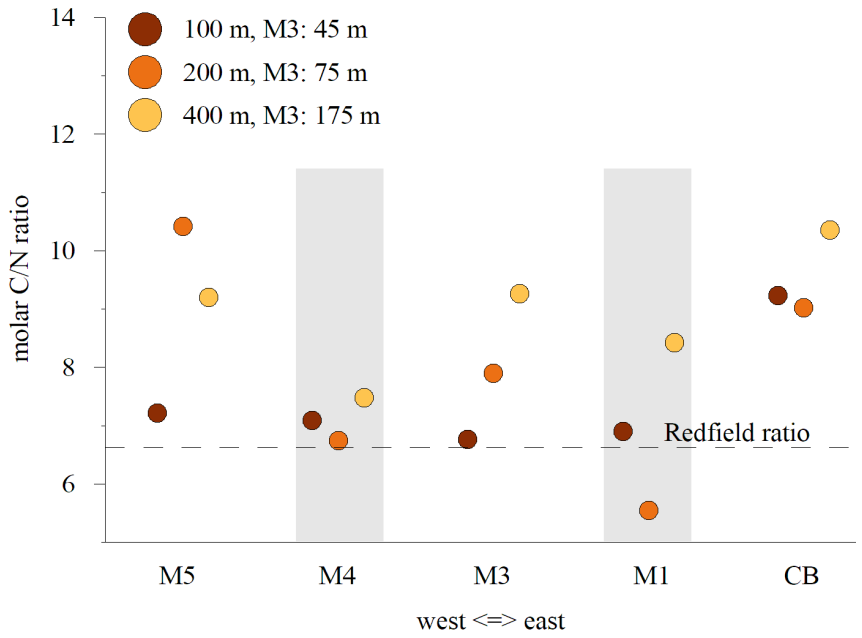

Figure 10. Depth profiles of molar C/N ratios in the DTs deployed during cruise JC134 in 2016.

5 Discussion

5.1 Atmospheric dust

During both cruises we encountered at least one dust event which was captured by the ship-board aerosol samplers as well as the DTs in the water. The aerosol sampling revealed atmospheric dust concentrations at sea level. Satellite images clearly show the dust leaving the African continent, and elevated AOD values along the transect support our direct on-board dust observations. Dust concentrations were highest during the dust event in January 2015 and exceeded 100 µg/m^3 (Fig. 2, Table S1). During the dust event in March 2016 we observed lower concentrations, around 50 µg/m^3 (Fig. 7, Table S2). Although peaks in AOD values co-occur with observed higher dust concentrations, the values differ in magnitude. While the 100 µg/m^3 of dust correspond to an AOD value of 1.6, the 50 µg/m^3 of dust leads to an AOD value of 0.5. An AOD value of 0.5 is however also recorded at M1 in 2016 (Fig. 7) when the dust collector collected too little material to determine the atmospheric dust concentrations. This shows that AOD gives a reasonable indication for atmospheric dust occurrence, but the values do not relate to the actual absolute dust concentrations at sea level. This might be reasoned in the altitude the dust is transported, as high AOD values would be recorded when dust is, for example at up to five km altitude during summer (Tsamalis et al., 2013), which dust would, however, not implicitly be sampled by shipboard dust collectors.

The transported dust had a modal grain size of approximately 4 µm during both cruises independent of its longitudinal location. However, grain-size distributions tended to show a coarse shoulder in the western region of our study (Fig. 3a, 8a). This behavior indicates a relatively larger amount of platy clay minerals over more solid quartz grains in the west, due to preferential settling of the heavy quartz grains close to the source. Similar differences in Saharan dust composition between the Cape Verde Islands, the Caribbean and Southern America were found by Glaccum and Prospero (1980), and changes in the element composition of lithogenic particles from moored sediment traps deployed along the 12°N transect support these conclusions (Korte et al., 2017).

A comparison of the transported (airborne) and deposited (marine) dust showed differences in particle size, as the oceanic dust deposition consisted of coarser-grained particles than those collected from the atmosphere. Van der Does et al. (2016) showed that the modal grain size in the ocean decreases from 18 µm in the eastern Atlantic Ocean to 7 µm in the western Atlantic Ocean. This fining trend across the

ocean is also seen in the modal grain size of Saharan dust collected by the DTs, although modal grain sizes were coarser-grained in 2016 (Fig. 3b, 8b). Fine-grained particles are held in suspension in the atmosphere for longer and are transported across the North Atlantic Ocean towards the Americas. Dust concentrations recorded on Barbados show large seasonal fluctuations from 5 to > 100 $\mu g/m^3$, but typically range between 20-30 $\mu g/m^3$ on average during summer months (Prospero, 1996; Mahowald et al., 2002; Prospero et al., 2002). These fluctuations are caused by the different seasonal winds that transport the dust across the Atlantic Ocean (Swap et al., 1996; Adams et al., 2012) and by wet dust deposition washing out the dust from the atmosphere (Friese et al., 2017; Chapter 3). The deposited dust is incorporated into marine snow in the surface waters and settles out as part of the downward export flux. This transport is quicker and more efficient when marine snow is ballasted by high density minerals (Iversen and Robert, 2015) such as Saharan dust (Van der Jagt et al., 2018). We observed high dust concentrations at sea level at station M1 during cruise 64PE395 in January 2015 (Fig. 2) indicative for an efficient particle downward export.

5.2 Role of Saharan dust for the downward export efficiency

A comparison of different parameters gathered during the 64PE395 and JC134 cruises in 2015 and 2016, suggests that Saharan dust efficiently transported marine organic matter through the upper water column. The clearest dust event was encountered from January 10th to January 15th, 2015, which was observed ship-board and was readily visible in satellite images as well as expressed by high AOD values (Fig. 2). On January 13-14th, DTs deployed during this dust event at station M1 (12°N, 23°W) showed well-sorted Saharan dust at all three sampling depths, comparable to the dust sampled in the atmosphere (Fig. 3a). In addition, the deposited dust's particle size compares well to dust collected by moored sediment traps at 1200 m water depth (Van der Does et al., 2016). Once deposited in the surface ocean waters, Van der Jagt et al. (2018) showed that Saharan dust both enhances formation of aggregates and their size-specific sinking velocity. Such fast(er) sinking decreases the time available for degradation of organic material formed in the surface ocean. During the time of the dust event in January 2015, the molar C/N ratios remained stable at a value of 8.1 at all sampling depths (standard deviation = 0.03), suggesting little biodegradation and fast marine snow export. The gel at 400 m water depth contained dark marine snow and fecal pellets, while individual sinking zooplankton molds were absent (Fig. 5, S2). This implies that the marine snow was exported by ballast materials,

such as the present Saharan dust.

At the other sampling sites, where less or no virtually dust was present in the atmosphere, the molar C/N ratios showed divergent patterns. AOD values peaked at M1 and decreased towards M2, leveling off towards station M3, M4 and M5 (Fig. 2). At station M2, the strongest increase in molar C/N ratios with increasing depth was recorded indicating highest degradation. This is likely due to slow downward transport of non-ballasted material as much time was available for preferential degradation of nitrogen over carbon in the upper water column (Gordon, 1971; Schneider et al., 2003). Although fecal pellets were abundant at M2, the amount of zooplankton, e.g. individual foraminfers was highest, settling alone without additional organic material (Fig. 5, Fig. S2). However, M2 still showed relatively high AOD values (0.6), but dust concentrations at sea level were already low (16 $\mu g/m^3$) and the mean particle sizes were the finest-grained along the transect. This suggests that the dust to the north of the main dust plume is too fine-grained (and light) to ballast OM sufficiently for rapidly acceleration of its downward transport. Moreover, due to the location of M2 towards the subtropical North Atlantic gyre, oligotrophic water conditions do not favor high primary production and thus the formation of marine snow aggregates. Indeed, only small downward particle export fluxes to the deep ocean were recorded by Korte et al. (2017), while Guerreiro et al. (2017) showed little coccolithophore primary productivity at M2. However, at M3, 220 km south of M2, not only the OM flux was higher along with a higher lithogenic fraction (Korte et al., 2017), but also the molar C/N ratios stayed relatively constant with depth (standard deviation = 0.08), suggesting a higher dust input and/or higher primary productivity than at M2. At station M4 and M5 in the west, the air was clear and AOD values were low, showing no dust present in the atmosphere. At these stations the molar C/N ratios increased with depth, although less than at station M2 (Fig. 6, Table 1), suggesting a slow downward transport of OM and therefore a proportionally increased exposure time to microbial degradation.

In 2016, the molar C/N ratios along the transect differed from the values found in 2015 and showed a different trend with increasing depth in the absence of a large dust event. At station M1 the molar C/N ratio at 100 m was lower than in 2015 and decreased towards 200 m after which it increased again towards 400 m (Fig. 10, Table 2). This sharp contrast with the near constant values in the presence of dust in 2015 suggests that different production and transport processes are active when dust is absent in the oligotrophic ocean. Although AOD values were relatively high (0.5) at M1 in 2016, dust concentrations could not be determined during the time of the

DTs deployment. Therefore, when dust is absent, slow downward export will lead to accumulation of differently aged OM with depth that may have originated in different places, with different molar C/N ratios.
At station M3, when dust was present in the atmosphere (Fig. 7), it was expected that the ratios would remain rather constant. This was, however, not the case. The molar C/N ratios increased with increasing depth (standard deviation = 1.25), which might be caused by the shallower sampling depths. The two shallowest sampling depths were within the mixed layer layer depth, making the results hard to compare to the other sampling depths.

5.3 The (a)biological control of molar C/N ratios in contrasting environments

The differences in the trapped material from the DTs during the two research cruises show diverging patterns and demonstrate biological interannual variation in winter, although surface ocean conditions during both cruises along the 12°N transect were similar. Overall, the DCM was located at similar depths along the transect, although with differences in its maximum phytoplankton concentration. Low nutrient concentrations were observed in the surface waters and a deepening of the nutricline was recorded towards the west (Fig. S1). In the westernmost surface waters, however, enhanced nutrient concentrations were recorded, especially in dissolved iron and silica, which are related to the freshwater input from the Amazon River to the west. At the same time, in the eastern Atlantic, phosphate concentrations from 50 m downwards were lower in the water column off Cape Blanc than at the nearest station M1 during both sampling years. Moreover, off Cape Blanc, phytoplankton concentrations in the surface waters were high (Fig. 9) due to coastal upwelling and continental input. Here, molar C/N ratios of around 9 were found in a similar progression as at M1 in 2016, with a decrease towards 200 m and an increase towards 400 m in 2016 (Fig. 10, Table 2). Karakaş et al. (2006) showed that in the region off Cape Blanc particle abundance is highest in the surface waters and in the subsurface between 200 and 400 m water depth which is related to surface primary productivity and lateral advection from the shallow shelf, respectively. These processes may lead to the differences in C/N, resulting from material produced or transported from different places. Algae produced under low phosphate concentrations were found to contain increased C/N ratios (Gervais and Riebesell, 2001). This may also have caused the higher C/N ratios in this study. In addition, off Cape Blanc, particle settling velocities of 5 m/d are relatively low (Karakaş et al., 2006), giving time for microbial

degradation. This degradation is reduced when particles sink faster (up to hundreds of meters per day), when they are ballasted by dust or digested in animal guts and exported as fecal pellets (Alldredge and Silver, 1988; Ploug et al., 2008).
In the western Atlantic Ocean, the captured material was different from the material in the eastern Atlantic Ocean. The gels from M5 captured large marine snow aggregates (Fig. 5), which are associated to the Amazon River discharge (Korte et al., 2017). As seen in the higher iron and silicate concentrations in the west, the Amazonian freshwater lense is thought to act as a nutrient source as well as nutrient retainer impacting the marine life as it spreads (Guerreiro et al., 2017). Regarding the contrasting DIC values in the eastern and the western Atlantic (Fig. 4), we suspect that there is a more efficient uptake of DIC in the west, which might be caused by the nutrient supply from the Amazon freshwater and the related diazotrophic nitrogen fixation (Subramaniam et al., 2008). In 2015, the molar C/N ratios at M4 were below the Redfield ratio (Fig. 6) indicating nitrogen overconsumption (Körtzinger et al., 2001) which might be caused by such nitrogen fixation.

6 Conclusions

Drifting traps, which were deployed across the equatorial Atlantic Ocean, are an important tool to assess the ballasting capacity of Saharan dust and its effects on marine biogeochemistry. Our observations imply that Saharan dust seems to impact the molar C/N ratios of sinking particles by acting as ballasting particles, and as a result of such ballasting we observed constant C/N ratios with increasing depth during a dust deposition event in 2015. Molar C/N ratios increased with increasing depth when dust was absent in the atmosphere and therefore dust deposition into the ocean was low, which is an indication of a higher degree of microbial degradation. However, consideration of only molar C/N ratios without a detailed look at the biology and composition of the exported material might be precarious since processes such as grazing and fecal pellet production can alter molar C/N ratios. Additionally, we observed regional changes with higher molar C/N ratios close to the continents, suggesting either lateral advection or riverine input influencing the C/N ratios at depth.

Acknowledgements

This project is funded by ERC (project no. 311152) and NWO (project no. 822.01.008). We thank the captains and crews and scientific parties of *RV Pelagia* cruise 64PE395 and *RRS James Cook* cruise JC134 as well as NIOZ technicians for their contributions. Sharyn Ossebaar is thanked for assistance with the C/N measurements and Karel Bakker for analyzing DIC concentrations. The authors also acknowledge the MODIS mission scientists and NASA personnel for satellite data production. Morten H. Iversen received funding for the Helmholtz Young Investigator Group SeaPump "Seasonal and regional food web interactions with the biological pump" (VH-NG-1000), the Alfred Wegner Institute for Polar and Marine Research, and the DFG-Research Center/Cluster of Excellence Marum, "The Ocean in the Earth System".

Table S1. Amount of dust on filter cuts (A_{cut}, surface area = 15.21 cm^2) and extrapolated weight on entire filter (A_{filter}, surface area = 402.48 cm^2) as well as calculated dust concentrations in the atmosphere during 64PE395. Orange shaded concentrations represent dust sampled along the NNW-SSE profile along the northwest African coast, blue shaded concentrations represent dust sampled along the 12°N transect.

Filter #	Dust per A_{cut} (mg)	Dust per A_{filter} (mg)	Air volume A_{filter} (L)	Dust/air volume (mg/L)	Dust concentration (µg/m^3)
1	2.47	65.36	960621	6.80 E-05	**68.0**
2	2.34	61.92	1115667	5.55 E-05	**55.5**
3	2.01	53.19	1082202	4.91 E-05	**49.1**
4	12.37	327.33	4475781	7.31 E-05	**73.1**
5	2.08	55.04	851264	6.47 E-05	**64.7**
6	5.66	149.77	2125777	7.05 E-05	**70.5**
7	3.69	97.64	1307511	7.47 E-05	**74.7**
8	15.31	405.13	3904661	1.04 E-04	**103.8**
9	0.38	10.06	109408	9.19 E-05	**91.9**
10	4.68	123.84	2025674	6.11 E-05	**61.1**
11	1.22	32.28	397237	8.13 E-05	**81.3**
12					
13	2.16	57.16	1083904	5.27 E-05	**52.7**
14	3.77	99.76	1693268	5.89 E-05	**58.9**
15	6.64	175.70	3337698	5.26 E-05	**52.6**
16	4.76	125.96	37223850	3.38 E-05	**33.8**
17	1.83	48.42	1693588	2.86 E-05	**28.6**
18	1.07	28.31	1534280	1.85 E-05	**18.5**
19	7.93	51.07	2996067	1.70 E-05	**17.0**
20	0.08	2.12	519399	4.08 E-06	**4.1**
21	0.90	23.82	14584482	1.60 E-05	**16.0**
22	1.80	47.63	2889363	1.65 E-05	**16.5**
23	1.77	46.84	3896964	1.20 E-05	**12.0**
24	1.42	37.58	7177664	5.24 E-06	**5.2**
25	2.88	76.21	15315801	4.98 E-06	**6.0**
26	2.51	66.42	9789904	6.78 E-06	**6.8**

Table S2. Amount of dust on filter cuts (A_{cut}, surface area = 16.47 cm²) and extrapolated weight on entire filter (A_{filter}, surface area = 402.48 cm²) as well as calculated dust concentrations in the atmosphere during JC134. Blue shaded concentrations represent dust sampled along the 12°N transect and orange shaded area represents dust concentrations at the NNW-SSE part of the transect.

Filter #	Dust per A_{cut} (mg)	Dust per A_{filter} (mg)	Air volume A_{filter} (L)	Dust/air volume (mg/L)	Dust concentration (µg/m³)
9	2.49	60.93	1465785	4.16 E-05	**41.6**
10	2.79	68.18	1218250	5.60 E-05	**56.0**
11	2.37	58.00	1306180	4.44 E-05	**44.4**
21	0.82	20.04	1420399	1.41 E-05	**14.1**
22	0.67	16.37	1440654	1.14 E-05	**11.4**

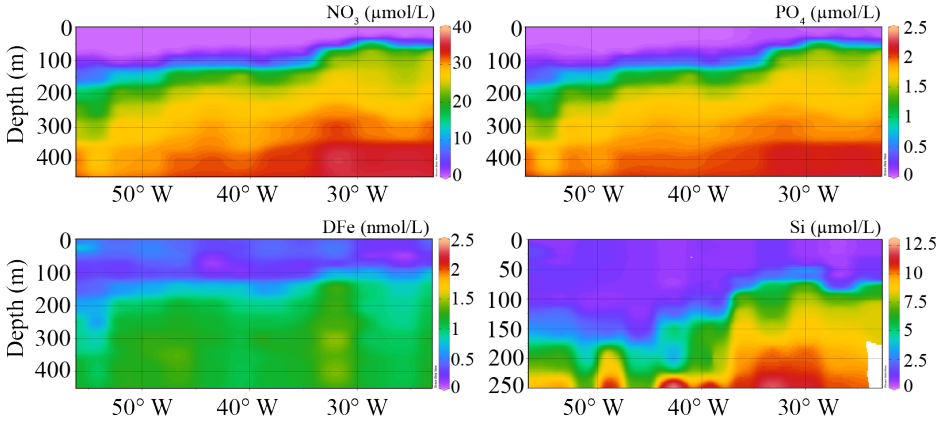

Figure S1. Nutrient profiles during cruise 64PE395 (NO_3, PO_4, DFe) and the JC134 cruise (Si) showing the deepening of the nutricline towards the west and elevated DFe in the western Atlantic surface waters (see also: Guerreiro et al., 2018, submitted).

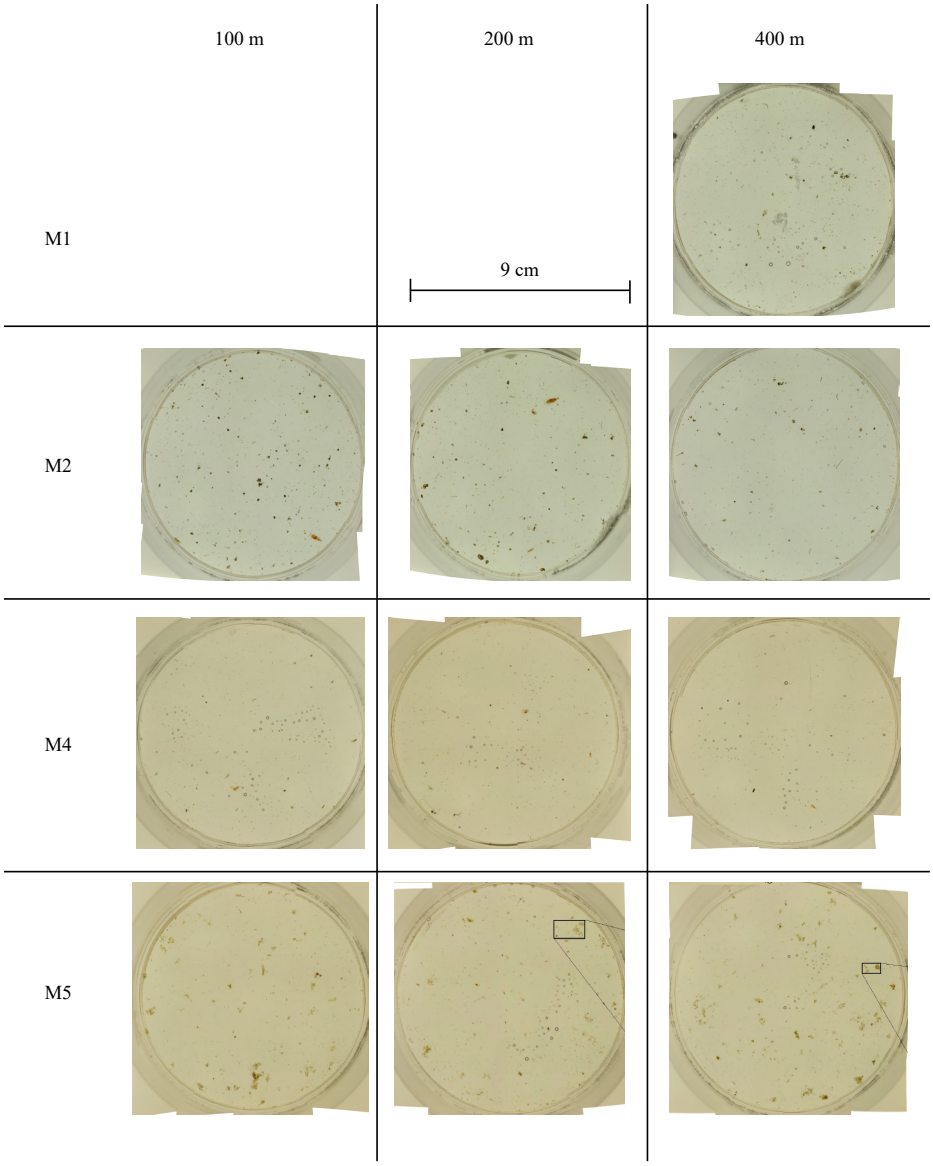

Figure S2. Stitched images of gel cups at station M1, M2, M4, and M5 at 100, 200 and 400 m. Gels from 100 and 200 m at M1 turned opaque and are therefore not shown.

CHAPTER 7

Conclusions and Outlook

Conclusions

This thesis is one step forward towards understanding Saharan dust deposition in the Atlantic Ocean and its impact on particle export fluxes. The field data and experimental results of this study provide new insights into open-ocean particle fluxes and reveal a complex interplay between multiple processes in the atmosphere and the equatorial North Atlantic Ocean in which Saharan dust is involved. From the previous chapters, I conclude that:

1. the dust particles collected by the subsurface sediment traps closest to the African coast are largest and most similar to the dust emitted from the Saharan Desert
2. the mineralogy and chemical composition of the dust changes downwind towards the Caribbean due to preferential settling of coarser dust particles in closer proximity to the sources
3. commonly used calculations to determine the lithogenic (dust) flux, significantly overestimate the 'true' mineral dust flux, since weighed dust fluxes are 2 to 18 times lower
4. closest to the African coast, seasonality is most prominent with high wet dust deposition fluxes in summer and fall and low dry dust deposition fluxes in winter and spring
5. Saharan dust delivers macro- and micronutrients (phosphate, silicate and dissolved iron) to the surface waters if processed in low pH rain (pH = 2)
6. in combination with a N-nutrient source, the nutrients from wet dust deposition may fertilize phytoplankton growth in the equatorial Atlantic Ocean
7. in the western Atlantic, biogenic marine particles fluxes are higher than in the central Atlantic and, especially the biogenic silica flux increases during times when the Amazon River water is retroflected towards the east
8. large particle export fluxes are generated by the coincidence of Amazon freshwater and wet dust deposition
9. the dust particles form marine snow aggregates with organic matter and transport (ballast) these effectively through the water column

Outlook

All observations made in this study contribute to the knowledge of Saharan dust deposition in the Atlantic Ocean and are important for the role of dust in ongoing climate change. The amount of dust which is ultimately deposited into the global ocean has to be determined as precisely as possible to (1) calculate and compare dust deposition fluxes from the atmosphere to estimates from satellite observations and (2) derive the dust's impact on the marine particle fluxes. Therefore, an accurate method is needed to determine the dust deposition flux from marine particles that have been sampled by submarine sediment traps (see Outlook #1).

In the previous chapters I show that wet dust deposition leads to higher nutrient concentrations in the oligotrophic surface waters. In a changing ocean that most likely will be more strongly stratified and depleted in nutrient concentration in the upper ocean, nutrient input from the top via wet dust deposition might be vital to sustain phytoplankton productivity within the photic zone of the water column. To what extent the associated nutrients become available to the phytoplankton and the mineral dust also ballasts the organic matter through the water column, should be experimentally tested by a combined fertilizing and ballasting experiment. This experiment should better constrain the dust's fertilizing and ballasting effect in the Atlantic Ocean and its impact on the global carbon cycle (see Outlook #2).

In the western Atlantic the biogenic marine particles fluxes are higher than in the central Atlantic and especially the biogenic silica flux increases during times when the Amazon River water is retroflected towards the east. In combination with additional dry or wet dust deposition from the atmosphere, the primary production within the river plume may be enhanced and produced particles are exported towards the deep. To gain more insights into the interplay of freshwater river plumes and dust deposition, it would be helpful to deploy floating buoys at the edges of river plumes with a moored sediment trap within the catchment area of the plume to understand and differentiate the downward particles flux (see Outlook #3). In this way, also the characteristics of long-range transported (LRT) dust, after being processed in the atmosphere, could be determined *in-situ* in remote areas across the globe. The characteristics of LRT dust would greatly help to tackle the question of how dust-derived nutrients become available for phytoplankton.

 # 1 A more accurate determination of Saharan dust particle fluxes to constrain deposition fluxes in the Atlantic Ocean.

Mostly, the lithogenic (dust) fraction is calculated by subtraction of the biogenically produced material from the total mass. To calculate the biogenic fractions (e.g. organic matter, calcium carbonate and biogenic opal), conversion factors are involved which vary between 2 and 2.5, depending on the geographical sampling location and water content in the biogenic opal (Mortlock and Froelich, 1989, Wefer and Fischer, 1993; Jickells et al., 1998; Klaas and Archer, 2002; Fischer et al., 2007; Thunell et al., 2007; Fischer and Karakas, 2009, **this study Chapters 2 and 3)**. Another way of estimating the lithogenic fraction is by using the aluminum (Al) concentrations in the sample as dust proxy (Bory and Newton, 2000; Bory et al., 2001), assuming that lithogenic material contains 8.4 % Al (Turekian and Wedepohl, 1961). Both methods contain flaws since the first method assumes stable conversion factors for all marine material and the second method generalizes that all dust consists of Al-silicates but ignores that quartz does not contain aluminum. In this study, the lithogenic fraction is calculated by subtraction of the biogenic sediment fractions from the total mass (**Chapters 2 and 3**). It turned out that the calculated lithogenic fraction severely overestimated the 'true' mineral dust fraction that was measured by weighing after isolating it chemically. The 'true' dust flux shows a 2 to 18 times lower flux (**Chapter 3).**

Therefore, a refined method for the determination of the mineral dust fraction is needed. The method applied in chapter 3, dissolving all marine particles and weighing only the refractory dust fraction should be applied to all marine particle fluxes when concentrating on the global mineral dust fraction. Moreover, samples from different regions (open ocean, upwelling, coastal regions) should be compared to quantify and calibrate the conventional methods and should, in addition, be analyzed by weight loss. Thermal gravimetric analysis (TGA), measuring the weight loss by thermal decomposition of the marine material at increasing temperatures, would successively decompose specific fractions (adsorbed water, hydrated biogenic silica, organic matter, carbonate phases). This would help to constrain the conversion factors for organic matter and biogenic silica resulting in a more accurate determination of the lithogenic fraction for different parts of the oceans. A refined dust flux to the global oceans would contribute to climate models to gain a more accurate forecasting of future climate.

 # 2 Conduct a comprehensive experiment on the fertilizing and the ballasting effect to elucidate and refine the impact of dust deposition on marine life in the Atlantic Ocean.

The bottle incubation experiments (**Chapter 4**) showed that wet Saharan dust deposition led to higher nutrient concentrations of phosphate, silicate and dissolved iron in the surface waters, but that a major fertilizing effect was absent. This was most likely caused by the absence of a nitrogen source. If a nitrogen source would be available, for example in the form of atmospheric HNO_3 deposition, the additional nutrients delivered by the Saharan dust may very well stimulate the phytoplankton communities resulting in CO_2 reduction due to the process of autotrophic photosynthesis. However, other studies have shown that Saharan dust may also influence the heterotrophic communities, which would end in a reverse effect of atmospheric CO_2 reduction (Marañon et al., 2010; Laghdass et al., 2011; Guieu et al., 2014a). The latter process was, however, not taken into account during this study. In addition, the ballast effect of Saharan dust could not be determined during the bottle incubation experiments, although observed under natural conditions by using drifting traps (**Chapter 6**).

To consider both effects fertilizing and ballasting, large mesocosms (~50 m^3) combined with a sediment trap deployed in the oligotrophic waters would provide the ideal set-up to disclose the role of Saharan dust in marine particle formation and transportation. The nutrient sources should include nutrients delivered by the dust, plus N-nutrients introduced by mimicking natural atmospheric processing, or the breakdown of organic matter produced by nitrogen fixation. The ballasting effect could be tested with different types of Saharan dust, characterized by different mineralogies, sizes and weights mimicking the spatial variability of Saharan dust particles and fluxes. Different parameters in the mesocosm could be sampled in a depth profile including carbon and nitrogen concentrations and uptake by the autotrophic and heterotrophic marine communities. The particle export fluxes could be collected by a sediment trap attached underneath the mesocosm. These measurements would help to get closer to the dust's role in the carbon cycle.

 # 3 Gain better insights into the characteristics of suspended dust transported in the atmosphere.

Saharan dust in the atmosphere is currently sampled by collectors mounted on floating buoys. The collectors consist of a carrousel holding 24 filters each, sampling the transported dust over a certain time period. We deployed these buoys the first

time in November 2013 at several sites the North Atlantic and they are sampling the atmosphere ever since (Van der Does, 2018, PhD thesis Chapter 6). First results show no clear seasonality in dust masses and are similar in grain size. Since the buoy collectors are synchronized with the sediment traps, future analyses should differentiate between the transported (buoys) and deposited (sediment traps) Saharan dust fluxes across the wide North Atlantic Ocean. Until now, the collectors of the buoys only sample the dry dust transport in the atmosphere, which comes close to dry deposition given the sampling height of a few meters above sea level. The sediment traps collect both dry and wet deposition. An additional carrousel on top of the buoys that only samples when it is raining would help to determine also the dust amounts deposited by wet deposition. This way, the difference of dry and wet deposition fluxes could be approximated and compared to dust collected by the sediment traps. As a result, a differentiation between both deposition types would highlight the impact of dust on the marine particle export fluxes in the sediment traps.

In addition, the dust which is collected on the buoy filters has been transported through the atmosphere and therefore been exposed to acid conditions, processing the dust particles. As the buoys are located at different distances from the dust source, the dust should be analyzed chemically in terms of nutrients to obtain insights into the spatial variability of atmospheric processing. The results should be compared with the meteorological data collected by the buoys. Especially the humidity is expecting to have the greatest impact on dust processing.

Regarding the global distribution of dust and the impact of lithogenic particles on the marine particle fluxes, it would be interesting to deploy a buoy at the edge of large river dispersals to distinguish between the dust and riverine impact on marine export fluxes. In **Chapter 5** it was argued that a combination of riverine input and dust deposition can create massive export fluxes, relevant for atmospheric CO_2 sequestration. Other locations around the globe, where both systems affect the ocean waters, would be for example:

- in the Mediterranean Sea with the Saharan desert as dust source and the Nile for riverine discharge,
- in the Bay of Bengal with Chinese loess as major dust source and the dispersal of the Ganges and Brahmaputra River,
- in the Southern Ocean offshore Australia where the Murray-Darling River discharges and the ocean waters are influenced by iron rich Australian dust.

CHAPTER 8

Appendix

A1 Splitting procedure

Once sediment trap samples were back at the NIOZ, the material of each sediment trap bottle was wet-split into equal aliquot subsamples using a rotary splitter (WSD-10, McLane Laboratories, Fig. A1). Splitting took place in a dedicated mercury chloride ($HgCl_2$) laboratory in a laminar flow hood. All samples were processed with filtered seawater of the original water depths where the traps had been. The bulk sediment trap material was wet-sieved (1 mm) to remove shell fragments, swimmers and large zooplankton. Particles > 1 mm were picked from the sieve and stored in supernatant of the sediment trap bottles containing $HgCl_2$. The sieved material was gently poured into the sample tray and equally split. After each sample, the splitter was washed with Milli-Q, dried with fabric lint free tissues, cleaned with ethanol, dried again and rinsed with Milli-Q.

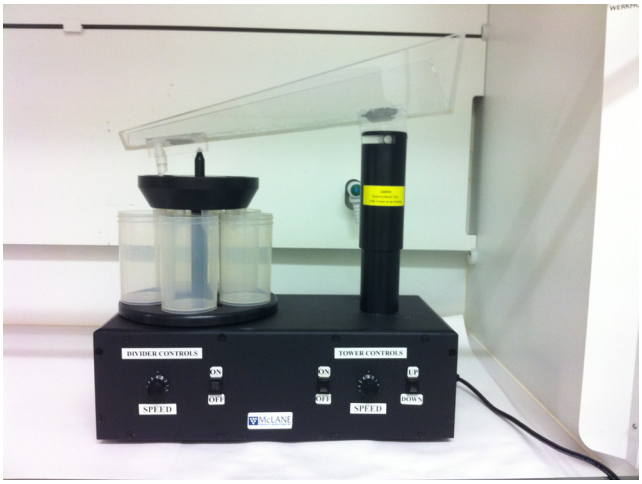

Figure A1. The rotary splitter used for generating equal aliquot subsamples. The sample tray holding the wet sample lifts up slowly by the piston on the right and the rotating carrousel splits the sample into five equal aliquots. The deviation between aliquots is < 5% (www.mclanelabs.com).

First, samples were split into five aliquots, and second, one aliquot was split again into another five aliquots resulting in total in four one-fifth and five twenty-fifth splits (Fig. A2). After splitting, subsamples were washed with Milli-Q or seawater (depending on the selected analyses) to remove the $HgCl_2$ and salts, and finally centrifuged. All splits targeted a specific sample analysis, for which the samples were treated accordingly:

Two one-fifth samples (① and ⑤) were used for total mass determination. To this end, falcon tubes were pre-weighed before sample addition and back-weighed after

washing, centrifuging and freeze drying. The average sample deviation between the two samples for the 2013 sediment trap series was 2.4 %. After weighing, split ① was ground and used for XRF-analysis as well as for the biogenic silica flux, and some selected samples for isotopes (strontium and neodymium) together with rare earth elements (Van der Does et al., 2018). At the NIOZ, the XRF-analyses were performed on the Avaatech XRF core scanner (Richter et al., 2006) and biogenic silica was analyzed using the leaching method of Koning et al. (2002), while isotopes and REE were extracted after Pourmand et al. (2014) and analyzed at the Rosenstiel School for Marine and Atmospheric Sciences (RSMAS) Miami, USA (Van der Does et al., 2018).

Split ⑤ was oxidized in a low-temperature asher to remove the organic matter leaving mineral particles for calcium carbonate phytoplankton assemblages, e.g. coccolithophore (Guerreiro et al., 2017) and foraminifera (Knebel, 2016).
After washing and centrifuging split ②, it was transferred into a glass vial in which it was freeze dried to use it for (in)organic carbon and nitrogen analysis, together with their isotopes, as well as for biomarker analysis (e.g. total lipids, diols, levoglucusan, (Schreuder et al., 2018a, b)). The glass was used to prevent carbon contamination from falcon tubes, especially important for biomarker analysis. The (in)organic carbon and nitrogen and its isotopes were analyzed at the NIOZ by an elemental analyzer coupled to a mass spectrometer (EA-IRMS).

Split ③ was left untreated and stored as archive sample. This sample still contains the $HgCl_2$ solution, which was used as biocide for the sediment traps preventing biofouling.

Split ④ was further subdivided into 5 twenty-fifth splits. These subsamples were used, tested or stored for:

- DNA (10 ml of the ④-1), for which the ethanol cleaning step was inevitable.
- Pigment analysis (④-1, analyzed for 13M4-upper).
- Pollen (④-2, tested but no pollen were present in the samples (pers. comm. Prof. H. Hooghiemstra, University of Amsterdam, the Netherlands)
- Sequential extraction (④-3, stored). An approach for a method set-up is given in Appendix, A2. This method describes a sequential extraction procedure targeting on specific mineral phases.
- Terrigenous (dust) fraction and dust particle size (④-4, Van der Does et al. 2016, Chapter 3)
- Terrigenous fraction and particle shape (④-5, stored)

Samples for pigment analysis (④-1) and the sequential leaching (④-3) were washed with filtered seawater to prevent pigment destruction and leaching of metals in low pH Milli-Q. Sample storage is given in Table A1.

Table A1. Storage information of split samples with 13M1-U8 as example.

Sample	Storage
13M1-U8 ①	**Room temperature, dark**
13M1-U8 ②	**Frozen -20°C**
13M1-U8 ③	**Room temperature, dark**
13M1-U8 ④-1	**Frozen -40°C**
13M1-U8 ④-2	**Frozen -20°C**
13M1-U8 ④-3	**Frozen -40°C**
13M1-U8 ④-4	**Cooled +4°C, dark**
13M1-U8 ④-5	**Cooled +4°C, dark**
13M1-U8 ⑤	**Room temperature, dark**

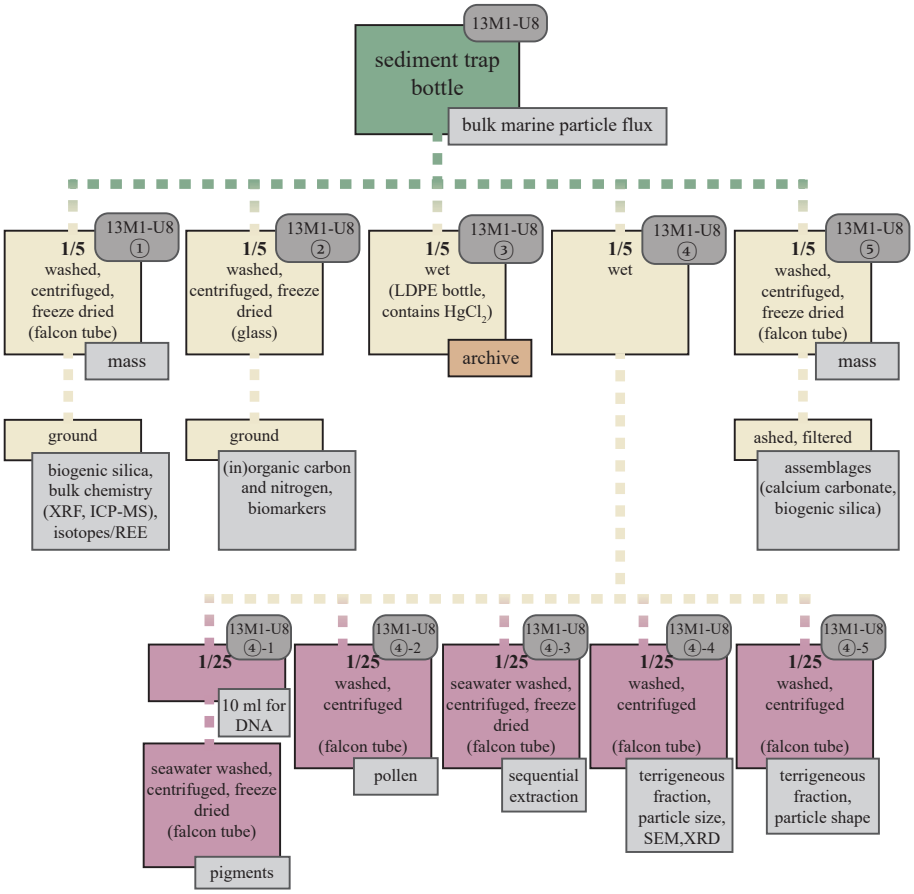

Figure A2. Overview of the splitting scheme illustrating individual subsamples and designated analysis. The sampling code of all samples is demonstrated by an example of sediment trap sample 13M1-U8. All samples were split with filtered seawater from respective sediment trap depths. Afterwards, all the samples were washed with Milli-Q, except split ④, subsamples ④-1 and ④-3, dedicated for pigment analysis and sequential extraction, were washed with filtered seawater to protect pigment destruction and avoid leaching metals in the low pH of Milli-Q.

A2 Sequential extraction of trace metals

Applying sequential extraction on trace metals in sediments gives detailed information about origin, occurrence, biological and physiochemical availability, mobilization, and transport of the metals (Tessier et al., 1979). Such a method is being developed to extract trace metals in the different fractions of the material in the marine sediment traps. The sediment traps collect all sinking material in the deep ocean, including detritus of phytoplankton and small zooplankton, dust, and potentially other particles of volcanogenic, cosmogenic and anthropogenic origin. To determine in which fraction trace metals are incorporated once they entered the marine biological food web and which metals are used by bacteria or phytoplankton from the Saharan dust, the sequential extraction method is targeting on:

1. Adsorbed ions
2. Amorphous oxides
3. Organics
4. Carbonates
5. and the residual fraction

Since sediment trap material is rare and valuable (i.e. small in volume), specific minerals incorporated in Saharan dust were bought from Ward's science (https://wardsci.com/store) to test and develop the method. In addition, two pure samples of Saharan dust collected by the MWAC samplers in Iouîk at the Mauritanian coast and three international standards, representing marine material, were incorporated in the test (Table A3).

Table A3. Minerals and samples used to test sequential extraction method.

Mineral/Sample	Description
Illite	Clay
Kaolinite	Clay
Chlorite	Clay
Quartz	Quartz
Calcite	Calcite
Microcline	Feldspar
Anorthite	Feldspar
Albite	Feldspar
Hematite	Iron oxide
Magnetite	Iron oxide
Goethite	Iron hydroxide
Saharan dust	Sampled in Iouîk in May
Saharan dust	Sampled in Iouîk in August
JSd-2*	Steam sediment powder, Japan
GBW07309*	Steam sediment powder, China
BCSS-1*	Sediment powder, Canada

*element concentrations are given by GeoRem (http://georem.mpch-mainz.gwdg.de/sample_query.asp).

Before the analysis, the minerals were crushed, ground and sieved through a < 20 µm mesh, while Saharan dust samples were only sieved (< 20 µm) and powder standard materials were used as provided. A total of 50 mg of each material was weighed into 8 ml centrifuge tubes (Oak Ridge Centrifuge Tube, PC) to which the chemicals were added sequentially. All samples were tested in triplicates and chemical treatments were carried out under clean-room conditions. The sequential extraction scheme and chemicals were based on Rutten and de Lange (2003) and adapted as given in Table A4.

Table A4. Chemicals and targeted mineral phase of seven sequential extraction steps

Step	Chemicals[1]	Leached mineral phase	Time (h)
1	ammonium chloride (NH_4Cl), pH 5.5	adsorbed ions	24, rotating plate
2	ascorbic acid/$NaHCO_3$/Na-citrate solution, pH 8	amorphous oxides	24, rotating plate
3	peroxide, ammonium hydroxide (H_2O_2, NH_4OH), pH 9.3	organics	3, in hot water bath (85°C)
4	ascorbic acid/$NaHCO_3$/Na-citrate solution, pH 8	hidden amorphous oxides	24, rotating plate
5	nitric acid, 1 M	carbonates and unreleased metals	1, rotating plate
6	EDTA, pH 4.4	complexes metals	24, rotating plate, 2x Milli-Q washed
7	hydrofluoric acid (HF), hydrogen chloride (HCl), perchloric acid ($HClO_4$)	total destruction of residual mineral	48, on hot block (125°C), 24, in hot block (125°C)

[1]List of chemicals is provided below.

A total of 2 ml of each chemical solution was added to the samples in step one to step six. The samples were kept in solution for a specific time on a vertical oriented rotating plate, or hot water bath (Table A4). Afterwards, samples were centrifuged (3000 rpm, 15 minutes), the supernatant pipetted into Digi Tubes and the sample washed with 2 ml Milli-Q, or 2 x 2 ml for step six due to the heavy EDTA. The Milli-Q was again centrifuged (3000 rpm, 15 min) and added to the respective Digi Tube. The solution in the Digi Tubes was acidified with HNO_3 to a dilution factor (DF) of 100 and stored cooled until analysis. During step three, the vials were kept open under a fume hood in the hot water bath to allow the peroxide to escape. Before step seven, the total destruction, all centrifuge tubes with the residual samples were filled with 1 ml Milli-Q, shaken well on the rotating plate and frozen. The frozen samples were freeze dried and the dry material was transferred to Savillex Teflon beakers. The beakers were weighed to estimate the amount which was actually transferred. Subsequently, each sample was mixed with 6.5 ml HF, 1 ml HCl and 1 ml $HClO_4$ and heated in the closed Savillex beaker on the hot block for 48 h. Once cooled, the beakers were connected to a second set of empty beakers via right-angled elbow tubes. The samples were placed into the sides of the hot blocks for 24 h so that

the chemical mixture evaporated and re-condensed in the second beaker, leaving the dry samples behind. The dry samples were diluted with 1 M HNO_3 and heated one more time on the hot block (125°C, 2h).

All samples were analyzed with the ICP-MS on medium resolution, resulting in elemental contents from rubidium (Rb) through tin (Sn) with special focus on iron (Fe). To prepare the samples for elemental analysis, samples were diluted in pony vials with an element standard (Sn_In 2-1) prepared in HNO_3. For step one and six samples were diluted to a total DF of 500, for step two through five to a total DF of 1000, and for step seven to a DF of 10000.

Preliminary results

Preliminary results are shown for Fe concentrations leached by the seven steps of the sequential extraction method (Fig. A3). Triplicate measurements are in good agreement. The average of the relative standard deviation (RSD = standard deviation divided by the average of replicates x 100 %) of the three standards is < 15 %. While most Fe was leached from the clay mineral chlorite, followed by the iron (hydro)oxides magnetite and goethite, by far the least amount of Fe was leached from calcite, followed by quartz, the feldspars (anorthite, albite and microcline) and kaolinite. The leached Fe from Saharan dust varied between almost no iron in step one, ~ 300 ppm Fe in steps two to six, and around $3 \cdot 10^4$ ppm Fe after the total destruction. The three standards (JsD-2, GBW07309, BCSS-1) show a similar pattern with minor Fe release during step 1 (~ 20 ppm Fe), between 300 and $2 \cdot 10^4$ ppm Fe in step two to step six, and most Fe release of ~ $4 \cdot 10^4$ ppm Fe after total destruction.

The individual steps show that almost no Fe is absorbed onto the sample material. The released Fe concentrations leached with ammonium chloride (step one) remain very low in comparison to the other steps. The chemicals of steps two to six display a rather uniform Fe release with little variation, seemingly implying similar Fe amounts bound to oxides and organics. Similar amounts of Fe were leached during the two ascorbate solution steps (steps two & four), targeting on amorphous oxides. The second ascorbate step (step four) was introduced to target on 'hidden' oxides behind organic material (step three). Surprisingly, Fe is released from organic minerals when exposed to the peroxide solution (step 3), although the organic contribution in the minerals should be negligible. The HNO_3 in step five released the Fe from carbonates and thus dissolved the calcite completely. The synthetic chelator EDTA used before the total destruction, complexed the available Fe and built metal chelates. Finally, most of the Fe was incorporated in the crystal structure of the minerals and

was only released by total destruction. These conditions are, however, not expected under natural conditions. Adding up all Fe concentrations from the seven steps, the three international standards yield on average 107±13 % of the Fe as certified by GeoRem. Best accordance was yielded by the JsD-2 standard (99 %), followed by the GBW07309 (102 %) and the BCSS-1 (122 %).

Comments

First results are promising in terms of replication of measurements and total element yield. However, the method needs more attention, testing and improvements:

- Since step two through six show similar Fe releasements, seemingly implying an equal amount of Fe released by oxides and organics, it is questionable if this is really the case. In other sequential extraction methods, reagent/sample ratios range between 8-100:1 (Tessier et al., 1979; Schultz et al., 1998; Poulton and Canfield, 2005), which is well in agreement with our test (40:1). However, it still might be that either 1) the added amount of reagent (2 ml) was too little in volume leaching all Fe from the sample (50 mg) before reaching saturation state during respective steps, or 2) the sample was not washed sufficiently, with too little volume of Milli-Q, in between the steps. Therefore, it seems that Fe was tailing into the next phases resulting in similar Fe concentrations. Also, that Fe was leached from minerals during the peroxide step targeting on organics (step three), although organic material should not be present in those minerals, points to Fe tailing into the next fraction. It was expected that the peroxide step only leaches Fe from the three standards due to a similar sample matrix as found in the sediment trap material; and not from the minerals. In addition, the EDTA complexes trace metals (Sunda et al., 2005) but does not leach Fe. This indicates that Fe in the samples was still available in step six that should have been leached or washed out already in steps one to five. Hence, the saturation states of the chemicals or the washing procedure need to be tested and volumes potentially need adjustments.

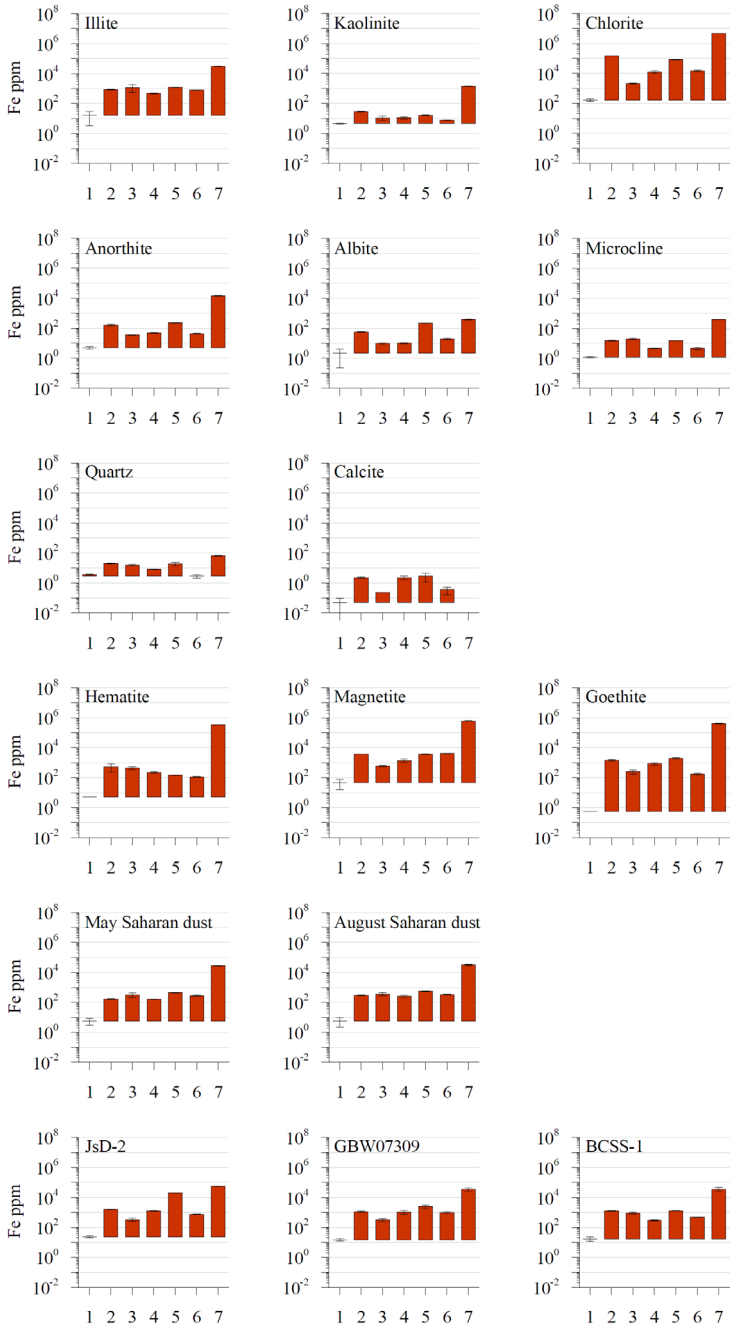

Figure A3. Fe concentrations of minerals, Saharan dust samples and international sediment standards for seven step sequential extraction.

- The used chemicals and/or the order in which the samples were exposed to the leaching fluids should be reconsidered as such. Schultz et al. (1998), for example, suggest placing the organic step early in the procedure since it may inhibit the reaction of other geochemical phases. Doing so, the two ascorbate steps targeting on the oxides, may be combined to a single step. Moreover, the EDTA step may be omitted since it only forms metal complexes but do not leach a specific fraction. To leach exchangeable ions, ammonium or sodium acetate, or magnesium chloride have been tested with the results that ammonium acetate in lower pH regimes may also attack carbonates (Tessier et al., 1979, and references within). Table A5 summarizes chemicals used in other sequential extraction methods.

  For further testing, it is suggested to use a five-step sequential extraction protocol, instead of the seven-step protocol, targeting the different fractions in the order of 1) exchangeable ions, 2) organics, 3) carbonates, 4) oxides and 5) the residual fraction, when extracting organic rich sediment trap material. Suggested adjustments to the used chemicals are as follows:

1. ammonium chloride (NH_4Cl) with a higher pH (pH = 8-9) for the exchangeable ions, but protecting carbonates,
2. ammonium acetate (NH_4OAc) or hydroxide (NH_4OH) solution in hydrogen peroxide (H_2O_2) for organics in hot water bath,
3. sodium acetate (NaOAc) and/or acetic acid (HOAc) at pH 5 for carbonates,
4. a mixture of ascorbic acid, sodium bicarbonate and sodium citrate (ascorbic acid/ $NaHCO_3$/Na-citrate solution for oxides,
5. and a mixture of nitric acid, hydrogen chloride, hydrogen fluoride and perchloride acid (HNO_3/HCl/HF/$HClO_4$) for total destruction.

- A final remark regards the peroxide step which produces bubbles as soon as the peroxide solution warms up in the hot water bath. It appeared that the used centrifuge tubes might be too narrow when samples contained high organic carbon contents. A lot of caution had to be taken that bubbles of the organic rich sample did not bubble over the rim of the tubes.

Table A5. Overview of chemicals used in sequential extraction methods

Target fraction	Chemicals	References	Notes
Exchangeable/ Adsorbed Ions	1 M $MgCl_2$, pH 7	Tessier et al. (1979), Chester et al. (1989), Poulton and Canfield (2005)	
	1 M NaOAc, pH 8.2	Tessier et al. (1979), Chester et al. (1989)	
	H_2O/0.04 M pH 5	Schultz et al. (1998)	
	1 M $MgCl_2$, pH 5.3	Rutten and de Lange (2003)	
	2 M NH_4Cl, pH 9	Rutten and de Lange (2003)	
	1 M Na_4Cl, pH 7	Lawrence et al. (2010)	dust leaching
Organics	0.02 M HNO_3 and 30% H_2O_2, pH 2 (85°C), after cooling: 3.2 M NH_4OAc in 20% (v/v) HNO_3	Tessier et al. (1979)	
	5-6% NaOCl, pH 7.5	Schultz et al. (1998)	
	ashed sampled leached in ultra-pure H_2O	Lawrence et al. (2010)	dust leaching
Carbonates	1 M NaOAc, adjusted to pH 5.0 with HOAc	Tessier et al. (1979)	
	1 M NaAc in 25% HAc, pH 4	Schultz et al. (1998)	
	1 M NaAc pH 5-6	Rutten and de Lange (2003)	
	1 M acetic acid	Lawrence et al. (2010)	dust leaching
Oxides	0.3 M Na_2S_2O4 + 0.175 M Na-citrate + 0.025 M H-citrate	Tessier et al. (1979)	
	0.04 M $NH_2OH{\cdot}HCl$ in 25% (v/v) HOAc	Tessier et al. (1979)	
	0.04 M $NH_2OH{\cdot}HCl$, pH 2 (HNO_3)	Schultz et al. (1998)	
	ascorbic acid/$NaHCO_3$/Na-citrate solution, pH 8	Rutten and de Lange (2003)	
Carbonate - Oxides	25% acetic acid + 0.25 M $NH_2OH{\cdot}HCl$	Chester et al. (1989)	
Organics - Residual	HNO_3, HF	Chester et al. (1989)	
Residual	HF-$HClO_4$ mixture	Tessier et al. (1979)	
	HNO_3/HCl/HF/$HClO_4$	Schultz et al. (1998), Lawrence et al. (2010)	dust leaching

[1]List of chemicals used in this test:

Ammonium chloride solution. 106.98 g of ammonium chloride [NH_4Cl for analysis, F_w 53.49, Merck Emsure, ACS, ISO, Reagent Ph.Eur] were dissolved in 1000 ml of Milli-Q water to obtain a 2 M solution with a pH of 5.5.

Ascorbate solution. 50 g of sodium bicarbonate [$NaHCO_3$, Fw 84.01, VWR BDH Prolabo] and 50 g of tri-sodium citrate dihydrate [Merck Emsure, ACS, ISO, Reagent Ph.Eur for analysis] were dissolved in 1000 ml of Milli-Q water. 20 g of ascorbic acid [VWR BDH Prolabo, Analar, Normapur, F_w 176.13] were slowly added to the solution to a final pH of 8.

Ammonium hydroxide solution. 16 ml of hydrogen peroxide [H_2O_2, 30%, Merck] were mixed with 84 ml of Milli-Q water. 0.45 ml of ammonium hydroxide [NH_4OH, 28-30%, Baker] were added to a final pH of 9.25.

EDTA solution. 14.6 g EDTA [Ethylenediaminetetraacetic acid, $C_{10}H_{16}N_2O_8$, F_w 292.24] were dissolved in 1000 ml of Milli-Q water to a final concentration of 0.05 M and a pH of 4.40.

Concentrated nitric acid solution. Suprapure nitric acid [HNO_3, 65%, 15M] was purchased from Merck Millipore.

Diluted nitric acid solution. 62.5 ml of the concentrated nitric acid solution was diluted with 937.5 ml of Milli-Q water to a final concentration of 1 M.

Hydrofluoric acid. Suprapure HF was purchased from Merck Millipore.

Hydrogen chloride. Plasmapure hydrochloric acid [HCl, 32-35%, ca. 10 M] was purchased from SCP Science.

Perchloric acid. Ultrapure perchloric acid [$HClO_4$, 70%, ca. 12 M] was purchased from Merck Millipore.

Table A6. Analyzed flux data of sediment trap series 2013. fall winter spring summer

TC = total carbon, TOC = total organic carbon, TIC = total inorganic carbon, BSi = biogenic silica, CaCO3 = carbonates (TIC·8.33), BSiO2 = biogenic silica (BSi·2.139), OM = organic matter (TOC·2), total mass flux being 100 %.Residual = 100 – CaCO3 – BSiO2 – OM.

Mass fluxes (mg m-2 d-1) are converted from weight percentages (wt %) with the total mass flux being 100 %.

M1-upper	mid sampling date	total mass flux mg m^{-2} d^{-1}	TC wt%	TOC wt%	TIC wt%	BSi wt%	$CaCO_3$ wt%	$BSiO_2$ wt%	OM wt%	Residual wt%	$CaCO_3$ mg m^{-2} d^{-1}	$BSiO_2$ mg m^{-2} d^{-1}	OM mg m^{-2} d^{-1}	Residual mg m^{-2} d^{-1}
13M1-U1	27/10/2012	**91.35**	**11.00**	**7.85**	3.15	**5.07**	26.25	10.84	15.69	47.2	23.98	9.90	14.34	43.14
13M1-U2	12/11/2012	**91.46**	**11.38**	**8.19**	3.18	**5.24**	26.50	11.21	16.39	45.9	24.24	10.25	14.99	41.98
13M1-U3	28/11/2012	**114.89**	**11.72**	**7.55**	4.16	**4.58**	34.69	9.80	15.11	40.4	39.85	11.26	17.36	46.42
13M1-U4	14/12/2012	**92.67**	**11.63**	**7.11**	4.53	**4.58**	37.72	9.80	14.21	38.3	34.95	9.08	13.17	35.47
13M1-U5	30/12/2012	**91.38**	**11.39**	**6.76**	4.63	**5.59**	38.59	11.95	13.52	35.9	35.26	10.92	12.36	32.84
13M1-U6	15/01/2013	**98.26**	**10.99**	**6.29**	4.70	**4.95**	39.15	10.60	12.58	37.7	38.47	10.41	12.36	37.02
13M1-U7	31/01/2013	**96.00**	**11.13**	**7.16**	3.97	**4.97**	33.08	10.62	14.32	42.0	31.75	10.20	13.75	40.30
13M1-U8	16/02/2013	**103.86**	**11.13**	**7.66**	3.48	**4.97**	28.97	10.63	15.31	45.1	30.09	11.04	15.90	46.83
13M1-U9	04/03/2013	**200.36**	**12.12**	**7.02**	5.10	**3.70**	42.47	7.91	14.05	35.6	85.09	15.85	28.14	71.28
13M1-U10	20/03/2013	**134.74**	**12.36**	**8.44**	3.92	**5.88**	32.62	12.59	16.89	37.9	43.95	16.96	22.76	51.07
13M1-U11	05/04/2013	**102.20**	**12.02**	**7.02**	5.00	**5.16**	41.69	11.03	14.04	33.2	42.61	11.27	14.35	33.97
13M1-U12	21/04/2013	**124.93**	**12.34**	**6.88**	5.45	**4.96**	45.41	10.61	13.77	30.2	56.73	13.25	17.20	37.74
13M1-U13	07/05/2013	**122.20**	**11.96**	**7.17**	4.79	**4.99**	39.92	10.67	14.33	35.1	48.79	13.04	17.51	42.86
13M1-U14	23/05/2013	**114.68**	**11.53**	**6.42**	5.11	**5.04**	42.56	10.79	12.84	33.8	48.81	12.38	14.72	38.78
13M1-U15	08/06/2013	**107.63**	**9.43**	**5.28**	4.15	**4.42**	34.57	9.45	10.56	45.4	37.20	10.18	11.37	48.88
13M1-U16	24/06/2013	**128.84**	**9.89**	**6.04**	3.85	**3.74**	32.03	8.00	12.08	47.9	41.27	10.30	15.57	61.70
13M1-U17	10/07/2013	**93.17**	**10.01**	**6.94**	3.06	**4.27**	25.53	9.12	13.88	51.5	23.79	8.50	12.93	47.95
13M1-U18	26/07/2013	**130.26**	**10.31**	**6.45**	3.86	**3.68**	32.17	7.87	12.89	47.1	41.90	10.25	16.79	61.31
13M1-U19	11/08/2013	**112.05**	**8.61**	**6.10**	2.51	**3.95**	20.90	8.45	12.21	58.4	23.42	9.47	13.68	65.48
13M1-U20	27/08/2013	**111.02**	**9.38**	**5.92**	3.46	**4.44**	28.84	9.50	11.84	49.8	32.02	10.54	13.14	55.32
13M1-U21	12/09/2013	**104.84**	**9.00**	**5.64**	3.36	**3.89**	27.96	8.32	11.28	52.4	29.31	8.73	11.83	54.97
13M1-U22	28/09/2013	**134.56**	**9.73**	**6.69**	3.04	**4.21**	25.28	9.00	13.38	52.3	34.02	12.11	18.01	70.42
13M1-U23	14/10/2013	**99.84**	**10.78**	**6.52**	4.26	**3.97**	35.50	8.49	13.03	43.0	35.45	8.48	13.01	42.90
13M1-U24	30/10/2013	**77.15**	**10.40**	**6.49**	3.91	**3.75**	32.58	8.03	12.98	46.4	25.14	6.20	10.01	35.81

M2-upper	mid sampling date	total mass flux mg m^{-2} d^{-1}	TC wt%	TOC wt%	TIC wt%	BSi wt%	$CaCO_3$ wt%	$BSiO_2$ wt%	OM wt%	Residual wt%	$CaCO_3$ mg m^{-2} d^{-1}	$BSiO_2$ mg m^{-2} d^{-1}	OM mg m^{-2} d^{-1}	Residual mg m^{-2} d^{-1}
13M2-U1	27/10/2012	**50.75**	**10.66**	**5.76**	4.90	**1.75**	40.80	3.73	11.51	44.0	20.70	1.89	5.84	22.31
13M2-U2	12/11/2012	**23.31**	**11.41**	**6.07**	5.34	**1.98**	44.52	4.23	12.14	39.1	10.38	0.99	2.83	9.12
13M2-U3	28/11/2012	**43.25**	**13.72**	**8.13**	5.59	**4.02**	46.59	8.61	16.25	28.6	20.15	3.72	7.03	12.35
13M2-U4	14/12/2012	**35.33**	**13.37**	**8.00**	5.37	**2.27**	44.72	4.85	16.01	34.4	15.80	1.71	5.66	12.16
13M2-U5	30/12/2012	**45.42**	**12.17**	**5.17**	7.00	**1.89**	58.30	4.03	10.34	27.3	26.48	1.83	4.70	12.41
13M2-U6	15/01/2013	**41.23**	**12.24**	**4.88**	7.36	**1.72**	61.28	3.68	9.76	25.3	25.27	1.52	4.03	10.42
13M2-U7	31/01/2013	**47.92**	**12.02**	**4.29**	7.74	**2.22**	64.44	4.74	8.57	22.2	30.88	2.27	4.11	10.66
13M2-U8	16/02/2013	**42.23**	**12.62**	**6.24**	6.37	**3.70**	53.09	7.91	12.49	26.5	22.42	3.34	5.27	11.20
13M2-U9	04/03/2013	**93.67**	**13.16**	**5.79**	7.37	**3.19**	61.38	6.82	11.58	20.2	57.50	6.39	10.85	18.94
13M2-U10	20/03/2013	**30.42**	**11.51**	**5.93**	5.58	**3.54**	46.50	7.57	11.86	34.1	14.15	2.30	3.61	10.37
13M2-U11	05/04/2013	**31.28**	**12.74**	**5.39**	7.35	**3.57**	61.19	7.63	10.78	20.4	19.14	2.39	3.37	6.38
13M2-U12	21/04/2013	**53.77**	**12.83**	**3.62**	9.21	**2.30**	76.72	4.93	7.23	11.1	41.25	2.65	3.89	5.98
13M2-U13	07/05/2013	**24.30**	**13.23**	**5.97**	7.25	**3.21**	60.43	6.86	11.94	20.8	14.68	1.67	2.90	5.05
13M2-U14	23/05/2013	**22.20**	**12.66**	**5.15**	7.51	**3.62**	62.53	7.75	10.31	19.4	13.88	1.72	2.29	4.31
13M2-U15	08/06/2013	**48.53**	**12.34**	**5.43**	6.91	**3.02**	57.55	6.47	10.86	25.1	27.93	3.14	5.27	12.19
13M2-U16	24/06/2013	**42.31**	**11.66**	**5.24**	6.42	**3.09**	53.52	6.61	10.48	29.4	22.64	2.80	4.43	12.44
13M2-U17	10/07/2013	**64.14**	**11.46**	**4.95**	6.51	**3.08**	54.20	6.59	9.90	29.3	34.76	4.22	6.35	18.80
13M2-U18	26/07/2013	**43.53**	**12.16**	**4.59**	7.57	**2.81**	63.05	6.00	9.19	21.8	27.45	2.61	4.00	9.47
13M2-U19	11/08/2013	**25.42**	**12.11**	**6.26**	5.85	**2.44**	48.69	5.22	12.52	33.6	12.38	1.33	3.18	8.53
13M2-U20	27/08/2013	**20.55**	**12.17**	**5.30**	6.87	**2.29**	57.23	4.90	10.60	27.3	11.76	1.01	2.18	5.60
13M2-U21	12/09/2013	**35.05**	**12.45**	**6.60**	5.85	**2.49**	48.75	5.33	13.20	32.7	17.08	1.87	4.63	11.47
13M2-U22	28/09/2013	**29.31**	**12.09**	**5.44**	6.65	**2.41**	55.37	5.16	10.89	28.6	16.23	1.51	3.19	8.38
13M2-U23	14/10/2013	**23.17**	**13.09**	**7.19**	5.90	**2.32**	49.18	4.96	14.38	31.5	11.39	1.15	3.33	7.30
13M2-U24	30/10/2013	**31.95**	**13.40**	**6.81**	6.59	**2.17**	54.88	4.64	13.62	26.9	17.54	1.48	4.35	8.58

M2-lower	mid sampling date	total mass flux mg m^{-2} d^{-1}	TC wt%	TOC wt%	TIC wt%	BSi wt%	$CaCO_3$ wt%	$BSiO_2$ wt%	OM wt%	Residual wt%	$CaCO_3$ mg m^{-2} d^{-1}	$BSiO_2$ mg m^{-2} d^{-1}	OM mg m^{-2} d^{-1}	Residual mg m^{-2} d^{-1}
13M2-L1	27/10/2012	**47.14**	**10.05**	**4.20**	5.85	**2.32**	48.76	4.95	8.39	37.9	22.98	2.34	3.96	17.87
13M2-L2	12/11/2012	**46.78**	**9.92**	**4.69**	5.24	**2.62**	43.61	5.59	9.37	41.4	20.40	2.62	4.38	19.37
13M2-L3	28/11/2012	**59.36**	**10.61**	**3.23**	7.38	**2.40**	61.49	5.13	6.46	26.9	36.50	3.04	3.84	15.98
13M2-L4	14/12/2012	**57.78**	**11.11**	**4.72**	6.39	**2.92**	53.26	6.24	9.43	31.1	30.78	3.60	5.45	17.95
13M2-L5	30/12/2012	**53.50**	**10.31**	**3.91**	6.40	**1.98**	53.34	4.25	7.82	34.6	28.54	2.27	4.18	18.51
13M2-L6	15/01/2013	**54.63**	**10.52**	**3.35**	7.17	**1.76**	59.73	3.77	6.70	29.8	32.63	2.06	3.66	16.28
13M2-L7	31/01/2013	**51.30**	**10.56**	**3.71**	6.85	**1.75**	57.07	3.74	7.41	31.8	29.28	1.92	3.80	16.30
13M2-L8	16/02/2013	**43.55**	**10.70**	**3.79**	6.91	**2.30**	57.56	4.92	7.58	29.9	25.07	2.14	3.30	13.04
13M2-L9	04/03/2013	**79.01**	**11.39**	**2.74**	8.65	**2.15**	72.07	4.60	5.48	17.8	56.94	3.63	4.33	14.10
13M2-L10	20/03/2013	**42.06**	**10.85**	**3.84**	7.02	**3.31**	58.44	7.09	7.68	26.8	24.58	2.98	3.23	11.27
13M2-L11	05/04/2013	**43.02**	**10.84**	**3.64**	7.20	**3.02**	60.00	6.45	7.27	26.3	25.82	2.77	3.13	11.30
13M2-L12	21/04/2013	**81.35**	**11.41**	**2.39**	9.03	**2.06**	75.18	4.41	4.78	15.6	61.16	3.58	3.89	12.72
13M2-L13	07/05/2013	**60.83**	**11.10**	**3.81**	7.29	**3.31**	60.71	7.07	7.62	24.6	36.93	4.30	4.63	14.96
13M2-L14	23/05/2013	**47.89**	**11.18**	**4.27**	6.90	**3.33**	57.48	7.12	8.55	26.8	27.53	3.41	4.09	12.86
13M2-L15	08/06/2013	**58.43**	**11.28**	**2.64**	8.63	**2.84**	71.90	6.08	5.29	16.7	42.01	3.55	3.09	9.78
13M2-L16	24/06/2013	**55.77**	**10.69**	**2.92**	7.77	**2.79**	64.73	5.98	5.85	23.4	36.10	3.33	3.26	13.08
13M2-L17	10/07/2013	**54.76**	**10.49**	**3.19**	7.30	**2.59**	60.81	5.53	6.38	27.3	33.30	3.03	3.49	14.94
13M2-L18	26/07/2013	**64.00**	**10.62**	**2.94**	7.68	**2.64**	63.95	5.64	5.88	24.5	40.93	3.61	3.76	15.70
13M2-L19	11/08/2013	**45.12**	**10.42**	**4.24**	6.18	**3.11**	51.49	6.65	8.48	33.4	23.23	3.00	3.83	15.06
13M2-L20	27/08/2013	**47.09**	**10.20**	**3.20**	7.00	**3.01**	58.29	6.45	6.40	28.9	27.45	3.04	3.01	13.59
13M2-L21	12/09/2013	**51.23**	**10.12**	**4.31**	5.80	**3.22**	48.32	6.90	8.63	36.2	24.76	3.53	4.42	18.52
13M2-L22	28/09/2013	**56.07**	**10.24**	**4.69**	5.56	**3.16**	46.28	6.76	9.37	37.6	25.95	3.79	5.25	21.07
13M2-L23	14/10/2013	**54.70**	**10.69**	**4.33**	6.37	**2.73**	53.03	5.85	8.65	32.5	29.01	3.20	4.73	17.76
13M2-L24	30/10/2013	**55.27**	**10.68**	**3.31**	7.37	**3.04**	61.38	6.51	6.62	25.5	33.92	3.60	3.66	14.09

M3-lower	mid sampling date	total mass flux mg m^{-2} d^{-1}	TC wt%	TOC wt%	TIC wt%	BSi wt%	$CaCO_3$ wt%	$BSiO_2$ wt%	OM wt%	Residual wt%	$CaCO_3$ mg m^{-2} d^{-1}	$BSiO_2$ mg m^{-2} d^{-1}	OM mg m^{-2} d^{-1}	Residual mg m^{-2} d^{-1}
13M3-L1	27/10/2012	**47.28**	**9.45**	**5.23**	4.23	**3.21**	35.20	6.88	10.46	47.5	16.64	3.25	4.94	22.44
13M3-L2	12/11/2012	**58.49**	**9.18**	**5.01**	4.17	**3.30**	34.72	7.05	10.03	48.2	20.30	4.12	5.86	28.19
13M3-L3	28/11/2012	**55.22**	**9.63**	**4.33**	5.30	**2.67**	44.16	5.70	8.67	41.5	24.38	3.15	4.79	22.90
13M3-L4	14/12/2012	**52.74**	**9.79**	**4.17**	5.62	**2.40**	46.82	5.14	8.34	39.7	24.69	2.71	4.40	20.94
13M3-L5	30/12/2012	**93.59**	**10.80**	**3.25**	7.55	**1.48**	62.90	3.17	6.49	27.4	58.87	2.97	6.08	25.68
13M3-L6	15/01/2013	**63.27**	**10.59**	**3.74**	6.85	**2.45**	57.06	5.25	7.49	30.2	36.10	3.32	4.74	19.11
13M3-L7	31/01/2013	**56.66**	**10.35**	**4.25**	6.11	**3.64**	50.87	7.79	8.49	32.8	28.82	4.41	4.81	18.61
13M3-L8	16/02/2013	**51.34**	**10.02**	**4.20**	5.82	**3.97**	48.51	8.49	8.39	34.6	24.90	4.36	4.31	17.77
13M3-L9	04/03/2013	**78.14**	**10.48**	**3.71**	6.77	**3.07**	56.43	6.56	7.42	29.6	44.09	5.12	5.80	23.13
13M3-L10	20/03/2013	**55.56**	**9.98**	**4.72**	5.25	**4.11**	43.76	8.79	9.45	38.0	24.31	4.89	5.25	21.11
13M3-L11	05/04/2013	**61.03**	**10.28**	**3.91**	6.38	**3.26**	53.14	6.96	7.81	32.1	32.43	4.25	4.77	19.58
13M3-L12	21/04/2013	**87.58**	**11.28**	**2.34**	8.94	**2.31**	74.51	4.93	4.68	15.9	65.26	4.32	4.10	13.91
13M3-L13	07/05/2013	**48.63**	**10.71**	**3.86**	6.85	**3.86**	57.07	8.26	7.73	26.9	27.75	4.02	3.76	13.10
13M3-L14	23/05/2013	**62.08**	**11.53**	**4.78**	6.75	**3.66**	56.24	7.83	9.57	26.4	34.91	4.86	5.94	16.37
13M3-L15	08/06/2013	**124.88**	**11.50**	**3.87**	7.64	**2.37**	63.61	5.08	7.73	23.6	79.43	6.34	9.65	29.46
13M3-L16	24/06/2013	**122.76**	**10.87**	**4.31**	6.56	**2.51**	54.68	5.37	8.62	31.3	67.12	6.60	10.58	38.46
13M3-L17	10/07/2013	**86.39**	**10.78**	**4.78**	6.00	**3.61**	49.94	7.72	9.57	32.8	43.14	6.67	8.27	28.31
13M3-L18	26/07/2013	**64.81**	**10.54**	**4.15**	6.39	**4.00**	53.22	8.55	8.31	29.9	34.49	5.54	5.38	19.39
13M3-L19	11/08/2013	**73.79**	**10.69**	**5.09**	5.61	**3.93**	46.69	8.41	10.18	34.7	34.45	6.20	7.51	25.62
13M3-L20	27/08/2013	**70.71**	**10.02**	**4.41**	5.62	**4.20**	46.80	8.98	8.81	35.4	33.09	6.35	6.23	25.04
13M3-L21	12/09/2013	**60.99**	**9.83**	**4.55**	5.28	**4.48**	44.01	9.59	9.10	37.3	26.84	5.85	5.55	22.75
13M3-L22	28/09/2013	**70.11**	**10.01**	**4.75**	5.26	**4.15**	43.82	8.87	9.50	37.8	30.72	6.22	6.66	26.51
13M3-L23	14/10/2013	**79.31**	**9.77**	**4.23**	5.54	**3.81**	46.18	8.16	8.46	37.2	36.63	6.47	6.71	29.50
13M3-L24	30/10/2013	**63.23**	**9.58**	**4.14**	5.44	**3.76**	45.29	8.05	8.29	38.4	28.64	5.09	5.24	24.26

M4-upper	mid sampling date	total mass flux mg m^{-2} d^{-1}	TC wt%	TOC wt%	TIC wt%	BSi wt%	$CaCO_3$ wt%	$BSiO_2$ wt%	OM wt%	Residual wt%	$CaCO_3$ mg m^{-2} d^{-1}	$BSiO_2$ mg m^{-2} d^{-1}	OM mg m^{-2} d^{-1}	Residual mg m^{-2} d^{-1}
13M4-U1	27/10/2012	**38.63**	**10.66**	**5.89**	4.77	**2.16**	39.72	4.62	11.78	43.9	15.35	1.78	4.55	16.95
13M4-U2	12/11/2012	**51.53**	**11.11**	**5.26**	5.85	**1.94**	48.73	4.15	10.51	36.6	25.11	2.14	5.42	18.87
13M4-U3	28/11/2012	**62.52**	**11.90**	**6.43**	5.46	**3.15**	45.52	6.75	12.87	34.9	28.46	4.22	8.04	21.80
13M4-U4	14/12/2012	**51.98**	**11.48**	**5.64**	5.84	**3.13**	48.64	6.69	11.28	33.4	25.28	3.48	5.86	17.36
13M4-U5	30/12/2012	**58.45**	**11.91**	**4.61**	7.30	**3.23**	60.81	6.90	9.21	23.1	35.54	4.03	5.38	13.49
13M4-U6	15/01/2013	**77.57**	**11.38**	**4.33**	7.04	**5.04**	58.68	10.79	8.67	21.9	45.52	8.37	6.72	16.96
13M4-U7	31/01/2013	**88.93**	**11.23**	**5.41**	5.83	**6.90**	48.54	14.76	10.81	25.9	43.16	13.13	9.62	23.03
13M4-U8	16/02/2013	**78.71**	**11.28**	**4.23**	7.05	**5.11**	58.73	10.93	8.46	21.9	46.22	8.60	6.66	17.22
13M4-U9	04/03/2013	**66.37**	**10.25**	**4.96**	5.29	**6.63**	44.08	14.19	9.92	31.8	29.26	9.42	6.58	21.11
13M4-U10	20/03/2013	**55.73**	**10.38**	**5.75**	4.64	**6.75**	38.62	14.44	11.50	35.4	21.53	8.05	6.41	19.75
13M4-U11	05/04/2013	**63.13**	**11.00**	**4.85**	6.14	**5.52**	51.17	11.81	9.71	27.3	32.30	7.45	6.13	17.24
13M4-U12	21/04/2013	**230.50**	**14.78**	**7.54**	7.24	**3.17**	60.29	6.78	15.09	17.9	138.96	15.62	34.77	41.15
13M4-U13	07/05/2013	**58.49**	**12.68**	**7.01**	5.67	**4.78**	47.21	10.23	14.02	28.5	27.62	5.99	8.20	16.69
13M4-U14	23/05/2013	**85.92**	**13.32**	**6.73**	6.59	**4.13**	54.87	8.83	13.47	22.8	47.14	7.59	11.57	19.62
13M4-U15	08/06/2013	**99.05**	**12.57**	**5.08**	7.49	**3.43**	62.38	7.34	10.17	20.1	61.79	7.27	10.07	19.93
13M4-U16	24/06/2013	**115.30**	**11.61**	**5.21**	6.40	**3.22**	53.29	6.88	10.43	29.4	61.45	7.93	12.02	33.90
13M4-U17	10/07/2013	**77.33**	**11.62**	**5.06**	6.56	**3.62**	54.65	7.74	10.13	27.5	42.26	5.98	7.83	21.25
13M4-U18	26/07/2013	**102.83**	**11.27**	**5.63**	5.65	**3.70**	47.06	7.91	11.25	33.8	48.39	8.14	11.57	34.73
13M4-U19	11/08/2013	**63.00**	**11.39**	**5.51**	5.88	**3.75**	48.97	8.03	11.02	32.0	30.85	5.06	6.94	20.15
13M4-U20	27/08/2013	**50.45**	**11.20**	**5.25**	5.95	**3.56**	49.56	7.62	10.50	32.3	25.01	3.84	5.30	16.30
13M4-U21	12/09/2013	**55.17**	**11.55**	**6.22**	5.33	**3.65**	44.38	7.80	12.44	35.4	24.49	4.30	6.86	19.52
13M4-U22	28/09/2013	**79.55**	**13.02**	**7.87**	5.15	**3.72**	42.91	7.95	15.74	33.4	34.14	6.33	12.52	26.57
13M4-U23	14/10/2013	**50.57**	**12.23**	**6.26**	5.97	**3.93**	49.76	8.41	12.51	29.3	25.16	4.25	6.33	14.82
13M4-U24	30/10/2013	**272.86**	**12.32**	**9.30**	3.02	**11.48**	25.14	24.56	18.60	31.7	68.59	67.02	50.76	86.50

M4-lower	mid sampling date	total mass flux mg m^{-2} d^{-1}	TC wt%	TOC wt%	TIC wt%	BSi wt%	$CaCO_3$ wt%	$BSiO_2$ wt%	OM wt%	Residual wt%	$CaCO_3$ mg m^{-2} d^{-1}	$BSiO_2$ mg m^{-2} d^{-1}	OM mg m^{-2} d^{-1}	Residual mg m^{-2} d^{-1}
13M4-L1	27/10/2012	**38.37**	**9.72**	**3.84**	5.88	**2.86**	48.96	6.12	7.68	37.2	18.78	2.35	2.95	14.29
13M4-L2	12/11/2012	**51.47**	**9.84**	**3.88**	5.96	**2.76**	49.66	5.91	7.76	36.7	25.56	3.04	3.99	18.88
13M4-L3	28/11/2012	**67.37**	**9.76**	**3.81**	5.95	**3.15**	49.56	6.74	7.62	36.1	33.39	4.54	5.13	24.30
13M4-L4	14/12/2012	**73.53**	**9.61**	**3.37**	6.24	**3.61**	51.98	7.71	6.73	33.6	38.22	5.67	4.95	24.69
13M4-L5	30/12/2012	**66.77**	**9.53**	**3.97**	5.57	**4.00**	46.37	8.55	7.94	37.1	30.96	5.71	5.30	24.80
13M4-L6	15/01/2013	**77.62**	**9.89**	**3.09**	6.80	**3.98**	56.60	8.52	6.19	28.7	43.94	6.61	4.80	22.27
13M4-L7	31/01/2013	**78.30**	**10.03**	**3.54**	6.50	**6.10**	54.12	13.06	7.07	25.7	42.38	10.22	5.54	20.16
13M4-L8	16/02/2013	**77.16**	**10.34**	**3.73**	6.61	**3.64**	55.10	7.79	7.46	29.7	42.52	6.01	5.76	22.88
13M4-L9	04/03/2013	**38.31**	**10.44**	**3.83**	6.61	**4.14**	55.08	8.85	7.66	28.4	21.10	3.39	2.94	10.88
13M4-L10	20/03/2013	**37.67**	**9.79**	**4.03**	5.76	**5.68**	48.00	12.16	8.05	31.8	18.08	4.58	3.03	11.98
13M4-L11	05/04/2013	**36.22**	**10.26**	**3.33**	6.93	**4.75**	57.76	10.15	6.66	25.4	20.92	3.68	2.41	9.21
13M4-L12	21/04/2013	**136.31**	**13.31**	**4.49**	8.82	**3.27**	73.48	6.99	8.97	10.6	100.16	9.53	12.23	14.40
13M4-L13	07/05/2013	**67.82**	**13.29**	**7.19**	6.10	**4.90**	50.78	10.49	14.38	24.3	34.44	7.11	9.75	16.51
13M4-L14	23/05/2013	**53.53**	**10.60**	**3.81**	6.79	**4.29**	56.54	9.18	7.62	26.7	30.27	4.91	4.08	14.27
13M4-L15	08/06/2013	**84.48**	**11.38**	**3.67**	7.71	**3.37**	64.23	7.21	7.33	21.2	54.26	6.09	6.19	17.93
13M4-L16	24/06/2013	**69.65**	**10.93**	**3.07**	7.86	**3.48**	65.51	7.43	6.14	20.9	45.63	5.18	4.27	14.57
13M4-L17	10/07/2013	**73.50**	**10.71**	**4.22**	6.49	**3.50**	54.07	7.49	8.44	30.0	39.74	5.51	6.20	22.05
13M4-L18	26/07/2013	**80.06**	**10.26**	**4.10**	6.16	**4.49**	51.34	9.61	8.19	30.9	41.10	7.69	6.56	24.71
13M4-L19	11/08/2013	**30.95**	**10.78**	**3.73**	7.05	**3.47**	58.73	7.42	7.46	26.4	18.18	2.30	2.31	8.17
13M4-L20	27/08/2013	**27.65**	**10.14**	**3.57**	6.57	**4.01**	54.76	8.58	7.13	29.5	15.14	2.37	1.97	8.17
13M4-L21	12/09/2013	**33.26**	**9.72**	**4.10**	5.62	**4.33**	46.82	9.27	8.21	35.7	15.57	3.08	2.73	11.87
13M4-L22	28/09/2013	**29.86**	**10.77**	**4.50**	6.27	**3.80**	52.20	8.12	9.01	30.7	15.58	2.42	2.69	9.16
13M4-L23	14/10/2013	**28.65**	**10.46**	**4.07**	6.39	**3.69**	53.25	7.90	8.13	30.7	15.26	2.26	2.33	8.80
13M4-L24	30/10/2013	**166.74**	**11.78**	**8.43**	3.36	**13.89**	27.98	29.70	16.85	25.5	46.65	49.53	28.10	42.47

M5-lower	mid sampling date	total mass flux mg m^{-2} d^{-1}	TC wt%	TOC wt%	TIC wt%	BSi wt%	$CaCO_3$ wt%	$BSiO_2$ wt%	OM wt%	Residual wt%	$CaCO_3$ mg m^{-2} d^{-1}	$BSiO_2$ mg m^{-2} d^{-1}	OM mg m^{-2} d^{-1}	Residual mg m^{-2} d^{-1}
13M5-L1	27/10/2012	**99.50**	**7.25**	**2.35**	4.90	**7.55**	40.84	16.14	4.70	38.3	40.64	16.06	4.68	38.12
13M5-L2	12/11/2012	**124.92**	**7.55**	**4.00**	3.55	**6.40**	29.56	13.68	8.01	48.8	36.93	17.09	10.00	60.90
13M5-L3	28/11/2012	**103.39**	**6.52**	**2.42**	4.10	**7.43**	34.13	15.90	4.85	45.1	35.29	16.44	5.01	46.65
13M5-L4	14/12/2012	**83.78**	**7.09**	**3.35**	3.74	**6.32**	31.13	13.52	6.71	48.6	26.08	11.33	5.62	40.75
13M5-L5	30/12/2012	**75.42**	**7.64**	**2.55**	5.09	**5.25**	42.38	11.23	5.10	41.3	31.96	8.47	3.85	31.14
13M5-L6	15/01/2013	**122.31**	**7.53**	**3.11**	4.42	**5.52**	36.83	11.82	6.22	45.1	45.04	14.45	7.61	55.21
13M5-L7	31/01/2013	**128.41**	**7.03**	**2.74**	4.30	**7.20**	35.82	15.40	5.47	43.3	45.99	19.78	7.02	55.61
13M5-L8	16/02/2013	**84.54**	**7.60**	**2.38**	5.23	**5.01**	43.53	10.72	4.76	41.0	36.80	9.06	4.02	34.65
13M5-L9	04/03/2013	**139.34**	**7.57**	**2.12**	5.44	**4.34**	45.33	9.27	4.25	41.1	63.17	12.92	5.92	57.33
13M5-L10	20/03/2013	**121.19**	**7.50**	**3.25**	4.25	**4.90**	35.40	10.48	6.49	47.6	42.90	12.70	7.87	57.72
13M5-L11	05/04/2013	**220.38**	**5.59**	**3.15**	2.44	**7.78**	20.33	16.63	6.30	56.7	44.81	36.66	13.89	125.02
13M5-L12	21/04/2013	**199.31**	**6.15**	**2.34**	3.82	**5.17**	31.79	11.07	4.68	52.5	63.35	22.06	9.32	104.58
13M5-L13	07/05/2013	**155.03**	**6.45**	**2.45**	4.00	**6.67**	33.29	14.27	4.90	47.5	51.61	22.12	7.60	73.71
13M5-L14	23/05/2013	**144.19**	**6.72**	**3.10**	3.61	**7.72**	30.09	16.52	6.21	47.2	43.39	23.82	8.95	68.03
13M5-L15	08/06/2013	**139.83**	**6.40**	**3.26**	3.15	**8.92**	26.20	19.09	6.52	48.2	36.63	26.69	9.11	67.39
13M5-L16c	24/06/2013	**167.31**	**6.30**	**2.83**	3.46	**11.85**	28.83	25.35	5.67	40.2	48.24	42.41	9.48	67.18
13M5-L17	10/07/2013	**171.83**	**6.28**	**2.77**	3.51	**10.71**	29.25	22.90	5.55	42.3	50.27	39.35	9.53	72.68
13M5-L18	26/07/2013	**112.67**	**6.22**	**2.41**	3.81	**11.30**	31.72	24.16	4.83	39.3	35.74	27.22	5.44	44.27
13M5-L19	11/08/2013	**54.47**	**6.12**	**2.72**	3.41	**10.74**	28.38	22.97	5.43	43.2	15.46	12.51	2.96	23.54
13M5-L20	27/08/2013	**41.13**	**6.95**	**3.13**	3.83	**9.66**	31.87	20.66	6.25	41.2	13.11	8.50	2.57	16.95
13M5-L21	12/09/2013	**51.58**	**6.66**	**2.37**	4.29	**9.72**	35.75	20.80	4.73	38.7	18.44	10.73	2.44	19.97
13M5-L22	28/09/2013	**74.28**	**6.90**	**3.28**	3.62	**9.55**	30.17	20.43	6.57	42.8	22.41	15.17	4.88	31.82
13M5-L23	14/10/2013	**86.28**	**7.08**	**2.93**	4.16	**9.76**	34.63	20.88	5.85	38.6	29.88	18.01	5.05	33.34
13M5-L24	30/10/2013	**73.11**	**7.26**	**3.22**	4.04	**9.09**	33.67	19.44	6.44	40.4	24.62	14.21	4.71	29.57

Nederlandse samenvatting

Dit proefschrift gaat over de invloed en gevolgen van Saharastof sedimentatie in de equatoriale Atlantische Oceaan op 12° noorderbreedte, onder 's werelds grootste stofwolk. Voor het eerst wordt Saharastof gevolgd van de bron in de woestijn waar het opgewerveld wordt, tot in de oceaan waar het afgezet wordt. Langs een trans-Atlantisch transect van 23°W in het oosten naar 57°W in het westen werden op vijf stations sedimentvallen verankerd. De sedimentvallen verzamelden gelijktijdig en synchroon zowel alle uitzinkende stofkorrels als mariene deeltjes op 1200 m en 3500 m diepte over periodes van 16 dagen, van oktober 2012 tot en met oktober 2014. Tijdens drie scheepsexpedities werden de sedimentvallen uitgezet en weer teruggehaald, en werd Saharastof uit de atmosfeer verzameld aan boord van het schip. Daarnaast werden op twee scheepsexpedities incubatie-experimenten uitgevoerd en driftvallen uitgezet. Al deze observaties en metingen vormen essentiële onderdelen van dit proefschrift en worden gebruikt om de volgende vragen te beantwoorden:

1) Hoe groot is de deeltjesstroom naar de diepzee langs het transect door de tijd heen?
2) Hoeveel draagt de afzetting van Saharastof bij aan de bemesting van de oceaan?
3) Wat is de interactie tussen de uitstroom van de Amazone en de neerslag van Saharastof, stikstoffixatie door blauwalgen, en de verdieping van de menglaag in de westelijke Noord-Atlantische Oceaan?
4) Versnelt het Saharastof het bezinken van organisch materiaal?

De resultaten van deze studie geven nieuwe inzichten in de tot nu weinig bekende mariene deeltjesstromen onder invloed van woestijnstof in de open oceaan. Zij dragen bij aan onze kennis over de rol van woestijnstof in de globale koolstofcyclus en uiteindelijk het klimaat. Stofmetingen zijn belangrijk voor veel disciplines die zich met klimaatveranderingen in het verleden en de toekomst bezighouden. De verkregen data zijn cruciaal omdat zij bijdragen aan onze kennis over deeltjesstromen wereldwijd, en daarmee het voorspellen van toekomstige klimaatscenario's.

Uit de resultaten van het eerste jaar bleek al dat (1) de lithogene deeltjes in de diepzee volledig vergelijkbaar zijn met het Saharastof dat langs de Afrikaanse kust in de atmosfeer werd bemonsterd, en dat (2) de bijdrage van lithogene elementen (zoals aluminium, ijzer en kalium) met toenemende afstand van de bron verandert. Elementen die typisch met kleimineralen zijn geassocieerd nemen relatief toe, en elementen die met kwarts geassocieerd zijn nemen relatief af. Dat komt doordat de zware ronde kwartsdeeltjes dichter bij de bron bezinken dan de lichte vlakke kleimineralen. Omdat de hoeveelheid, grootte, en samenstelling van de stofdeeltjes

ook de stralingseigenschappen van het stof in de atmosfeer bepaalt, zijn ze van invloed op de inkomende zonnestraling en uitgaande warmtestraling van de aarde.

De lithogene deeltjesstroom blijkt seizoensafhankelijk. Tijdens de zomer en herfst is de hoeveelheid stof die zich het dichtst bij de bron op 12°N, 23°W bevindt het hoogst, en tijdens de winter en lente het laagst. Dit wordt toegeschreven aan de verschillende windsystemen in de zomer en de winter. Tijdens de zomer wordt het stof in de 'Saharan Air Layer' op grote hoogte getransporteerd en voornamelijk door regen (natte depositie) onder invloed van de 'Intertropical Convergence Zone' afgezet. In deze periode zijn de stofuitbraken op de locatie van de sedimentvallen duidelijk zichtbaar op de satellietbeelden in de hogere delen van de atmosfeer. In de winter wordt het stof op lagere hoogte getransporteerd, waardoor het zicht vanuit satellieten wordt bemoeilijkt door wolken. Daarnaast wordt het traceren van individuele stofuitbraken beperkt door een combinatie van de relatief lage bemonsteringresolutie van de sedimentvallen, de vertraging van de zinkende deeltjes van het oppervlaktewater naar de diepte van de sedimentvallen, en de laterale verspreiding van stof.

De hoeveelheid stof die door de sedimentvallen wordt verzameld, wordt doorgaans berekend op basis van het gewicht van alle deeltjes minus dat wat door plankton is gevormd, zoals calciumcarbonaat, organisch materiaal, en biogeen opaal. Voor die berekening worden doorgaans standaard omrekeningsfactoren gebruikt, maar die blijken de werkelijke stoffractie zwaar te overschatten, met name door de omrekening van het organische koolstofgehalte naar het gewicht van organisch materiaal en het negeren van water in het biogene opaal. Hoewel de algemene patronen wel overeenkwamen, bleek de werkelijke stoffractie tenminste 2 tot 18 keer lager dan eerder berekend met de traditionele omrekeningsfactoren.

De hoeveelheid Saharastof die in het oppervlaktewater terechtkomt is ook belangrijk voor de potentiële aanvoer van meststoffen die leiden tot een verhoogde primaire productie van algen. In hoeverre dat het geval is, werd onderzocht middels incubatie-experimenten tijdens een van de expedities, uitgevoerd met twee soorten Saharastof in lage en hoge concentraties, en met dezelfde korrelgrootte-verdeling als gemeten langs het transect. Om natte depositie te simuleren werd het stof eerst blootgesteld aan kunstmatig regenwater met dezelfde lage zuurgraad als in de atmosfeer. Voor droge depositie werd het stof zonder bewerking aan de incubatieflessen toegevoegd. Daarbij kwamen grote verschillen aan het licht: terwijl droge depositie niet leidde tot een toename van de meststoffen in het oceaanwater, resulteerde natte stofdepositie tot een verhoogde fosfaat-, kiezelzuur-, en ijzergehalte wanneer de stofconcentratie hoog was. Hoewel het experiment aantoonde dat Saharastof meststoffen kan afgeven,

bleef een duidelijk bemestingseffect op de algen, gemeten in de toename van het organisch koolstofgehalte, uit. Dit komt waarschijnlijk door een ontbrekende bron van stikstof in dit gedeelte van de Atlantische Oceaan. Toch kan Saharastof ook zonder bemestingseffect invloed hebben op de mariene deeltjesstroom, omdat het stof namelijk in aggregaten van organisch materiaal ('mariene sneeuw') kan worden opgenomen die daardoor zwaarder worden en sneller uitzinken. Zowel natte als droge depositie resulteerde in dezelfde organische koolstofconcentraties aan het einde van de incubatie-experimenten, wat er op wijst dat Saharastof de vorming en transport van mariene sneeuw stimuleert.

In de westelijke Atlantische Oceaan werd een combinatie van verschillende processen waargenomen die invloed kunnen hebben op de mariene deeltjes. Dit bleek toen in de herfst verdund rivierwater van de Amazone werd aangetroffen in de Atlantische Oceaan, veel noordwestelijker dan gedacht (12°N, 49°W). Dit seizoensgebonden fenomeen beïnvloedt het oceanische oppervlaktewater in sommige jaren sterk. De Amazone bleek de productiviteit van vooral blauwalgen en kiezelwieren enorm te verhogen, toevallig samenvallend met een verhoogde natte depositie van Saharastof. Beide processen hadden mogelijk een productieverhogend effect op kalkalgen op een grotere diepte door verdieping van de menglaag, wat mede leidde tot een zeer hoge en snelle export van organische koolstof naar de diepzee.

Terwijl de droge stofdepositie domineert in de winter en de lente, neemt de natte stofdepositie in de zomer en herfst toe door de toename van de neerslag. De natte stofdepositie en organische koolstofstroom laten een sterke correlatie zien. Dit suggereert dat Saharastof zowel de primaire productiviteit in de ondiepe oceaan kan stimuleren, alsmede de aggregaten van organische koolstof kan ballasten. Beide processen die van belang zijn voor een doeltreffende onttrekking uit de atmosfeer van CO_2, en CO_2 afvoer naar de zeebodem. De ballasttheorie werd met drijfvallen onder natuurlijke omstandigheden getest in tien experimenten op vijf stations, tijdens twee expedities. De drijfvallen verzamelden mariene deeltjes gedurende 24 uur op drie verschillende dieptes (100, 200 en 400 m). Om de afbraak van organische koolstof en stikstof te bepalen, werd gekeken naar de verhouding van organische kool- en stikstof in de mariene aggregaten. Omdat stikstofcomponenten in organisch materiaal sneller worden afgebroken, duidt een constante koolstof-stikstof verhouding op de verschillende dieptes op een snel transport (met lage afbraak door ballasting) van het Saharastof. In onze experimenten hadden we geluk met een stofuitbraak op tenminste één station tijdens beide expedities. Tijdens de meest krachtige uitbraak in januari 2015 bleef de verhouding van organische kool- en stikstof gelijk op alle dieptes,

terwijl die in een stofvrije atmosfeer varieerden. Dit is een goede aanwijzing voor versneld transport door de waterkolom, aangedreven door Saharastof.

Samenvattend kan worden vastgesteld dat Saharastof de mariene deeltjesstroom in de equatoriale Atlantische Oceaan op verschillende manieren beïnvloedt. De bronnen van Saharastof produceren stofdeeltjes van verschillende samenstelling en grootte, die met de wind getransporteerd worden via actieve en seizoensafhankelijke windsystemen. Terwijl grof en zwaar stof dichtbij de bron wordt afgezet, wordt fijn en licht stof verder naar het westen en tot het Caraïbisch gebied getransporteerd. Door deze sortering wordt natte depositie met toenemende afstand vanaf de bron steeds belangrijker om fijne deeltjes die niet meer door de zwaartekracht worden afgezet, uit de atmosfeer te wassen. Tijdens het transport door de atmosfeer wordt het stof blootgesteld aan sterk verzuurde omstandigheden, waardoor voedingsstoffen en sporenmetalen uit het stof vrijkomen. Na deze atmosferische bewerking worden de voedingsstoffen gemakkelijker aan het zeewater afgegeven, vooral als ze door natte depositie in het water terechtkomen. Hoewel Saharastof de voor algen essentiële meststoffen in het oppervlaktewater verhoogt, ontbrak in de incubatie-experimenten een stikstofbron. Wanneer Saharastof in de atmosfeer met salpeterzuur in contact komt, kan dit de stikstofbron vormen die samen met de andere meststoffen de algengroei in Atlantische Oceaan stimuleert. Ook levert de verdieping van de menglaag stikstofrijke voedingsstoffen terug aan het oppervlaktewater, afkomstig uit de afbraak van organisch materiaal dat oorspronkelijk werd gevormd door blauwalgen en bepaalde kiezelalgen. Vooral in de warme voedingstofarme wateren van de westelijke Noord-Atlantische Oceaan produceert het samengaan van verschillende processen hoge deeltjesstromen die van belang zijn voor de koolstofcyclus. Bovendien levert de Amazone voedingsstoffen (vooral silica en ijzer) wanneer het rivierwater oostwaarts uitstroomt in de Noord-Atlantische Oceaan, die de regionale productie van blauwalgen en bepaalde kiezelwieren stimuleren. Als woestijnstof door natte depositie in de oceaan terechtkomt, brengt het (1) aanvullende voedingsstoffen, en (2) fungeert het als een ballast mineraal na opname in mariene sneeuw wat de export naar de diepzee versnelt. De exportstromen worden ook versneld na droge depositie, hoewel dit de concentraties van meststoffen in het oppervlakwater niet verhoogt. Van het oosten naar het westen nemen die exportstromen af, waarbij droge depositie in de winter domineert, en natte depositie in de zomer. Deze gradiënten suggereren dat verschillende stof-gerelateerde processen per seizoen en locatie overheersen, en afhankelijk van de mate van atmosferische bewerking, droge en/of natte depositie, bemesting en/of ballast, de omvang van de mariene deeltjesstroom, en daarmee de koolstofcyclus, bepalen.

Deutsche Zusammenfassung

Diese Dissertation beschäftigt sich mit den Auswirkungen von Saharastaubablagerungen im äquatorialen Nordatlantik unterhalb der weltgrößten Staubwolke bei 12° nördlicher Breite. Zum ersten Mal wurde die Saharastaub-ablagerung von der Quelle in der Sahara bis zur Senke im Atlantik überwacht. Entlang eines trans-Atlantik Transekts wurden an fünf Stationen, von 23°W im Osten bis hin zu 57°W im Westen, marine Sedimentfallen eingesetzt. Diese fingen den sinkenden marinen Partikelfluss simultan und synchron in 1200 m und 3500 m Wassertiefe von Oktober 2012 bis Oktober 2014 auf. Die Sedimentfallen wurden während drei Forschungsfahrten ausgesetzt und wieder eingeholt. Darüber hinaus wurden auf zwei weiteren Forschungsfahrten Flaschen-Inkubationsexperimente durchgeführt sowie Treibfallen ausgesetzt. Auf allen Ausfahrten wurde vom Schiff aus Staub aus der Atmosphäre gesammelt. All diese Beobachtungen und Messungen sind wesentliche Bestandteile dieser Arbeit, um die folgenden Fragen zu beantworten:

1) Wie hoch ist der Partikelfluss im Ozean entlang des Transekts durch die Zeit?
2) Wieviel trägt die Saharastaubablagerung zur Düngung des Ozeans bei?
3) Wie ist das Zusammenspiel vom Eintrag des Amazonas Flusswassers, der Saharastaubablagerung, Stickstofffixierung von Cyanobakterien und der Vertiefung der ozeanischen Mischungsschicht im westlichen Nordatlantik?
4) Beschleunigt der Saharastaub das Sinken von organischem Material?

Die Ergebnisse dieser Studie liefern neue Einblicke in die bisher wenig bekannten Partikelflüsse des offenen Ozeans und tragen zu unserer Kenntnis der Rolle des Staubs im globalen Kohlenstoffkreislauf, und letztendlich des globalen Klimas, bei. Da Staubmessungen für viele Disziplinen, die sich mit dem Klimawandel in der Vergangenheit und der Zukunft beschäftigen, von Interesse sind, sollen die hier gewonnenen Felddaten dazu beitragen, die globalen Partikelflüsse, sowie Vorhersagen zukünftiger Klimaszenarien, zu verfeinern.

Die Haupterkenntnisse aus dem ersten Probennahmejahr zeigen, dass (1) die lithogenen Partikel in den Sedimentfallen denen des Saharastaubs ähneln, der an der afrikanischen Küste aus der Atmosphäre gesammelt wurde und dass, (2) sich mit zunehmender Entfernung von der Staubquelle die Mineralogie des Staubes ändert. Lithogene Elemente, die mit Tonmineralen in Verbindung gebracht werden, nehmen relativ zu, während Elemente, die mit Quarz in Verbindung gebracht werden, relativ abnehmen. Letztere lagern sich näher an der Quelle ab. Es wird angenommen, dass die bevorzugte Partikelablagerung die Strahlungseigenschaften des Staubes in der Atmosphäre bestimmen und diese auf die einfallenden Sonnenstrahlen der Erde

Einfluss nehmen. Zudem hängen die Strahlungseigenschaften des Staubes auch von der Staubmenge und der Staubkorngröße ab.

Diese Studie zeigt, dass der lithogene Partikelfluss in den Sedimentfallen saisonal beeinflusst ist. Während des Sommers und Herbsts ist der lithogene Partikelfluss am dichtesten zur Staubquelle bei 12°N, 23°W am höchsten, während er im Winter und Frühling am niedrigsten ist. Dies wird den verschiedenen aktiven Windsystemen im Sommer und Winter zugeschrieben. Im Sommer wird der Staub in der 'Saharan Air Layer' in großen Höhen transportiert und mit Regen (nasser Deposition), unter Einfluss der innertropischen Konvergenzzone, abgelagert. Zu dieser Jahreszeit ist eine Rückverfolgung von Staubausbrüchen, die auf Satellitenbildern sichtbar sind, bis hin zur Ankunft in den Sedimentfallen am deutlichsten. Im Winter wird der Staub in niedrigeren Höhen transportiert, sodass Staubausbrüche auf Satellitenbildern durch Wolken verdeckt werden können. Zudem ist die Rückverfolgung von einzelnen Staubausbrüchen durch die niedrige Probennahmeauflösung der Sedimentfallen, der Zeitverzögerung der sinkenden marinen Partikel von der Oberfläche des Wassers bis hin zur Sedimentfallentiefe, und den lateralen Transport des Staubs, eingeschränkt.

Der lithogene Partikelfluss wurde aus dem totalen Partikelfluss berechnet, indem konventionelle Umrechnungsfaktoren für biogenes Kalziumkarbonat ($CaCO_3$), organisches Material (OM) und biogener Kieselsäure ($BSiO_2$) angewendet wurden. Die biogenen Flussraten wurden von der totalen Flussrate abgezogen, wodurch die lithogene (Staub)-Fraktion bestimmt wurde. Jedoch scheint die Anwendung dieser Umrechnungsfaktoren die lithogene Fraktion in dieser Studie zu überschätzen, insbesondere durch die Umrechnung von organischem Kohlenstoff zu organischem Material und das Ignorieren des Wassergehaltes in der biogenen Kieselsäure Fraktion. Tatsächlich war die gemessene Staubfraktion 2 bis 18 Mal niedriger als die unter der Verwendung der herkömmlichen Umrechnungsfaktoren berechnete Fraktion, obwohl sich die Muster entsprachen. Demzufolge muss man sich beim Arbeiten mit lithogenen Partikelflüssen, die von totalen Partikelflüssen bestimmt wurden, bewusst sein, wie die verschiedenen Fraktionen analysiert und interpretiert wurden.

Die Staubmenge, die in das Oberflächenwasser abgelagert wird, ist auch wichtig in Bezug auf den potentiellen Nährstoffeintrag des Staubes für die Primärproduktion. Zu welchem Ausmaß Saharastaub die marine Produktivität anregt, wurde mit Flaschen-Inkubationsexperimenten empirisch getestet. Zwei Saharastaubtypen mit Korngrößenverteilungen, die denen entlang des Transekts entsprechen, wurden in niedriger (0,25 mg L^{-1}) und hoher (1,5 mg L^{-1}) Konzentration zu den Inkubationsflaschen gegeben. Für die nasse Ablagerung wurde der Staub vorerst

künstlichem Regenwasser mit niedrigem pH (H_2SO_4, pH = 2) ausgesetzt, um die chemische Bearbeitung vom Staub in der Atmosphäre nachzuahmen. Für die trockene Ablagerung wurde der Staub unbearbeitet zu den Inkubationsflaschen gegeben. Die Ergebnisse von trockener und nasser Ablagerung zeigen große Unterschiede in der resultierenden Nährstoffkonzentration. Während die trockene Ablagerung zu keiner Erhöhung der Nährstoffkonzentration im Oberflächenwasser führt, führt die nasse Staubablagerung zu einer erhöhten Phosphor (P), Silikat (Si) und gelösten Eisen (DFe) Konzentration, wenn die Staubkonzentration hoch ist. Allerdings, auch wenn das Experiment zeigte, dass Saharastaub das Potential hat, Makro- und Mikronährstoffe (P, Si, DFe) zu liefern, blieb ein Düngungseffekt des Phytoplanktons und die Produktion von organischen Kohlenstoff, ausgehend von diesen Nährstoffen, aus. Dies ist wahrscheinlich einer fehlenden Stickstoffquelle im stickstofflimitieren Atlantik zuzuschreiben. Jedoch könnte Saharastaub auch ohne Düngungseffekt einen Einfluss auf die marinen Partikel haben, indem er in den sogenannten ‚Meeresschnee' eingebaut wird. Der Meeresschnee wird durch den Saharastaub dichter und wird somit schwerer, sodass die gebildeten Aggregate schneller durch die Wassersäule sinken. Beide Ablagerungen – nass und trocken – resultierten in ähnlich hohen organischen Kohlenstoffkonzentrationen zum Ende des Inkubationsexperiments, was darauf hindeutet, dass die Meeresschneebildung mit Saharastaub in den Inkubationsflaschen effektiver ist. Allerdings konnte der Ballasteffekt als solcher in den Flaschenexperimenten nicht bestimmt werden, da die gebildeten Aggregate nicht aus den Flaschen exportiert werden.

Im westlichen Atlantik wurde eine Kombination aus verschiedenen Prozessen beobachtet, welche auf den marinen Partikelfluss einwirkten. Es wurde festgestellt, dass das Flusswasser des Amazonas zu den Zeiten, wenn der Nord-Brasilenstrom in den Nordatlantischen-Gegenstrom gelenkt wird, weit in den offenen Ozean des äquatorialen Westatlantiks bis zumindest 49°W und 12°N transportiert wird. Somit beeinflusst das Flusswasser das ozeanische Oberflächenwasser dort saisonal. Der Amazonas wirkte auf das Oberflächenwasser ein, indem er die cyanobakterielle Stickstofffixierung und die Diatomeen-diazotrophische Aktivität im Herbst anregte. XRF-Messungen zeigen, dass nahezu die gesamte Kieselsäure im westlichen Atlantik von marinen Algen (Diatomeen) produziert wurde. Zudem könnte die nasse Ablagerung von Saharastaub zu einer Eisendüngung geführt haben. Während somit die Nährstoffe im Herbst von oben in das Oberflächenwasser gelangten, wurden sie im Frühling von unten, durch die Vertiefung der Mischungsschicht in das untere Oberflächenwasser transportiert. Diese Nährstoffe lösten einen erhöhten Partikelfluss von Kalziumkarbonat aus.

Während im Winter und Frühling die trockene Staubablagerung vorherrscht, nimmt die nasse Ablagerung im Sommer und Herbst durch den steigenden Niederschlag zu. Saharastaubablagerung und der organische Kohlenstofffluss zeigen eine starke Korrelation während nasser Staubablagerung, was sowohl auf Düngung als auch auf Ballast von organischem Kohlenstoff durch Saharastaub hindeutet. Beide Prozesse sind relevant für eine effektive CO_2 Senke.

Die Ballasttheorie wurde letztendlich mit Treibfallen unter Naturbedingungen getestet. Treibfallen wurden in zehn Experimenten an fünf Stationen während zwei Forschungsfahrten ausgesetzt. Die Treibfallen sammelten marine Partikel in drei verschiedenen Tiefen (100, 200 und 400 m) für 24 Stunden. Molare Kohlenstoff (C) und Stickstoff (N) Verhältnisse von den marinen Partikeln wurden als Proxy verwendet, um den Abbau des organischen Kohlenstoffs und Stickstoffs zu bestimmen. Da N-Komponenten in organischem Material schneller abgebaut werden, zeigen stabile molare C/N Verhältnisse in den verschiedenen Tiefen einen durch Saharastaub beeinflussten schnelleren Partikeltransport mit geringem Abbau in der Wassersäule an. In unseren Experimenten hatten wir das Glück, einen Staubausbruch, zumindest an einer Station während beider Ausfahrten, zu erfahren. Für den stärkeren Ausbruch im Januar 2015 blieben die molaren C/N Verhältnisse stabil, während in einer staubfreien Atmosphäre die molaren C/N Verhältnisse mit der Tiefe variierten. Dies deutet auf einen beschleunigten Partikeltransport durch die Wassersäule an, der durch Saharastaubablagerung getrieben ist.

Zusammenfassend zeigt diese Dissertation, dass Saharastaub den marinen Partikelfluss im äquatorialen Nordatlantik auf mehreren Wegen beeinflusst. Die Saharastaubquellen emittieren Staubpartikel unterschiedlicher Mineralogie und Korngrößen, welche mit dem Wind transportiert werden, dessen aktives System von den Jahreszeiten abhängig ist. Während grobe und schwere Staubpartikel näher an der Quelle abgelagert werden, werden feine und flache Partikel sehr viel weiter nach Westen transportiert. Durch diesen Sortierungsgradienten wird die nasse Ablagerung mit zunehmender Distanz zur Quelle immer wichtiger um die feinen Partikel, die nicht mehr durch Gravitation abgelagert werden, aus der Atmosphäre zu waschen. Während des Transports durch die Atmosphäre ist der Staub sauren Bedingungen ausgesetzt, welche die Nährstoffe und Metalle, die für die Primärproduktion wichtig sind, von den Staubpartikeln lösen. Nach der atmosphärischen Bearbeitung werden die Nährstoffe vom Staub leichter an das Meerwasser abgegeben, besonders wenn sie mit nasser Ablagerung ins Wasser gelangen. In der Tat erhöht Saharastaub die für das Phytoplankton wichtigen Makro- und Mikro-Nährstoffkonzentrationen

(Phosphat, Silikat und gelöstes Eisen) im Oberflächenwasser. Allerdings bleibt eine Stickstoffzufuhr, die für das Phytoplankton im Nordatlantik unverzichtbar ist, aus. Eine Stickstoffzufuhr könnte jedoch auch vom Staub in den Ozean eingetragen werden, wenn der Staub in der Atmosphäre mit Salpetersäure (HNO_3) in Berührung gekommen ist. Stickstoff-Nährstoffe gelangen auch durch die Vertiefung der Mischungsschicht in das Oberflächenwasser, sowie durch den Abbau von organischem Material, welches durch diazotrophe Stickstofffixierer gebildet wurde. Besonders in den oligotrophen warmen Wässern des westlichen Nordatlantik erzeugt das Zusammentreffen der verschiedenen Prozesse hohe Partikelflüsse, die für den globalen organischen Kohlenstoffkreislauf relevant sind. Zudem liefert der Amazonas Nährstoffe (insbesondere Silikat und Eisen), wenn das Flusswasser nach Osten in den Nordatlantischen-Gegenstrom gelenkt wird und demzufolge die dortige Diatomeen-diazotrophische Aktivität und Stickstofffixierung anregt. Wenn Staub mit nasser Ablagerung in den Ozean eingetragen wird, bringt er (1) zusätzliche Nährstoffe und (2) agiert als Ballastmineral durch die Einbettung in Meeresschnee. Durch Letzteres wird der Partikelexport in die Tiefen des Ozeans beschleunigt. Die Exportflüsse werden auch von der trockenen Ablagerung beeinflusst. Zwar erhöht diese Ablagerung die Nährstoffkonzentrationen im Oberflächenwasser nicht, die Staubpartikel agieren jedoch noch stets als Ballastmaterial. Entlang des Transekts nehmen die Partikelflüsse mit dem Wind von Osten nach Westen ab, wobei die trockene Ablagerung im Winter und die nasse Ablagerung im Sommer dominiert. Dieser Ablagerungsgradient deutet verschiedene vorherrschende Prozesse an, die je nach atmosphärischer Staubbearbeitung, Saison und geographischer Lage, durch trockene und/oder nasse Ablagerung, Ballast und/oder Düngung, das Ausmaß des marinen Partikelflusses und damit den globalen Kohlenstoffkreislauf beeinflussen.

References

Adams, A. M., Prospero, J. M., and Zhang, C., **2012**. CALIPSO-Derived Three-Dimensional Structure of Aerosol over the Atlantic Basin and Adjacent Continents, *Journal of Climate*, 25(19), 6862–6879. https://doi.org/10.1175/JCLI-D-11-00672.1.

Albani, S., Mahowald, N. M., Perry, A. T., Scanza, R. A., Zender, C. S., Heavens, N. G., Maggi, V., Kok, J. F., and Otto-Bliesner, B. L., **2014**. Improved dust representation in the Community Atmosphere Model, *Journal of Advances in Modeling Earth Systems*, 6(3), 541-570. https://doi.org/10.1002/2013MS000279.

Alldredge, A. L., and Silver, M. W., **1988**. Characteristics, dynamics and significance of marine snow, *Progress in Oceanography*, 20(1), 41–82. https://doi.org/cb9rkr.

Anadón, R., Alvarez-Marqués, F., Fernández, E., Varela, M., Zapata, M., Gasol, J. M., and Vaqué, D., **2002**. Vertical biogenic particle flux during austral summer in the Antarctic Peninsula area, *Deep-Sea Research II*, 49(4–5), 883–901. https://doi.org/fcxpxx.

Armstrong, R. A., Lee, C., Hedges, J. I., Honjo, S., and Wakeham, S. G., **2001**. A new, mechanistic model for organic carbon fluxes in the ocean based on the quantitative association of POC with ballast minerals, *Deep-Sea Research II*, 49(1–3), 219–236. https://doi.org/fnb3dd.

Armstrong, R. A., Peterson, M. L., Lee, C., and Wakeham, S. G., **2009**. Settling velocity spectra and the ballast ratio hypothesis, *Deep-Sea Research II*, 56(18), 1470–1478. https://doi.org/10.1016/j.dsr2.2008.11.032.

Atkinson, J. D., Murray, B. J., Woodhouse, M. T., Whale, T. F., Baustian, K. J., Carslaw, K. S., Dobbie, S., O'Sullivan, D., and Malkin, T. L., **2013**. The importance of feldspar for ice nucleation by mineral dust in mixed-phase clouds, *Nature*, 498, 355. https://doi.org/10.1038/nature12278. https://www.nature.com/articles/nature12278#supplementary-information.

Avila, A., Queralt, I., Gallart, F., and Martin-Vide, J., **1996**. African Dust Over Northeastern Spain: Mineralogy and Source Regions, in: *The Impact of Desert Dust Across the Mediterranean*, edited by: Guerzoni, S., and Chester, R., Springer, Dordrecht, 201–205, https://doi.org/10.1007/978-94-017-3354-0_19.

Baker, A. R., Adams, C., Bell, T. G., Jickells, T. D., and Ganzeveld, L., **2013**. Estimation of atmospheric nutrient inputs to the Atlantic Ocean from 50°N to 50°S based on large-scale field sampling: Iron and other dust-associated elements, *Global Biogeochemical Cycles*, 27(3), 755–767. https://doi.org/10.1002/gbc.20062.

Baker, A. R., and Croot, P. L., **2010**. Atmospheric and marine controls on aerosol iron solubility in seawater, *Marine Chemistry*, 120(1–4), 4–13. https://doi.org/10.1016/j.marchem.2008.09.003.

Baker, A. R., Kelly, S. D., Biswas, K. F., Witt, M., and Jickells, T. D., **2003**. Atmospheric deposition of nutrients to the Atlantic Ocean, *Geophysical Research Letters*, 30(24). https://doi.org/10.1029/2003GL018518.

Baker, A. R., Lesworth, T., Adams, C., Jickells, T. D., and Ganzeveld, L., **2010**. Estimation of atmospheric nutrient inputs to the Atlantic Ocean from 50°N to 50°S based on large-scale field sampling: Fixed nitrogen and dry deposition of phosphorus, *Global Biogeochemical Cycles*, 24(3), n/a-n/a. https://doi.org/10.1029/2009GB003634.

Basha, G., Kishore, P., Venkat Ratnam, M., Ouarda, T. B. M. J., Velicogna, I., and Sutterley, T., **2015**. Vertical and latitudinal variation of the intertropical convergence zone derived using GPS radio occultation measurements, *Remote Sensing of Environment*, 163, 262-269. https://doi.org/10.1016/j.rse.2015.03.024.

Bauersachs, T., Schouten, S., Compaoré, J., Wollenzien, U., Stal, L. J., Damsteé, S., and Jaap, S., **2009**. Nitrogen isotopic fractionation associated with growth on dinitrogen gas and nitrate by cyanobacteria, *Limnology and Oceanography*, 54(4), 1403–1411. https://doi.org/10.4319/lo.2009.54.4.1403.

Beers, J. R., Steven, D. M., and Lewis, J. B., **1968**. Primary productivity in the Caribbean Sea off Jamaica and the tropical North Atlantic off Barbados, *Bulletin of Marine Science*, 18(1), 86–104. http://www.ingentaconnect.com/content/umrsmas/bullmar/1968/00000018/00000001/art00005.

Berelson, W. M., **2002**. Particle settling rates increase with depth in the ocean, *Deep-Sea Research II*, 49(1–3), 237–251. https://doi.org/bdhnsj.

Bergametti, G., Gomes, L., Remoudaki, E., Desbois, M., Martin, D., and Buat-Ménard, P., **1989**. Present transport and deposition patterns of African dusts to the north-western Mediterranean, in: *Paleoclimatology and Paleometeorology: Modern and Past Patterns of Global Atmospheric Transport*, edited by: Leinen M., and M., S., Springer, Dordrecht, 227–252, https://doi.org/10.1007/978-94-009-0995-3_9.

Berger, W. H., and Keir, R. S., **1984**. Glacial-Holocene changes in atmospheric CO_2 and the deep-sea record, in: *Climate Processes and Climate Sensitivity*, edited by: Hansen, J. E., and Takahashi, T., American Geophysical Union, Washington, D. C, 337–351, https://doi.org/10.1029/GM029p0337.

Blain, S., Guieu, C., Claustre, H., Leblanc, K., Moutin, T., Quèguiner, B., Ras, J., and Sarthou, G., **2004**. Availability of iron and major nutrients for phytoplankton in the northeast Atlantic Ocean, *Limnology and Oceanography*, 49(6), 2095–2104. https://doi.org/10.4319/lo.2004.49.6.2095.

Bonnet, S., Guieu, C., Chiaverini, J., Ras, J., and Stock, A., **2005**. Effect of atmospheric nutrients on the autotrophic communities in a low nutrient, low chlorophyll system, *Limnology and Oceanography*, 50(6), 1810–1819. https://doi.org/10.4319/lo.2005.50.6.1810.

Bonnin, J., Van Haren, H., Hosegood, P., and Brummer, G.-J. A., **2006**. Burst resuspension of seabed material at the foot of the continental slope in the Rockall Channel, *Marine Geology*, 226(3–4), 167–184. https://doi.org/10.1016/j.margeo.2005.11.006.

Boon, A. R., and Duineveld, G. C. A., **1996**. Phytopigments and fatty acids as molecular markers for the quality of near-bottom particulate organic matter in the North Sea, *Journal of Sea Research*, 35(4), 279–291. https://doi.org/cp5253.

Bory, A., Dulac, F., Moulin, C., Chiapello, I., Newton, P., Guelle, W., Lambert, C., and Bergametti, G., **2002**. Atmospheric and oceanic dust fluxes in the northeastern tropical Atlantic Ocean: how close a coupling?, *Annales Geophysicae*, 20(12), 2067–2076. https://hal.archives-ouvertes.fr/hal-00329324.

Bory, A., Jeandel, C., Leblond, N., Vangriesheim, A., Khripounoff, A., Beaufort, L., Rabouille, C., Nicolas, E., Tachikawa, K., Etcheber, H., and Buat-Ménard, P., **2001**. Downward particle fluxes within different productivity regimes off the Mauritanian upwelling zone (EUMELI program), *Deep-Sea Research I*, 48(10), 2251–2282. https://doi.org/chkgdz.

Bory, A. J. M., and Newton, P. P., **2000**. Transport of airborne lithogenic material down through the water column in two contrasting regions of the eastern subtropical North Atlantic Ocean, *Global Biogeochemical Cycles*, 14(1), 297–315. https://doi.org/10.1029/1999GB900098.

Bourlès, B., Gouriou, Y., and Chuchla, R., **1999**. On the circulation in the upper layer of the western equatorial Atlantic, *Journal of Geophysical Research*, 104(C9), 21151–21170. https://doi.org/10.1029/1999JC900058.

Boyd, P. W., Law, C. S., Wong, C. S., Nojiri, Y., Tsuda, A., Levasseur, M., Takeda, S., Rivkin, R., Harrison, P. J., Strzepek, R., Gower, J., McKay, R. M., Abraham, E., Arychuk, M., Barwell-Clarke, J., Crawford, W., Crawford, D., Hale, M., Harada, K., Johnson, K., Kiyosawa, H., Kudo, I., Marchetti, A., Miller, W., Needoba, J., Nishioka, J., Ogawa, H., Page, J., Robert, M., Saito, H., Sastri, A., Sherry, N., Soutar, T., Sutherland, N., Taira, Y., Whitney, F., Wong, S.-K. E., and Yoshimura, T., **2004**. The decline and fate of an iron-induced subarctic phytoplankton bloom, *Nature*, 428, 549–553. https://doi.org/10.1038/nature02437.

Boyd, P. W., Strzepek, R., Fu, F., and Hutchins, D. A., **2010**. Environmental control of open-ocean phytoplankton groups: Now and in the future, *Limnology and Oceanography*, 55(3), 1353–1376. https://doi.org/10.4319/lo.2010.55.3.1353.

Boyd, P. W., and Trull, T. W., **2007**. Understanding the export of biogenic particles in oceanic waters: Is there consensus?, *Progress in Oceanography*, 72(4), 276-312. https://doi.org/10.1016/j.pocean.2006.10.007.

Boyd, P. W., Watson, A. J., Law, C. S., Abraham, E. R., Trull, T., Murdoch, R., Bakker, D. C. E., Bowle, A. R., Buesseler, K. O., Chang, H., Charette, M., Croot, P., Downin, K., Frew, R., Gall, M., Hadfield, M., Hall, J., Harvey, M., Jameson, G., LaRoche, J., Liddicoat, M., Ling, R., Maldonado, M. T., McKay, R. M., Nodder, S., Pickmere, S., Pridmore, R., Rintoul, S., Safi, K., Sutton, P., Strzepek, R., Tanneberger, K., Turner, S., Walte, A., and Zeldis, J., **2000**. A mesoscale phytoplankton bloom in the polar Southern Ocean stimulated by iron fertilization, *Nature*, 407, 695–702. https://doi.org/10.1038/35037500.

Bressac, M., and Guieu, C., **2013**. Post-depositional processes: What really happens to new atmospheric iron in the ocean's surface?, *Global Biogeochemical Cycles*, 27(3), 859–870. https://doi.org/10.1002/gbc.20076.

Bressac, M., Guieu, C., Doxaran, D., Bourrin, F., Desboeufs, K., Leblond, N., and Ridame, C., **2014**. Quantification of the lithogenic carbon pump following a simulated dust-deposition event in large mesocosms, *Biogeosciences*, 11(4), 1007–1020. https://doi.org/10.5194/bg-11-1007-2014.

Bressac, M., Guieu, C., Doxaran, D., Bourrin, F., Obolensky, G., and Grisoni, J.-M., **2012**. A mesocosm experiment coupled with optical measurements to assess the fate and sinking of atmospheric particles in clear oligotrophic waters, *Geo-Marine Letters*, 32(2), 153–164. https://doi.org/10.1007/s00367-011-0269-4.

Bristow, C. S., Hudson-Edwards, K. A., and Chappell, A., **2010**. Fertilizing the Amazon and equatorial Atlantic with West African dust, *Geophysical Research Letters*, 37(14). https://doi.org/10.1029/2010gl043486.

Brummer, G. J. A., and van Eijden, A. J. M., **1992**. “Blue-ocean” paleoproductivity estimates from pelagic carbonate mass accumulation rates, *Marine Micropaleontology*, 19(1–2), 99–117. https://doi.org/brm5q8.

Brust, J., Schulz-Bull, D., Leipe, T., Chavagnac, V., and Waniek, J., **2011**. Descending particles: From the atmosphere to the deep ocean—A time series study in the subtropical NE Atlantic, *Geophysical Research Letters*, 38(6). https://doi.org/10.1029/2010GL045399.

Buck, C. S., Landing, W. M., Resing, J. A., and Measures, C. I., **2010**. The solubility and deposition of aerosol Fe and other trace elements in the North Atlantic Ocean: Observations from the A16N CLIVAR/CO_2 repeat hydrography section, *Marine Chemistry*, 120(1–4), 57–70. https://doi.org/10.1016/j.marchem.2008.08.003.

Buesseler, K. O., Antia, A. N., Chen, M., Fowler, S. W., Gardner, W. D., Gustafsson, O., Harada, K., Michaels, A. F., van der Loeff, M. R., and Sarin, M., **2007**. An assessment of the use of sediment traps for estimating upper ocean particle fuxes, *Journal of Marine Research*, 65, 345-416. https://doi.org/10.1357/002224007781567621.

Cachier, H., Liousse, C., Buat-Menard, P., and Gaudichet, A., **1995**. Particulate content of savanna fire emissions, *Journal of Atmospheric Chemistry*, 22(1–2), 123–148. https://doi.org/10.1007/BF00708185.

Capone, D. G., **2001**. Marine nitrogen fixation: what's the fuss?, *Current Opinion in Microbiology*, 4(3), 341–348. https://doi.org/cvz8pd.

Caquineau, S., Gaudichet, A., Gomes, L., and Legrand, M., **2002**. Mineralogy of Saharan dust transported over northwestern tropical Atlantic Ocean in relation to source regions, *Journal of Geophysical Research*, 107(D15), AAC 4-1–AAC 4-12. https://doi.org/10.1029/2000JD000247.

Carlson, T. N., and Prospero, J. M., **1972**. The large-scale movement of Saharan air outbreaks over the northern equatorial Atlantic, *Journal of Applied Meteorology*, 11(2), 283–297. https://doi.org/chz4zw.

Carpenter, E. J., Montoya, J. P., Burns, J., Mulholland, M. R., Subramaniam, A., and Capone, D. G., **1999**. Extensive bloom of a N_2-fixing diatom/cyanobacterial association in the tropical Atlantic Ocean, *Marine Ecology Progress Series*, 185, 273–283. http://www.jstor.org/stable/24853216.

Chester, R., Lin, F. J., and Murphy, K. J. T., **1989**. A three stage sequential leaching scheme for the characterisation of the sources and environmental mobility of trace metals in the marine aerosol, *Environmental Technology Letters*, 10(10), 887–900. https://doi.org/10.1080/09593338909384810.

Chiapello, I., Bergametti, G., Chatenet, B., Bousquet, P., Dulac, F., and Soares, E. S., **1997**. Origins of African dust transported over the northeastern tropical Atlantic, *Journal of Geophysical Research*, 102(D12), 13701–13709. https://doi.org/10.1029/97JD00259.

Chiapello, I., Bergametti, G., Gomes, L., Chatenet, B., Dulac, F., Pimenta, J., and Santos Suares, E., **1995**. An additional low layer transport of Sahelian and Saharan dust over the north-eastern tropical Atlantic, *Geophysical Research Letters*, 22(23), 3191–3194. https://doi.org/10.1029/95GL03313.

Chiapello, I., and Moulin, C., **2002**. TOMS and METEOSAT satellite records of the variability of Saharan dust transport over the Atlantic during the last two decades (1979–1997), *Geophysical Research Letters*, 29(8), 17-11–17-14. https://doi.org/10.1029/2001GL013767.

Coale, K. H., Johnson, K. S., Chavez, F. P., Buesseler, K. O., Barber, R. T., Brzezinski, M. A., Cochlan, W. P., Millero, F. J., Falkowski, P. G., Bauer, J. E., Wanninkhof, R. H., Kudela, R. M., Altabet, M. A., Hales, B. E., Takahashi, T., Landry, M. R., Bidigare, R. R., Wang, X., Chase, Z., Strutton, P. G., Friederich, G. E., Gorbunov, M. Y., Lance, V. P., Hilting, A. K., Hiscock, M. R., Demarest, M., Hiscock, W. T., Sullivan, K. F., Tanner, S. J., Gordon, R. M., Hunter, C. N., Elrod, V. A., Fitzwater, S. E., Jones, J. L., Tozzi, S., Koblizek, M., Roberts, A. E., Herndon, J., Brewster, J., Ladizinsky, N., Smith, G., Cooper, D., Timothy, D., Brown, S. L., Selph, K. E., Sheridan, C. C., Twining, B. S., and Johnson, Z. I., **2004**. Southern Ocean iron enrichment experiment: carbon cycling in High-and Low-Si waters, *Science*, 304(5669), 408–414. https://doi.org/10.1126/science.1089778.

Coale, K. H., Johnson, K. S., Fitzwater, S. E., Blain, S. P., Stanton, T. P., and Coley, T. L., **1998**. IronEx-I, an *in situ* iron-enrichment experiment: Experimental design, implementation and results, *Deep-Sea Research II*, 45(6), 919–945. https://doi.org/d6psxv.

Coale, K. H., Johnson, K. S., Fitzwater, S. E., Gordon, R. M., Tanner, S., Chavez, F. P., Ferioli, L., Sakamoto, C., Rogers, P., Millero, F., Steinberg, P., Nightingale, P., Cooper, D., Cochlan, W. P., Landry, M. R., Constantinou, J., Rollwagen, G., Trasvina, A., and Kudela, R., **1996**. A massive phytoplankton bloom induced by an ecosystem-scale iron fertilization experiment in the equatorial Pacific Ocean, *Nature*, 383, 495–501. https://doi.org/10.1038/383495a0.

Cooley, S., Coles, V., Subramaniam, A., and Yager, P., **2007**. Seasonal variations in the Amazon plume-related atmospheric carbon sink, *Global Biogeochemical Cycles*, 21(3). https://doi.org/10.1029/2006GB002831.

Creamean, J. M., Suski, K. J., Rosenfeld, D., Cazorla, A., DeMott, P. J., Sullivan, R. C., White, A. B., Ralph, F. M., Minnis, P., Comstock, J. M., Tomlinson, J. M., and Prather, K. A., **2013**. Dust and Biological Aerosols from the Sahara and Asia Influence Precipitation in the Western U.S, *Science*, 339(6127), 1572–1578. https://doi.org/10.1126/science.1227279.

Del Vecchio, R., and Subramaniam, A., **2004**. Influence of the Amazon River on the surface optical properties of the western tropical North Atlantic Ocean, *Journal of Geophysical Research*, 109(C11). https://doi.org/10.1029/2004JC002503.

DeMaster, D. J., **1981**. The supply and accumulation of silica in the marine environment, *Geochimica et Cosmochimica acta*, 45(10), 1715-1732. https://doi.org/fcw3dc.

DeMott, P. J., Sassen, K., Poellot, M. R., Baumgardner, D., Rogers, D. C., Brooks, S. D., Prenni, A. J., and Kreidenweis, S. M., **2003**. African dust aerosols as atmospheric ice nuclei, *Geophysical Research Letters*, 30(14), 1732. https://doi.org/10.1029/2003GL017410.

Desboeufs, K., Leblond, N., Wagener, T., Nguyen, E. B., and Guieu, C., **2014**. Chemical fate and settling of mineral dust in surface seawater after atmospheric deposition observed from dust seeding experiments in large mesocosms, *Biogeosciences*, 11(19), 5581–5594. https://doi.org/10.5194/bg-11-5581-2014.

Desboeufs, K. V., Losno, R., and Colin, J. L., **2001**. Factors influencing aerosol solubility during cloud processes, *Atmospheric Environment*, 35(20), 3529–3537. https://doi.org/dfzqtm.

Deuser, W., Muller-Karger, F., and Hemleben, C., **1988**. Temporal variations of particle fluxes in the deep subtropical and tropical North Atlantic: Eulerian versus Lagrangian effects, *Journal of Geophysical Research*, 93(C6), 6857–6862. https://doi.org/10.1029/JC093iC06p06857.

Deuser, W. G., Brewer, P. G., Jickells, T. D., and Commeau, R. F., **1983**. Biological control of the removal of abiogenic particles from the surface ocean, *Science*, 219(4583), 388–391. https://doi.org/10.1126/science.219.4583.388.

Dobson, M., and Fothergill, J., **1781**. An Account of the Harmattan, a Singular African Wind. By Matthew Dobson, MDFRS; Communicated by John Fothergill, MDFRS, *Philosophical Transactions of the Royal Society of London*, 71, 46–57.

Droop, M., **1973**. Some thoughts on nutrient limitation in algae, *Journal of Phycology*, 9(3), 264–272. https://doi.org/10.1111/j.1529-8817.1973.tb04092.x.

Dubief, J., **1979**. Review of the North African climate with particular emphasis on the production of eolian dust in the Sahel zone and in the Sahara, in: *Saharan dust: Mobilization, Transport, Deposition*, John Wiley & Sons, Chichester, 27–48.

Duce, R. A., Liss, P. S., Merrill, J. T., Atlas, E. L., Buat-Menard, P., Hicks, B. B., Miller, J. M., Prospero, J. M., Arimoto, R., Church, T. M., Ellis, W., Galloway, J. N., Hansen, L., Jickells, T. D., Knap, A. H., Reinhardt, K. H., Schneider, B., Soudine, A., Tokos, J. J., Tsunogai, S., Wollast, R., and Zhou, M., **1991**. The atmospheric input of trace species to the world ocean, *Global Biogeochemical Cycles*, 5(3), 193–259. https://doi.org/10.1029/91GB01778.

Dufois, F., Hardman-Mountford, N. J., Greenwood, J., Richardson, A. J., Feng, M., and Matear, R. J., **2016**. Anticyclonic eddies are more productive than cyclonic eddies in subtropical gyres because of winter mixing, *Science Advances*, 2(5). https://doi.org/10.1126/sciadv.1600282.

Dulac, F., Buat-Ménard, P., Ezat, U., Melki, S., and Bergametti, G., **1989**. Atmospheric input of trace metals to the western Mediterranean: uncertainties in modelling dry deposition from cascade impactor data, *Tellus B*, 41B(3), 362–378. https://doi.org/10.1111/j.1600-0889.1989.tb00315.x.

Eppley, R. W., and Peterson, B. J., **1979**. Particulate organic matter flux and planktonic new production in the deep ocean, *Nature*, 282, 677–680. https://doi.org/10.1038/282677a0.

Falkowski, P. G., **1997**. Evolution of the nitrogen cycle and its influence on the biological sequestration of CO_2 in the ocean, *Nature*, 387, 272–275. https://doi.org/10.1038/387272a0.

Falkowski, P. G., Barber, R. T., and Smetacek, V., **1998**. Biogeochemical Controls and Feedbacks on Ocean Primary Production, *Science*, 281(5374), 200–206. https://doi.org/10.1126/science.281.5374.200.

Filipsson, H. L., Romero, O. E., Stuut, J.-B. W., and Donner, B., **2011**. Relationships between primary productivity and bottom-water oxygenation off northwest Africa during the last deglaciation, *Journal of Quaternary Science*, 26(4), 448-456. https://doi.org/10.1002/jqs.1473.

Fischer, G., Donner, B., Ratmeyer, V., Davenport, R., and Wefer, G., **1996**. Distinct year-to-year particle flux variations off Cape Blanc during 1988-1991: Relation to delta δ^{18}O-deduced sea-surface temperatures and trade winds, *Journal of Marine Research*, 54(1), 73–98. https://doi.org/10.1357/0022240963213484.

Fischer, G., and Karakas, G., **2009**. Sinking rates and ballast composition of particles in the Atlantic Ocean: implications for the organic carbon fluxes to the deep ocean, *Biogeosciences*, 6(1), 85–102. https://doi.org/10.5194/bg-6-85-2009.

Fischer, G., Karakas, G., Blaas, M., Ratmeyer, V., Nowald, N., Schlitzer, R., Helmke, P., Davenport, R., Donner, B., Neuer, S., and Wefer, G., **2007**. Mineral ballast and particle settling rates in the coastal upwelling system off NW Africa and the South Atlantic, *International Journal of Earth Sciences*, 98(2), 281–298. https://doi.org/10.1007/s00531-007-0234-7.

Fischer, G., Reuter, C., Karakas, G., Nowald, N., and Wefer, G., **2009**. Offshore advection of particles within the Cape Blanc filament, Mauritania: Results from observational and modelling studies, *Progress in Oceanography*, 83(1–4), 322–330. https://doi.org/10.1016/j.pocean.2009.07.023.

Fischer, G., Romero, O., Merkel, U., Donner, B., Iversen, M., Nowald, N., Ratmeyer, V., Ruhland, G., Klann, M., and Wefer, G., **2016**. Deep ocean mass fluxes in the coastal upwelling off Mauritania from 1988 to 2012: variability on seasonal to decadal timescales, *Biogeosciences*, 13(10), 3071–3090. https://doi.org/10.5194/bg-13-3071-2016.

Fischer, G., and Wefer, G., **1996**. Long-term Observation of Particle Fluxes in the Eastern Atlantic: Seasonality, Changes of Flux with Depth and Comparison with the Sediment Record, in: *The South Atlantic*, Springer, Berlin, Heidelberg, 325–344. https://doi.org/10.1007/978-3-642-80353-6_18.

Fischer, G., Wefer, G., Romero, O., Dittert, N., Ratmeyer, V., and Donner, B., **2004**. Transfer of particles into the deep Atlantic and the global ocean: control of nutrient supply and ballast production, in: *The South Atlantic in the Late Quaternary*, edited by: Wefer G., Mulitza S., and V., R., Springer, Berlin, Heidelberg, 21–46. https://doi.org/10.1007/978-3-642-18917-3_2.

Fowler, S. W., and Knauer, G. A., **1986**. Role of large particles in the transport of elements and organic compounds through the oceanic water column, *Progress in Oceanography*, 16(3), 147–194. https://doi.org/ffkvf6.

Francois, R., Honjo, S., Krishfield, R., and Manganini, S., **2002**. Factors controlling the flux of organic carbon to the bathypelagic zone of the ocean, *Global Biogeochemical Cycles*, 16(4), 34-31–34-20. https://doi.org/10.1029/2001gb001722.

Fratantoni, D. M., and Glickson, D. A., **2002**. North Brazil Current Ring Generation and Evolution Observed with SeaWiFS*, *Journal of Physical Oceanography*, 32(3), 1058–1074. https://doi.org/czjxzj.

Fréon, P., Arístegui, J., Bertrand, A., Crawford, R. J. M., Field, J. C., Gibbons, M. J., Tam, J., Hutchings, L., Masski, H., Mullon, C., Ramdani, M., Seret, B., and Simier, M., **2009**. Functional group biodiversity in Eastern Boundary Upwelling Ecosystems questions the wasp-waist trophic structure, *Progress in Oceanography*, 83(1–4), 97–106. https://doi.org/10.1016/j.pocean.2009.07.034.

Friese, C. A., van Hateren, H., Vogt, C., Fischer, G., and Stuut, J. B. W., **2017**. Seasonal provenance changes of present-day Saharan dust collected in and off Mauritania, *Atmos. Chem. Phys.*, 17(16), 10163–10193. https://doi.org/10.5194/acp-2017-131.

Froelich, P. N., Atwood, D. K., and Giese, G. S., **1978**. Influence of Amazon River discharge on surface salinity and dissolved silicate concentration in the Caribbean Sea, *Deep-Sea Research*, 25(8), 735–744. https://doi.org/cxjmmz.

Fry, B., and Wainright, S. C., **1991**. Diatom sources of ^{13}C-rich carbon in marine food webs, *Marine Ecology Progress Series*, 76(2), 149–157 http://www.jstor.org/stable/24825558.

Gao, Y., Fan, S.-M., and Sarmiento, J. L., **2003**. Aeolian iron input to the ocean through precipitation scavenging: A modeling perspective and its implication for natural iron fertilization in the ocean, *Journal of Geophysical Research*, 108(D7). https://doi.org/10.1029/2002JD002420.

Gardner, W. D., **1985**. The effect of tilt on sediment trap efficiency, *Deep Sea Research Part A. Oceanographic Research Papers*, 32(3), 349-361. https://doi.org/fnnd5b.

Gervais, F., and Riebesell, U., **2001**. Effect of phosphorus limitation on elemental composition and stable carbon isotope fractionation in a marine diatom growing under different CO_2 concentrations, *Limnology and Oceanography*, 46(3), 497–504. https://doi.org/10.4319/lo.2001.46.3.0497.

Ginoux, P., Chin, M., Tegen, I., Prospero, J. M., Holben, B., Dubovik, O., and Lin, S.-J., **2001**. Sources and distributions of dust aerosols simulated with the GOCART model, *Journal of Geophysical Research*, 106(D17), 20255–20273. https://doi.org/10.1029/2000JD000053.

Glaccum, R. A., and Prospero, J. M., **1980**. Saharan aerosols over the tropical North Atlantic – mineralogy, *Marine Geology*, 37(3–4), 295–321. https://doi.org/fbkbs6.

Goes, J. I., Gomes, H. d. R., Chekalyuk, A. M., Carpenter, E. J., Montoya, J. P., Coles, V. J., Yager, P. L., Berelson, W. M., Capone, D. G., Foster, R. A., Steinberg, D. K., Subramaniam, A., and Hafez, M. A., **2014**. Influence of the Amazon River discharge on the biogeography of phytoplankton communities in the western tropical north Atlantic, *Progress in Oceanography*, 120, 29–40. https://doi.org/10.1016/j.pocean.2013.07.010.

Goossens, D., and Offer, Z. Y., **2000**. Wind tunnel and field calibration of six aeolian dust samplers, *Atmospheric Environment*, 34(7), 1043–1057. https://doi.org/fvfqc3.

Gordon, D. C., **1971**. Distribution of particulate organic carbon and nitrogen at an oceanic station in the central Pacific, *Deep-Sea Research and Oceanographic Abstracts*, 18(11), 1127–1134. https://doi.org/fr524v.

Goudie, A. S., and Middleton, N. J., **2001**. Saharan dust storms: nature and consequences, *Earth-Science Reviews*, 56(1–4), 179–204. https://doi.org/bsfpk9.

Grasshoff, K., Ehrhardt, M., and Kremling, K., **1983**. Determination of nutrients, in: *Methods of seawater analysis*, Verlag Chemie, 159 pp.

Griffin, D. W., Garrison, V. H., Herman, J. R., and Shinn, E. A., **2001**. African desert dust in the Caribbean atmosphere: Microbiology and public health, *Aerobiologia*, 17(3), 203–213. https://doi.org/10.1023/A:1011868218901.

Guerreiro, C. V., Baumann, K.-H., Brummer, G.-J. A., Fischer, G., Korte, L. F., Sá, C., and Stuut, J.-B. W., **2018**. Wind-forced transatlantic gradients in coccolithophore species fluxes, *submitted to Progress in Oceanography*.

Guerreiro, C. V., Baumann, K. H., Brummer, G. J. A., Fischer, G., Korte, L. F., Merkel, U., Sá, C., de Stigter, H., and Stuut, J. B. W., **2017**. Coccolithophore fluxes in the open tropical North Atlantic: influence of thermocline depth, Amazon water, and Saharan dust, *Biogeosciences*, 14(20), 4577–4599. https://doi.org/10.5194/bg-14-4577-2017.

Guieu, C., Aumont, O., Paytan, A., Bopp, L., Law, C. S., Mahowald, N., Achterberg, E. P., Marañón, E., Salihoglu, B., Crise, A., Wagener, T., Herut, B., Desboeufs, K., Kanakidou, M., Olgun, N., Peters, F., Pulido-Villena, E., Tovar-Sanchez, A., and Völker, C., **2014a**. The significance of the episodic nature of atmospheric deposition to Low Nutrient Low Chlorophyll regions, *Global Biogeochemical Cycles*, 28(11), 1179–1198. https://doi.org/10.1002/2014GB004852.

Guieu, C., Dulac, F., Desboeufs, K., Wagener, T., Pulido-Villena, E., Grisoni, J. M., Louis, F., Ridame, C., Blain, S., Brunet, C., Bon Nguyen, E., Tran, S., Labiadh, M., and Dominici, J. M., **2010**. Large clean mesocosms and simulated dust deposition: a new methodology to investigate responses of marine oligotrophic ecosystems to atmospheric inputs, *Biogeosciences*, 7(9), 2765–2784. https://doi.org/10.5194/bg-7-2765-2010.

Guieu, C., Ridame, C., Pulido-Villena, E., Bressac, M., Desboeufs, K., and Dulac, F., **2014b**. Impact of dust deposition on carbon budget: a tentative assessment from a mesocosm approach, *Biogeosciences*, 11(19), 5621–5635. https://doi.org/10.5194/bg-11-5621-2014.

Hamm, C. E., **2002**. Interactive aggregation and sedimentation of diatoms and clay-sized lithogenic material, *Limnology and Oceanography*, 47(6), 1790–1795. https://doi.org/10.4319/lo.2002.47.6.1790.

Harrison, S. P., Kohfeld, K. E., Roelandt, C., and Claquin, T., **2001**. The role of dust in climate changes today, at the last glacial maximum and in the future, *Earth-Science Reviews*, 54(1–3), 43–80. https://doi.org/d2f353.

Herut, B., Zohary, T., Krom, M. D., Mantoura, R. F. C., Pitta, P., Psarra, S., Rassoulzadegan, F., Tanaka, T., and Frede Thingstad, T., **2005**. Response of East Mediterranean surface water to Saharan dust: On-board microcosm experiment and field observations, *Deep-Sea Research II*, 52(22–23), 3024–3040. https://doi.org/10.1016/j.dsr2.2005.09.003.

Hinga, K. R., Arthur, M. A., Pilson, M. E. Q., and Whitaker, D., **1994**. Carbon isotope fractionation by marine phytoplankton in culture: The effects of CO_2 concentration, *p*H, temperature, and species, *Global Biogeochemical Cycles*, 8(1), 91–102. https://doi.org/10.1029/93GB03393.

Honjo, S., Dymond, J., Collier, R., and Manganini, S. J., **1995**. Export production of particles to the interior of the equatorial Pacific Ocean during the 1992 EqPac experiment, *Deep-Sea Research II*, 42(2–3), 831–870. https://doi.org/10.1016/0967-0645(95)00034-n.

Honjo, S., Manganini, S. J., and Cole, J. J., **1982**. Sedimentation of biogenic matter in the deep ocean, *Deep-Sea Research*, 29(5), 609–625. https://doi.org/fq4fwj.

Honjo, S., Manganini, S. J., Krishfield, R. A., and Francois, R., **2008**. Particulate organic carbon fluxes to the ocean interior and factors controlling the biological pump: A synthesis of global sediment trap programs since 1983, *Progress in Oceanography*, 76(3), 217–285. https://doi.org/10.1016/j.pocean.2007.11.003.

Hoose, C., Lohmann, U., Bennartz, R., Croft, B., and Lesins, G., **2008**. Global simulations of aerosol processing in clouds, *Atmospheric Chemistry Physics*, 8(23), 6939–6963. https://doi.org/10.5194/acp-8-6939-2008.

Huang, J., Zhang, C., and Prospero, J. M., **2010**. African dust outbreaks: A satellite perspective of temporal and spatial variability over the tropical Atlantic Ocean, *Journal of Geophysical Research*, 115(D05202). https://doi.org/10.1029/2009JD012516.

Hurrell, J. W., Holland, M. M., Gent, P. R., Ghan, S., Kay, J. E., Kushner, P. J., Lamarque, J.-F., Large, W. G., Lawrence, D., Lindsay, K., Lipscomb, W. H., Long, M. C., Mahowald, N., Marsh, D. R., Neale, R. B., Rasch, P., Vavrus, S., Vertenstein, M., Bader, D., Collins, W. D., Hack, J. J., Kiehl, J., and Marshall, S., **2013**. The Community Earth System Model: A Framework for Collaborative Research, *Bulletin of the American Meteorological Society*, 94(9), 1339-1360. https://doi.org/10.1175/bams-d-12-00121.1.

Ittekkot, V., **1991**. Particle flux studies in the Indian Ocean, *Eos, Transactions American Geophysical Union*, 72(47), 527–530.

Ittekkot, V., **1993**. The abiotically driven biological pump in the ocean and short-term fluctuations in atmospheric CO_2 contents, *Global and Planetary Change*, 8(1–2), 17–25. https://doi.org/fpcqbr.

Ittekkot, V., and Haake, B., **1990**. The terrestrial link in the removal of organic carbon in the sea, *Facets of modern biogeochemistry*, 318–325.

Ittekkot, V., Haake, B., Bartsch, M., Nair, R., and Ramaswamy, V., **1992**. Organic carbon removal in the sea: the continental connection, *Geological Society, London, Special Publications*, 64(1), 167–176. https://doi.org/10.1144/GSL.SP.1992.064.01.11.

Ittekkot, V., Humborg, C., and Schäfer, P., **2000**. Hydrological Alterations and Marine Biogeochemistry: A Silicate Issue? Silicate retention in reservoirs behind dams affects ecosystem structure in coastal seas, *BioScience*, 50(9), 776–782. https://doi.org/frfq3c.

Iversen, M. H., and Ploug, H., **2010**. Ballast minerals and the sinking carbon flux in the ocean: carbon-specific respiration rates and sinking velocity of marine snow aggregates, *Biogeosciences*, 7(9), 2613-2624. https://doi.org/10.5194/bg-7-2613-2010.

Iversen, M. H., and Robert, M. L., **2015**. Ballasting effects of smectite on aggregate formation and export from a natural plankton community, *Marine Chemistry*, 175, 18–27. https://doi.org/10.1016/j.marchem.2015.04.009.

Jickells, T., Boyd, P., and Hunter, K. A., **2014**. Biogeochemical impacts of dust on the global carbon cycle, in: *Mineral Dust*, edited by: Knippertz P., and B., S. J., Springer, Dordrecht, 359–384, https://doi.org/10.1007/978-94-017-8978-3_14.

Jickells, T., Knap, A., Church, T., Galloway, J., and Miller, J., **1982**. Acid rain on Bermuda, *Nature*, 297, 55–57. https://doi.org/10.1038/297055a0.

Jickells, T. D., **1999**. The inputs of dust derived elements to the Sargasso Sea; a synthesis, *Marine Chemistry*, 68(1–2), 5–14. https://doi.org/bfkp9q.

Jickells, T. D., An, Z. S., Andersen, K. K., Baker, A. R., Bergametti, G., Brooks, N., Cao, J. J., Boyd, P. W., Duce, R. A., Hunter, K. A., Kawahata, H., Kubilay, N., laRoche, J., Liss, P. S., Mahowald, N., Prospero, J. M., Ridgwell, A. J., Tegen, I., and Torres, R., **2005**. Global Iron Connections Between Desert Dust, Ocean Biogeochemistry, and Climate, *Science*, 308(5718), 67-71. https://doi.org/10.1126/science.1105959.

Jickells, T. D., Deuser, W. G., Fleer, A., and Hemleben, C., **1990**. Variability of some elemental fluxes in the western tropical atlantic-ocean, *Oceanologica Acta*, 13(3), 291–298.

Jickells, T. D., Dorling, S., Deuser, W. G., Church, T. M., Arimoto, R., and Prospero, J. M., **1998**. Air-borne dust fluxes to a deep water sediment trap in the Sargasso Sea, *Global Biogeochemical Cycles*, 12(2), 311–320. https://doi.org/10.1029/97GB03368.

Jickells, T. D., Newton, P. P., King, P., Lampitt, R. S., and Boutle, C., **1996**. A comparison of sediment trap records of particle fluxes from 19 to 48°N in the northeast Atlantic and their relation to surface water productivity, *Deep-Sea Research I*, 43(7), 971–986. https://doi.org/d8nbpq.

Kaly, F., Marticorena, B., Chatenet, B., Rajot, J. L., Janicot, S., Niang, A., Yahi, H., Thiria, S., Maman, A., Zakou, A., Coulibaly, B. S., Coulibaly, M., Koné, I., Traoré, S., Diallo, A., and Ndiaye, T., **2015**. Variability of mineral dust concentrations over West Africa monitored by the Sahelian Dust Transect, *Atmospheric Research*, 164–165, 226–241. https://doi.org/10.1016/j.atmosres.2015.05.011.

Kandler, K., Schütz, L., Deutscher, C., Ebert, M., Hofmann, H., Jäckel, S., Jaenicke, R., Knippertz, P., Lieke, K., Massling, A., Petzold, A., Schladitz, A., Weinzierl, B., Wiedensohler, A., Zorn, S., and Weinbruch, S., **2009**. Size distribution, mass concentration, chemical and mineralogical composition and derived optical parameters of the boundary layer aerosol at Tinfou, Morocco, during SAMUM 2006, *Tellus B*, 61(1), 32–50. https://doi.org/10.1111/j.1600-0889.2008.00385.x.

Kandler, K., Schütz, L., Jäckel, S., Lieke, K., Emmel, C., Müller-Ebert, D., Ebert, M., Scheuvens, D., Schladitz, A., Šegvić, B., Wiedensohler, A., and Weinbruch, S., **2011**. Ground-based off-line aerosol measurements at Praia, Cape Verde, during the Saharan Mineral Dust Experiment: microphysical properties and mineralogy, *Tellus B*, 63(4), 459–474. https://doi.org/10.1111/j.1600-0889.2011.00546.x.

Kanitz, T., Engelmann, R., Heinold, B., Baars, H., Skupin, A., and Ansmann, A., **2014**. Tracking the Saharan Air Layer with shipborne lidar across the tropical Atlantic, *Geophysical Research Letters*, 41(3), 1044–1050. https://doi.org/10.1002/2013GL058780.

Karakaş, G., Nowald, N., Blaas, M., Marchesiello, P., Frickenhaus, S., and Schlitzer, R., **2006**. High-resolution modeling of sediment erosion and particle transport across the northwest African shelf, *Journal of Geophysical Research*, 111(C6). https://doi.org/10.1029/2005JC003296.

Karl, D., Michaels, A., Bergman, B., Capone, D., Carpenter, E., Letelier, R., Lipschultz, F., Paerl, H., Sigman, D., and Stal, L., **2002**. Dinitrogen fixation in the world's oceans, in: *The Nitrogen Cycle at Regional to Global Scales*, edited by: Boyer, E. W., and Howarth, R. W., Springer, Dordrecht, 47–98. https://doi.org/10.1007/978-94-017-3405-9_2.

Klaas, C., and Archer, D. E., **2002**. Association of sinking organic matter with various types of mineral ballast in the deep sea: Implications for the rain ratio, *Global Biogeochemical Cycles*, 16(4), 63-61–63-14. https://doi.org/10.1029/2001gb001765.

Klunder, M. B., Laan, P., Middag, R., De Baar, H. J. W., and van Ooijen, J. C., **2011**. Dissolved iron in the Southern Ocean (Atlantic sector), *Deep Sea Research Part II: Topical Studies in Oceanography*, 58(25), 2678-2694. https://doi.org/https://doi.org/10.1016/j.dsr2.2010.10.042.

Knappertsbusch, M., and Brummer, G.-J. A., **1995**. A sediment trap investigation of sinking coccolithophorids in the North Atlantic, *Deep-Sea Research I*, 42(7), 1083–1109. https://doi.org/10.1016/0967-0637(95)00036-6.

Knauer, G., and Asper, V., **1989**. Sediment Trap Technology and Sampling, *Report of the US GOFS*.

Knebel, O., **2016**. Production and export fluxes of biomineralising microplankton in the equatorial mid North Atlantic Ocean, MSc Thesis (AM_1147, 24 etcs), Vrije Universiteit Amsterdam, Amsterdam, the Netherlands, 190 pp.

Kok, J. F., Ridley, D. A., Zhou, Q., Miller, R. L., Zhao, C., Heald, C. L., Ward, D. S., Albani, S., and Haustein, K., **2017**. Smaller desert dust cooling effect estimated from analysis of dust size and abundance, *Nature Geosci*, 10(4), 274-278. https://doi.org/10.1038/ngeo2912.

Kok, J. F., Ward, D. S., Mahowald, N. M., and Evan, A. T., **2018**. Global and regional importance of the direct dust-climate feedback, *Nature Communications*, 9(1), 241.
Koning, E., Epping, E., and Van Raaphorst, W., **2002**. Determining biogenic silica in marine samples by tracking silicate and aluminium concentrations in alkaline leaching solutions, *Aquatic Geochemistry*, 8(1), 37–67. https://doi.org/10.1023/A:1020318610178.

Korte, L. F., Brummer, G. J. A., van der Does, M., Guerreiro, C. V., Hennekam, R., van Hateren, J. A., Jong, D., Munday, C. I., Schouten, S., and Stuut, J. B. W., **2017**. Downward particle fluxes of biogenic matter and Saharan dust across the equatorial North Atlantic, *Atmos. Chem. Phys.*, 17(9), 6023–6040. https://doi.org/10.5194/acp-17-6023-2017.

Körtzinger, A., Koeve, W., Kähler, P., and Mintrop, L., **2001**. C: N ratios in the mixed layer during the productive season in the northeast Atlantic Ocean, *Deep-Sea Research I*, 48(3), 661–688. https://doi.org/drmfvb.

Kraay, G. W., Zapata, M., and Veldhuis, M. J. W., **1992**. Separation of chlorophylls c_1,c_2, and c_3 of marine phytoplankton by reversed-phase-C18-High-Performance Liquid Chromatography, *Journal of Phycology*, 28(5), 708–712. https://doi.org/10.1111/j.0022-3646.1992.00708.x.

Laghdass, M., Blain, S., Besseling, M., Catala, P., Guieu, C., and Obernosterer, I., **2011**. Effects of Saharan dust on the microbial community during a large in situ mesocosm experiment in the NW Mediterranean Sea, *Aquatic Microbial Ecology*, 62(2), 201–213. https://doi.org/10.3354/AME01466.

Lambert, F., Delmonte, B., Petit, J. R., Bigler, M., Kaufmann, P. R., Hutterli, M. A., Stocker, T. F., Ruth, U., Steffensen, J. P., and Maggi, V., **2008**. Dust–climate couplings over the past 800,000 years from the EPICA Dome C ice core, *Nature*, 452, 616–619. https://doi.org/10.1038/nature06763.

Lawrence, C. R., Painter, T., Landry, C., and Neff, J., **2010**. Contemporary geochemical composition and flux of aeolian dust to the San Juan Mountains, Colorado, United States, *Journal of Geophysical Research*, 115(G3). https://doi.org/10.1029/2009JG001077.

Laws, E. A., Falkowski, P. G., Smith, W. O., Ducklow, H., and McCarthy, J. J., **2000**. Temperature effects on export production in the open ocean, *Global Biogeochemical Cycles*, 14(4), 1231–1246. https://doi.org/10.1029/1999GB001229.

Lee, C., Peterson, M. L., Wakeham, S. G., Armstrong, R. A., Cochran, J. K., Miquel, J. C., Fowler, S. W., Hirschberg, D., Beck, A., and Xue, J., **2009**. Particulate organic matter and ballast fluxes measured using time-series and settling velocity sediment traps in the northwestern Mediterranean Sea, *Deep Sea Research Part II: Topical Studies in Oceanography*, 56(18), 1420-1436. https://doi.org/b89sg2.

Li, X., Maring, H., Savoie, D., Voss, K., and Prospero, J., **1996**. Dominance of mineral dust in aerosol light-scattering in the North Atlantic trade winds, *Nature*, 380(6573), 416-419. https://doi.org/10.1038/380416a0.

Liu, Z., Omar, A., Vaughan, M., Hair, J., Kittaka, C., Hu, Y., Powell, K., Trepte, C., Winker, D., Hostetler, C., Ferrare, R., and Pierce, R., **2008**. CALIPSO lidar observations of the optical properties of Saharan dust: A case study of long-range transport, *Journal of Geophysical Research*, 113(D7). https://doi.org/10.1029/2007JD008878.

Logan, B. E., and Hunt, J. R., **1987**. Advantages to microbes of growth in permeable aggregates in marine systems, *Limnol. Oceanogr*, 32(5), 1034–1048. https://doi.org/10.4319/lo.1987.32.5.1034.

Longhurst, A., **1993**. Seasonal cooling and blooming in tropical oceans, *Deep-Sea Research I*, 40(11–12), 2145–2165. https://doi.org/dg78mq.

Longhurst, A. R., and Glen Harrison, W., **1989**. The biological pump: Profiles of plankton production and consumption in the upper ocean, *Progress in Oceanography*, 22(1), 47–123. https://doi.org/bb34fk.

Louis, J., Pedrotti, M. L., Gazeau, F., and Guieu, C., **2017**. Experimental evidence of formation of Transparent Exopolymer Particles (TEP) and POC export provoked by dust addition under current and high pCO_2 conditions, *PLoS ONE*, 12(2). https://doi.org/10.1371/journal.pone.0171980.

Mahaffey, C., Williams, R. G., Wolff, G. A., Mahowald, N., Anderson, W., and Woodward, M., **2003**. Biogeochemical signatures of nitrogen fixation in the eastern North Atlantic, *Geophysical Research Letters*, 30(6). https://doi.org/10.1029/2002GL016542.

Maher, B. A., Prospero, J. M., Mackie, D., Gaiero, D., Hesse, P. P., and Balkanski, Y., **2010**. Global connections between aeolian dust, climate and ocean biogeochemistry at the present day and at the last glacial maximum, *Earth-Science Reviews*, 99(1–2), 61–97. https://doi.org/10.1016/j.earscirev.2009.12.001.

Mahowald, N., Albani, S., Kok, J. F., Engelstaeder, S., Scanza, R., Ward, D. S., and Flanner, M. G., **2014**. The size distribution of desert dust aerosols and its impact on the Earth system, *Aeolian Research*, 15, 53–71. https://doi.org/10.1016/j.aeolia.2013.09.002.

Mahowald, N., Ward, D. S., Kloster, S., Flanner, M. G., Heald, C. L., Heavens, N. G., Hess, P. G., Lamarque, J.-F., and Chuang, P. Y., **2011**. Aerosol Impacts on Climate and Biogeochemistry, *Annual Review of Environment and Resources*, 36(1), 45–74. https://doi.org/10.1146/annurev-environ-042009-094507.

Mahowald, N. M., Baker, A. R., Bergametti, G., Brooks, N., Duce, R. A., Jickells, T. D., Kubilay, N., Prospero, J. M., and Tegen, I., **2005**. Atmospheric global dust cycle and iron inputs to the ocean, *Global Biogeochemical Cycles*, 19(4). https://doi.org/10.1029/2004GB002402.

Mahowald, N. M., and Luo, C., **2003**. A less dusty future?, *Geophysical Research Letters*, 30(17). https://doi.org/10.1029/2003GL017880.

Mahowald, N. M., Zender, C. S., Luo, C., Savoie, D., Torres, O., and del Corral, J., **2002**. Understanding the 30-year Barbados desert dust record, *Journal of Geophysical Research*, 107(D21). https://doi.org/10.1029/2002JD002097.

Marañon, E., Fernández, A., Mouriño-Carballido, B., MartÍnez-GarcÍa, S., Teira, E., Cermeño, P., Chouciño, P., Huete-Ortega, M., Fernández, E., Calvo-DÍaz, A., Morán, X. A. G., Bode, A., Moreno-Ostos, E., Varela, M. M., Patey, M. D., and Achterberg, E. P., **2010**. Degree of oligotrophy controls the response of microbial plankton to Saharan dust, *Limnology and Oceanography*, 55(6), 2339–2352. https://doi.org/10.4319/lo.2010.55.6.2339.

Marticorena, B., Chatenet, B., Rajot, J.-L., Traoré, S., Coulibaly, M., Diallo, A., Koné, I., Maman, A., NDiaye, T., and Zakou, A., **2010**. Temporal variability of mineral dust concentrations over West Africa: analyses of a pluriannual monitoring from the AMMA Sahelian Dust Transect, *Atmos. Chem. Phys.*, 10(18), 8899–8915. https://doi.org/10.5194/acp-10-8899-2010.

Martin, J. H., **1990**. Glacial-interglacial CO_2 change: the iron hypothesis, *Paleoceanography*, 5(1), 1-13. https://doi.org/10.1029/PA005i001p00001.

Martin, J. H., Coale, K. H., Johnson, K. S., Fitzwater, S. E., Gordon, R. M., Tanner, S. J., Hunter, C. N., Elrod, V. A., Nowicki, J. L., Coley, T. L., Barber, R. T., Lindley, S., Watson, A. J., Van Scoy, K., Law, C. S., Liddicoat, M. I., Ling, R., Stanton, T., Stockel, J., Collins, C., Anderson, A., Bidigare, R., Ondrusek, M., Latasa, M., Millero, F. J., Lee, K., Yao, W., Zhang, J. Z., Friederich, G., Sakamoto, C., Chavez, F., Buck, K., Kolber, Z., Greene, R., Falkowski, P., Chisholm, S. W., Hoge, F., Swift, R., Yungel, J., Turner, S., Nightingale, P., Hatton, A., Liss, P., and Tindale, N. W., **1994**. Testing the iron hypothesis in ecosystems of the equatorial Pacific Ocean, *Nature*, 371, 123–129. https://doi.org/10.1038/371123a0.

Martin, J. H., and Fitzwater, S., **1988**. Iron deficiency limits phytoplankton growth in the north-east Pacific subarctic, *Nature*, 331(3414343), 947-975. https://doi.org/10.1038/331341a0.

Martin, J. H., Knauer, G. A., Karl, D. M., and Broenkow, W. W., **1987**. VERTEX: carbon cycling in the northeast Pacific, *Deep-Sea Research*, 34(2), 267–285. https://doi.org/df6fcw.

Masson, S., and Delecluse, P., **2001**. Influence of the Amazon River runoff on the tropical atlantic, *Physics and Chemistry of the Earth*, 26(2), 137–142. https://doi.org/c39mwb.

McGregor, H. V., Dupont, L., Stuut, J.-B. W., and Kuhlmann, H., **2009**. Vegetation change, goats, and religion: a 2000-year history of land use in southern Morocco, *Quaternary Science Reviews*, 28(15–16), 1434–1448. https://doi.org/10.1016/j.quascirev.2009.02.012.

McTainsh, G. H., Nickling, W. G., and Lynch, A. W., **1997**. Dust deposition and particle size in Mali, West Africa, *CATENA*, 29(3–4), 307-322. https://doi.org/b9sz3p.

Meskhidze, N., Chameides, W. L., Nenes, A., and Chen, G., **2003**. Iron mobilization in mineral dust: Can anthropogenic SO_2 emissions affect ocean productivity?, *Geophysical Research Letters*, 30(21). https://doi.org/10.1029/2003GL018035.

Miller, R. L., Cakmur, R. V., Perlwitz, J., Geogdzhayev, I. V., Ginoux, P., Koch, D., Kohfeld, K. E., Prigent, C., Ruedy, R., Schmidt, G. A., and Tegen, I., **2006**. Mineral dust aerosols in the NASA Goddard Institute for Space Sciences ModelE atmospheric general circulation model, *Journal of Geophysical Research*, 111(D6). https://doi.org/10.1029/2005JD005796.

Mills, M. M., Ridame, C., Davey, M., La Roche, J., and Geider, R. J., **2004**. Iron and phosphorus co-limit nitrogen fixation in the eastern tropical North Atlantic, *Nature*, 429, 292–294. https://doi.org/10.1038/nature02550.

Mittelstaedt, E., **1991**. The ocean boundary along the northwest African coast: circulation and oceanographic properties at the sea surface, *Progress in Oceanography*, 26(4), 307–355. https://doi.org/b2q79z.

Montoya, J. P., Carpenter, E. J., and Capone, D. G., **2002**. Nitrogen fixation and nitrogen isotope abundances in zooplankton of the oligotrophic North Atlantic, *Limnology and Oceanography*, 47(6), 1617–1628. https://doi.org/10.4319/lo.2002.47.6.1617.

Moore, C. M., Mills, M. M., Arrigo, K. R., Berman-Frank, I., Bopp, L., Boyd, P. W., Galbraith, E. D., Geider, R. J., Guieu, C., Jaccard, S. L., Jickells, T. D., La Roche, J., Lenton, T. M., Mahowald, N. M., Maranon, E., Marinov, I., Moore, J. K., Nakatsuka, T., Oschlies, A., Saito, M. A., Thingstad, T. F., Tsuda, A., and Ulloa, O., **2013**. Processes and patterns of oceanic nutrient limitation, *Nature Geoscience*, 6, 701–710. https://doi.org/10.1038/ngeo1765.

Moore, M. C., Mills, M. M., Achterberg, E. P., Geider, R. J., LaRoche, J., Lucas, M. I., McDonagh, E. L., Pan, X., Poulton, A. J., Rijkenberg, M. J. A., Suggett, D. J., Ussher, S. J., and Woodward, E. M. S., **2009**. Large-scale distribution of Atlantic nitrogen fixation controlled by iron availability, *Nature Geoscience*, 2, 867–871. https://doi.org/10.1038/ngeo667.

Mortlock, R. A., and Froelich, P. N., **1989**. A simple method for the rapid determination of biogenic opal in pelagic marine sediments, *Deep-Sea Research*, 36(9), 1415–1426. https://doi.org/fgh5gb.

Moulin, C., Lambert, C. E., Dulac, F., and Dayan, U., **1997**. Control of atmospheric export of dust from North Africa by the North Atlantic Oscillation, *Nature*, 387, 691–694. https://doi.org/10.1038/42679.

Muhs, D. R., **2013**. The geologic records of dust in the Quaternary, *Aeolian Research*, 9, 3–48. https://doi.org/10.1016/j.aeolia.2012.08.001.

Mulitza, S., Prange, M., Stuut, J. B., Zabel, M., von Dobeneck, T., Itambi, A. C., Nizou, J., Schulz, M., and Wefer, G., **2008**. Sahel megadroughts triggered by glacial slowdowns of Atlantic meridional overturning, *Paleoceanography*, 23(4). https://doi.org/10.1029/2008PA001637.

Muller-Karger, F. E., McClain, C. R., and Richardson, P. L., **1988**. The dispersal of the Amazon's water, *Nature*, 333, 56–59. https://doi.org/10.1038/333056a0.

Murphy, J., and Riley, J. P., **1962**. A modified single solution method for the determination of phosphate in natural waters, *Analytica Chimica Acta*, 27, 31–36. https://doi.org/fdbgvv.

Neale, R. B., Richter, J., Park, S., Lauritzen, P. H., Vavrus, S. J., Rasch, P. J., and Zhang, M., **2013**. The Mean Climate of the Community Atmosphere Model (CAM4) in Forced SST and Fully Coupled Experiments, *Journal of Climate*, 26(14), 5150-5168. https://doi.org/10.1175/jcli-d-12-00236.1.

Neuer, S., Freudenthal, T., Davenport, R., Llinás, O., and Rueda, M.-J., **2002**. Seasonality of surface water properties and particle flux along a productivity gradient off NW Africa, *Deep-Sea Research II*, 49(17), 3561–3576. https://doi.org/fbm5pj.

Neuer, S., Ratmeyer, V., Davenport, R., Fischer, G., and Wefer, G., **1997**. Deep water particle flux in the Canary Island region: seasonal trends in relation to long-term satellite derived pigment data and lateral sources, *Deep-Sea Research I*, 44(8), 1451–1466. https://doi.org/ddxg6b.

Neuer, S., Torres-Padrón, M. E., Gelado-Caballero, M. D., Rueda, M. J., Hernández-Brito, J., Davenport, R., and Wefer, G., **2004**. Dust deposition pulses to the eastern subtropical North Atlantic gyre: Does ocean's biogeochemistry respond?, *Global Biogeochemical Cycles*, 18(4). https://doi.org/10.1029/2004GB002228.

Newton, P. P., Lampitt, R. S., Jickells, T. D., King, P., and Boutle, C., **1994**. Temporal and spatial variability of biogenic particle fluxes during the JGOFS northeast Atlantic process studies at 47ºN, 20ºW, *Deep Sea Research I*, 41(11–12), 1617-1642. https://doi.org/dtgfgd.

Nicholson, S. E., **2000**. The nature of rainfall variability over Africa on time scales of decades to millennia, *Global and planetary change*, 26, 137-158. https://doi.org/cn7cb8.

Nowald, N., Iversen, M. H., Fischer, G., Ratmeyer, V., and Wefer, G., **2015**. Time series of in-situ particle properties and sediment trap fluxes in the coastal upwelling filament off Cape Blanc, Mauritania, *Progress in Oceanography*, 137(Part A), 1–11. https://doi.org/10.1016/j.pocean.2014.12.015.

Pabortsava, K., Lampitt, R. S., Benson, J., Crowe, C., McLachlan, R., Le Moigne, F. A. C., Mark Moore, C., Pebody, C., Provost, P., Rees, A. P., Tilstone, Gavin H., and Woodward, E. M. S., **2017**. Carbon sequestration in the deep Atlantic enhanced by Saharan dust, *Nature Geoscience*, 10, 189–194. https://doi.org/10.1038/ngeo2899.

Pace, M. L., Knauer, G. A., Karl, D. M., and Martin, J. H., **1987**. Primary production, new production and vertical flux in the eastern Pacific Ocean, *Nature*, 325, 803–804. https://doi.org/10.1038/325803a0.

Passow, U., and De la Rocha, C. L., **2006**. Accumulation of mineral ballast on organic aggregates, *Global Biogeochemical Cycles*, 20(1). https://doi.org/10.1029/2005gb002579.

Ploug, H., Iversen, M. H., Koski, M., and Buitenhuis, E. T., **2008**. Production, oxygen respiration rates, and sinking velocity of copepod fecal pellets: Direct measurements of ballasting by opal and calcite, *Limnology and Oceanography*, 53(2), 469–476. https://doi.org/10.4319/lo.2008.53.2.0469.

Poulton, S. W., and Canfield, D. E., **2005**. Development of a sequential extraction procedure for iron: implications for iron partitioning in continentally derived particulates, *Chemical Geology*, 214(3–4), 209–221. https://doi.org/10.1016/j.chemgeo.2004.09.003.

Pourmand, A., Prospero, J. M., and Sharifi, A., **2014**. Geochemical fingerprinting of trans-Atlantic African dust based on radiogenic Sr-Nd-Hf isotopes and rare earth element anomalies, *Geology*, 42(8), 675–678. https://doi.org/10.1130/G35624.1.

Prospero, J. M., **1996**. Saharan dust transport over the North Atlantic Ocean and Mediterranean: an overview, in: *The Impact of Desert Dust Across the Mediterranean*, edited by: Guerzoni, S., and Chester, R., Kluwer Academic, Dordrecht, 133–151. https://doi.org/10.1007/978-94-017-3354-0_13.

Prospero, J. M., **1999**. Long-range transport of mineral dust in the global atmosphere: Impact of African dust on the environment of the southeastern United States, *Proceedings of the National Academy of Sciences*, 96(7), 3396–3403. https://doi.org/10.1073/pnas.96.7.3396.

Prospero, J. M., Bonatti, E., Schubert, C., and Carlson, T. N., **1970**. Dust in the Caribbean atmosphere traced to an African dust storm, *Earth and Planetary Science Letters*, 9(3), 287–293. https://doi.org/c8zf6c.

Prospero, J. M., and Carlson, T. N., **1972**. Vertical and areal distribution of Saharan dust over the western equatorial North Atlantic Ocean, *Journal of Geophysical Research*, 77(27), 5255–5265. https://doi.org/10.1029/JC077i027p05255.

Prospero, J. M., Collard, F.-X., Molinie, J., and Jeannot, A., **2014**. Characterizing the annual cycle of African dust transport to the Caribbean Basin and South America and its impact on the environment and air quality, *Global Biogeochemical Cycles*, 28(7), 757–773. https://doi.org/10.1002/2013gb004802.

Prospero, J. M., Ginoux, P., Torres, O., Nicholson, S. E., and Gill, T. E., **2002**. Environmental characterization of global sources of atmospheric soil dust derived from the NIMBUS7 TOMS absorbing aerosol product, *Reviews of Geophysics*, 40(1), 2-1–2-31. https://doi.org/10.1029/2000RG000095.

Prospero, J. M., Glaccum, R. A., and Nees, R. T., **1981**. Atmospheric transport of soil dust from Africa to South America, *Nature*, 289, 570–572. https://doi.org/10.1038/289570a0.

Prospero, J. M., and Lamb, P. J., **2003**. African droughts and dust transport to the Caribbean: climate change implications, *Science*, 302(5647), 1024–1027. https://doi.org/10.1126/science.1089915.

Prospero, J. M., Landing, W. M., and Schulz, M., **2010**. African dust deposition to Florida: Temporal and spatial variability and comparisons to models, *Journal of Geophysical Research: Atmospheres*, 115(D13). https://doi.org/10.1029/2009JD012773.

Prospero, J. M., and Nees, R. T., **1986**. Impact of the North African drought and El Nino on mineral dust in the Barbados trade winds, *Nature*, 320, 735–738. https://doi.org/10.1038/320735a0.

Pulido-Villena, E., Baudoux, A.-C., Obernosterer, I., Landa, M., Caparros, J., Catala, P., Georges, C., Harmand, J., and Guieu, C., **2014**. Microbial food web dynamics in response to a Saharan dust event: results from a mesocosm study in the oligotrophic Mediterranean Sea, *Biogeosciences*, 11(19), 5607–5619. https://doi.org/10.5194/bg-11-5607-2014.

Pulido-Villena, E., Rerolle, V., and Guieu, C., **2010**. Transient fertilizing effect of dust in P-deficient LNLC surface ocean, *Geophysical Research Letters*, 37(1). https://doi.org/10.1029/2009GL041415.

Pye, K., **1987**. Aeolian dust and dust deposits, Academic Press, London, 334 pp.
Ratmeyer, V., Balzer, W., Bergametti, G., Chiapello, I., Fischer, G., and Wyputta, U., **1999a**. Seasonal impact of mineral dust on deep-ocean particle flux in the eastern subtropical Atlantic Ocean, *Marine Geology*, 159, 241–252. https://doi.org/dwhg6k.

Ratmeyer, V., Fischer, G., and Wefer, G., **1999b**. Lithogenic particle fluxes and grain size distributions in the deep ocean off northwest Africa: Implications for seasonal changes of aeolian dust input and downward transport, *Deep-Sea Research I*, 46(8), 1289–1337. https://doi.org/bgjz7q.

Rea, D. K., **1994**. The paleoclimatic record provided by eolian deposition in the deep sea: the geologic history of wind, *Reviews of Geophysics*, 32(2), 159–195. https://doi.org/10.1029/93RG03257.

Redfield, A. C., **1958**. The biological control of chemical factors in the environment, *American Scientist*, 46(3), 205–221. http://www.jstor.org/stable/27827150.

Redfield, A. C., **1963**. The influence of organisms on the composition of seawater, in: *The sea*, edited by: Hill, M. N., John Wiley, New York, 26–77.
Richter, T. O., Van der Gaast, S., Koster, B., Vaars, A., Gieles, R., de Stigter, H. C., De Haas, H., and van Weering, T. C., **2006**. The Avaatech XRF Core Scanner: technical description and applications to NE Atlantic sediments, *Geological Society, London, Special Publications*, 267(1), 39–50. https://doi.org/10.1144/GSL.SP.2006.267.01.03.

Ridame, C., Dekaezemacker, J., Guieu, C., Bonnet, S., L'Helguen, S., and Malien, F., **2014**. Contrasted Saharan dust events in LNLC environments: impact on nutrient dynamics and primary production, *Biogeosciences*, 11(17), 4783–4800. https://doi.org/10.5194/bg-11-4783-2014.

Ridame, C., and Guieu, C., **2002**. Saharan input of phosphate to the oligotrophic water of the open western Mediterranean Sea, *Limnology and Oceanography*, 47(3), 856–869. https://doi.org/10.4319/lo.2002.47.3.0856.

Rixen, T., Guptha, M. V. S., and Ittekkot, V., **2005**. Deep ocean fluxes and their link to surface ocean processes and the biological pump, *Progress in Oceanography*, 65(2–4), 240–259. https://doi.org/10.1016/j.pocean.2005.03.006.

Roelke, D. L., Eldridge, P. M., and Cifuentes, L. A., **1999**. A model of phytoplankton competition for limiting and nonlimiting nutrients: Implications for development of estuarine and nearshore management schemes, *Estuaries*, 22(1), 92–104. https://doi.org/10.2307/1352930.

Romero, E., Peters, F., Marrasé, C., Guadayol, Ò., Gasol, J. M., and Weinbauer, M. G., **2011**. Coastal Mediterranean plankton stimulation dynamics through a dust storm event: An experimental simulation, *Estuarine, Coastal and Shelf Science*, 93(1), 27–39. https://doi.org/10.1016/j.ecss.2011.03.019.

Rosenberg, P. D., Parker, D. J., Ryder, C. L., Marsham, J. H., Garcia-Carreras, L., Dorsey, J. R., Brooks, I. M., Dean, A. R., Crosier, J., McQuaid, J. B., and Washington, R., **2014**. Quantifying particle size and turbulent scale dependence of dust flux in the Sahara using aircraft measurements, *Journal of Geophysical Research: Atmospheres*, 119(12), 7577-7598. https://doi.org/10.1002/2013JD021255.

Rosenfeld, D., Rudich, Y., and Lahav, R., **2001**. Desert dust suppressing precipitation: A possible desertification feedback loop, *Proceedings of the National Academy of Sciences*, 98(11), 5975-5980. https://doi.org/10.1073/pnas.101122798.

Rutten, A., and de Lange, G. J., **2003**. Sequential extraction of iron, manganese and related elements in S1 sapropel sediments, eastern Mediterranean, *Palaeogeography, Palaeoclimatology, Palaeoecology*, 190, 79–101. https://doi.org/cz4cf5.

Ryder, C. L., Highwood, E. J., Rosenberg, P. D., Trembath, J., Brooke, J. K., Bart, M., Dean, A., Crosier, J., Dorsey, J., Brindley, H., Banks, J., Marsham, J. H., McQuaid, J. B., Sodemann, H., and Washington, R., **2013**. Optical properties of Saharan dust aerosol and contribution from the coarse mode as measured during the Fennec 2011 aircraft campaign, *Atmos. Chem. Phys.*, 13(1), 303-325. https://doi.org/10.5194/acp-13-303-2013.

Sarnthein, M., Tetzlaff, G., Koopmann, B., Wolter, K., and Pflaumann, U., **1981**. Glacial and interglacial wind regimes over the eastern subtropical Atlantic and North-West Africa, *Nature*, 293(17 September), 193-196. https://doi.org/10.1038/293193a0.

Scheuvens, D., Schütz, L., Kandler, K., Ebert, M., and Weinbruch, S., **2013**. Bulk composition of northern African dust and its source sediments — A compilation, *Earth-Science Reviews*, 116, 170–194. https://doi.org/10.1016/j.earscirev.2012.08.005.

Schlitzer, R., **2015**. Ocean Data View. http://odv.awi.de.

Schlosser, C., Klar, J. K., Wake, B. D., Snow, J. T., Honey, D. J., Woodward, E. M. S., Lohan, M. C., Achterberg, E. P., and Moore, C. M., **2014**. Seasonal ITCZ migration dynamically controls the location of the (sub) tropical Atlantic biogeochemical divide, *Proceedings of the National Academy of Sciences*, 111(4), 1438-1442. https://doi.org/10.1073/pnas.1318670111.

Schneider, B., Schlitzer, R., Fischer, G., and Nöthig, E.-M., **2003**. Depth-dependent elemental compositions of particulate organic matter (POM) in the ocean, *Global Biogeochemical Cycles*, 17(2). https://doi.org/10.1029/2002GB001871.

Schott, F. A., Brandt, P., Hamann, M., Fischer, J., and Stramma, L., **2002**. On the boundary flow off Brazil at 5–10°S and its connection to the interior tropical Atlantic, *Geophysical Research Letters*, 29(17), 21-21-21-24. https://doi.org/10.1029/2002GL014786.

Schreuder, L. T., Hopmans, E. C., Stuut, J. B. W., Sinninghe Damsté, J. S., and Schouten, S., **2018a**. Transport and deposition of levoglucosan across the tropical North Atlantic Ocean, *Geochimica et Cosmochimica Acta*.

Schreuder, L. T., Stuut, J.-B. W., Korte, L. F., Damsté, J. S. S., and Schouten, S., **2018b**. Aeolian transport and deposition of plant wax n-alkanes across the tropical North Atlantic Ocean, *Organic Geochemistry*, 115, 113–123. https://doi.org/10.1016/j.orggeochem.2017.10.010.

Schultz, M. K., Burnett, W. C., and Inn, K. G., **1998**. Evaluation of a sequential extraction method for determining actinide fractionation in soils and sediments, *Journal of Environmental Radioactivity*, 40(2), 155–174. https://doi.org/bqhkpt.

Schulz, M., Prospero, J. M., Baker, A. R., Dentener, F., Ickes, L., Liss, P. S., Mahowald, N. M., Nickovic, S., Garcia-Pando, C. P., Rodriguez, S., Sarin, M., Tegen, I., and Duce, R. A., **2012**. Atmospheric Transport and Deposition of Mineral Dust to the Ocean: Implications for Research Needs, *Environmental Science & Technology*, 46(19), 10390–10404. https://doi.org/10.1021/es300073u.

Shao, Y., Wyrwoll, K.-H., Chappell, A., Huang, J., Lin, Z., McTainsh, G. H., Mikami, M., Tanaka, T. Y., Wang, X., and Yoon, S., **2011**. Dust cycle: An emerging core theme in Earth system science, *Aeolian Research*, 2(4), 181–204. https://doi.org/10.1016/j.aeolia.2011.02.001.

Shi, Z., Krom, M. D., Bonneville, S., Baker, A. R., Bristow, C., Drake, N., Mann, G., Carslaw, K., McQuaid, J. B., and Jickells, T., **2011**. Influence of chemical weathering and aging of iron oxides on the potential iron solubility of Saharan dust during simulated atmospheric processing, *Global biogeochemical cycles*, 25(2). https://doi.org./10.1029/2010GB003837.

Shi, Z., Krom, M. D., Bonneville, S., Baker, A. R., Jickells, T. D., and Benning, L. G., **2009**. Formation of iron nanoparticles and increase in iron reactivity in mineral dust during simulated cloud processing, *Environmental science & technology*, 43(17), 6592–6596. https://doi.org/10.1021/es901294g.

Shi, Z., Krom, M. D., Jickells, T. D., Bonneville, S., Carslaw, K. S., Mihalopoulos, N., Baker, A. R., and Benning, L. G., **2012**. Impacts on iron solubility in the mineral dust by processes in the source region and the atmosphere: A review, *Aeolian Research*, 5, 21–42. https://doi.org/10.1016/j.aeolia.2012.03.001.

Shinn, E. A., Smith, G. W., Prospero, J. M., Betzer, P., Hayes, M. L., Garrison, V., and Barber, R. T., **2000**. African dust and the demise of Caribbean coral reefs, *Geophysical Research Letters*, 27(19), 3029–3032. https://doi.org/10.1029/2000GL011599.

Sholkovitz, E. R., Allsup, G. P., Arthur, R., Hosom, D. S., and McKenney, K., **1998**. Development of an autonomous aerosol sampler for ocean buoys and land sites, *Woods Hole Oceanographic Institution*. https://doi.org/10.1575/1912/258.

Siegel, D. A., and Deuser, W. G., **1997**. Trajectories of sinking particles in the Sargasso Sea: modeling of statistical funnels above deep-ocean sediment traps, *Deep-Sea Research I*, 44(9–10), 1519–1541. https://doi.org/d8tzfp.

Skonieczny, C., Bory, A., Bout-Roumazeilles, V., Abouchami, W., Galer, S. J. G., Crosta, X., Diallo, A., and Ndiaye, T., **2013**. A three-year time series of mineral dust deposits on the West African margin: Sedimentological and geochemical signatures and implications for interpretation of marine paleo-dust records, *Earth and Planetary Science Letters*, 364, 145–156. https://doi.org/10.1016/j.epsl.2012.12.039.

Skonieczny, C., Bory, A., Bout-Roumazeilles, V., Abouchami, W., Galer, S., Crosta, X., Stuut, J. B., Meyer, I., Chiapello, I., Podvin, T., Chatenet, B., Diallo, A., and Ndiaye, T., **2011**. The 7–13 March 2006 major Saharan outbreak: Multiproxy characterization of mineral dust deposited on the West African margin, *Journal of Geophysical Research*, 116(D18). https://doi.org/10.1029/2011JD016173.

Sohm, J. A., Webb, E. A., and Capone, D. G., **2011**. Emerging patterns of marine nitrogen fixation, *Nature Reviews Microbiology*, 9, 499–508. https://doi.org/10.1038/nrmicro2594.

Sokolik, I. N., and Toon, O. B., **1999**. Incorporation of mineralogical composition into models of the radiative properties of mineral aerosol from UV to IR wavelengths, *Journal of Geophysical Research*, 104(D8), 9423–9444. https://doi.org/10.1029/1998JD200048.

Spokes, L. J., and Jickells, T. D., **1996**. Factors controlling the solubility of aerosol trace metals in the atmosphere and on mixing into seawater, *Aquatic Geochemistry*, 1(4), 355-374. https://doi.org/10.1007/bf00702739.

Spokes, L. J., Jickells, T. D., and Lim, B., **1994**. Solubilisation of aerosol trace metals by cloud processing: A laboratory study, *Geochimica et Cosmochimica Acta*, 58(15), 3281–3287. https://doi.org/b8gnxk.

Stocker, T. F., Qin, D., and Plattner, G.-K., **2013**. Climate change 2013: the physical science basis. Contribution of Working Group I to the Fifth Assessment Report of the Intergovernmental Panel on Climate Change, *Cambridge University Press*, 33-115.
Stoll, M. H. C., Bakker, K., Nobbe, G. H., and Haese, R. R., **2001**. Continuous-flow analysis of dissolved inorganic carbon content in seawater, *Analytical Chemistry*, 73(17), 4111–4116. https://doi.org/10.1021/ac010303r.

Stramma, L., and Schott, F., **1999**. The mean flow field of the tropical Atlantic Ocean, *Deep-Sea Research II*, 46(1–2), 279–303. https://doi.org/d7mdf8.

Strickland, J. D. H., and Parsons, T. R., **1972**. A practical handbook of seawater analysis. http://epic.awi.de/39262/1/Strickland-Parsons_1972.pdf.

Stuut, J.-B., Smalley, I., and O'Hara-Dhand, K., **2009**. Aeolian dust in Europe: African sources and European deposits, *Quaternary International*, 198(1–2), 234–245. https://doi.org/10.1016/j.quaint.2008.10.007.

Stuut, J.-B. W., Boersen, B., Brück, H. M., Hansen, A., Koster, B., van der Does, M., and and Witte, Y., **2012**. Cruise Report RV Meteor M89, TRAFFIC I: Transatlantic Fluxes of Saharan Dust. 3 - 25 October 2012. http://melia.nioz.nl/public/dmg/rpt/crs/m89.pdf.

Stuut, J.-B. W., Brummer, G. J. A., van der Does, M., Friese, C., Geerken, E., van der Heide, R., Korte, L., Koster, B., Metcalfe, B., Munday, C. I., van Ooijen, J., Siccha, M., Veldhuizen, R., de Visser, J.-D., Witte, Y., and and Wuis, L., **2013**. Cruise Report RV Pelagia 64PE378, TRAFFIC II: Transatlantic Fluxes of Saharan Dust. 9 November - 6 December 2013. http://melia.nioz.nl/public/dmg/rpt/crs/64pe378.pdf.

Stuut, J.-B. W., Witte, Y., de Visser, J.-D., Boersen, B., Koster, B., Bakker, K., Laan, P., van der Does, M., Korte, L., Munday, C. I., and and van Hateren, H., **2015**. Cruise Report RV Pelagia 64PE395, TRAFFIC III: Transatlantic Fluxes of Saharan Dust. 11 January - 6 February 2015. http://melia.nioz.nl/public/dmg/rpt/crs/64pe395.pdf.

Stuut, J.-B. W., Zabel, M., Ratmeyer, V., Helmke, P., Schefuß, E., Lavik, G., and Schneider, R. R., **2005**. Provenance of present-day eolian dust collected off NW Africa, *Journal of Geophysical Research*, 110(D4). https://doi.org/10.1029/2004JD005161.

Stuut, J. B., Boekschoten, B., Boersen, B., Brummer, G. J., Brussaard, C., de Boer, J., de Bruin, T., Jong, D., Knebel, O., Kooijman, K., Korte, L., Koster, B., Laan, P., Martens, M., Munday, C., Noordeloos, A., Pausch, F., Roepert, A., Rosell-Mele, T., Schreuder, L., Sevenster, L., van der Does, M., Venhuizen, G., Guerreiro, C. V., and Witte, Y., **2016**. DUSTTRAFFIC IV: Transatlantic fluxes of Saharan dust. http://melia.nioz.nl/public/dmg/rpt/crs/jc134.pdf.

Subramaniam, A., Yager, P., Carpenter, E., Mahaffey, C., Björkman, K., Cooley, S., Kustka, A., Montoya, J., Sañudo-Wilhelmy, S., Shipe, R., and Capone, D. G., **2008**. Amazon River enhances diazotrophy and carbon sequestration in the tropical North Atlantic Ocean, *Proceedings of the National Academy of Sciences*, 105(30), 10460–10465. https://doi.org/10.1073/pnas.0710279105.

Suess, E., **1980**. Particulate organic carbon flux in the oceans—surface productivity and oxygen utilization, *Nature*, 288, 261–263.

Sunda, W. G., Price, N. M., and Morel, F. M., **2005**. Trace metal ion buffers and their use in culture studies, *Algal Culturing Techniques*, 4, 35–63.

Swap, R., Garstang, M., Greco, S., Talbot, R., and Kållberg, P., **1992**. Saharan dust in the Amazon Basin, *Tellus*, 44B(2), 133-149. https://doi.org/10.1034/j.1600-0889.1992.t01-1-00005.x.

Swap, R., Garstang, M., Macko, S. A., Tyson, P. D., Meanhaut, W., Artaxo, P., Kållberg, P., and R., T., **1996**. The long-range transport of southern African aerosols to the tropical South Atlantic, *Journal of Geophysical Research*, 101(D19), 23,777-723,791. https://doi.org/10.1029/95JD01049.

Tegen, I., Werner, M., Harrison, S. P., and Kohfeld, K. E., **2004**. Relative importance of climate and land use in determining present and future global soil dust emission, *Geophysical Research Letters*, 31(5). https://doi.org/10.1029/2003GL019216.

Ternon, E., Guieu, C., Loÿe-Pilot, M.-D., Leblond, N., Bosc, E., Gasser, B., Miquel, J.-C., and Martín, J., **2010**. The impact of Saharan dust on the particulate export in the water column of the North Western Mediterranean Sea, *Biogeosciences*, 7(3), 809–826. https://doi.org/10.5194/bg-7-809-2010.

Ternon, J. F., Oudot, C., Dessier, A., and Diverres, D., **2000**. A seasonal tropical sink for atmospheric CO_2 in the Atlantic ocean: the role of the Amazon River discharge, *Marine Chemistry*, 68(3), 183–201. https://doi.org/b95nnz.

Tessier, A., Campbell, P. G. C., and Bisson, M., **1979**. Sequential Extraction Procedure for the Speciation of Particulate Trace Metals, *Analytical Chemistry*, 51(7), 844–851. https://doi.org/10.1021/ac50043a017.

Thunell, R., Benitez-Nelson, C., Varela, R., Astor, Y., and Muller-Karger, F., **2007**. Particulate organic carbon fluxes along upwelling-dominated continental margins: Rates and mechanisms, *Global Biogeochemical Cycles*, 21(1). https://doi.org/10.1029/2006gb002793.

Tindale, N. W., and Pease, P. P., **1999**. Aerosols over the Arabian Sea: Atmospheric transport pathways and concentrations of dust and sea salt, *Deep-Sea Research II*, 46(8–9), 1577–1595. https://doi.org/fc6sg3.

Tjallingii, R., Röhl, U., Kölling, M., and Bickert, T., **2007**. Influence of the water content on X-ray fluorescence core-scanning measurements in soft marine sediments, *Geochemistry, Geophysics, Geosystems*, 8(2). https://doi.org/10.1029/2006GC001393.

Tsamalis, C., Chédin, A., Pelon, J., and Capelle, V., **2013**. The seasonal vertical distribution of the Saharan Air Layer and its modulation by the wind, *Atmos. Chem. Phys.*, 13(22), 11235–11257. https://doi.org/10.5194/acp-13-11235-2013.

Turekian, K. K., and Wedepohl, K. H., **1961**. Distribution of the elements in some major units of the earth's crust, *Geological Society of America Bulletin*, 72(2), 175–192. https://doi.org/bwd2ts.

Twohy, C. H., Kreidenweis, S. M., Eidhammer, T., Browell, E. V., Heymsfield, A. J., Bansemer, A. R., Anderson, B. E., Chen, G., Ismail, S., DeMott, P. J., and Van Den Heever, S. C., **2009**. Saharan dust particles nucleate droplets in eastern Atlantic clouds, *Geophysical Research Letters*, 36(1). https://doi.org/10.1029/2008GL035846.

Twomey, S. A., Piepgrass, M., and Wolfe, T. L., **1984**. An assessment of the impact of pullotion and global cloud albedo, *Tellus B*, 36B(5), 356–366. https://doi.org/10.1111/j.1600-0889.1984.tb00254.x.

Van der Does, M., **2018**. Seasonality in Saharan dust particle characteristics across the Atlantic Ocean: transport versus deposition, in: *Saharan Dust from a Marine Perspective - Transport and Deposition along a Transect in the Atlantic Ocean*, PhD thesis.

Van der Does, M., Korte, L. F., Brummer, G. J. A., Brussaard, C. P. D., Van Crimpen, F. C. J., Laan, P., Mahowald, N. M., Merkel, U., Pausch, F., Prospero, J. M., Trimborn, S., Yu, H., Zuidema, P., and Stuut, J. B. W., **2018** Tropical rains control Saharan dust deposition and bio-availability of nutrients, *in preparation for Geophysical Research Letters*.

Van der Does, M., Korte, L. F., Munday, C. I., Brummer, G. J. A., and Stuut, J. B. W., **2016**. Particle size traces modern Saharan dust transport and deposition across the equatorial North Atlantic, *Atmos. Chem. Phys.*, 16(21), 13697–13710. https://doi.org/10.5194/acp-16-13697-2016.

Van der Does, M., Pourmand, A., Sharifi, A., and Stuut, J.-B. W., **2018**. North African mineral dust across the tropical Atlantic Ocean: Insights from dust particle size, radiogenic Sr-Nd-Hf isotopes and rare earth elements (REE), *Aeolian Research*, 33, 106-116. https://doi.org/10.1016/j.aeolia.2018.06.001.

Van der Jagt, H., Friese, C., Stuut, J.-B. W., Fischer, G., and Iversen, M. H., **2018**. The ballasting effect of Saharan dust deposition on aggregate dynamics and carbon export: Aggregation, settling, and scavenging potential of marine snow, *Limnology and Oceanography*. https://doi.org/10.1002/lno.10779.

Van Raaphorst, W., Malschaert, H., van Haren, H., Boer, W., and Brummer, G.-J., **2001**. Cross-slope zonation of erosion and deposition in the Faeroe-Shetland Channel, North Atlantic Ocean, *Deep-Sea Research I*, 48(2), 567–591. https://doi.org/dkp4d3.

Waniek, J., Koeve, W., and Prien, R. D., **2000**. Trajectories of sinking particles and the catchment areas above sediment traps in the northeast Atlantic, *Journal of Marine Research*, 58(6), 983–1006. https://doi.org/10.1357/002224000763485773.

Waniek, J. J., Schulz-Bull, D. E., Blanz, T., Prien, R. D., Oschlies, A., and Müller, T. J., **2005**. Interannual variability of deep water particle flux in relation to production and lateral sources in the northeast Atlantic, *Deep Sea Research Part I: Oceanographic Research Papers*, 52(1), 33-50. https://doi.org/http://dx.doi.org/10.1016/j.dsr.2004.08.008.

Watson, A., Law, C., Van Scoy, K., Millero, F., Yao, W., Friederich, G., Liddicoat, M., Wanninkhof, R., Barber, R., and Coale, K., **1994**. Minimal effect of iron fertilization on sea-surface carbon dioxide concentrations, *Nature*, 371, 143–145. https://doi.org/10.1038/371143a0.

Wefer, G., and Fischer, G., **1993**. Seasonal patterns of vertical particle flux in equatorial and coastal upwelling areas of the eastern Atlantic, *Deep-Sea Research I*, 40(8), 1613–1645. https://doi.org/b8tq2k.

Weinzierl, B., Ansmann, A., Prospero, J. M., Althausen, D., Benker, N., Chouza, F., Dollner, M., Farrell, D., Fomba, W. K., Freudenthaler, V., Gasteiger, J., Groß, S., Haarig, M., B., H., Kandler, K., Kristensen, T. B., Mayol-Bracero, O. L., Müller, T., Reitebuch, O., Sauer, D., Schäfler, A., Schepanski, K., Spanu, A., Tegen, I., Toledano, C., and Walser, A., **2016**. The Saharan Aerosol Long-range Transport and Aerosol-Cloud-Interaction Experiment (SALTRACE): overview and selected highlights, *Bulletin of the American Meteorological Society*, 98(7), 1427–1451. https://doi.org/10.1175/BAMS-D-15-00142.1.

Weltje, G. J., and Tjallingii, R., **2008**. Calibration of XRF core scanners for quantitative geochemical logging of sediment cores: theory and application, *Earth and Planetary Science Letters*, 274(3–4), 423–438. https://doi.org/10.1016/j.epsl.2008.07.054.

Woodward, S., Roberts, D., and Betts, R., **2005**. A simulation of the effect of climate change–induced desertification on mineral dust aerosol, *Geophysical Research Letters*, 32(18). https://doi.org/10.1029/2005GL023482.

Wright, S., and Jeffrey, S., **1987**. Fucoxanthin pigment markers of marine phytoplankton analysed by HPLC and HPTLC, *Marine Ecology Progress Series*, 38(3), 259–266. http://www.jstor.org/stable/24825629.

Yasunari, T. J., Koster, R. D., Lau, W. K. M., and Kim, K.-M., **2015**. Impact of snow darkening via dust, black carbon, and organic carbon on boreal spring climate in the Earth system, *Journal of Geophysical Research*, 120(11), 5485–5503. https://doi.org/10.1002/2014JD022977.

Yeung, L. Y., Berelson, W. M., Young, E. D., Prokopenko, M. G., Rollins, N., Coles, V. J., Montoya, J. P., Carpenter, E. J., Steinberg, D. K., Foster, R. A., Capone, D. G., and Yager, P. L., **2012**. Impact of diatom-diazotroph associations on carbon export in the Amazon River plume, *Geophysical Research Letters*, 39(18). https://doi.org/10.1029/2012GL053356.

Yu, H., Chin, M., Bian, H., Yuan, T., Prospero, J. M., Omar, A. H., Remer, L. A., Winker, D. M., Yang, Y., Zhang, Y., and Zhang, Z., **2015a**. Quantification of trans-Atlantic dust transport from seven-year (2007–2013) record of CALIPSO lidar measurements, *Remote Sensing of Environment*, 159, 232–249. https://doi.org/10.1016/j.rse.2014.12.010.

Yu, H., Chin, M., Remer, L. A., Kleidman, R. G., Bellouin, N., Bian, H., and Diehl, T., **2009**. Variability of marine aerosol fine-mode fraction and estimates of anthropogenic aerosol component over cloud-free oceans from the Moderate Resolution Imaging Spectroradiometer (MODIS), *Journal of Geophysical Research: Atmospheres*, 114(D10). https://doi.org/10.1029/2008JD010648.

Yu, H., Chin, M., Yuan, T., Bian, H., Remer, L. A., Prospero, J. M., Omar, A., Winker, D., Yang, Y., Zhang, Y., Zhang, Z., and Zhao, C., **2015b**. The fertilizing role of African dust in the Amazon rainforest: A first multiyear assessment based on data from Cloud-Aerosol Lidar and Infrared Pathfinder Satellite Observations, *Geophysical Research Letters*, 42(6), 1984–1991. https://doi.org/10.1002/2015GL063040.

Zhao, T., Gong, S., Zhang, X., and McKendry, I., **2003**. Modeled size-segregated wet and dry deposition budgets of soil dust aerosol during ACE-Asia 2001: Implications for trans-Pacific transport, *Journal of Geophysical Research*, 108(D23). https://doi.org/10.1029/2002JD003363.

Zhu, X., Prospero, J. M., Millero, F. J., Savoie, D. L., and Brass, G. W., **1992**. The solubility of ferric ion in marine mineral aerosol solutions at ambient relative humidities, *Marine Chemistry*, 38(1–2), 91–107. https://doi.org/10.1016/0304-4203(92)90069-M.

Bibliography

Peer-reviewed:

Van der Does, M., **Korte, L.F.**, Munday, C.I., Brummer, G.J.A., Stuut, J.B.W., 2016. Particle size traces modern Saharan dust transport and deposition across the equatorial North Atlantic. *Atmospheric Chemistry and Physics* 16 (21), 13697–13710.

Korte, L.F., Brummer, G.J.A., van der Does, M., Guerreiro, C.V., Hennekam, R., van Hateren, J.A., Jong, D., Munday, C.I., Schouten, S., Stuut, J.B.W., 2017. Downward particle fluxes of biogenic matter and Saharan dust across the equatorial North Atlantic. *Atmospheric Chemistry and Physics* 17 (9), 6023–6040.

Guerreiro, C.V., Baumann, K.H., Brummer, G.J.A., Fischer, G., **Korte, L.F.**, Merkel, U., Sá, C., de Stigter, H., Stuut, J.B.W., 2017. Coccolithophore fluxes in the open tropical North Atlantic: influence of thermocline depth, Amazon water, and Saharan dust. *Biogeosciences* 14 (20), 4577–4599.

Schreuder, L.T., Stuut, J.-B.W., **Korte, L.F.**, Damsté, J.S.S., Schouten, S., 2018. Aeolian transport and deposition of plant wax n-alkanes across the tropical North Atlantic Ocean. *Organic Geochemistry* 115, 113–123.

About the author

Laura Franziska Korte was born on October 7th 1986 in Coesfeld, Germany. After finishing school she studied Geoscience at both the University of Münster (BSc) and the University of Bremen (MSc) in Germany. In 2013, she moved to the Netherlands to fulfill her PhD at the Royal Netherlands Institute for Sea Research (NIOZ) on Texel. During her work as a PhD student she participated in three research cruises across the equatorial North Atlantic Ocean and conducted bottle-incubation experiments on one of the cruises.

Next to her work she enjoyed living in the North of Holland and experienced the Dutch culture and windy weather. She liked it so much that she started working at the NIOZ as a postdoc.

Acknowledgements

It is the time to thank all the people who supported, helped and joined me during the last years.

I'd like to start with Jan-Berend. You gave me the unique opportunity to join your dusty team. I totally remember the day when you called me to offer me the position. I was on a student conference in Berlin and didn't know what to say. I thought I was winning the lottery and maybe it was even better than that! I have never regretted my decision to come to Texel. I mean, working on an island where others do their vacations, can't be too bad, right? No, but honestly, all the opportunities you gave us, to join three cruises and attend so many conferences, I enjoyed it and learnt a lot! All your trust and support you had when I had to give a presentation I was so nervous about, gave me a good feeling and made me more confident, many thanks for that!

Geert-Jan, you're next. What I do remember: You were sitting next to me when I had the job interview and when I asked about the cruises to the Caribbean you said: Oh yes, Piña Colada! We've never had that Piña Colada in the Caribbean but at least a few drinks on the ferry back to Den Helder. I'd like to thank you for your support and opinion on the work I did. Especially the effort you put into our 'Amazon' story. It was not always easy to find a good way between your and Jan-Berends point of view, but I'm really satisfied with our final result.

At this point, I'd like to thank the reading committee: Kay Beets, Karin Desboeufs, Cécile Guieu, Tim Jickells, Gerold Wefer, and Guido van der Werf. Thanks for your time reading and evaluating my thesis.

Michèlle, it was a pleasure working with you and sharing an office with you for the last years! Our dust group totally profited from your precision and organising skills. How you make sure that everything is packed for cruises, that (nice!) AirBnB's are booked for conferences, that all needed forms for anything are signed, is just great. Many thanks also for all your very detailed comments on my manuscripts ;) they really made me more conscious about my writing style. But moreover, I'd like to thank you for the fantastic time we've had in the Caribbean. Your 'down-to-earth' attitude and love for the Caribbean made it to unforgettable trips that were fun and enjoyable. And finally, many thanks for being my paranimf. I'm so happy that we finish this together!

Chris, my 'Australian colleague'. You never were annoyed by all my questions and 'difficulties' I had during my work. I could always pop in your office for a chat, thanks for that! Also, I'd like to thank you for your helping hand with the incubation experiment. Your effort was marked by bruises and fairly tanned underarms :) I also

enjoyed the time on the cruises, playing darts and sharing the one or other drink with you.

I'd like to thank people from the OCS and MMB departments. Piet, thank you for your support in the trap lab and the work you did for the leaching experiment. You gave me a good feeling about the chemicals and I could always come back to you with questions. I also would like to thank you for your company during coffee and lunch breaks and that you listened to my Dutch stories.

Sharyn, thank you for all your immediate support in the lab, for your tips and tricks and all your explanations of the analyses! I think also due to your work I really like doing lab work. The same holds for Jort and Ronald. I always liked talking to you about my difficult samples for the elemental analyser. But preparing new series was always fun because I knew that you do your best to analyse the samples.

Furu, I'd like to thank you for your explanations of the technical instruments on our moorings and dealing with this data. Due to your work, I got more insights into the coherence of our data. And I'm looking forward to a good collaboration in the coming year.

Wim and Inge, I'd like to thank both of you for having me as your housemate on Texel. It was not long, but at least I can say that I lived in Den Burg. Wim, also thanks for your approachability and help in the clean lab. And Inge, thanks for your occasional office visits and talks during coffee break. For your future science work I wish you all the best, and don't lose your humour between all the German people ;)

Juliane, it was such an enrichment having you in our dusty team for a short time period! You did so much work during that time so that Michèlle and I could concentrate on our PhD work. Thanks for that!

For the incubation experiment I had a lot of help from Corina and technical support from Anna, Kirsten, and Tessa. Moreover, Scarlett and Franzi, you helped me with planning and organising the experiment as well as with the data interpretation. Without your contribution, I wouldn't have been able to conduct the experiment. Many thanks for that!
I also would like to thank Anne, Catarina, Dirk, Laura, Michèlle, Monica, and Oliver for carrying incubation bottles and/or taking samples.

Karel, Jan, and Patrick, I'd like to thank you for your analysis on board and back at the NIOZ. I could always come back to you to ask for extra explanation. Bob, thanks for all your amazing work on the cruises. Especially for buoy Laura of which you

fixed the electronics so that she was able to sample again. Rineke, I like to thank you for your help with the XRF scanner. And Evaline, thanks for analyzing the pigment concentration in our sediment trap samples.

Many thanks to our students and interns Korinna, Katharina, Fleur, Monica, Hans, Dirk, Jaap, and Oliver who helped in the lab and joined cruises.

I also would like to thank the ship's crews and technicians I sailed with. Jan-Dirk, Yvo, Leon, and Barry, thanks for all your work on board, especially for deploying and retrieving sediment traps and buoys. Also, many thanks to all technicians I met in the workshop. Edwin, Roel, Martin, Frank, and Johan, thanks not only for your work on constructing the buoys but also for your excellent work on building and fixing all the bits and pieces we needed in the lab.

Marijke, I'm so glad that we 'started talking' at EGU in 2016. Although it was quite late in our NIOZ career, I enjoyed all the little breaks we've had together at the reception. But not only at NIOZ, also outside, it was good talking to you and having you as a friend. You're a good listener and your understanding of stuff showed me that we're often in the same boat. I wish you all the best for your future!

Catarina, my Portuguese friend. I'm so happy that our paths have crossed at the NIOZ. I'd like to thank you for all your help, discussions and talks we've had via various channels. Your love of science is remarkable. And to me, it's still a miracle how you find the time for everything. Besides your endurance on writing proposals, you still find time discussing data with me, being funny and relaxing. It's great working with you and I'm glad to have you as my paranimf. Beijos!

Toni und Frank, seit Bremen seid Ihr wahrscheinlich die zwei, die am meisten davon mitbekommen haben, wie es für mich war auf Texel zu arbeiten. Auch wenn wir uns im Moment nicht häufig sehen, es ist toll, Freunde zu haben, die für einen da sind, wenn man sie braucht. Ich danke euch dafür!

Auch alle meine Freunde zu Hause: Allison, Nathalie, Rebecca, Isabel, Sara, Kerstin. Es ist so schön euch zu sehen oder mit euch zu telefonieren, auch mit längeren Pausen dazwischen wo man sich eigentlich gar nicht sieht oder spricht. Ihr macht es mir sehr einfach wieder dort anzuknüpfen, wo wir aufgehört haben. Danke!

Nanni, ich bin so froh, dass wir uns in Den Helder getroffen haben! Obwohl wir uns ja gar nicht kannten, hatte ich direkt das Gefühl, dass wir uns einfach verstehen. Danke für Dein offenes Ohr und guten Ratschläge.

Adri, thanks for your blunt honesty and your incredible support. Your confidence and modesty calmed me down and made me realize that everything is relative. You're amazing!

And last but not least, I'd like to thank my family: Mama, Papa, Britta, Sven, Bennet und Joris, ich danke euch so sehr für Euer Vertrauen und Eure stetige Unterstützung. Ich konnte immer auf Euch zählen, sei es zu den praktischen Dingen, wie den unzähligen Umzügen oder den Fahrten zu Bahnhöfen um mich wegzubringen oder abzuholen, oder auch Eure zahlreichen Besuche in Den Helder. Ich wusste zu jeder Zeit, dass ich auch dort nicht allein bin. Und es ist so toll, wenn die Kinder einem voller Freude zeigen, dass das Meerwasser in Den Helder salzig schmeckt :) Danke!